Investigations into the Carbon Nanotube/Silicon Heterojunction Solar Device

By

Tom Stewart Lane Grace

Thesis
Submitted to Flinders University
for the degree of

Doctor of Philosophy

College of Science and Engineering

29-01-2020

Table of Contents

List of Figures

List of Tables

List of Equations

Acknowledgements

I will first acknowledge that the research and thesis writing components of my PhD took place on the land of the Kaurna people. I acknowledge the Elders, families and forebears – the traditional owners and custodians. Their land was stolen and never ceded. It always was, and always will be, Aboriginal land.

I would like to acknowledge Flinders University for the opportunity to peruse my PhD candidature. I would also like to thank Flinders University, the Research Higher Degree Scholarship and the Australian Government Research Training Program Scholarship for financial assistance during my candidature. Additionally, I would like to acknowledge Associate Professor Prahant Sonar from Queensland University of Technology, and Professor Lianzhou Wang from The University of Queensland for supplying DAD and MoO_x interlayer materials respectively.

I would like to thank Dr. Mahnaz Dadkhah Jazi, Dr. Christopher Gibson, Dr. Jason Gascooke, Dr. Ashley Slattery, and Dr. Cameron Shearer for their support and assistance with technical equipment and their expertise. I would also like to thank my other colleagues in the institute for Nanoscale Science and Technology at Flinders University for their support and assistance. Additionally, the technical staff at Flinders Univeristy were invaluable support in a range of areas. A special mention goes out to Sandra Marshall and Mel Schlein from for being incredibly helpful on many occasions.

I would like to thank Dr. LePing Yu for being alongside me for the majority of my PhD journey. Without his input and support, both scientific and personal, this thesis would not be the way it is today. Also, thanks goes to Prof. Jamie Quinton for help and support on multiple occasions throughout my candidature.

Special thanks goes to Dr. Daniel Tune, my adjunct supervisor, for assisting with experimental design and thesis writing and editing. Not to mention for teaching me many important laboratory techniques prior to starting my PhD. Dr. Tune also wrote the custom program I used to analyse my device results.

Heartfelt thanks go to my principal supervisor Professor Joe Shapter for guiding me on my PhD journey and putting up with me through a variety of experimental and technical problems. Also for his invaluable input in structuring my PhD process and for reviewing my thesis more times than anyone would want to. I am incredibly grateful.

Thanks must also go to my incredibly supportive friends and family, who have given unflinching and invaluable support, both emotional, and through helpful editing, throughout my journey. To my loving parents, Heather and Colin, I thank you for providing me with a house to live in and food to eat as well as continual support throughout my PhD. To my dearest friend Helen, I thank you for your unwavering and fierce support during the toughest moments of my journey. To my friends who have shared my journey through science education: Emma, Callum, Connor, Alex, Cheylan, Jade, Renzo, Ruby, Belinda, Zoe, Liam, and Russell as well as those friends from other walks of life: Sean, Ben and Cassy, for helping me with scientific support when needed, emotional support when needed, and distractions when needed. I couldn't have done it without any of the above people.

Gratitude also goes to my friends in my other life pursuits for being supportive and understanding when my focus was elsewhere and my time was limited by PhD.

“Perhaps nanotubes are the tool of the Gods; conversely, they may just be for mortal men. What’s important is that they are the greatest thing of all time. They are brilliantly fantastical tubular wonders that just do a swell job at anything you could possibly think of. The glory of carbon nanotubes is second to none. They can transport electrons like it’s their lifelong passion and their strength rivals Superman. They truly are the greatest discovery in the history of the universe and I, for one, welcome our new carbonaceous overlords.”

-Tom Grace, 2017

Declaration

I certify that this thesis does not incorporate without acknowledgment any material previously submitted for a degree or diploma in any university; and to the best of my knowledge and belief, does not contain any material previously published or written by another person except where due reference is made in the text.

Publication declaration

Sections of this thesis were published, in whole or in part, during the PhD research time period.

Large sections from the introduction chapter were published in a chapter titled "Use of Carbon Nanotubes in Third-Generation Solar Cells" in a text book titled *"Industrial Applications of Carbon Nanotubes"*, edited by Huishen Peng, Qingwen Li and Tao Chen. The book was published by Elsevier in 2017.

The research presented in the first research results chapter: Nanotube Wall Number Effects were published as a research paper entitled *"Investigating the Effect of Carbon Nanotube Diameter and Wall Number in Carbon Nanotube/Silicon Heterojunction Solar Cells"*. The work was published in the journal *Nanomaterials* in 2016 and the leading author was the author of this thesis.

Abbreviations/Chemical Names

AFM: Atomic Force Microscopy

AP: As Prepared

BOE: Buffered Oxide Etch

BWF: Breit-Wigner-Fano

CNT: Carbon Nanotube

CNT/GO: Carbon Nanotubes and Graphene Oxide

DeS: Diethyl Sulfide

DAD: 4,10-bis(bis(4-methoxyphenyl)amino)naptho[7,8,1,2,3-*nopqr*]tetraphene-6,12-dione

DOS: Density of States

DWCNT: Double-Walled Carbon Nanotube

GO: Graphene Oxide

HF: Hydrofluoric Acid

HOMO: Highest Occupied Molecular Orbital

J_{SC}: Short Circuit Current Density

LUMO: Lowest Unoccupied Molecular Orbital

MCE: Mixed Cellulose Ester

MWCNT: Multi-Walled Carbon Nanotube

PANI: Polyaniline

PCE: Percent Conversion Efficiency

PEDOT:PSS: Poly(3,4-ethylenedioxythiophene)-poly(styrenesulfonate)

PS: Poly(styrene sulfonate)

RBM: Radial Breathing Mode

R_{series}: Series Resistance

R_{shunt}: Shunt Resistance

SDS: Sodium Dodecyl Sulphate

SEM: Scanning Electron Microscopy

$SOCl_2$: Thionyl Chloride

SWCNT: Single-Walled Carbon Nanotube

Triton X-100: Polyethylene glycol *p*-(1,1,3,3-tetramethylbutyl)-phenyl ether

VHS: Van Hove Singularities

V_{OC}: Open Circuit Voltage

Abstract
The search for novel solar cell designs as an alternative to standard silicon solar cells is important for the future of renewable energy production. One such alternative design is the carbon nanotube/silicon (CNT/Si) heterojunction solar device. In this thesis, various aspects of the CNT/Si device are investigated. The history of these devices is catalogued, with a focus on the electronic properties of the heterojunction and the use of chemical dopants, conductive interlayers and light trapping layers to improve those properties.

For the first experimental investigation, a comparative study was performed between single walled, double walled, and multi walled CNTs (SWCNTs, DWCNTs, and MWCNTs) with different wall diameters. The majority of previous research on the CNT/Si device has used SWCNTs, although some research has looked into CNTs with multiple walls. However, there has not been much comparative work done to determine the optimal number of walls to use. Previous work used different techniques to suspend different CNT species and thus created an additional variable making it difficult to directly compare the effect of CNTs with different wall number on device efficiency. The work presented in this thesis found that large diameter SWCNTs give the best CNT/Si device performance. The main reason, in this study, for their superior performance was an ability to form a homogeneous, concentrated suspension in an aqueous solution with a 1 % surfactant concentration. Additionally, it was found that, whilst chemical *p*-doping gave significant conductivity improvement to SWCNT and DWCNT films, the effect is muted somewhat on MWCNT films, likely due to the shielding effect the outer tube has on the inner tubes.

The morphology of CNT films is an important factor in device performance. Previously, the films have been prepared via vacuum filtration from aqueous suspensions. Whilst this enables strong films to be formed quickly, they are highly disordered on the micron scale, with many charge traps and gaps forming in the films. It has been previously established that lowering the filtration speed enables more ordered films to be formed. Research is presented in this thesis on the use of slow, gravity filtration to improve the morphology of CNT films used in the CNT/Si device. A comparison was performed with

devices fabricated with both slow and fast filtered SWCNT films. It was found that slow filtration can produce similar photovoltaic results with thinner films. However, it was also found that slow filtration causes significant macroscale inhomogeneity of the CNT films, with concentrated thick regions, surrounded by larger thinner areas. Thus, slow filtration did not form films of uniform light transmittance over an extended area, causing an increase in the variation in performance between individual devices compared to fast filtered films. By using atomic force microscopy (AFM) and scanning electron microscopy (SEM), it was determined that there was no large improvement in directional organisation of the CNTs on the microscale. However, the films were found to be much smoother on the microscale, with arithmetic and root mean square average height deviation values roughly 3 times lower for slow filtered films compared to fast filtered films.

A major focus of this thesis is on scaling up the active area of CNT/Si devices. This is an important step on the road to commercial use. The vast majority of research has been on CNT/Si devices with small active areas (<< 1 cm^2). This is suitable to test the viability of CNT/Si devices, to analyse junction properties and to examine the effect of various chemical dopants, interlayers and coatings. It is notable, however, that the best performance results were achieved with devices with smaller active areas. Thus, it is important to analyse the effect of increasing the active area. To this end, a CNT/Si device design was produced with an active area of 1.5 × 1.5 cm (2.25 cm^2). Initially, this design was found to perform significantly worse than the smaller area devices. The addition of a gold grid across the CNT/Si junction to enhance the CNT film's ability to transport charge was found to provide significant improvement. The addition of an aluminium back contact was also performed to improve homogeneity between devices.

The biggest factor limiting the performance of large area devices compared to small area devices was a significantly lower short circuit current density. This was determined to be due to multiple factors, the largest of which was inhomogeneity in the light spot used to illuminate the devices for testing. A 2D map of irradiance was measured for the spot, and it was found that irradiance decreased radially

outwards from the centre. This phenomenon had a more pronounced negative effect on the large area devices as more of the light spot was required for total illumination. Inherent device performance decreases due to power loss over the active area were another cause of lower short circuit current densities.

In order to further improve the performance of the large area CNT/Si devices, a series of materials were trialled for use as an interlayer between the CNT film and the silicon surface. Various materials have been used in previous CNT/Si device research to improve junction performance, the current carrying properties of the CNT film, or both. The interlayer materials studied in this thesis were two conducting polymers which have been previously used in CNT/Si devices: Poly(3,4-ethylenedioxythiophene)-poly(styrenesulfonate) (PEDOT:PSS) and polyaniline (PANI). A novel organic material, 4,10-bis(bis(4-methoxyphenyl)amino)naptho[7,8,1,2,3-*nopqr*]tetraphene-6,12-dione (DAD) and two inorganic materials: copper thiocyanate (CuSCN), and molybdenum oxide (MoO_x) were also implemented. Additionally, devices were produced with a thin gold film in place of the CNT film to test the effect of the interlayers with an alternative conductive film. Overall, the effects of each interlayer were examined and compared with physical properties of the interlayers determined from SEM and AFM imaging. The interlayer thickness was varied for each material to determine an optimal thickness for device performance.

CHAPTER 1 INTRODUCTION

The search for efficient, low-cost renewable energy sources is one of great importance in the modern world. As the conventional fossil fuel sources of electricity become scarcer, and are discovered to cause more and more severe problems for our planet's climate, it becomes all the more imperative to seek out new and innovative ways of exploiting sustainable resources.[1]

Solar power is one of the most promising renewable sources of electricity and has the potential to solve some, if not all, of our planet's energy concerns. The sun is a reliable and renewable energy source, which is present throughout the world and will exist for long enough that it can be considered a never-ending source of energy. In addition, solar power technology is already being used to produce electricity in many locations around the globe, with the top five countries (in terms of both photovoltaic (PV) and concentrated solar thermal power generation) coming from every continent except South America and Australia at the end of 2013[2]. PV devices, which convert solar energy directly into electrical energy, have been shown to have great potential in smaller scale electricity generation applications, such as individual buildings and facilities, as well as on portable devices. PV cells are also one of the two main methods for electricity generation on space vessels, along with nuclear fission.

In producing energy, PV devices do not consume fuel or produce waste and, due to their lack of moving parts,[3] they require little maintenance once established. In addition, PV technology will reduce the reliance on an electricity grid system. This would significantly improve the efficiency of our energy use, as about 25% of produced electricity is currently lost in distribution.[4] However, there are some significant disadvantages of current commercial solar cells. Firstly, silicon solar panels have a high manufacturing cost[5] due to the need for high purity, processed silicon to produce high efficiency solar panels. Whilst other semiconducting materials may be used in PV devices, they will generally consist of alloys of rare and/or toxic elements such as arsenic, cadmium, indium, gallium, germanium, and ruthenium.[4-6] As rising coal, gas, and oil prices make solar cells more competitive, it is preferable to conduct research into modifying solar cells to make them cheaper and more efficient to boost

economic viability. Some methods of improving the economic viability of solar capture technology involve investigating solar cells containing organic molecules, quantum dots, or dye-sensitised solar cells (DSSCs).[7] Carbon nanotubes (CNTs) have been incorporated into a variety of device designs in an effort to improve performance. CNTs have been incorporated into DSSCs as a replacement for other expensive and inefficient electrode materials.[8] Additionally, thin films of CNTs have been incorporated as transparent electrodes and hole-collecting layers in devices such as flexible polymer-fullerene cells[9], P3HT-PCBM devices,[10] and as a replacement for complex metal hole collecting electrodes such as In_2O_3:Sn (ITO).[11] CNTs have also been incorporated into the rapidly growing field of perovskite solar cells, giving improvements in efficiency as well as a decrease in thermal degradation and hysteresis along with improved stability.[12, 13] This thesis will examine a novel solar device design where *p*-doped CNTs replace the *p*-doped silicon layer in a silicon *pn* junction solar cell.

1.1 Carbon Nanotubes

CNTs are tubes of a hexagonal carbon lattice structure. They have a very high aspect ratio which allows them to be classed as one-dimensional objects.[14] CNTs possess a wide range of unique and interesting properties such as high charge carrier mobilities, ballistic transport properties, high optical transmittance, and low light reflectance. The band gap of semiconducting CNTs varies over a wide range (from around 0.5 eV to around 10 meV[15]) and CNTs demonstrate photoelectrochemical effects under light irradiation.[16-21] In addition to the above properties, CNTs are highly resistant to damage, whether it be mechanical, chemical, or radiation induced.[17] Coupled with their potential low cost due to the abundance of carbon[22] and a steady increase in their commercial availability,[14] it is clear why they are an exciting material for research.[1] These properties mean that CNTs have been considered for a wide range of applications, from structural support to energy storage devices or even artificial muscles.[23] Solar cells consisting of a heterojunction between a silicon (generally *n*-doped) substrate and a CNT film have been shown to be an appealing prospect for the future of solar energy capture technologies.[24, 25] In the following thesis, research on these devices will be reviewed and research on the CNT/silicon solar device will be presented and discussed.

1.1.1 Carbon Nanotube Discovery and Potential

CNTs were first reported by Iijima *et al.* in 1991 and were produced by arc-discharge from a carbon electrode.[26] CNTs are an allotrope of carbon, consisting of a rolled-up sheet of graphene**.** As a novel nanomaterial, they have attracted a lot of interest due to their interesting properties, both in terms of strength[27] and electrical properties.[15, 28, 29] CNTs possess high tensile strength, significantly higher than conventional carbon fibre.[30] CNTs are also excellent conductors, with the ability to ballistically conduct electrons along the long axis.[15] When formed into sheets or films they exhibit high optical transmittance, low light reflectance, and individual tubes have been shown to exhibit photoelectrochemical effects under light irradiation.[16-19, 21, 22, 31, 32]

Due to their remarkable properties, CNTs have been incorporated into many technologies and used in various scientific fields.[33] CNTs can be incorporated in other structures to form nanocomposites,[29] including in industrial epoxy to give a 70% increase in thermal conductivity,[34] in collagen-CNT composites for scaffolds in medical applications,[35] and as a replacement outer conductor material in coaxial cables to greatly reduce cable weight.[36] Alternatively, CNTs are formed into fibers, films or arrays and used in a variety of electrical or energy based devices. For example, CNT films for use in touch screens and energy-storage devices are nearing the commercial application stage.[37] So far, it is likely that we have only scratched the surface of the possible applications of CNTs and it can be expected that many more products incorporating CNTs will become available over the next few decades.

CNTs can also be functionalised at surface defect sites, by covalently reacting molecules with the tubes, formation of noncovalent complexes via polymer wrapping or mixing with surfactants, and 'endohedral' functionalisation, where molecules are placed inside the tube.[38] Functionalisation of CNTs allows them to enter suspensions and be otherwise incorporated into other materials to increase the scope of CNT application. Polymerisation can be performed from the surface of CNTs after functionalising with methyl methacrylate or *tert*-butyl acrylate initiators. Additionally, these surface functionalisations lead to CNTs being soluble in organic solvents or water.[39] Functionalisation of

CNTs allows them to be incorporated into polymer matrices without aggregation,[40] and to be conjugated with proteins for utilization in bionanomaterials.[40] Functionalised nanotubes have been shown to be able to immobilise specific proteins or other biomolecules.[41]

1.1.2 Carbon Nanotube Characterisation

There are a few key parameters, which can be used to describe and define different groups of CNTs.

1.1.2.1 Number of Walls

Firstly, CNTs can be described by the number of concentric tubes present. The general image of a CNT consists of a single tube of hexagonally bonded carbon and is known as a single-walled CNT or a SWCNT. This is the most commonly used CNT species in this thesis. Other types of CNTs consist of multiple cylinders of nanotubes and are collectively known as multi-walled CNTs or MWCNTs. Often CNTs with two sets of walls are described as double-walled CNTs or DWCNTs.[42] A visual representation of SWCNTs, DWCNTs, and MWCNTs, can be seen in Figure 1-1. The multiple walls in MWCNTs (and DWCNTs) can be organised in one of two ways. The most commonly observed arrangement is where concentric cylinders of decreasing radius are assembled within each other. This organisation is known generally as the 'Russian Doll' model.[30] The alternative arrangement is where a single sheet of graphene has been rolled upon itself multiple times, producing a spiral organisation of the hexagonally bonded carbon sheet. This organisation is generally called the 'Parchment' model and is often referred to as a 'nanoscroll' rather than a nanotube.[30, 43]

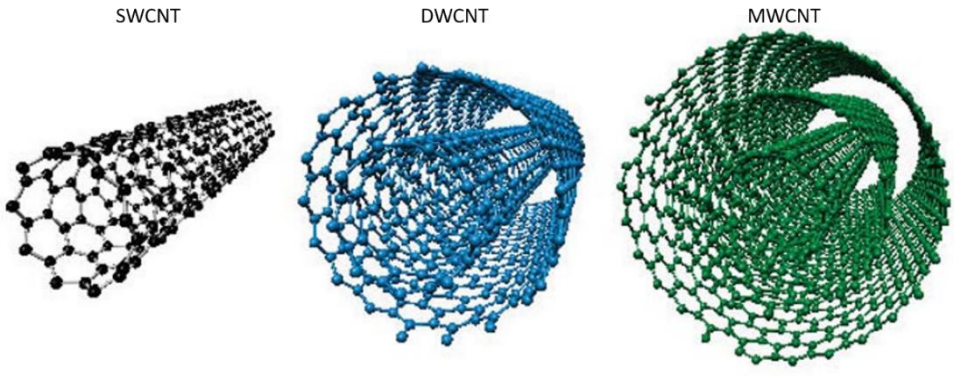

Figure 1-1: Ball and stick models of a SWCNT, a DWCNT and an MWCNT.[44]

1.1.2.2 Chirality

SWCNTs are further segregated by describing the precise orientation of the carbon hexagon structures present in the tube. CNTs are a rolled up sheet of hexagonally bonded carbon (graphene) and thus can

be rolled in various orientations.[43, 45, 46] When SWCNTs are considered, the orientation of the hexagons in the SWCNT with respect to the long axis is referred to as the 'chirality' of the SWCNT, and has a large effect on the electronic characteristics of the SWCNT.[1, 20, 43, 45, 47-49] Some of the nanotube orientations act as a metal, however the majority of nanotubes chiralities are semiconducting in nature. In some of these cases, the bandgap is so small that the nanotube exhibits quasi-metallic properties at room temperature. [5, 50-52]

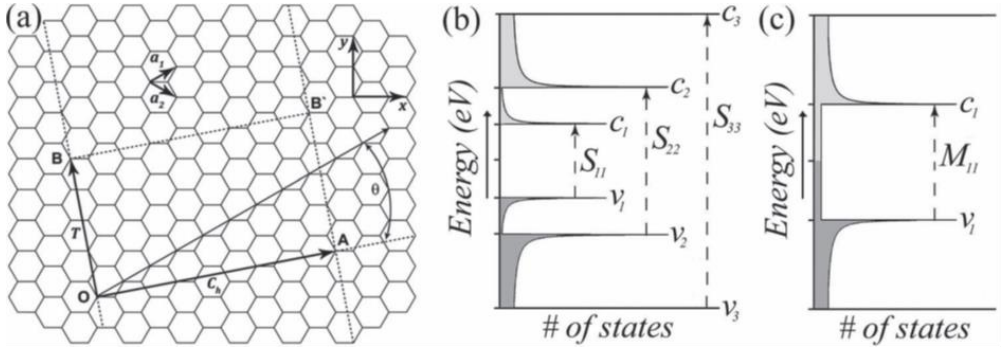

Figure 1-2: a) An unrolled SWCNT, showing the chiral vector OA (C_h) and the translational vector OB (T), the graphene lattice vectors in real space (a1 and a2) and the chiral angle (θ). The SWCNT in this example is a (4,2) nanotube.[1] b) and c) show density of state diagrams for a semiconducting (b) or a metallic (c) SWCNT.[24]

SWCNT chirality is described by referring to a chiral vector present in the structure, examples of which are shown in Figure 1-2 a) and Figure 1-3. The chiral vector, C_h, can be used to fully describe a SWCNT with the exception of its length. The vector itself is described using the equation $C_h = m\boldsymbol{a_1} + n\boldsymbol{a_2}$ where the integers *n* and *m* (often combined into a bracketed (*n*,*m*) descriptor) represent the number of steps along the carbon lattice and the vectors $\boldsymbol{a_1}$ and $\boldsymbol{a_2}$ are the graphene lattice basis vectors in real space (see Figure 1-2 a)).[53] In general, the larger *n* and *m* are, the larger the diameter of the SWCNT.[14] The chiral vector makes an angle with the basis vector $\boldsymbol{a_1}$ that is known as the chiral angle θ. The chiral angle is an important descriptor for the orientation of the SWCNT in question. The chiral angle can vary between 0° and 30° and forms two limiting cases at these extremes. These cases are known as 'zig-zag' at 0° and 'armchair' at 30°. These names are derived from the orientation of the carbon hexagons at these two extremes. There also exists many conformations where the chiral angle lies between 0° and 30° and these are known simply as 'chiral' SWCNTs[42], see Figure 1-3.

FIGURE REMOVED COPYWRITE PERMISSION NOT OBTAINED

Figure 1-3: Depiction of SWCNT chiral orientations with accompanying chiral angles and example (n,m) tube parameters.[54]

1.1.2.3 Fabrication Method

In the past, CNTs were an exotic material and were not commonly available.[14] They were produced by techniques such as carbon vapour growth from arc-evaporation of metal-doped carbon electrodes,[55-57] laser vapourisation of metal-doped carbon targets,[58, 59] or via catalytic deposition of carbonaceous gaseous molecules such as C_2H_4, CO, and CH_4. These methods produced nanotubes at relatively low rates (grams or even milligrams per hour).[58, 60, 61] Thanks to the large amount of research encouraged by the exciting properties of CNTs, this has changed in the years since their discovery. CNTs are now widely available due to industrial-scale production techniques such as, catalytic chemical vapour deposition (CCVD), high pressure carbon monoxide (HiPco) growth, and Co-Mo catalyst (CoMo CAT) growth methods.[33, 58, 62, 63]

The method by which SWCNTs are manufactured leads to different selections of nanotube chiralities being produced. Originally, SWCNT manufacturing methods were not able to produce chiral specific SWCNTs (generally producing a ratio of roughly 2:1 semiconducting:metallic SWCNTs).[14, 52] However, as more and more uses of CNTs were discovered, the desire to grow nanotubes of specific structure, chirality, and morphology increased.[46] The optimisation of fabrication methods that produce chiral specific SWCNT species is on-going, with research being conducted in a range of areas including: “cloning” from open-ended SWCNTs as the catalysts,[64] growing using specifically chosen template molecular precursors,[65] and chemical vapour deposition (CVD) growth on structurally matching catalyst substrates.[33, 46, 66, 67] Alternatively, post fabrication techniques such as surfactant wrapping gel chromatography,[68] selective chemical functionalisation and separation,[69] selective destruction by diameter or chiral angle,[69] electrophoretic separation[69] and, more recently, selective dispersion via polymer wrapping[70] can be used to separate pre-grown SWCNTs by wall number. Thus, enriching a given sample by SWCNT electronic type (metallic or semiconducting) and increasingly by chiral species specifically is becoming more and more viable.

1.1.3 Photoelectrical Properties of CNTs

Carbon nanotubes are a one-dimensional material, and this gives them unique properties when compared to bulk materials such as silicon. The electrons are confined, due to the 1D nature of the CNTs, and this leads to the formation of spikes in the electronic density of states of the tube, called van Hove singularities (VHS), see Figure 1-2 b) and c). These operate somewhere between standard valence and conduction bands, and highest occupied molecular orbital (HOMO) and lowest unoccupied molecular orbital (LUMO) levels of an aromatic system.[14] In semiconducting SWCNTs, the VHS give rise to a series of distinct optical transitions (S_{11}, S_{22} … S_{nn}) with the exact excitation wavelength dependent on the properties (tube diameter and chirality) of a given tube. This allows the use of optical absorption and fluorescence spectra to probe a nanotube sample for different semiconducting species. It has been shown that the absorption of photons at these optical transition energies give rise to closely linked electron-hole states or Frenkel excitons with binding energies of less than 1 eV for S_{11} transitions[14, 71-73] although some tubes have higher S_{11} binding energies. Metallic SWCNTs also possess a series of optical transitions (M_{11}, M_{22} … M_{nn}) but there is no band gap analogous to a 3D semiconductor, unlike semiconducting SWCNTs, and thus the use of optical absorbance and fluorescent spectra to identify chiral species is not applicable.[14]

The semiconducting (s-) and metallic (m-) SWCNT optical transitions are important to consider when using SWCNT films in photovoltaic devices, as there will be some species which will absorb across the same wavelengths as silicon, and thus will interfere with photovoltaic performance (unless the SWCNTs are themselves contributing photocurrent). Larger diameter SWCNTs, such as those produced via arc-discharge of a carbon electrode, will possess optical transitions at around 1850, 1050, and 700 nm for the first two transition orders (S_{11} and S_{22}) of s-SWCNTs and the first transition order (M_{11}) of m-SWCNTs respectively. Whereas, for smaller diameter tubes produced via the HiPCO method the transitions occur at lower wavelengths.[14] It is important to consider the optical spectra of the nanotube sample before use in a photovoltaic design to ensure as little spectral overlap as possible for optimal performance.

1.2 Carbon Nanotube/Silicon Heterojunction Solar Devices

Carbon nanotubes were first incorporated into photovoltaic devices as nanoscale fillers in a polymer matrix to provide an electron transport path, or as a transparent conducting electrode for hole collection.[23, 25, 74-76] In these applications the nanotubes did not participate in the generation of a photocurrent; they merely assisted in the transport of already generated photoelectrons.[25, 74, 75] This thesis looks at a device architecture in which CNTs not only transport charge carriers but also assist in forming the junction to separate and collect photovoltaic charge carriers.[24, 77, 78] In such devices, the Fermi level equilibrates at the junction between the nanotubes and the silicon, causing band bending of the silicon and the generation of a depletion layer. This built in potential separates electron-hole pairs (excitons) which are produced when photons are absorbed by the silicon.[79] These devices are generally called carbon nanotube/silicon heterojunction solar devices (CNT/Si heterojunction devices or CNT/Si devices). The first such devices were designed by Wei *et al.* in 2007[25] using DWCNTs deposited via water expansion and aqueous film transfer of a film made of CVD DWCNTs,[24, 25] (Figure 1-4). Similarly, in 2008, Arena *et al.* used CVD grown MWCNTs to form a CNT/Si heterojunction.[23] Whilst these devices had a photo-conversion efficiency of only 1.3%[25] and 3.0%[23] respectively (compared to commercial devices at 20-30%) many improvements have since been made to the device design and doping methods, with 15% efficiencies reported in 2012,[7] and 17% efficiencies reported in 2015.[16, 80] Thus, in less than a decade the device efficiency was improved by a factor of 10. This rapid improvement, coupled with potential cost savings and the relative simplicity of the junction structure, compared with multilayer DSSCs and perovskite devices, are the reasons for much excitement around this device design. In addition, these devices are exciting for future research as their manufacturing process is both simple and scalable.[77]

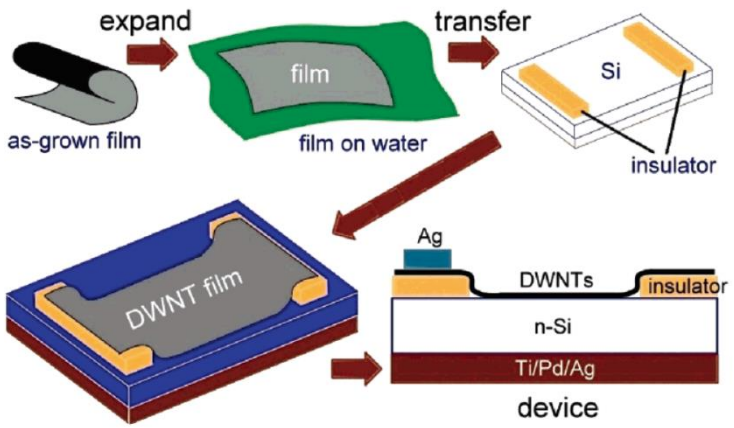

Figure 1-4: Fabrication and final device schematic for the first CNT/Si device produced by Wei *et al*.[25]

1.2.1 Improvements on the CNT/Si Heterojunction Solar Device

The typical architecture for these devices is much like that of a single junction crystalline solar device with the emitter layer replaced by a film of *p*-doped CNTs.[24] Whilst the initial design used DWCNTs, most designs use SWCNTs, however MWCNTs may also be used.[77, 81] In all these cases the CNT film acts as a component of the heterojunction to set up a built-in potential and enable charge separation, as a highly conductive network for charge transport and collection, and as a transparent electrode to allow good light illumination of the silicon and thus good photocurrent generation.[37, 77]

The energy generation within photovoltaic devices is a complex process which involves several steps including photon absorption, charge separation, charge transport, and charge collection.[82] As such, there are a large number of effects that must be examined in order to attain higher efficiency devices. The record efficiency for CNT/Si devices has risen considerably since their first use in 2007. The first significant improvement was made by the same research group who had initially published the device. Jia *et al.*[77] achieved an efficiency of 7.4 % from DWCNT/Si devices. This was done by substituting the original mica window with a much thinner silicon oxide (SiO_x) window, allowing the nanotube film to sit more smoothly on the silicon surface.[24]

In 2010, Jia *et al.*[83] performed the first comparison between SWCNTs, DWCNTs, and MWCNTs for use in CNT/Si devices in terms of area density of the films. It was found that SWCNTs are superior to MWCNTs at low densities. It was also found that the density (and thus optical transmittance) is highly important in the performance of these devices. Increasing film transparency (lowering CNT density)

increases the efficiency of the devices by allowing more light to reach the silicon, whilst decreasing the transparency (increasing the CNT density) increases the efficiency by lowering the sheet resistance across the film.[24, 83] Thus, some optimal thickness must exist to achieve maximum efficiency as discussed further later in this chapter (Figure 1-18). This research team also found their DWCNT devices to be significantly superior to both the SWCNT and MWCNT devices. However their DWCNT films were produced using a different method to the SWCNT and MWCNT films[83]. This makes it difficult to draw a good comparison, as the nanotube film properties are highly dependent on film morphology.[24]

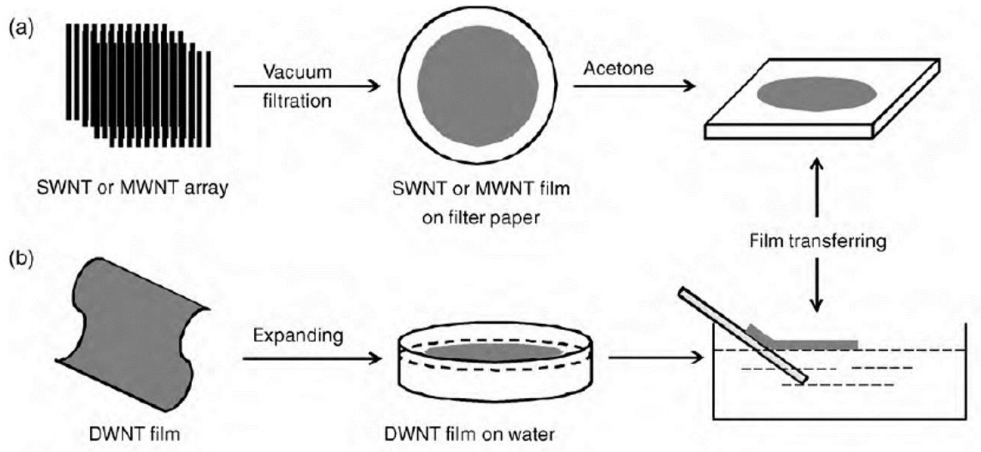

Figure 1-5: Comparison of film formation processes between: a) standard vacuum filtration of CNTs, and b) flotation of self-assembled DWCNT films. From the wall number comparison work by Jia *et al.*[83]

Wadhwa *et al.*[84] used SWCNTs to produce a CNT/Si device with an efficiency of 8.5% in 2010. This efficiency was improved to 11% by the use of an electrolyte gate, consisting of a second SWCNT film on a gold electrode, connected to the photoactive junction via an electrolyte solution of 1-ethyl-3-methylimidazolium bis(trifluoromethylsulfonyl)imide (Figure 1-6). By changing the bias on the gate electrode, the open circuit voltage (V_{OC}) for the device could be adjusted reversibly, leading to a range of efficiencies from 11% (at a bias of -0.75 V) to 4% (at a bias of 0.75 V).[84] This effect is caused by the gate-induced modulation of the SWCNT Fermi level and enhancement or suppression of the interface dipole at the CNT/Si junction.[24, 84] Additionally, in 2011, Wadhwa *et al.*[79] found that by applying only a sparse grid of CNTs, as opposed to a continuous film, and applying an ionic electrolyte to the junction, PCE values of up to 12% could be achieved with a gate voltage of -0.75 V. The

electrolyte serves as a capacitor, raising the capacitance of the system set up by the nanotube-silicon Fermi level offset.[79] The system also has the additional advantage of having large open areas, where a greater percentage of photons will be able to interact with the silicon surface. This increased photon incidence was displayed by an increase in short circuit current density.[79]

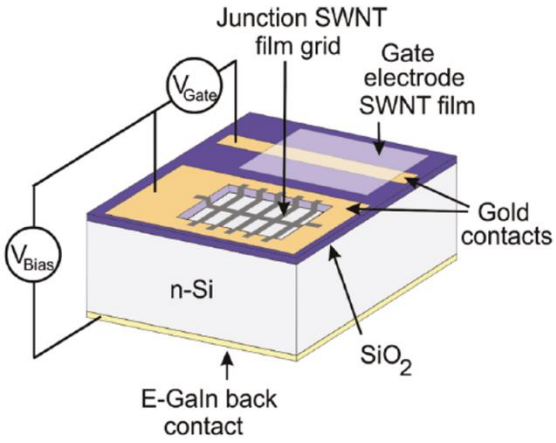

Figure 1-6: Schematic of the gated CNT/Si device used by Wadhwa *et al*. Not shown is the liquid ionic electrolyte that extends across both the gate electrode, CNT film and the n-Si junction.[79]

1.2.2 Nanotube Film Doping

One of the major techniques through which large improvements have been gained in the CNT/Si heterojunction device is via chemical doping of the CNT film. The doping of CNTs in this thesis, refers exclusively to chemical treatment of the CNT films post device fabrication. Although CNTs can also be doped by the addition of different species via substitution of the carbon atoms in the lattice,[85, 86] intercalated between CNTs in a bundle or by endohedral doping (encapsulation within the core of the CNT)[14, 87]. In 2008, Li *et al*.[74] found that post-fabrication treatment of their SWCNT layer with the *p*-dopant thionyl chloride ($SOCl_2$) increased the power conversion efficiency of the devices by over 45 % (see Figure 1-7) by lowering the sheet resistance, and increasing the short circuit current density and open circuit voltage. Hall Effect measurements showed that the $SOCl_2$ treatment lead to an increase of carrier density from 3.1×10^{15} cm^{-2} to 4.6×10^{17} cm^{-2} and an improvement from 0.23 $cm^2\ V^{-1}\ s^{-1}$ to 1.02 $cm^2\ V^{-1}\ s^{-1}$ of the effective mobilities[24, 74] In addition, it was found that $SOCl_2$ treatment adjusted the Fermi level and shifted the major conduction mechanism in the SWCNT layer from hopping towards tunnelling.[88, 89] This was the first of many research papers to investigate using doping materials to improve the conductivity or transparency of the CNT film. However a major

caveat with $SOCl_2$ doping is that it has been shown to be a temporary effect and thus would require stabilising in order to be useful for commercial photovoltaic devices.[14]

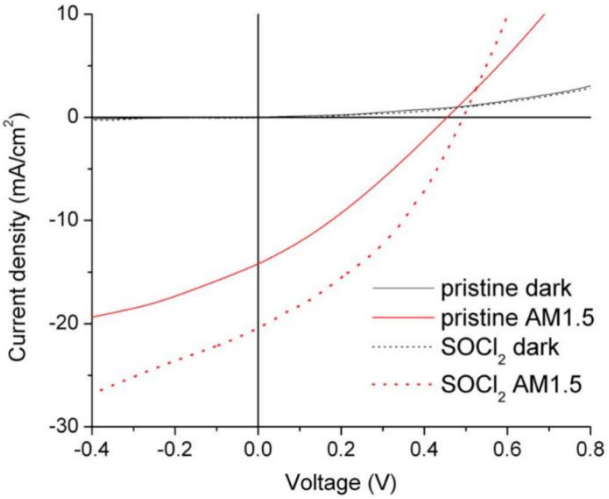

Figure 1-7: Improvement in device performance after $SOCl_2$ treatment from research by Li *et al*.[74] (Pristine, in this context, refers to device performance prior to $SOCl_2$ treatment.

Jia *et al*.[90] experimented with doping the nanotube film using nitric acid (HNO_3) in 2011. Post acid-doped devices achieved very high power conversion efficiencies of over 13 % (whilst the un-doped devices only exhibited efficiencies of 6.2 %). This increase in efficiency was attributed to a lowering of the series resistance in the SWCNT network, producing J-V curves with a higher fill factor than in un-doped devices. This decrease in series resistance is thought to be caused by *p*-type doping plus the removal of residual molecules (such as surfactant) from the SWCNT network.[3, 90-92] It is known that HNO_3, like $SOCl_2$, injects large hole densities into SWCNTs and thus lowers the Fermi level in SWCNT films.[22, 93] In addition, the acid infiltrates the CNT film and creates a semiconductor-electrolyte interface, allowing nanotubes which do not directly contact the silicon substrate to still collect and transport charge carriers produced at the junction, via the HNO_3 electrolyte.[24, 90] This is a similar effect to that observed by Wadhwa *et al.* in their electrolyte work.[79] In this situation Si-acid-SWCNT units are formed which act as photoelectrochemical devices, with the silicon as the anode and the SWCNTs as the cathode. This hypothesis was verified in two ways. Firstly, a device was created with the SWCNT film separated from the silicon by 300 nm with a HNO_3 solution in between. This device also produced an appreciable photocurrent. Secondly the HNO_3 was replaced by a NaCl solution. Devices treated in this manner also showed an improvement in current density, due to the

electrolyte effect, but did not show the *p*-doping effects attributed to doping with nitric acid.[24, 90] Jia *et al*. also showed that other acids, such as H_2SO_4, also produced an increase in device efficiency, but not to the extent of the HNO_3.[90] In terms of stability, it was found that when dried in air, the efficiency dropped down to a stable 8-9%. Once the acid was re-infiltrated into the SWCNT network the efficiency rose again and remained above 9% for 10 days.[90] In a similar study, Tantang *et al*.[92] performed treatments using sulfuric acid and found that this acid also assists in the removal of surfactants. Sun *et al*. used HNO_3 to dope CNT/flexible silicon devices and saw a PCE increase from 6 % to 13.8 %.[94] Additionally, H_2SO_4 produces COOH and SO_3H functionalities on the nanotube surface and it is suggested that this functionalisation, coupled with *p*-doping caused by the oxidative nature of strong acids, reduces the sheet resistance and enhances the overall device properties.[92] However, Jung *et al.*[95] also showed that droplets of liquid resting on the surface act as lenses to give a light concentrating effect, improving the power conversion efficiency and calling into question the validity of earlier results where improved performance was observed when a droplet of acid was placed on the devices.[96]

Other *p*-dopants have been used in the treatment of CNT films in order to increase the efficiency of the CNT/Si heterojunction device such as $NOBF_4$ and gold chloride ($AuCl_3$).[97] $AuCl_3$ functions as a *p*-dopant as the Au^{3+} ion will extract valance electrons from CNTs to be reduced to Au (see Figure 1-8). However it is also proposed that the Au^{3+} ions act as a precursor for Cl^- ion adsorption allowing for further electron extraction from the CNTs.[97] This effect was verified by annealing the doped CNT film at high temperatures. At 500 ˚C – 700 ˚C annealing, the Cl^- ions were completely desorbed from the film and the film conductivity was only 30 – 40 % of that prior to the annealing. Thus Cl atoms account for 60 % – 70 % of the resistance improvement from $AuCl_3$ doping.[97] This chlorine effect is also the explanation as to why there was a gradual decay in efficiency with aging, as the chlorine atoms were slowly desorbed and replaced by atmospheric water molecules.[97] However, Li *et al*.[96] and Harris *et al*.[98] performed $AuCl_3$ treatment on CNT/Si heterojunction solar devices and observed the expected increase in short-circuit current density, leading to improved efficiencies of above 10 % in

both cases. In addition, Li *et al*. found that, if a large amount of gold nanoparticles were deposited on the nanotube film the device performance would degrade due to a 'shorting' effect in which the Au particles form contacts with the silicon substrate.[96, 99] The $AuCl_3$ used here was prepared from an $AuCl_3$ suspension in nitromethane. Alternatively Yu *et al*.[100] performed $AuCl_3$ doping from a chloroauric acid solution in water on CNT/Si devices with an organic hole transporting interlayer. It was found that the aqueous gold chloride doping improved the performance of the devices with the interlayer due to a short circuit current increase. However, the above mentioned shorts lead to a decrease in performance for devices with no interlayer.[100]

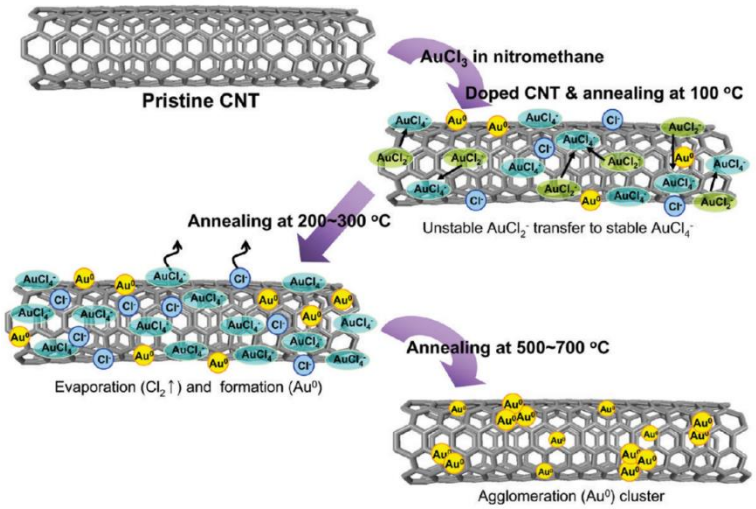

Figure 1-8: Doping schematic of $AuCl_3$ nanoparticles after annealing from Kim *et al*.[97]

An important consideration when chemically doping CNTs in this way is the opacity of the dopant chemical residue. $AuCl_3$ and similar silver nanoparticle dopants are opaque and thus will reduce the photon flux to the silicon substrate which leads to degradation in performance. Partially offsetting the improvements these dopants offer. In this way, $SOCl_2$ is advantageous in that it leaves no opaque residue on the surface of the device. Li *et al*. have made progress in this sector by examining the use of easy to handle, tunable, metallocene compounds such as nickelocene, cobaltocene or bis(benzene)chromium and related complexes.[101] It was found that simply spin coating these materials onto a SWCNT film could be used to further *p*-dope the SWCNTs or to *n*-dope the SWCNTs depending on the electronic structure of the dopant. Additionally, different metallocene compounds

doped the SWCNTs to a different extent, also depending on the electronic structure of the dopant, thus opening the door to tunable doping of SWCNT films.[101]

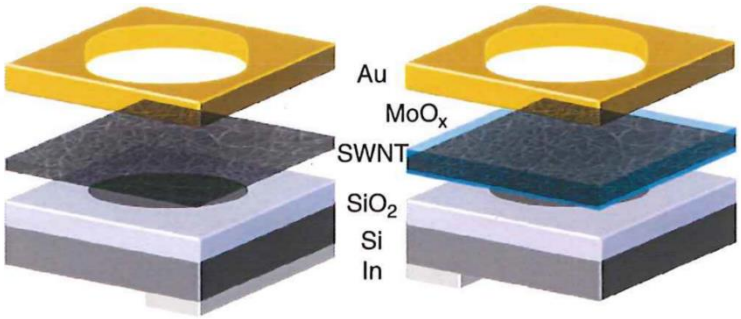

Figure 1-9: Device schematics from Wang *et al*. where a molybdenum oxide interlayer gave device performance of 17.0%.[16]

Other dopant chemicals based on metal oxides have been investigated for *p*-doping of SWCNTs without greatly disrupting the transparency of the film. Wang *et al*. investigated molybdenum oxide and zinc oxide (MoO_x and ZnO) (Figure 1-9) on *p*-SWCNT/*n*-Si and *n*-SWCNT/*p*-Si heterojunction solar devices respectively. These gave significant improvements in both device designs, giving the current record PCE value of 17 % for the *p*-SWCNT/*n*-Si architecture (albeit with a very small active area).[16] This was due to an improvement in charge carrier extraction and a reduction in the proposed Schottky barrier between the SWCNT film and the gold top electrode. The ZnO performed a similar role by improving electron transport in the *n*-SWCNT/*p*-Si architecture. These oxides also had a role to play in reducing the amount of light reflecting from the silicon substrate,[16] which will be discussed in Section 1.2.4. More recently Cui *et al*. used a $CuCl_2/Cu(OH)_2$ solid state redox pair to dope SWCNT films.[102] The most exciting thing about this particular doping strategy is that the significant improvement in SWCNT film sheet resistance (64 Ω sq^{-1} at 90 % transmittance) was retained for over a year, indicating that this couple is a promising long-term doping option. The redox pair dopes the SWCNT film to improve device performance, while not greatly interfering with light transmittance, and is stable over long periods. With this redox couple, devices with PCE values of over 14 % were fabricated and these were also found to be stable over time. It was suggested that the $CuCl_2/Cu(OH)_2$ redox couple unpinned the Fermi level and enhanced the tunnelling of change carriers in the SWCNT

film, giving rise to the magnificent sheet resistance data.[102] It was found that the redox couple also serves as an anti-reflection layer similar to the MoO_x and ZnO discussed earlier.[102]

1.2.3 CNT/Si Heterojunction Device Operating Mechanism

An important research focus of the CNT/Si heterojunction solar device design has been around the underlying mechanism of the photovoltaic device. Despite many years of research, it is not yet fully understood, although much progress has been made. The discussion is focussed around which known photovoltaic device model best represents the CNT/Si heterojunction device. The options considered are: a *p*-*n* junction (as is the case for *p*-Si/*n*-Si) devices where the nanotubes are the *p* half of the junction, a Schottky junction with the nanotube film acting as the metal, or the similar metal-insulator-semiconductor (MIS) junction with the nanotubes acting as the metal.[14] MIS photovoltaic devices can be minority or majority carrier driven. The fact that CNTs have a work function higher than the electron affinity of silicon (4.6 eV vs 4.05 eV approximately)[14] indicates that if the junction did function as a MIS junction it would be minority carrier driven and therefore would resemble a p-n junction in many ways. It is well known and understood that a thin layer of graphene forms a Schottky junction with silicon but there is much disagreement as to whether CNT based devices can be placed in the same category.[98] Additionally, nanotube films generally exist as a widely diverse mix of nanotube chiral species, each with their own unique electronic states. Thus, modelling of the CNT/Si heterojunction is understandably difficult. To combat this, research has been done where the SWCNTs used are pre-sorted by electronic type, however even this work has not been completely conclusive.

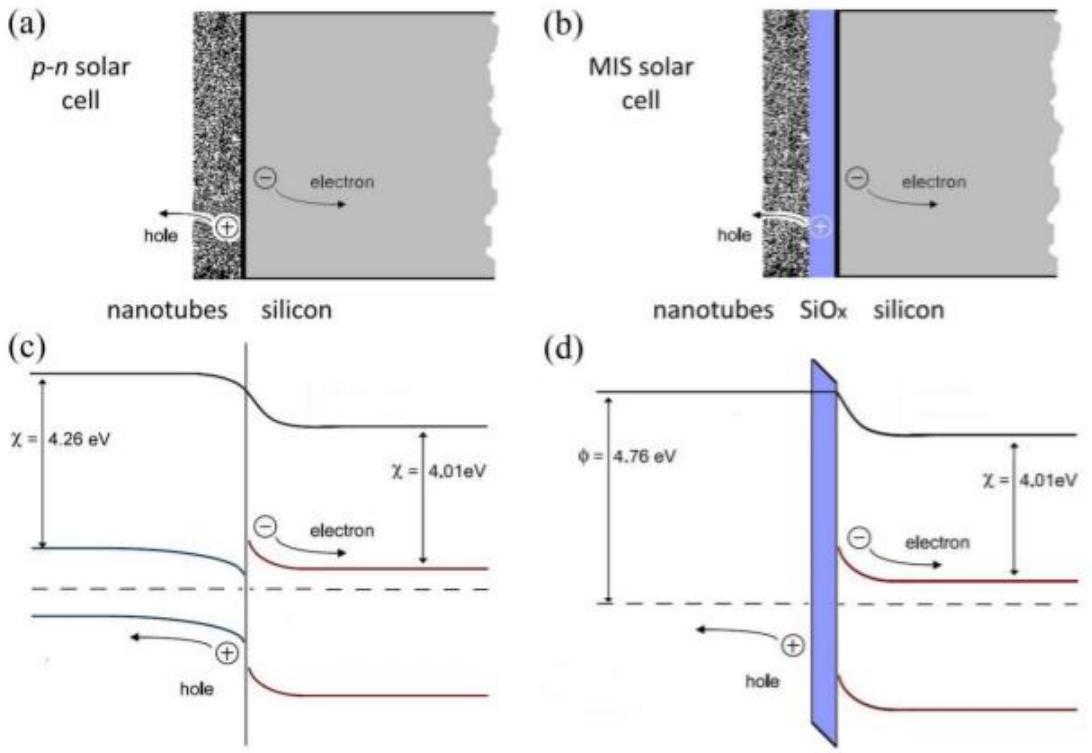

Figure 1-10: Schematics and energy diagrams for the CNT/Si device. a) and c) are the schematic and energy diagram for a p-n junction, whilst b) and d) are for an MIS device.[24]

Del Gobbo *et al.* fabricated devices with either semiconducting SWCNTs or metallic SWCNTs and found hints that the metallic SWCNTs contribute to the photocurrent but overall found that, for SWCNT species which overlap the absorbance spectra of silicon, the SWCNTs absorbed photons but did not contribute to the photocurrent.[14, 103] The latter observation here was also seen in work by Tune *et al.*[104] In a separate study, Tune *et al*.[89] investigated the effects of fabricating devices with pure metallic or semiconducting nanotubes vs devices with an as-grown mix of types. It was discovered that, initially, the films containing purely metallic nanotubes significantly outperformed both the semiconducting and unsorted films. After the films were doped with $SOCl_2$ the situation became very different. The *p*-dopant greatly improved the efficiency of the semiconducting and mixed film devices by a factor of 20 and 40 respectively, but had a much smaller effect on the metallic film devices, only prompting a doubling of the PCE.[89] This is expected as, whilst the $SOCl_2$ lowers the contact resistance between the nanotubes and adjusts the Fermi level for all types, it cannot lower the Fermi level sufficiently low enough to reach the HOMO level in metallic tubes.[89] Thus, provided a *p*-dopant is used, sorting of SWCNTs by electronic character does not appear to be necessary.[14, 105] Harris *et*

al. expanded on this work in 2015 where they compared SWCNTs enriched by length, electronic type and chirality in CNT/Si devices.[98] However, they determined that the PCE had no dependence on SWCNT metallicity as the *p*-doping shifts the Fermi level and renders semiconducting nanotubes effectively metallic.[14] It was postulated that the more ideal the diode, the more the junction would function like a p-n junction but that in general the CNT/Si device exhibits both the properties of a Schottky and a p-n junction simultaneously. It was also suggested that the bandgap of the nanotubes is an important consideration going forward in the field.[14, 98] The variation in observations is possibly explained by the presence of an amorphous carbon matter formed around semiconducting nanotubes due to the use of cholate to separate them from a mixed species CNT powder.[14] This phenomenon increases the desire for a SWCNT fabrication method that produces electronically or chirally specific species. The gated/electrolyte work by Wadhwa *et al*., suggested that the mechanism of photocurrent generation in the CNT/Si heterojunction device is via the Schottky model, through thermionic emission over a barrier at the metal/semiconductor interface.[37, 84] The gate electrode modulation mechanism, however, could apply to both a Schottky junction or a *p-n* junction.[24]

Another point of consideration in the p-n vs Schottky or MIS discussion is the formation of a silicon oxide layer between the silicon substrate and the CNT film. In a Schottky or MIS based device a thin interfacial SiO_x layer is essential for efficient charge separation based on tunnelling.[95] Additionally, an oxide layer with a thickness of 13-20 Å would improve a Schottky device by depinning the Fermi level and passivating the surface.[106] On the other hand, the oxide layer would be expected to dampen the effectiveness of the p-n junction model. The device would not function at all with a thick oxide layer (≈100 nm) at the junction as the oxide will act as an insulator and will not allow separation of photo-electron/hole pairs at the interface, nor the passage of charge carriers across the junction.[107] A thin oxide layer (≈1 nm), however, was found to suppress dark saturation current, inhibit recombination and lead to an increase in minority carrier lifetime and open circuit voltage (V_{OC}).[82] The passage of majority carriers across the junction is suppressed by the oxide, whereas the tunnelling-based passage of minority carriers is unaffected. Thus, the recombination rate is reduced

and the V_{OC} is increased.[82, 108] HNO_3 treatment was shown to produce an oxide on the surface of the silicon with a depth of approximately 1 nm.[82] In addition, Jia *et al.*[82] encapsulated a SWCNT/Si device within a poly(dimethylsiloxane) (PDMS) coating and found that this improved the stability over a period of 20 days. However after this point there was a slight reduction in efficiency due to the growth of an oxide layer which was too thick for tunnelling.[24, 82] The observed positive effect of a thin oxide layer has been used as proof that the Schottky or MIS model is correct. However, research in 2012 by Jung *et al.* fabricated devices that performed best with no oxide present.[95] It is also known that an extremely thin passivating oxide layer can improve the performance of p-n junction devices[14] and thus, again, the situation is not clear cut. Further research has served to muddy the waters even more as Cui *et al*. found that an oxide layer at the theoretical Schottky or MIS ideal improvement thickness of 13-15 Å lowered the effectiveness of their devices compared to devices with an oxide thickness of 6.9 Å.[106] However, simulations of the CNT/Si junction using detailed modelling software found that the oxide thickness effected performance in the same way as standard Schottky or MIS solar devices and determined that a thickness of around 10 Å is optimal.[109] Additional research on the composition of the interfacial oxide layer via x-ray photoelectron spectroscopy (XPS) determined that, not only the thickness, but also the Si:O ratio plays an important role in device performance [3, 14, 76].

A direct photocurrent response from the CNT film in the CNT/Si device would be evidence towards a p-n heterojunction model, as the metal component of a Schottky *device* (the nanotubes in this case, as the silicon acts as the semiconductor) does not contribute to photocurrent generation.[24, 110] Work done by Ong *et al*.[110] found that there was a strong comparison between a SWCNT absorption band (S_{11}, the first interband transition for the (7,6) and (8,6) chiralities) and a photocurrent band at around 1150 nm.[110] This seemed to imply that the nanotubes are involved in the production of the photocurrent as a light absorber, and not simply as a charge separator, transporter and collector. However there is a significant chance this could be a contribution from the silicon rear junction instead.[104] In 2007, Tzolov *et al*.[17] achieved a broad photoresponse in the mid-IR range, separate

from the expected strong silicon response at photon energies of 1.1-1.2 eV. It was claimed that this response was proof that CNTs participate in exciton generation themselves. However, this feature could be due to free carrier absorption in the silicon substrate.[24, 111, 112] Thus, neither the work of Ong *et al.* or Tzolov *et al.* conclusively proved that the nanotubes contribute to the photocurrent and thus create a *p-n* junction.[24, 104] Other possible observations of photocurrent increase with CNT films present can be attributed to the anti reflective property of the film, which gives an increase in the photocurrent generation in the silicon substrate.[14] In 2013, Tune *et al.* deliberately probed the CNT film for a photocurrent response, choosing specific chiral species of SWCNT in order to best observe any photocurrent generation. No photocurrent generation due to the SWCNTs was observed suggesting the film operates more as a front contact electrode and heterojunction forming element in the device.[104] Recently, Li *et al.* used transient absorption spectroscopy to probe for a CNT contribution and found that SWCNTs may generate excited charge carriers and inject them into the silicon substrate if they are generated within a few nanometers of the substrate. In future this may give rise to devices with CNTs possessing absorbance ranges beyond that of silicon providing extra photocurrent to a photovoltaic devices.[14, 113]

It is worth stating that, even if the CNTs are capable of producing and contributing their own photocurrent to the CNT/Si heterojunction device, it is unlikely to be a significant boon to photovoltaic performance. In order for exciton recombination to be lowered the CNT film must be very thin (less than 10 nanometres). This will mean that the film has high light transmittance percentage (%T) and thus will not absorb much light in order to produce the theoretical photocurrent. It is also questionable as to whether the junction architecture would be able to deal properly with charge carriers produced in the SWCNT film due to the high binding energy of excitons produced in the CNT film.[14] Crochet *et al*. found that photoexcitation of SWCNTs produced free carriers rather than excitons[45] whilst Bindl *et al*. found that no potential difference was required to form these carriers and estimated a free carrier generation yield of around 6 %.[114] This is very low when considering most SWCNT/Si devices currently consist of a mix of semiconducting and metallic SWCNTs coupled with a very high

transmittance.[14] In addition to this, the best performing devices currently use strong *p*-dopants to improve the conductivity of the SWCNT film and thus the performance of the device. The effect of these dopants is to shift the Fermi level into the VHS. This bleaches the first optical transition in semiconducting SWCNTs (S_{11}) and in turn destroys the ability of the semiconducting SWCNTs to absorb photons in the desired region. Thus, the generation of free carriers in semiconducting SWCNTs is an unimportant question in the CNT/Si device, but may be of importance when considering similar architectures being used for other applications, such as photodetectors or light-switchable logic circuits.[14]

In order to try and rectify the apparent inability to easily match the CNT/Si device to either a p-n junction, a Schottky, or an MIS junction one could turn to work by Sinha *et al*. who analysed the junction in graphene/Si devices and stated that a new transport model is required to describe this junction.[115] They suggested a model based on adding the Landauer transport formalism into the ideal diode equation, indicating that the rate of injection from graphene to silicon is the main factor for the transport properties and that the finite density of states present in graphene is crucial to the junction's operation.[115] The graphene/Si junction is not directly analogous to the CNT/Si junction, due to the electronic differences between CNTs and graphene and the fact that sheets of graphene will form a better contact with the silicon than a rough, porous CNT film.[98] However, this is still an interesting approach that could be adjusted to describe the CNT/Si junction.[14]

Analysis of the CNT/Si device in search of parameters comparable with either a p-n junction model or a Schottky or MIS junction model has been carried out as another approach to determine the model that best describes the CNT/Si device. Jung *et al*. found an activation energy of around 1.56 eV, significantly higher than a theoretical Schottky barrier height, a minority carrier lifetime of 34 μs, and a linearity in the inverse capacitance squared vs voltage plot, all of which indicates an asymmetric p-n junction. However, they determined their V_{oc} to be roughly equivalent to that of graphene/Si Schottky junction devices.[95] Meanwhile, Harris *et al*. found much evidence pointing towards Schottky barrier driven system, such as: agreement in donor density, correct modelling of CNT

activation energy (5.07 eV), and an incompatibility of current density under negative bias with diffusion-dominated transport. However, it was also determined that the minority carrier lifetime was 1-2 µs, shorter than that shown by Jung *et al.* but significantly longer than the expected picosecond or nanosecond region for a Schottky junction[14, 98], and that the V_{oc} is independent of diode ideality.[98] Additional studies have also found minority carrier lifetimes in the order of tens of micro seconds.[14, 96]

Overall, the conclusion is, at time of writing, that there is no definite model to describe the CNT/Si device and that the correct model is likely to exist somewhere in between the known p-n junction and Schottky barrier models.[98] One option, suggested by Harris *et al*. is the use of a high blocked heterojunction or abrupt np^+ heterojunction.[98] However, it must be stressed that the complex electronic character of CNTs, especially when diameter and electronic type are mixed and doping is applied, make it difficult to draw a clear conclusion.

1.2.4 Light Reflectance

Light reflectance at the front surface of the CNT/Si heterojunction device detracts significantly from photocurrent production.[116] Smooth silicon is a very reflective surface, with an average reflectance of 36 % in the UV-Visible region.[7, 116-118] This is caused by the large difference in refractive index between air and silicon.[119] The reflection of light is an issue for PV devices as the light which is reflected cannot be collected and converted to a photocurrent. As such, efforts to subdue the reflective properties of silicon have been of high priority in solar device research.[120, 121] The usual industry methods of reducing light reflectance are a refractive index matching coating of silicon nitride (SiN) or an alkaline etching process which produces pyramid structures on the silicon surface.[121] Petterson *et al.*[122] used an array of silicon nanowires to increase light absorbance and saw reduced light reflectance and improved photovoltaic performance. Black silicon[123] is a surface modification of silicon in which nanoscale features are formed via the use of a more highly controlled etching process than alkaline etching.[120, 121] Yu *et al.*[124] investigated the use of an alkaline etching process on the surface of the silicon in CNT/Si devices in 2018 (see Figure 1-11). There was initially a

concern that the roughness of the patterned silicon would hamper the ability of the CNT film to conform to the surface and form a good amount of CNT/Si contact points. To address this, graphene oxide (GO) was incorporated in the CNT films to form films with enhanced lateral strength. These were used in a float transfer method which gave good adherence of the film to the surface.[124] The black silicon substrate produced devices with an average PCE of 13.01 %.

FIGURE REMOVED COPYWRITE PERMISSION NOT OBTAINED

Figure 1-11: SEM images of silicon pyramids produced by Yu *et al.* both with (b, c, and d) and without (a) a GOCNT film.[124]

Another, more commonly investigated, method of reducing light reflection in CNT/Si devices is the use of a polymer coating over the CNT film.[80] Polymers are the preferable material as they have controllable morphology and pore size, can adhere well to a substrate and are cheap and easy to manufacture on a large scale.[118] Whilst this field is still in its infancy, many varied methods of manufacturing thin films as anti-reflection (AR) coatings have been investigated for a variety of applications such as light emitting diode coatings, flat panel displays, and solar devices.[118] Along with these many methods, a huge array of polymers have been trialled as AR coatings for general surface use including fluoropolymer, polystyrene, poly(methyl-methacrylate), poly(4-vinylpyridine), poly(allylamine hydrochloride), poly(acrylic acid), poly(diallyldimethyl ammonium), poly(4-styrene sulfonate), poly(2,2,2-trifluoroethylmethacrylate) and poly(dimethyl siloxane).[80, 116, 118] In the CNT/Si device the polymer layer can be doubly effective, both by reducing the reflectance and by protecting the nanotube film and the CNT/Si interface to some degree.[80] In addition, this method does not damage the silicon surface, and causes no interference between the CNT film and the silicon.[7] Polymeric anti-reflection layers can also assist in the stability of CNT/Si devices, by reducing the amount of oxygen that can pass through to the silicon surface. Atmospheric oxygen can react with the silicon surface in the regular device design, growing a silicon oxide layer between the silicon and the carbon nanotube film which can lead to a decrease in performance when it grows too thick[80] as discussed in Section 1.2.3. Polymer encapsulation in this way can also give additional benefits as they

can trap adsorbed dopant species such as Cl^- and SO_2 from escaping from the CNT film, enhancing the longevity of these dopants.

Li *et al*.[116] used a coating of poly(methylmethacrylate) (PMMA) as an anti-reflection layer for a CNT/Si device. This film improved efficiency from 7.1 % to 11.5 %. This was mainly because of a large increase in the short circuit current density (J_{sc}) in the device, due to PMMA's anti-reflection properties. This was further confirmed as the external quantum efficiency (EQE) increased from 60 % at wavelengths of 400 nm - 900 nm to above 80 % from 500 nm - 800 nm, indicating more photon-electron conversion was taking place.[116] Yu *et al*.[80] used poly(dmiethylsiloxane) (PDMS) and polystyrene (PS), in addition to PMMA, as anti-reflection coatings. It was found that, whilst all the polymers performed successfully as anti-reflection coatings and managed to increase the efficiency of the device design, the effect was dependent on the thickness of the coating. It was discovered that the PS and PMMA, which were spin-coated, were more successful at isolating the device from atmospheric effects than the PDMS layer which was applied by simple attachment.[80] The layers help to improve the stability of the CNT/Si devices and thus polymer layers are a very viable addition to these devices as they confer a two-fold bonus.

Depositions of uniform thin films of substances such as titanium dioxide (TiO_2), silicon nitride (Si_3N_4) and tantalum oxide (Ta_2O_5) use destructive interference to decrease the amount of reflected light[116] instead of light scattering or trapping.[7] One of the most recent attempts to reduce the large amount of silicon reflectance was made by spin coating a TiO_2 nanoparticle layer of 50 nm - 80 nm thickness on the surface of CNT/Si devices (see Figure 1-12). This had previously (1985) been a method used to lower the reflectance of standard silicon solar devices, leading to greatly lowered reflectance (approaching 0.04%) and improved device efficiencies by up to 44 % when coated with thermal SiO_2 and TiO_2 thin films.[125] In the case of the CNT/Si devices the layer subdued the light reflection significantly (decreased reflection from 30 % - 40 % to below 5 % in some wavelength regions (Figure 1-12)) and increased the incident photon to current efficiency (IPCE) from 60 % to 90 %, whilst still allowing post device fabrication doping treatments to reach the nanotube network. Together with

nitric acid and hydrogen peroxide doping this anti-reflection layer allowed for then record high device efficiencies of above 15 %.[7]

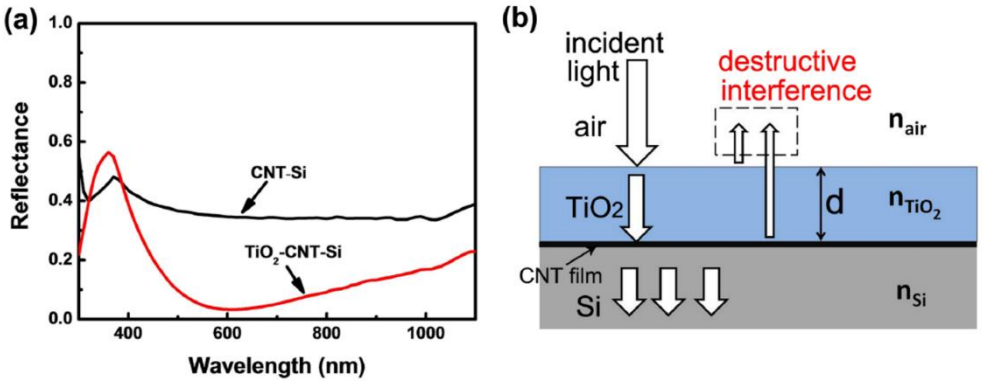

Figure 1-12: Light reflectance spectra (a) and mechanism illustration (b) for the light trapping effect of a TiO_2 layer from Shi *et al.*[7]

As mentioned previously, Wang *et al.* investigated the application of molybdenum oxide (MoO_x) and zinc oxide (ZnO) as cheap, environmentally friendly anti-reflection layers.[16] Using these films allowed this research group to reach a record efficiency for the CNT/Si device of 17 % (with sub square millimetre active areas) and achieve a relatively high efficiency for a device using *n*-doped nanotubes of 4 %.[16] The MoO_x coating improved the properties of the standard CNT/Si device, with a higher J_{sc} and much improved diode properties. In this case, the MoO_x layer has improved the device in two ways. Firstly by acting as an anti-reflection layer (due to having a refractive index of 2.2,[126] between that of air, 1, and silicon, 3+ at wavelengths from 280 nm to 1400 nm[127]) and consequently reducing the average reflectance in the UV-Visible region of the device from around 30 % to less than 20 %.[16] Secondly by reducing the proposed Schottky barrier at the CNT/Au interface and thus providing a more efficient 'hole' transport path. However, as the exact mechanism of this device architecture is not understood, this explanation may be incorrect. This improvement in current transport efficiency improves the J_{SC}, lowers the series resistance and lessens current leakage, thus forming a better diode than the pure CNT/Si device.[16]

1.2.5 Application of an interlayer

In addition to using polymers as an anti-reflection layer, research has been done on the use of a thin, conductive layer of polymer placed in-between the CNT layer and the silicon substrate.[128] The

addition of polymer layers in this way can be an improvement over chemical treatment procedures such as HNO_3 treatment as they have no effect on the nanotubes themselves.[128] Polyaniline (PANI) has previously been studied as a photovoltaic material by placing a thin film on a silicon substrate.[129, 130] These junctions suffered due to the limited lateral conductivity in the PANI film. CNT films can overcome this issue due to their good conductivity.[128] Tune *et al*.[128] studied a device design with a layer of PANI underneath the SWCNT film on an *n*-silicon substrate (see Figure 1-13). The SWCNT-PANI-Si junctions showed a maximum efficiency of 9.7 %, significantly higher than a pure PANI/Si efficiency of 0.005 % and higher than the efficiencies achieved by SWCNT/Si devices in this experiment (3.3 %). This was due to the improved depletion region owing to a more complete surface covering provided by the polymer and the high conductivity and current carrying capacity of the SWCNT film.[128]

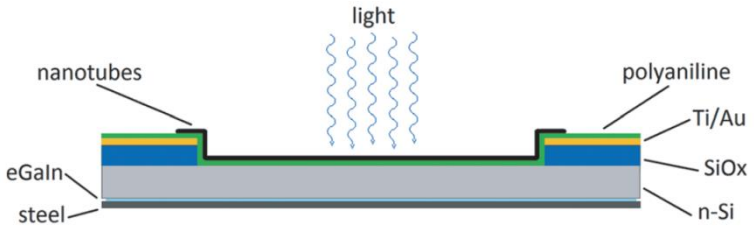

Figure 1-13: Schematic of a CNT/Si device with a polyaniline interlayer, from Tune *et al.*[128]

Aside from studying the anti-reflection effects of polymer coatings, Yu *et al.*[131] investigated the use of the polymer poly(3,4-ethylenedioxythiophene) polystyrene sulfonate (PEDOT:PSS) in the CNT/Si device as an interlayer as well as reinvestigating the use of PANI. In this 2015 work, roughly 10 nm thick layers of each conducting polymer were applied to the standard CNT/Si device as an interlayer between the CNT film and the silicon substrate.[131] It was found that the addition of these layers led to an improvement in device performance from around 5 % PCE to up to 7.7 % (and up to 8.7 % with an additional PS anti-reflection layer). This PCE gain was due to the improvement of the depletion layer in the silicon substrate thanks to the more conformal covering of the thin conducting polymer layers. PEDOT:PSS was found to be the preferable interlayer, possibly due to it forming the smoothest coating on the silicon surface and thus causing the least amount of light scattering.[131]

More recently, Yu *et al.*[100, 132] investigated the effect of alternate organic interlayer materials which were being used in a similar role in the field of perovskite solar devices. In particular the chemicals examined were 2,2',7,7'-tetrakis(N,N'-di-*p*-methoxyphenylamine)-9,9'-spirobifluorene (spiro-OMeTAD) (see Figure 1-14), 4,4'-(naphthalene-2,6-diyl)bis(N,N-bis(4-methoxyphenyl)aniline) (NAP), and (E)-4',4'''-(ethene-1,2-diyl)bis(N,N-bis(4-methoxyphenyl)-[1'',1'''-biphenyl]-4amine) (BPV) these were compared to PEDOT:PSS. Together, these materials are referred to as hole-transporting materials (HTMs) due to their ability to improve hole transport in a device.[100, 132, 133] These devices differed from the previous interlayer work mentioned here as graphene oxide (GO) single-walled carbon nanotube (GOCNT) films were used in lieu of plain CNT films as the attachment method required floating the film in a solvent bath and the addition of GO allows the film to maintain its physical integrity while free floating in acetone or water. The GOCNT films were doped with a gold chloride ($AuCl_3$) solution, via a spin-coating process for the spiro-OMeTAD devices and a bath doping process for the PEDOT:PSS, NAP and BPV devices.[100, 132] These devices showed a significant PCE improvement, especially once doped with $AuCl_3$, over those discussed in the previous paragraph, as shown in Table 1-1.

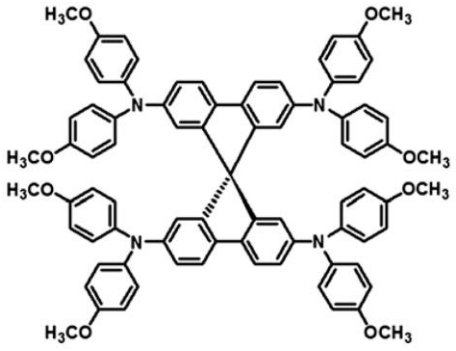

Figure 1-14: Chemical structure of Spiro-OMeTAD, from Kwon *et al*.[134]

Table 1-1: PCE results for HTM interlayers in GOCNT/Si heterojunction solar devices after doping with $AuCl_3$.[100, 132]

	PEDOT:PSS	*NAP*	*BPV*	*spiro-OMeTAD*
PCE ± % Error	12.05 ± 0.21	10.57 ± 0.37	10.68 ± 0.27	12.83 ± 0.22

1.2.6 Active Area Size

For the majority of the research carried out on the CNT/Si device the active area (the heterojunction itself) has been very small, less than 1 cm^2, and sometimes less than 1 mm^2.[14, 135] This was useful for proof-of-concept designs and initial improvement methods but, in order for this design to continue to increase in relevance and gain significance in the 'real-world', the active area needs to be scaled up. One issue encountered when increasing the size of the active area is that the CNT film is required to transport charge carriers over a much larger distance. CNT thin films generally display sheet resistance values from 100 Ω sq^{-1} to several kΩ sq^{-1} (higher than the 10-20 Ω sq^{-1} seen in silicon emitters in conventional solar devices). These high resistances will have a greater detrimental effect on device performance as shown by the resistive power loss equation (Equation 1-1). Equation 1-1 shows that the power loss is proportional to the series resistance and the area and thus it is apparent that device performance will degrade with an increase in active area.[99]

Equation 1-1: Equation for resistive power loss, where R_s is sheet resistance, A is device active area and J_{max} is the current density at the maximum power point.

$$P_{loss}(Wcm^{-2}) = \frac{V(V) \times I(A)}{A(cm^2)} = \frac{R_s(\Omega) \times {I_{max}}^2(A^2)}{A(cm^2)} = R_s(\Omega) \times A(cm^2) \times {J_{max}}^2(A^2cm^{-4})$$

Additionally, the current that must be transported by this film increases as the active area increases. Thus, any flaws in ability of the CNT film to transport charge become a significant hurdle to overcome. It was found that when simply increasing the active area the internal series resistance increases and thus the fill factor drops as the porous, imperfect CNT network is forced to carry charge carriers over larger distances, leading to a higher probability of charge recombination.[136, 137] This drop in fill factor has also been observed in organic devices with no CNT element present.[138] Increasing the thickness of the CNT film would decrease the sheet resistance and address the problem. However, this will lower the optical transmittance of the film and will thus reduce the amount of light incident on the silicon substrate, which will result in lower exciton generation.[136, 139] One way to approach this issue is to take a leaf out of the *p*-Si/*n*-Si commercial designs and apply a metallic grid over the surface of the active area[140] to significantly reduce the distance the CNT film is required to transport

charges. In work done by Yu *et al.* in 2017[136] the standard CNT/Si device was modified with the addition of a gold/chromium grid across the active area with a range of grid line widths and spacings. Additionally, the active area of the devices was varied from 0.04 cm^2 to 0.09 cm^2.[136] It was found that an increase in active area was accompanied by a degradation in diode properties caused by an increasing area (and thus resistance) of the CNT film and an increase in charge carrier recombination. An optimal grid structure was found which produced devices with PCE values above 10 % with thin (86 % transmittance) CNT films[136]. Note that the addition of this gold grid could allow thinner CNT films to be used, as the sheet resistance of the film becomes less of an issue as the charge carrier distance is reduced. Theoretically, the device is converted from a single large active area device to a network of smaller active area devices connected by the surface grid electrode. Conversely, grid lines can negatively affect device performance as they optically block parts of the active area and reduce the CNT/Si contact area both under the grid lines and adjacent to them as the film must curve down to contact the silicon. Xu *et al*.[135] approached the idea of a surface grid pattern in a different way. Their research looked at devices with active areas in excess of 2 cm^2 and used a series of flattened CNT strips on top of the CNT film to form high conductivity pathways for charge carrier extraction without introducing an additional contact barrier (see Figure 1-15). Using this method, large area devices were fabricated with PCE values of around 10 % using CNT films of roughly 85 % transmittance and CNT strips of around 1.5 % transmittance.[135] Thus, film conductivity is improved whilst giving little to no decrease in photon intensity on the silicon in the areas not obscured by the CNT strips. Alternatively, Li *et al*. mitigated the resistive power loss problem by casting silver nanowires across the surface of 49 mm^2 devices (see Figure 1-16). These devices gave a maximum PCE of over 10 %, due to significantly lower sheet resistances for the silver nanowire/SWCNT films compared to pure SWCNT films.[99]

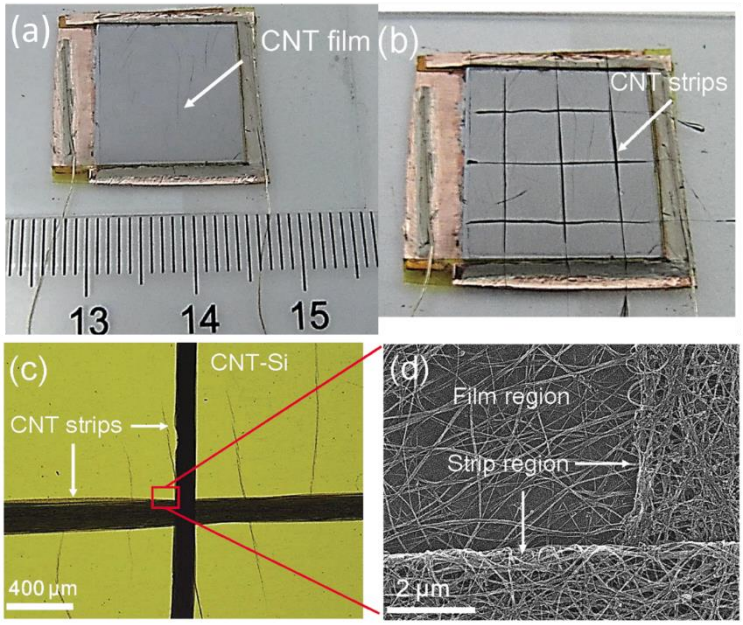

Figure 1-15: Images of a large active area device from Xu *et al.* a) scale of device, b) optical image of CNT strips, c) optical microscope image of CNT strips, d) SEM image of CNT strips and CNT film.[135]

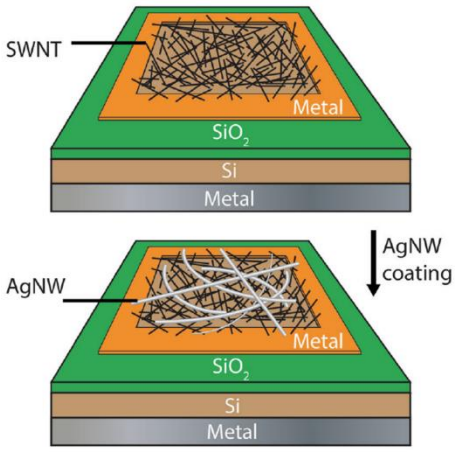

Figure 1-16: Application of silver nanowires (AgNW) to a large area SWCNT/Si device by Li *et al*.[99]

1.2.7 CNT Film Morphology

One of the limiting factors in the performance of the CNT/Si device is the CNT film morphology. The CNT film is of vital importance in transporting charge carriers from the CNT/Si interface to the top electrode. Thus, the properties of the film must be carefully controlled, either during preparation or post-fabrication treatment, to ensure conductivity across the film is sufficient to give good device performance.

Many methods have been used for film fabrication. Most commonly, the nanotubes are suspended in a surfactant solution and formed into a film by spray coating with an air brush,[74, 141, 142] or by filtering the nanotubes onto a substrate via simple vacuum filtration.[83, 89, 143-147] Some groups

have also grown CNT (mainly DWCNT) networks via CVD and floated them onto the desired substrate.[7, 25, 75] The issue with these methods is that the films formed consist of a random array of nanotubes, which can suppress the properties that carbon nanotubes possess independently. This is because a random alignment of tubes can lead to 'charge traps' and holes within the film which can inhibit charge carrier transport across the network. There has been some research done in order to produce highly ordered, aligned CNT films. Many techniques have been tried such as solution shearing from superacids[96, 148] or so-called 'nanotubides',[149] the controlled collapsing of vertically aligned CVD grown CNT forests,[150-152] horizontal CNT growth from lithography controlled CVD,[153] exfoliation of CVD grown CNT forests,[154] and evaporation based self-assembly of CNTs via surfactant stabilisation, sidewall-funtionalisation, polymer wrapping, and floating evaporative self-assembly.[155-160] In most of these cases the aligned nanotube films are used for experiments other than CNT/Si devices, however, Jung *et al*. and Li *et al*.[95, 96] used the super acid chlorosulfonic acid, whilst Tune *et al.*[149] used sodium nanotubide polyelectrolytes, to form true high concentration SWCNT solutions, rather than metastable suspensions. These solutions were at high enough concentrations to reach a liquid crystal phase, allowing the nanotubes to align on a surface when a droplet of the solution was sheared rapidly between two glass slides[95, 96, 149] (Figure 1-17). This ordered alignment of the SWCNTs allowed a thin, highly transparent, very smooth film to be produced, which did not suffer from the draw-backs of ultra-thin films produced via other methods (such as poor contact with the silicon substrate and a poorly formed nanotube network with many charge traps and holes in the film). These films were found to benefit the devices, by allowing more photons to reach the silicon whilst also providing morphological uniformity, leading to a higher PCE after doping, when compared with disordered films on the same substrates.

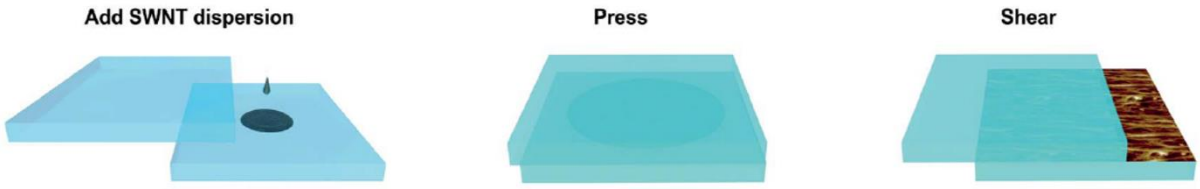

Figure 1-17: Schematic of the liquid shear process for producing aligned CNT films from Li *et al.*[96]

Research was carried out by Tune *et al.*[4] in 2013 to find an optimal thickness for a film using large diameter arc-discharge SWCNTs with high carboxyl functionality. These films were produced by filtration from suspension and were thus randomly ordered. It was determined that a film transmittance of 70 % gave an optimal efficiency, although thicker films displayed relatively stable efficiencies. The device efficiency was found to taper significantly with thinner films. This was due to a decrease in the amount of SWCNT/Si contacts for charge separation and an exponential increase in sheet resistance as the film conductivity became dominated by the limited pathways in very thin SWCNT films.[4] A plot of device efficiency vs transmittance is shown in Figure 1-18.

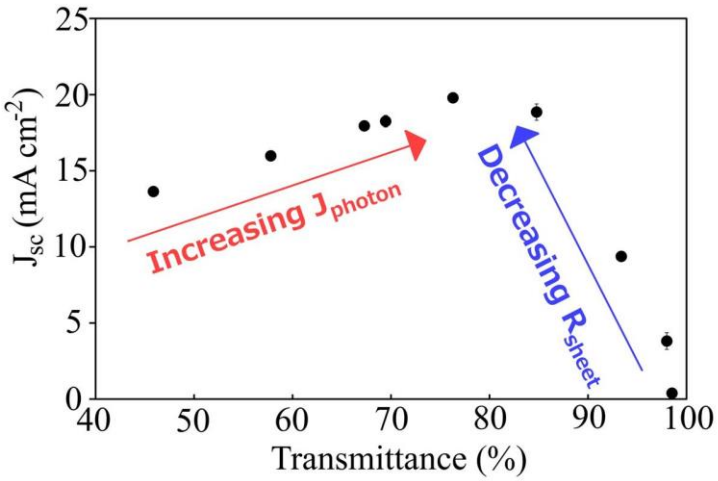

Figure 1-18: Plot of device efficiency vs SWCNT film transmittance in SWCNT/Si solar devices.[4]

Nanotubes are known to conduct charge carriers ballistically. Thus, the rate-limiting factor in terms of conduction across a given CNT film is the performance of the tube-tube junctions. This is why the application of dopants that improve the performance of the tube-tube junctions, such as $AuCl_3$ are important in the performance of CNT/Si devices. An alternative option to address this issue is by using longer CNTs in the film. The longer the average length of the CNTs in a film, the less tube-tube junctions are required to transport a charge carrier from its separation point at the CNT/Si interface to the top electrode, thus there is less resistance and improved current generation. An ideal situation can be envisaged where a metallic grid is placed over the active area with windows that are slightly smaller (in length and height) than the length of long nanotubes and, therefore, a monolayer film of long CNTs aligned to bridge the top contact and form a smooth, consistent contact with the silicon

substrate. Of course, the nanotubes would have to be on the order of several millimetres long at least to make this a viable strategy. Most of the devices discussed here use CNT films produced by suspending the tubes in liquid and filtering, spray coating or similar onto the substrate. This makes the CNTs and the CNT films simple to deal with and gives short processing times. The disadvantage here is that suspending the nanotubes often involves sonication, centrifugation or similar abrasive processes. This serves to reduce the average length of the nanotubes[161] which, as has been explained here, increases the resistivity of the film by increasing the number of tube-tube junctions required to transport charge carriers. There are options for how to form a good CNT film on a solar device substrate without pre-processing the tubes, one such method is the simple idea of scraping the inside wall of a CVD chamber to pick up as grown CNTs and place them on the substrate. Even simpler is the idea of holding a substrate in the CVD chamber during CNT growth to catch the tubes on the substrate as grown and thus avoid all forms of pre-device-fabrication processing.

1.2.8 n-CNT/p-Si Heterojunction Solar Devices

For the most part, CNT/Si devices have consisted of a *p*-doped CNT layer and an *n*-doped silicon substrate. This is the simplest method of device organisation as CNTs gain *p*-doping characteristics from adsorbed oxygen from the atmosphere,[104, 162] which is difficult to remove.[163] Despite this, there have been a few attempts to produce a CNT/Si device with the reverse doping situation i.e. an *n*-doped CNT layer connected to a *p*-doped silicon substrate.[16, 163] One such attempt by Li *et al*.[163] involved the use of hydrofluoric acid vapour to remove the adsorbed oxygen from the carbon nanotubes and allow them to become *n*-doped. Wang *et al.*[16] experimented with *n*-doped nanotubes in their research on metal oxide layers. Overall, the efficiencies of *n*-SWCNT/*p*-Si devices have been less than those achieved by the standard *n*-SWCNT/*p*-Si device. Wang *et* al. only managed to achieve 4 % efficiencies for their ZnO-*n*-SWCNT devices where-as they achieved a record 17 % with the standard doping organisation.[16] Likewise, the HF vapour method fabricated devices which achieved a highest efficiency of 5.88 %.[163] Whilst this is an impressive value for an *n*-SWCNT/*p*-Si heterojunction device, it is significantly lower than values achievable by *p*-SWCNT/*n*-Si devices.[163]

The major reasons for this lower efficiency appear to be a lower open circuit voltage (V_{OC}) and a lower fill factor. The lower fill factor is due to a higher sheet resistance across the film (due to the oxygen desorption in the case of the HF vapour study).[101, 163] The V_{OC} is highly influenced by the built-in potential of the device, and thus the Fermi level of the nanotubes. Thus the lower V_{OC} is due to a less efficient *n*-doping when compared with *p*-doping.[101]

1.2.9 Summary of CNT/Si Device Research

Table 1-2: Recorded history of device architecture and performance for CNT/Si heterojunction photovoltaic devices.[107]

Type of nanotube used	*Device active area (cm^2)*	*Reported PCE (%)*	*Film preparation/deposition method*	*Publication Year*	*Footnote*
SWCNT	0.25	~1.3	Spray:DMF	2008	[74]
SWCNT	0.25	4.5	Spray:DMF	2009	[164]
SWCNT	0.25	1.7	Spray:DCB	2010	[141]
SWCNT	0.08	10.9	Filtration:MCE/MCE dissolution	2010	[84]
SWCNT	0.09	13.8	CVD chamber/free transfer	2011	[165]
SWCNT	0.09	10.9	CVD chamber	2011	[166]
SWCNT	0.08	12.0	Filtration:MCE/MCE dissolution	2011	[79]
SWCNT	0.15	15.1	CVD chamber wall/aqueous film transfer	2012	[7]
SWCNT	0.09	11.5	Slide castubg:CSA/aqueous film transfer	2013	[96]
SWCNT	0.08	9.7	Filtration:MCE/MCE dissolution	2013	[128]
SWCNT	0.08	4.5	Filtration:MCE/MCE dissolution	2014	[105]
SWCNT	0.49	10.8	Liquid shear on glass slide transfer aqueous flotation	2014	[99]
SWCNT	0.008	17.0	Filtration:MCE/dry transfer	2015	[16]
SWCNT	0.08	15.1	Spray, filtration:MCE/spray, MCE dissolution	2015	[122]
SWCNT	0.08	4.5	Slide casting:Na polyelectrolyte/aqueous film transfer	2015	[149]
SWCNT	0.08	8.7	Filtration:MCE/MCE dissolution	2015	[131]
SWCNT	2 - 2.5	10.34	Floating catalyst CVD	2016	[135]
SWCNT	0.09	12	Filtration:MCE/MCE dissolution	2017	[167]

SWCNT	0.09	12.05	Filtration:MCE/MCE dissolution (Flotation)	2017	[132]
SWCNT	0.09	12.83	Filtration:MCE/MCE dissolution (Flotation)	2017	[100]
SWCNT	0.04 – 0.09	9.52	Filtration:MCE/MCE dissolution	2017	[136]
SWCNT	0.04	6.45	Filtration:MCE/MCE dissolution	2018	[168]
SWCNT	0.08	13.01	Filtration:MCE/MCE dissolution (Flotation)	2018	[124]
DWCNT	0.49	1.4	CVD chamber wall/aqueous film transfer	2007	[25]
DWCNT	0.49	7.4	CVD chamber wall/aqueous film transfer	2008	[75]
DWCNT	0.49	4.1	CVD chamber wall/aqueous film transfer	2010	[83]
DWCNT	0.13	13.1	Array drawing/free transfer	2014	[116]
MWCNT	0.01	~3	Drop cast: SDS	2008	[23]
MWCNT	0.09	8.8	CVD chamber wall/aqueous film transfer	2012	[169]
MWCNT	0.04	10	Filtration:MCE/MCE dissolution	2016	[170]
SWCNT, DWCNT and MWCNT	0.08	4.8	Filtration:MCE/MCE dissolution	2016	[31]

Table 1-2 displays a brief history of publications on the CNT/Si heterojunction device, sorted chronologically by tube type (SWCNT, DWCNT, and MWCNT). A general increase in PCE can be seen over time, however it is notable that each listed publication varied other parameters including active area, interlayer use, and doping type.

1.2.10 Conclusions and Thesis Aims

Overall, photovoltaic devices consisting of a CNT/Si heterojunction are exciting prospects for the future of solar energy capture technology. An efficiency increase from 1.7 % to 17 % in less than 10 years is a rapid improvement with more efficiency gains possible in the future, with the advantage of using cheaper CNTs in place of one of the doped silicon layers. There are still many avenues of research available to improve these device designs such as more doping methods, more anti-reflection methods, and more comparisons of different nanotube types i.e. chirality and number of walls.

In this thesis, key aspects of the CNT/Si device will be investigated. The aim of this project was to contribute to the body of work on the CNT/Si device, particularly in the areas of CNT film fabrication and device area scale-up.

Aqueous suspensions of five CNT samples, including SWCNTs, DWCNTs, and MWCNTs and of different diameters will be produced in an identical manner. CNT films produced from these suspensions will be analysed for film morphology, light transmittance, sheet resistance, and Raman spectra. The films will also be incorporated into the CNT/Si heterojunction device to investigate the effects of different wall number and diameter on device performance. Additionally, the effect of dopant chemicals on film sheet resistance will also be examined.

Gravity filtration will be applied as a novel method of producing smooth and aligned CNT films. The produced films will be analysed with SEM, AFM and UV/Visible spectrophotometry. Light transmittance, sheet resistance, surface morphology, and surface roughness will be compared between films produced via gravity filtration and standard vacuum filtration. Polarised Raman spectroscopy will also be used to investigate CNT alignment. Both types of film will be incorporated into CNT/Si devices to investigate the effect of slow filtration on performance.

Chapters 5 and 6 will both deal with scaling up the CNT/Si device area from less than 0.1 cm^2 to 2.25 cm^2. Chapter 5 will detail the design of the large area device, and the design of the large area CNT film. The thickness of the top contact will also be optimised and a new aluminium back contact designed to replace the gallium-indium eutectic/steel contact used previously. Additionally, the use of alumina filtration membranes instead of organic membranes will be attempted to produce smoother CNT films, and measurement inconsistencies with the large area device documented.

The penultimate chapter will document attempts to improve the performance of the large area CNT/Si device by applying a series of interlayers. The interlayers investigated will be Poly(3,4-ethylenedioxythiophene)-poly(styrenesulfonate) (PEDOT:PSS), polyaniline (PANI), molybdenum oxide (MoO_x), copper thiocyanate (CuSCN), and 4,10-bis(bis(4-methoxyphenyl)amino)naptho[7,8,1,2,3-

nopqr]tetraphene-6,12-dione (DAD). The morphology of the films as spun on substrates will be investigated and relationships between spin coating speed and film thickness determined. Based on this, optimal film formation parameters for application in the CNT/Si device will be determined and the performance of each interlayer compared.

CHAPTER 2 EXPERIMENTAL DETAILS

2.1 Fabrication Techniques

2.1.1 CNT Suspension Preparation

CNTs were purchased from various sources for the experiments covered in this thesis. For the research covered in chapters 4-6, arc-discharge produced SWCNTs were purchased from Carbon Solutions. For chapter 3, four additional CNT samples were sourced. SWCNTs from NanoIntegris, DWCNTs from Sigma-Aldrich and Carbon Allotropes, and MWCNTs from Sigma-Aldrich (Table 2-1). For application in solar devices and attachment to other surfaces for characterisation, the CNTs were suspended in an aqueous solution using one of two methods.

Table 2-1: CNT samples used in this thesis.

Type	*Fabrication Method*	*Company*	*Diameter (nm)*	*Length (nm)*	*Purity (%)*
SWCNT	Arc Discharge	Carbon Solutions	1.4 - 1.5	500 – 1500	90
SWCNT	HiPCO	NanoIntegris	0.8 - 1.2	100 – 1000	95
DWCNT	Plasma enhanced CVD	Carbon Allotropes	2 – 4	<1500	>>60
DWCNT	CoMoCAT Catalytic CVD	Sigma-Aldrich	3.5	3000	90
MWCNT	Catalytic CVD	Sigma-Aldrich	9.5	1500	95

2.1.1.1 Bath Sonication Method

Bath sonication preparation of CNT or CNT/GO suspensions was the general method used for the majority of the experiments based on previously published work[132, 171] and for the experiments in this thesis. A surfactant solution was formed by adding either sodium dodecyl sulfate (SDS) or Triton X-100 to water at a concentration of 1 % w/v or v/v. This mixture was bath sonicated (≈50 W_{RMS} (root mean squared Watts) (Elmasonic S 30 H) for 20 minutes before dry CNTs were added to the mixture at a concentration of 0.5 mg mL^{-1} or 1 mg mL^{-1}. For the more recent research, graphene oxide (GO) was also included in the mixture at a GO:CNT ratio of 1:2.25 in order to increase the strength of the CNT films. To suspend the CNTs in the solution, the mixture was bath sonicated in 3-4 20 min periods. The bath water was replaced after each period to keep the bath at around room temperature. Once the suspension was formed, it was centrifuged at 17,500 g for 1 hour to remove material that was not well dispersed. The top 2/3 of the centrifuged mixture was collected and the remaining 1/3 was centrifuged for an additional hour to increase yield, with the top 2/3 collected from this second run.

The centrifuge used for the majority of sample preparation was a Beckmann-Coulter Allegra X-22. For some samples a Dynamica Velocity 14R refrigerated centrifuge was used.

2.1.1.2 Tip Sonication Method

Alternatively, a tip sonicator was used instead of bath sonication for a constant period of 40 minutes. The CNT suspension was placed in an ice bath during sonication to control the temperature. The tip sonicator used was a VCX 750 from Sonics with a 750W power supply at a power level of 40 %. The advantage of tip sonication over bath sonication is an increase in suspension concentration of the CNTs, however the additional vibrational energy may also serve to decrease the average CNT length to a greater extent than bath sonication.

2.1.2 CNT Film Production

CNT films were produced from suspension using vacuum filtration. A Buchner flask was attached to a water aspiration vacuum via tubing, and a glass frit was placed in the top with a rubber bung providing the seal. A series of two filtration membranes were placed on the frit (See Figure 2-1). The bottom membrane was a mixed cellulose ester (MCE) template membrane (VSWP, Millipore, 0.025 µm pore size). This membrane was patterned with the shape desired for the final film. For small device production a pattern consisting of 4 small holes was used to make 4 identical films. From these films one would be attached to glass (see section 2.1.3.1 Heat/Press Attachment Method) and used for light transmittance and conductivity testing whilst the other three were used in device production. For large area devices, only one film was made per filtration due to membrane size constraints. In the latter part of the large area devices project a variant template was used where the size of the large hole was increased in size, to assist with coverage of the film, and a smaller ‘window’ hole was added to produce a film that could be attached to glass and used for light transmittance and conductivity testing. See Figure 2-2 for images of the patterned template designs.

The second (top) membrane is an MCE membrane (HAWP, Millipore, 0.45 µm pore size). A solution of approximately 250 mL of ultra-pure water containing an aliquot of CNT suspension was filtered through this set up. The flow rate of the solution was faster through the patterned holes in the lower

membrane than through the 0.05 µm pores. Thus, the nanotubes were deposited in the same pattern as the lower template paper. After the initial filtration an additional filtration of 250 mL of ultra-pure water was performed in order to ensure any CNT or CNT/GO residue was washed from the glassware on to the film. Additionally, this step could assist in washing some surfactant from the CNTs in the film.

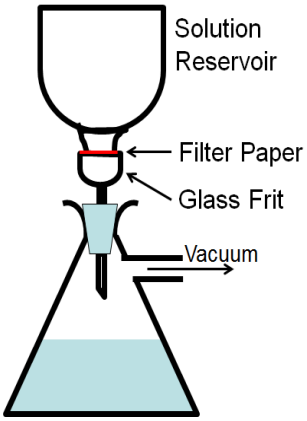

Figure 2-1: Vacuum filtration setup for CNT film formation.

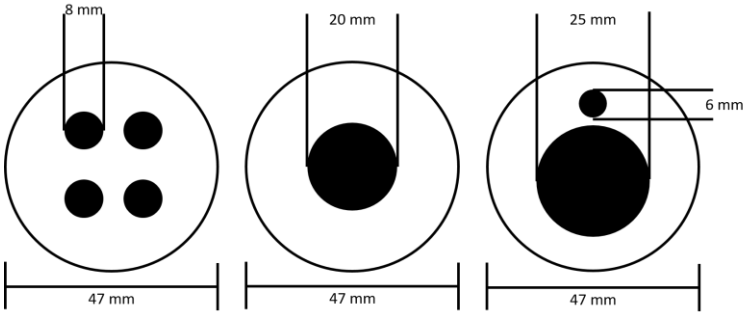

Figure 2-2: Vacuum filtration template schematics used throughout the projects. From left to right: 4 hole template for small device production, large film template for large device production, larger film for large device production with testing 'window'.

2.1.3 CNT Film Attachment

Once filtered, CNT or CNT/GO films on MCE membranes were attached to a variety of substrates (glass, silicon or gold/silicon solar device substrates) in one of two ways.

2.1.3.1 Heat/Press Attachment Method

The nanotube film was cut (using scissors or a shim hole punch) from the excess MCE membrane and was placed, nanotube side down, on to the desired substrate. The film was then wetted with ultra-pure water, with any excess water siphoned away via a pipette. The film was moved to the desired location on the substrate and was then dried by applying manual pressure to the wet film with absorbent paper. This pressure has the added advantage of ensuring any air pockets trapped between the film and the substrate were forced out prior to attachment. A piece of Teflon was placed over the

film, followed by a piece of glass to form a substrate/CNT film/Teflon/glass sandwich. The Teflon was placed to prevent the MCE/nanotube film attaching to the upper layer of glass rather than the substrate. Once the sandwich was formed it was heated at 80 °C for 15 min. This heating dries the film, leading to strong attachment to the substrate. After heating, the film was left to cool for 2-5 min to prevent the film detaching from the substrate when the MCE membrane was dissolved. To dissolve the MCE, the substrate with attached film was submerged in a bath of acetone for 30 min. Following this, the acetone was replaced, and the substrate was again submerged for 30 min with stirring. The substrate was then washed with fresh acetone and dried under a N_2 gas flow. This process gives strong attachment to the substrate, with manual scratching only succeeding in removing small portions of the film where the scratching took place.

2.1.3.2 Film flotation film attachment method

In some of the experiments in this thesis, an interlayer was placed between the silicon substrate and the CNT/GO film. The heat/press method of film attachment in section 2.1.3.1 was not conducive to these experiments as the acetone bath could damage the interlayers. Thus, an alternative CNT/GO film attachment method was implemented. Firstly, the excess MCE around the edges of the CNT/GO film was clipped away and the CNT/GO film on MCE membrane was placed in an acetone bath for 10 min until the MCE had completely dissolved, leaving a free-floating CNT/GO mat in the bath. The acetone (with dissolved MCE) was removed via pipetting until only a very thin layer of acetone remained. The bath was then refilled with acetone for a further 10 min, this was followed by three more acetone refills for 10 min each. After the fifth acetone wash the solvent was replaced with water and the mat was left to float for 10 min to flush acetone from the CNT/GO matrix. This process was repeated an additional two times to ensure all acetone was removed from the bath. Note that the CNT/GO film had a very fluid shape (like a jellyfish) when floating in acetone but stabilised and spread into a flat mat when floating in water due to the hydrophobic nature of the CNTs. To attach the free-floating film to a substrate, the substrate was prepared (Section 2.1.5) and then submerged underneath the film in the water bath. The substrate was then raised through the solvent, taking the

CNT/GO film with it. The substrate could be re-submerged to properly align the film until it covered the desired area. The substrate was then carefully dried under a low flow nitrogen gas stream to avoid dislodging or deforming the film whilst it was still wet. CNT/GO films attached using this method displayed the same attachment strength as films attached using the heat/press method (section 2.1.3.1). To ensure the film had the required strength to hold itself together during the flotation process only films containing GO were used when flotation was the required attachment method.

When attaching to substrates with a solution processed MoO_x layer, the film was floated onto the substrate in the acetone bath after the final acetone replacement as water was found to remove the solution processed MoO_x. The CNT/GO film was manoeuvred above the substrate and pinned to the surface using forceps before the acetone was gently remove from the bath (via pipetting) to leave the film attached to the substrate.

2.1.3.3 Alumina film flotation attachment method

Part of the research in this thesis used alumina filtration membranes instead of the MCE top membrane. The alumina filters had a smaller pore size than the organic filters used in the above sections and thus the same template membrane used in section 2.1.2 was not used. Instead, the polyolefin and wax blend self-sealing thermos plastic Parafilm was used as the template membrane. Due to the brittle and rigid nature of alumina filtration membranes the heat/press method of attachment was not applicable. Therefore, CNT/GO films filtered onto alumina substrates were attached to a silicon or glass substrate in a similar method to the film flotation method detailed in Section 2.1.3.2. The difference was that, instead of the initial acetone bath, an aqueous solution of 3 M NaOH was used to dissolve the alumina substrate. This difference in initial solution led to two benefits of this method over the MCE film flotation method. Firstly, the initial solution was aqueous and thus the resultant CNT/GO film did not lose its shape as was the case with acetone. Secondly, the remove and refill method of replacing the 3 M NaOH with neutral water was easier to quantify as a pH measurement was taken to ensure the solution was no longer basic. In order to help achieve a slightly acidic solution a droplet of 3 M HCl solution was added to the final bath. However, a major

disadvantage of this method was the brittle nature of the alumina membranes. This caused simple procedures, such as separation of the alumina membrane from the Parafilm membrane (especially as the Parafilm membrane was stickier than the cellulose ester membrane), to become fraught with risk as even slight flexing of the alumina membrane could cause it to snap and thus cleave the CNT/GO film.

2.1.4 Graphene Oxide Synthesis

Graphene oxide was used in some experiments in this thesis to improve the strength of SWCNT films. The synthesis method used was based on the paper by Marcano *et al.*[172] A mixture of graphite flakes and $KMnO_4$ was prepared, and an acidic solution made using a 9:1 ratio of H_2SO_4/H_3PO_4 was added. The mixture was heated to 50 °C and stirred for 12 hr. After stirring, the reaction was cooled and poured onto ice made from purified water with 30 % H_2O_2. The mixture was sifted to remove any remaining graphite and then centrifuged, with the solid material retained. This material was washed six times, twice with water, twice with 30 % HCl, and twice with ethanol. The mixture was centrifuged after each wash. The remaining solid was filtered and vacuum dried overnight at room temperature, leaving dark grey graphene oxide flakes.

2.1.5 Solar device Substrate Production

Silicon wafers 100 mm in diameter were purchased from Active Business Company. The wafers were n-doped with phosphorous and had a 100 nm thick thermally grown SiO_2 layer. The wafers were pre-cleaned with Pirahna solution (3:1 mix of neat H_2SO_4 and H_2O_2) for 10 minutes, to remove any organic contaminants on the surface.

2.1.5.1 Small Area Photolithographic Patterning

Photolithography was used to produce a patterned surface on the silicon wafers. For the research in Chapters 3 and 4 the wafers were split into four pieces and a layer of AZ-1518 negative photoresist (methoxypropyl acetate, MicroChemicals) was spin coated on with a speed of 3000 rpm for 30 s using a Laurell WS-400B-6NPP/LITE Spin Coater. The wafer was baked for 50 s at 100 ˚C before UV light was shone on the photoresist through a template (Figure 2-3) to pattern the surface. The light was

manually applied using a UV torch for 240 s. The wafer was developed in AZ 326 developer (trimethyl ammonium hydroxide, MicroChemicals) for 30 s and post baked at 100 ˚C for 50 s.

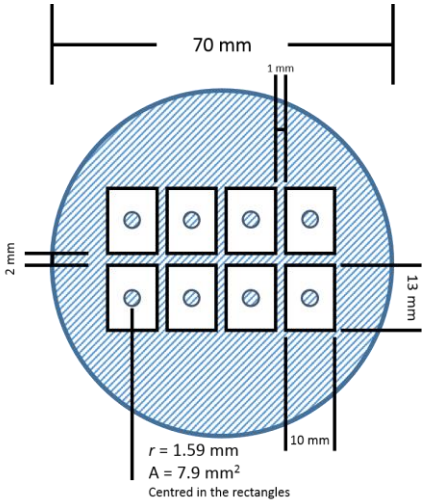

Figure 2-3: Template for device substrate photolithography where r and A are the radius and area of the inner circles (active area).

2.1.5.2 Large Area Photolithographic Patterning

For the research in Chapters 5 and 6, an enhanced photolithographic method was used to pattern the surface of the silicon to produce the substrates. This procedure was performed in an ISO-5 clean room. The substrate was spin-coated with a thin layer of AZ-1518 positive photoresist (MicroChemicals) and pre-baked at 100 °C for 50 s. The resist was then patterned using an EVG 610 mask alignment system with a UV exposure time of ten seconds. The mask used in this case was larger to allow wafers to be patterned without being cut (see Figure 2-4). The wafers were submerged in AZ 726 developer solution (MicroChemicals) for 30 s to dissolve the UV exposed photoresist sections. A water rinse was used to remove excess developer and dissolved photoresist. The wafer was then examined under an optical microscope to ensure the features on the surface had been well formed. A final post-bake was performed for 50 s at 110 ˚C. Small area device production was also moved to wafer style production using a mask aligner at this time.

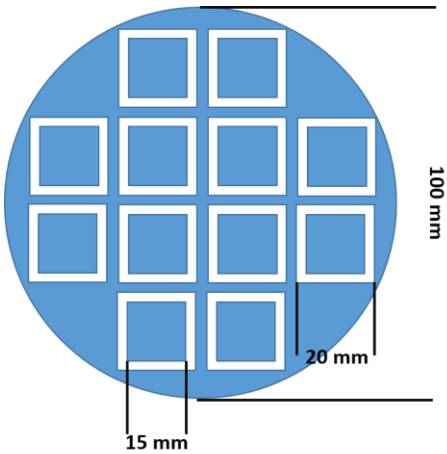

Figure 2-4: Full wafer scale substrate design. Note the blue squares inside each device are themselves patterned with 40 um grid lines (Figure 5-1).

More in depth details of the photolithographic pattern used in Figure 2-4 will be provided in Chapter 5 (Figure 5-1).

2.1.5.3 Metal Attachment

The pattered wafer was then coated with 5 nm of Cr and then with 145 nm – 745 nm of Au using a Q300T-D Dual Target Sputter Coater to form the top contact for the substrates. The Cr is required to ensure the gold layer attaches well to the silicon. After sputter coating, the wafer was submerged in acetone for 20 min to begin removing the photoresist and thus the Cr/Au from undesired areas. When smaller wafer segments were patterned as in Section 2.1.5.1, the pieces were placed in beakers of acetone and bath sonicated briefly. For wafer scale patterning (Section 2.1.5.2) the wafer was submerged in a dish of acetone for 30 min. Following this, a cotton bud was used to assist in the removal of the metal layer from the photoresist patterned areas. Use of manual force in this regard did not have an effect on the Cr/Au attached to the silicon oxide. It was important to submerge the metal coated wafer in acetone rapidly following the sputtering process to speed up the photoresist dissolving process. For the earlier experiments in this thesis, this was as far as the process went. For later research, an aluminium back contact was formed on the wafers before individual devices were separated.

2.1.5.4 Aluminium back contact formation

The Cr/Au patterned wafers were re-cleaned in a piranha solution. Following this, the back surface 100 nm SiO_2 layer was removed via etching with buffered oxide etch (BOE, 6:1 ammonium fluoride:

hydrofluoric acid). BOE etching time is temperature dependent so etching completion was observed by dewetting of the silicon surface by the aqueous acid solution. Once etched, the wafers were left in atmosphere for various amounts of time (5 min – 180 min, with 90 min determined to be optimal). The aluminium back contact was formed by evaporating aluminium on to the back surface of the wafers to a thickness of 300 nm in an ISO-5 clean room using an Angstrom Nexdep thermal evaporator. The aluminium was annealed for 30 min at 300°C.

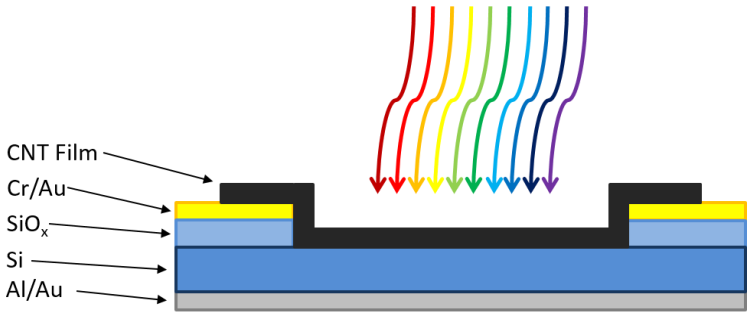

Figure 2-5: Schematic of a CNT/Si solar device with an annealed aluminium back contact and no solution processed interlayer.

2.1.6 Solar device Manufacture

Individual device substrates were separated from the wafers for solar device fabrication. This was done by scoring the wafer with a diamond-tipped scribe before gently applying force to one side of the wafer, causing it to split at the scored line. The active area of the devices was etched with BOE to remove the 100 nm oxide present on the surface. For each batch etch, a sacrificial piece of silicon with a 100 nm oxide (generally from the same wafer as the substrates) was etched with BOE and the time was measured from BOE deposition to dewetting of the surface by the aqueous BOE solution to give an approximate etching time. Care was taken to observe this etching time as it could change significantly with room temperature. Etching the substrates for too short a time could lead to a significant amount of silicon oxide remaining on the surface. Etching for too long could lead to undercutting of the top gold layer due to the isotropic nature of wet etching treatment. The time could not be determined using a substrate itself, as the grid network made it difficult to accurately observe the moment when dewetting occurred.

After removal of the SiO_2 layer in the active area, either a CNT film was directly attached (Section 2.1.3) or a solution processed interlayer was spin coated before CNT film attachment (Section 2.1.9). Before attachment, a variety of different surface oxide treatments were carried out, depending on the experiment. For most experiments, the substrates were used immediately after etching, or after a 30 min wait to allow a small amount of SiO_x regrowth, although for some experiments the wait period was longer. Alternatively, a few drops of H_2O_2 were placed on the active area to encourage SiO_x growth for 5 s before being rinsed with ultra-pure water, ethanol, and dried with nitrogen.

2.1.6.1 Back Contact Formation (eGaIn/Steel)

Prior to the use of an annealed 300 nm aluminium back contact (Chapters 3 and 4), a stainless-steel back contact was used. For this style of back contact the reverse side of an individual device substrate was scratched with a diamond-tipped scribe to access the silicon underneath the 100 nm silicon oxide layer. A small amount of gallium-indium eutectic (eGaIn) was then applied to the scratched area and a roughly 4 cm^2 square of stainless steel was attached to the silicon. The eGaIn serves two purposes in this architecture. It ensures a good electrical contact between the silicon and the steel back contact, and it provides adhesion to keep the substrate attached to the steel plate.

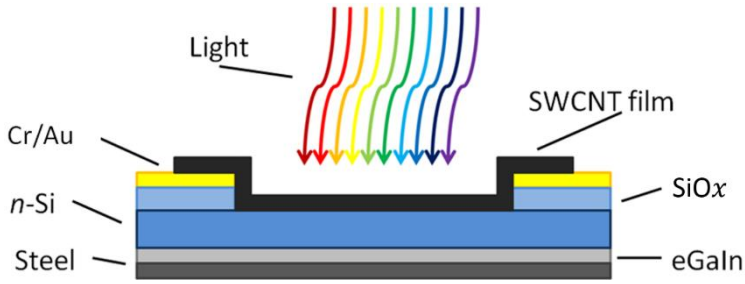

Figure 2-6: Schematic of a SWCNT/Si solar device with an eGaIn/steel back contact and no solution processed interlayer.

2.1.8 Post-Fabrication Treatment Procedures

Once fabricated, the CNT/Si devices were treated with a range of chemical dopants to improve their properties.

2.1.8.1 Thionyl Chloride Doping

Thionyl Chloride ($SOCl_2$) was used to dope the CNT or CNT/GO film post-fabrication. The doping was performed by dropping a small amount of the $SOCl_2$ solution over the nanotube film and allowing the

liquid to evaporate over roughly 1 min – 2 min. Once the droplet had evaporated the device was washed with ethanol to remove any remaining unreacted $SOCl_2$ and dried under a nitrogen stream.

Alternatively, $SOCl_2$ doping was carried out using vapour rather than direct liquid contact, where the corrosive nature of the $SOCl_2$ would cause a problem to the device makeup. An amount of $SOCl_2$ was poured in a glass petri dish and the substrates to be doped were attached to the underside of the petri dish lid with double sided tape. The lid was placed over the $SOCl_2$ bath for 2 min to allow the vapours to dope the CNT or CNT/GO film. No ethanol wash was performed after this process as, generally, the ethanol would damage the device make up similarly to the $SOCl_2$.

2.1.8.2 Gold Chloride Doping

Gold chloride ($AuCl_3$) was used to dope the CNT or CNT/GO film post device fabrication. The doping was performed by dissolving solid chloroauric acid (Sigma-Aldrich) in water at a concentration of 5 mM. The resultant pale-yellow suspension was dropped onto the film and left for 30 s before spin-coating at 5000 rpm for 30 s using a Laurell WS-400B-6NPP/LITE Spin Coater. Note that this $AuCl_3$ doping was performed from aqueous solution similar to Yu *et al.,*[100] as the more commonly used nitromethane could damage the interlayers on the substrate used in chapter 6.

2.1.8.3 Hydrofluoric Acid (2 %) Etches

The device fabrication and many post-fabrication procedures involve the use of oxidisers or heating which can cause silicon oxide to grow on the surface of the silicon active area. As mentioned in Chapter 1, a thin atmospheric oxide has been shown to improve the device performance. Oxides grown in the presence of liquid oxidisers or with heat are thicker and, thus, less desirable. To remove these oxide layers, a 10 s etch using a 2 % solution of HF was performed. In many cases this is the final treatment performed to give a device's final properties. In many cases two 2 % HF etches were performed both before and after doping of the CNT film. The labels HF-1 and HF-2 are used to refer to the two etches, with HF-1 indicating the etch prior to doping and HF-2 indicating the final etch.

2.1.9 Application of Solution Processed Interlayers

For some experiments, a solution processed interlayer was placed on the etched device substrate prior to CNT or CNT/GO film attachment. These layers were generally attached via spin-coating with a following annealing process.

2.1.9.1 Application of DAD hole transport layer

4,10-bis(bis(4-methoxyphenyl)amino)naphtha[7,8,1,2,3-nopqr]tetraphene-6,12-dione (DAD) solid was provided by Prashant Sonar's research group at the Queensland University of Technology. A suspension of DAD was prepared by dissolving solid DAD in chlorobenzene at a concentration of 60 mg mL^{-1}. The DAD mixture was sonicated for 30 min in an Elmasonic sonicator in order to allow the DAD solid to dissolve. After this process, any solid DAD remaining was removed by filtering through a 0.45 µm filter to give a deep-green solution. This solution was spin-coated on to solar device substrates at a variety of volumes for 30 s at a range of spin speeds using a Laurell WS-400B-6NPP/LITE Spin Coater.[173]

2.1.9.2 Application of a Molybdenum Oxide Layer

An aqueous MoO_X precursor solution was provided by Lianzhou Wang's group from the University of Queensland. The MoO_x precursor solution was spin-coated on to device substrates at a variety of volumes for 60 s at a range of spin speeds using a Laurell WS-400B-6NPP/LITE Spin Coater. The substrates were then heated at 80 ˚C for 30 min to produce a MoO_x layer on the surface from the precursor solution.

2.1.9.3 Application of a PEDOT:PSS Interlayer

An aqueous PEDOT:PSS solution was purchased from Heraeus for use in these experiments. The solution was diluted at a 1:10 ratio with MilliQ water, a 1:5 ratio with IPA or a 1:1 ratio with IPA, prior to use. The PEDOT:PSS solution was spin-coated on to the solar device substrate at a variety of volumes for 60 s at a range of spin speeds using a Laurell WS-400B-6NPP/LITE Spin Coater. After spin coating the device substrates were heated at 130 ˚C for 30 min, immersed in a methanol bath for 10 min, and then dried at 140˚C for 5 min. This procedure was important to improve stability in the PEDOT:PSS film in ambient conditions.[131]

2.1.9.4 Application of a PANI Interlayer

A solution of PANI was prepared by dissolving an emeraldine base (M_W: 10000, Sigma) in 80 % acetic acid or dimethyl formamide (DMF) at a range of concentrations followed by filtering through a 0.45 µm membrane to remove remaining particulate matter. The PANI solution was spin-coated on to the device substrate at a variety of volumes for 60 s at a range of spin speeds using a Laurell WS-400B-6NPP/LITE Spin Coater. The resultant PANI film on the solar device substrate was heated at 130 ˚C for 2 hr.

2.1.9.5 Application of a CuSCN Interlayer

Two different suspensions of CuSCN were used. Solid CuSCN (Sigma Aldrich) was dissolved in either aqueous ammonia (ammonium hydroxide) or diethyl sulphide (DeS, Sigma Aldrich) by stirring at 50 ˚C for 1 hr. The grey solid formed a blue suspension when dissolved in aqueous ammonia and a pale-yellow suspension when dissolved in DeS. Once formed, the suspensions were filtered through 0.45 µm filters to remove any un-suspended particulate matter. As per previous work, the suspensions were left overnight to ensure the solution reached thermodynamic equilibrium.[174] The CuSCN suspension was spin coated onto substrates at a variety of volumes and speeds for 60 s using a Laurell WS-400B-6NPP/LITE Spin Coater. CuSCN dissolved in aqueous ammonia was also deposited on substrates by placing droplets of solution on substrates and leaving the solvent to evaporate.

2.2 Characterisation and Analysis Techniques

2.2.1 Solar device Testing Procedure

Throughout the work outlined in this thesis, photovoltaic devices were tested to measure a variety of performance parameters. For a given device a current density vs voltage (J/V) curve was created both in dark conditions and under controlled intense illumination. A J/V curve is created by measuring the current passing through the device as the voltage is shifted, in this case, from 1 V to -1 V. The current is then divided by the known area of the active junction of the device to produce a current density measurement. Thus, a plot of current density 'J' (mA cm^{-2}) vs voltage 'V' (V) is produced. Examples of J/V curves under both dark and light conditions are shown here in Figure 2-7, Figure 2-8, and Figure 2-9. The J/V curve formed under illumination allows four important parameters to be obtained for a

device. Firstly, the short circuit current density (J_{SC}) is the current measured at the point where the circuit is shorted (i.e. a voltage of 0 V). The open circuit voltage (V_{OC}) is the voltage at which the circuit is open (i.e. a current/current density of 0 mA/mA cm^{-2}). These two parameters are used to find an 'ideal maximum power' by extrapolating straight lines perpendicular to the axes on the J/V curve and this resultant rectangle is compared with the actual maximum power point along the curve of the graph and which produces a smaller rectangle (see Figure 2-7). The ratio of the actual rectangle compared to the ideal rectangle gives the third important measurement, called the fill factor (FF) which can clearly vary from 0 to 1. The overall percent current efficiency (PCE) of the device is then calculated by multiplying the J_{SC}, the V_{OC} and the FF together, dividing by the known power of the incident light and multiplying by 100 % (see Equation 2-1).

Equation 2-1: Percent current efficiency calculation, where V_{oc} is the open circuit voltage, J_{sc} is the short circuit current density, FF is the fill factor and Pin is the incident power.

$$PCE(\%) = \frac{Voc \times Jsc \times FF}{Pin} \times 100\%$$

For some of the experiments in the following chapters a power of 100 W cm^{-1} was used and thus the equation can be simplified to a simple multiplication of the three parameters. However, due to a spot size vs active area size issue, the experiments involving large devices used a power at roughly half that. This was taken into account when calculating the PCE for these devices. Illumination was provided by a Newport 150 W Xenon lamp in a Newport arc lamp power supply model 69907. Analysis of the intensity spectrum of the light source is shown here in Section 2.2.2. Lamp irradiation intensity was kept constant using a silicon reference device (PV Measurements, NIST-traceable calibration).

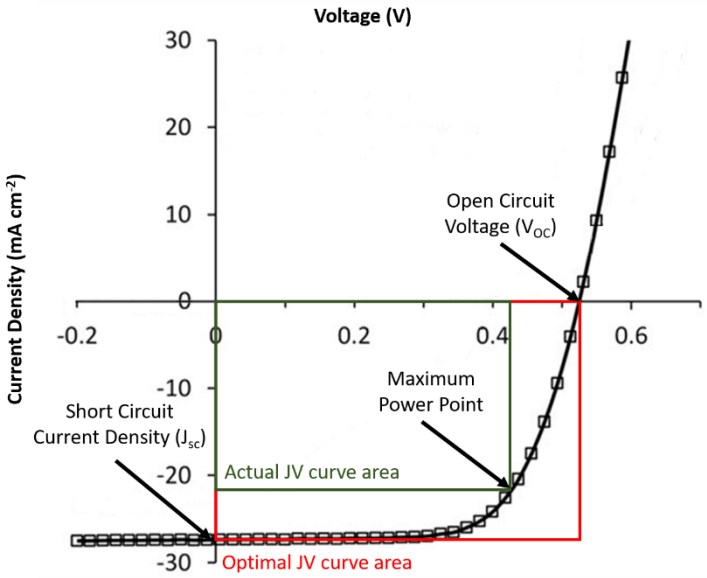

Figure 2-7: An example J/V curve formed under illumination where the maximum power point is calculated by multiplying the V_{oc} by the J_{sc} and the FF. The FF itself is the area ratio of the green actual rectangle to the red optimal rectangle.

The curve produced when the device is shielded from illumination (a 'dark curve') (see Figure 2-8) does not extend into the 4th quadrant of the plot, unlike an illuminated J/V curve. This is because a PV device will not produce a photocurrent when no illumination is incident with the surface. Whilst the 'dark' curve as plotted in Figure 2-8 is not very useful, more information can be gleaned from analysing a semilog plot of the $\log_{10}$ of the current density vs the voltage from a dark curve as shown in Figure 2-9. This curve is useful for acquiring different information to the J/V curve under illumination. This gives a plot with a significantly different shape, from which diode structure information such as the reverse saturation current density and a diode ideality measurement can be extracted. For the research in this thesis, recorded solar device data was processed using a custom program written in LabView, connected to a Keithley data acquisition unit, which calculated the vital parameters from the J/V curve, both under illumination and in the dark. Figure 2-9 shows that the series and shunt resistances can be calculated from the slope at two different points on the semi-log plot of the dark curve.

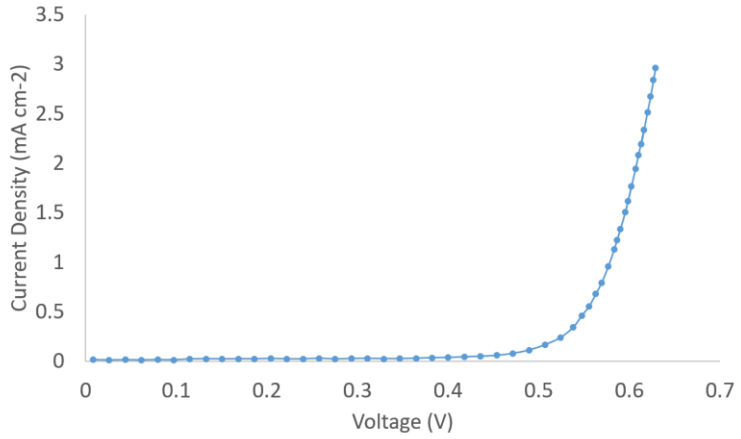

Figure 2-8: Example 'dark' J/V Curve[127]

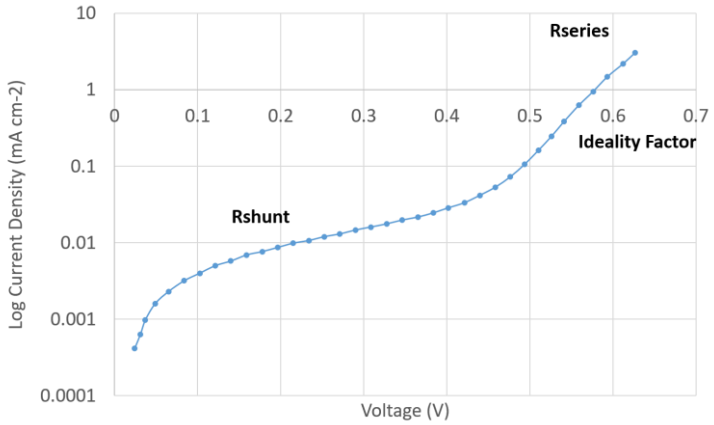

Figure 2-9: Example 'dark' J/V semi-log curve[127]

2.2.2 Solar Testing Lamp Spot Size Adjustments.

The light source used for the small device (active area 0.074 to 0.09 cm^2) experiments in this thesis was an AM1.5 source with an output power of roughly 100 mW cm^{-2}. However, the large area devices (active area 2.25 cm^{-2}) did not fit under the spot area without portions of the active area being un-illuminated. A rough current output analysis using the silicon reference device when moved under an illumination spot showed that, as soon as part of the device was un-illuminated, the current undergoes a sharp drop-off. Thus, the lamp spot used for small device experiments cannot be used for large device experiments.

A compromise was used in which the lamp height was adjusted to give a larger spot size which could encompass the entire large area device. The downside here was that the intensity (and thus power)

per unit area produced by the lamp was reduced. To compensate for this the lamp spot was adjusted to give an output power of roughly 50 mW cm^{-2} (half of that used previously) and the J/V data analysis program was adjusted to account for the reduced irradiation power. Under the 50 mW cm^{-2} source the current produced, and thus the J_{sc}, of a device will be less than the current produced under the full 100 mW cm^{-2} source. Ideally, by applying the reduced irradiation power in the PCE equation (Equation 2-1) the same PCE value would result at any input power. However, this is not the case, it has been seen from experimental observation that the PCE of the silicon reference device (used to calibrate the light source in this thesis) drops as input power is lowered.

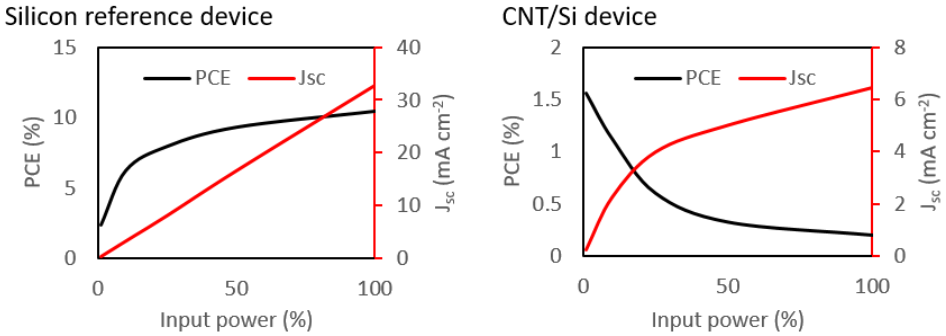

Figure 2-10: Effect of changing input power on photovoltaic properties in the silicon reference device and a CNT/Si device. The input power is a percentage of the optimal power of 100 mW cm^{-2}.

Figure 2-10 shows that, whilst the silicon reference cell displays the ideal linear trend of J_{sc} vs input power, the CNT/Si device does not. Furthermore, the PCE for the reference device decreases slightly over most of the plot before sharply dropping at low input powers. The opposite is true for the CNT/Si device where the PCE increases sharply from around 25 % and lower. This is likely due to resistive power loss in the CNT film having a greater effect as the film is required to transport greater currents. Thus, the devices cannot be directly compared if a different light source power has been applied. More thorough investigation of the effect of changing input power is required to properly test and compare large area CNT/Si devices.

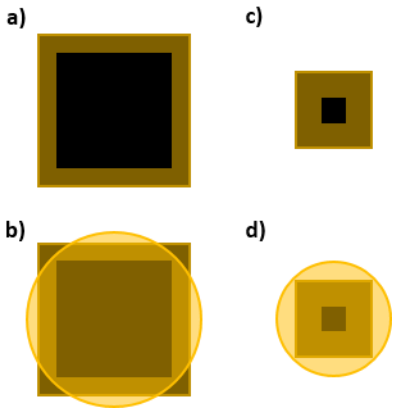

Figure 2-11: Schematic showing the relative sizes of the different active area devices and their relationship with the different light spot sizes used. a) large active area device. b) large active area device under 50 mW cm^{-2} light spot. c) small active area device. d) small active area device under 100 mW cm^{-2} light spot.

2.2.2.1 Lamp Spot Inhomogeneity

Another very important property of the light source that must be discussed is lamp spot homogeneity. The above discussion assumes that the lamp power output does not vary across the diameter of the lamp spot. However, it could be seen visibly that the lamp spot was not equally intense across the area. To image this inhomogeneity a thin aperture (approximately 1.5 mm by 9.5 mm) was placed over the silicon reference device and this aperture was moved from one outside edge of the light spot area to the other edge, with the current output recorded for each 1 mm step in both the horizontal and vertical directions.

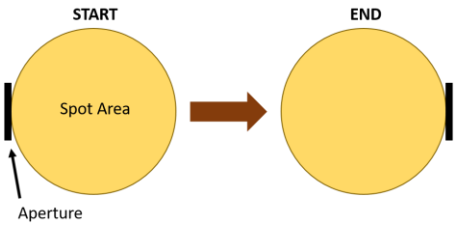

Figure 2-12: Schematic of spot area current testing. The aperture began outside, but adjacent to the edge of the spot and was moved in mm increments until it was adjacent to the opposite edge and completely outside the spot area. This schematic represents the horizontal measurements, for vertical measurements the aperture began adjacent to, but outside the top edge of the spot and was moved until it was adjacent to the bottom edge and was completely outside the spot.

Figure 2-13 shows the current map for the large spot size used to test the large area (2.25 cm^2) devices. The measured current is not consistent across the spot area, with smaller currents on both sides of the centre in the *x*-axis direction. In the *y*-axis direction, the current profile is less symmetrical, with a peak closer to the top edge of the light spot.

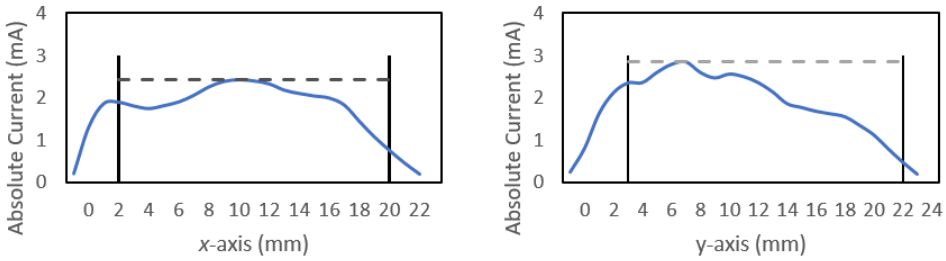

Figure 2-13: Lateral absolute current values for large area spot size for both axes. Black vertical lines bracket the region where the aperture was entirely within the spot area. The horizontal grey dashed line represents an ideal case where there is no intensity drop off across the spot area.

The same experiment was performed on the smaller spot size (that used for small devices that gives a power output of 100 mW cm^{-2}), and this is shown in Figure 2-14. The same trends are visible when these current values are plotted vs lateral shift.

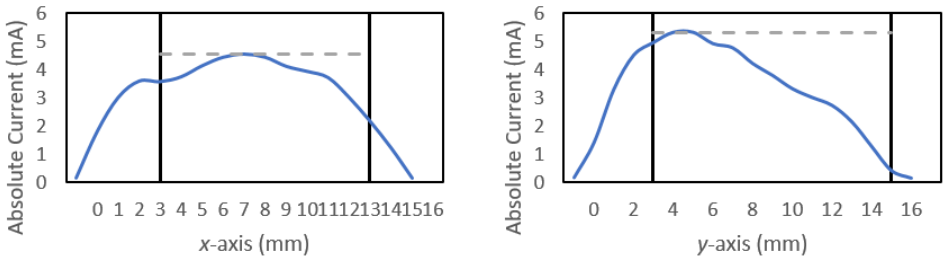

Figure 2-14: Lateral absolute current values for small area spot size for both axes. Black vertical lines bracket the region where the aperture was entirely within the spot area. The horizontal grey dashed line represents an ideal case where there is no intensity drop off across the spot area.

It is obvious that there is significant inhomogeneity present in the AM1.5 source used for the experiments in this thesis. The large area devices suffer a greater detrimental effect due to this intensity inhomogeneity as a large area device positioned for maximum intensity (and thus maximum current output) will experience less irradiance, per unit area, compared to a small area device also positioned for maximum irradiance. This is because a large area device will be exposed to a greater proportion of the total light spot than a small area device.

In order to perform a more complete analyse of the inhomogeneity of the lamp spot area, the silicon reference device was covered to leave only a 1 mm^2 aperture and was moved precisely across the large spot area both vertically and horizontally to image each square millimetre of the spot. The data produced from this experiment was plotted on a grid with µA values for each mm^2. A colour gradient was applied to better visualise the intensity change across the spot area.

6	7	8	10	13	17	21	29	60	81	60	99	88	65	56	35	19	13	10	9	7	6	5	5
8	8	11	15	19	20	68	115	121	115	121	116	107	94	81	92	58	23	27	15	10	8	7	6
10	12	17	24	65	120	144	126	139	143	147	152	145	135	115	99	95	49	33	33	15	11	8	6
12	15	22	48	133	143	148	138	151	151	162	171	179	175	156	146	125	83	47	66	31	14	10	8
14	20	45	130	154	156	150	151	180	177	183	184	191	187	176	173	142	93	96	117	69	29	14	9
18	33	111	153	180	178	182	192	204	210	207	191	191	188	198	165	140	117	122	129	83	84	31	13
22	58	139	157	171	186	189	212	227	220	215	198	190	185	185	162	140	104	104	123	78	59	37	15
33	89	138	166	149	170	196	217	222	222	218	208	213	199	183	170	140	96	108	90	70	65	57	22
46	115	135	153	145	165	201	226	236	213	220	215	220	216	173	145	142	121	122	118	101	82	67	28
52	125	152	172	173	179	196	207	232	223	239	262	232	227	200	162	135	127	135	139	111	94	64	36
74	126	164	183	183	199	204	212	224	228	242	256	242	225	206	152	130	142	153	138	117	111	74	40
94	145	162	184	195	210	222	202	210	213	236	236	261	252	189	157	151	156	159	144	117	101	62	43
102	170	155	170	183	195	224	229	204	205	243	275	213	186	180	178	169	167	151	144	119	93	75	49
82	145	162	187	179	186	208	233	225	216	207	218	204	183	179	183	172	168	156	141	126	102	78	46
36	104	184	193	179	194	197	220	200	185	185	180	183	180	170	172	173	164	143	126	111	60	68	29
18	66	142	200	183	212	205	207	193	154	162	165	175	164	160	165	162	147	124	116	122	93	49	18
14	27	117	198	221	222	195	185	163	148	161	160	159	147	146	135	140	125	120	113	102	87	28	14
11	17	77	168	219	192	189	179	177	157	133	138	138	137	126	113	120	123	118	115	95	52	18	11
9	13	36	126	171	198	190	179	184	164	146	129	126	126	122	126	125	125	113	110	75	27	14	9
8	10	15	40	80	114	157	179	202	178	162	142	125	121	129	127	120	112	97	72	28	15	10	7
6	8	11	14	26	64	129	142	191	180	165	163	137	125	112	112	106	95	58	15	15	11	8	6
5	6	8	10	13	19	49	81	129	168	173	161	153	126	99	88	66	34	18	13	10	8	6	5
4	6	7	9	10	12	16	21	38	88	106	94	88	73	54	32	19	15	12	10	8	7	6	5

Figure 2-15: Current output 'heat map' of AM1.5 spot area. Each square represents 1 mm^2 of area, each value is in µA. The darker red areas indicate higher current, whilst green areas indicate very low current (generally outside the spot area).

The image, with colour gradient, makes it clear that the irradiance of the lamp spot is not consistent across the whole area. There is also a region on the top right and centre right of the image that is clearly less intense than areas at similar radii. Overall, it can be seen that the large area devices will suffer from these low intensity outer areas as the smaller devices are only illuminated by light closer to the centre. To determine the effect of the non-homogenous spot area, the active areas for both the small, large and reference devices were placed under the centre of the spot area map to calculate a theoretical current output to compare with actual produced J_{sc}. These will be presented in order of smallest to largest active area. As the spot area covers an odd number of mm^2 devices in the *y*-plane and an even number in the *x*-plane it is not possible to easily determine the centre. To account for this, on the axis where the mm^2 devices would not fit evenly under the active area (*x*-plane for the 3 x 3 mm^2 small device and the 15 x 15 mm^2 large device and the *y*-plane for the 10 x 10 mm^2 reference

cell) an extra row/column of devices was taken and the outer rows/columns were halved in value to give the best possible area determination.

Table 2-2: Theoretical current production per mm² for 3 x 3 mm² devices from spot area data in µA.

	Total Halved			Total Halved
	242	255.5	241.6	224.6
	235.8	236	261.2	251.5
	243.3	274.5	213.1	186
Total	360.55	766	715.9	331.05

For each area the overall current is summed, converted from µA to mA and divided by the active area in question to give a theoretical current density for the device under ideal conditions. The calculated theoretical current for the 3 x 3 mm^2 device was 2.17 mA, which when divided by the area of 0.09 cm^2 gives a theoretical current density of 24.15 mA cm^{-2}. The same process was performed for the 1 cm^2 reference device and for the 2.25 cm^2 large area device. The top and bottom rows of values were halved for the reference device and the left and right columns were halved for the large area device.

Table 2-3: Theoretical current production per mm² for 1 x 1 cm² reference device from spot area data in µA.

Pre-Halved	106	113.55	110	107.3	99.2	95.1	92.65	92.25	80.75	70
	216.8	222.4	221.5	217.8	208	212.8	198.7	182.5	170	140
	225.5	235.5	213	220	215	220	215.5	172.8	144.5	141.5
	206.5	231.8	222.6	238.5	261.7	231.5	226.5	200	162	135.4
	212	224	227.5	242	255.5	241.6	224.6	205.5	152	130
	202	210	213	235.8	236	261.2	251.5	188.8	156.6	150.5
	229	204.2	204.5	243.3	274.5	213.1	186	180	178.1	168.8
	233	225	216.1	207.1	218	204	182.5	179	182.8	171.7
	220	200	185	184.5	180	182.6	180	170	171.5	172.6
	207	193	154	162	164.7	175	164	160	165	161.5
Pre-Halved	92.65	81.55	74.15	80.55	79.75	79.5	73.5	73	67.55	69.8
Total	2150.45	2141	2041.35	2138.85	2192.35	2116.4	1995.45	1803.85	1630.8	1511.8

The summed current values for the 1 x 1 cm^2 reference device gives 19.72 mA, which gives a theoretical current density of 19.72 mA cm^{-2} when divided by the device area of 1 cm^2.

Table 2-4: Theoretical current production per mm² for 2.25 cm² large area device from spot area data in µA.

	Pre-Halved															Pre-Halved
	76.75	155.8	150	150.5	179.8	177	183	183.5	191	186.5	175.5	173.3	142	92.5	95.5	58.25
	90	178.3	182.4	192	204	209.5	206.75	191.4	191	188	197.5	164.5	139.5	116.8	122	64.5
	85.55	185.5	189	212	227.1	220	214.6	198.4	190.2	185.3	184.5	161.5	140	104	103.5	61.5
	74.25	170	195.5	216.8	222.4	221.5	217.8	208	212.8	198.7	182.5	170	140	95.5	107.5	45
	72.25	164.5	201	225.5	235.5	213	220	215	220	215.5	172.8	144.5	141.5	121	122	58.75
	86.5	179	195.5	206.5	231.8	222.6	238.5	261.7	231.5	226.5	200	162	135.4	127.3	135.4	69.35
	91.5	199	204	212	224	227.5	242	255.5	241.6	224.6	205.5	152	130	141.5	152.5	68.75
	97.25	210	222.3	202	210	213	235.8	236	261.2	251.5	188.8	156.6	150.5	156.2	158.7	72
	91.3	194.8	223.5	229	204.2	204.5	243.3	274.5	213.1	186	180	178.1	168.8	167.2	151.2	72
	89.5	185.5	207.7	233	225	216.1	207.1	218	204	182.5	179	182.8	171.7	168	156.2	70.65
	89.5	193.7	196.6	220	200	185	184.5	180	182.6	180	170	171.5	172.6	163.5	143	62.75
	91.5	212	205	207	193	154	162	164.7	175	164	160	165	161.5	147.2	123.8	57.95
	110.4	221.7	195.4	185.3	163.1	148.3	161.1	159.5	159	147	146	135.1	139.6	124.5	120	56.3
	109.55	192	189	179.1	177	156.8	133.4	137.6	137.7	137.4	125.8	112.7	120	122.8	118.2	57.5
	85.6	197.8	190	179	184.4	163.8	146	129	125.8	125.5	122.3	125.7	125.1	124.5	113.1	54.75
Total	**1341.4**	**2839.6**	**2946.9**	**3049.7**	**3081.3**	**2932.6**	**2995.85**	**3012.8**	**2936.5**	**2799**	**2590.2**	**2355.3**	**2178.2**	**1972.5**	**1922.6**	**930**

The summed current values for the large area device give a total current of 39.88 mA which gives a theoretical current density of 17.73 mA cm^{-2} when divided by the device area of 2.25 cm^2.

The calculated current density is not the same for the different device sizes. Instead it decreases with area, due to the intensity gradient from the centre of the light spot to the edges. As the reference device is used to calibrate the light intensity before testing devices, the calculated current densities for the two device sizes can be compared to the theoretical intensity for the reference device to further calibrate for the difference in intensity across the spot area.

Firstly, the theoretical current density for a 1 x 1 cm^2 area under the spot was calculated at 19.72 mA cm^{-1} however the spot size that was used gave an actual current output of approximately 16.4 mA when the reference device was measured in the centre of the spot. Thus, there is a difference between the theoretical and actual current outputs. The same reference device (with a 1 mm^2 aperture) was used to create the 2D spot area map and thus this difference is not due to differences in device performance.

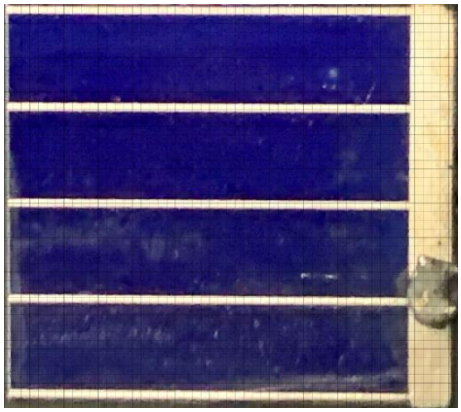

Figure 2-16: Image of the 1 x 1 cm^2 reference device used in these experiments. The blue area is the silicon active area and the gold lines are metal electrodes.

Rather, the difference is likely caused by shadowing from the metallic fingers, which affects the current density when the whole device is illuminated. This was not taken into account during 2D map creation as the 1 mm^2 aperture was deliberately placed between the fingers. In the photograph shown in Figure 2-16, each finger is approximately 47 grid squares long and 1 grid square thick. Thus 188 grid squares are obscured by the metal fingers. The 1 cm^2 area is approximately 46 by 47 grid squares and thus approximately 188/(46 × 47) × 100 % of the device is directly obscured. This gives a shadowing due to the metallic fingers of 8.7 %, which reduces the theoretical current to 18.00 mA cm^{-2}. An additional reason for the differential between the actual and theoretical current density could be light scattering through the glass between the aperture and the silicon surface. This would cause an area slightly larger than 1 mm^2 to be illuminated and thus, give a higher estimate of current production.

The spot area used in this analysis was chosen to apply a power of 50 mW cm^{-2} and this was confirmed by a current measurement from the reference device of 16.4 mA (half of the 100 mW cm^{-2} value of 32.7 mA). However, it is obvious that the inhomogeneity of the spot area will mean devices with areas smaller than the reference device will receive power densities higher than intended and devices larger will receive power densities lower than intended. The above calculated theoretical current data and measured current data from devices of different area, can be compared to find the difference in power density output and thus develop a scaling factor to apply to large area devices. This scaling factor should ensure that two ideal devices of different sizes would produce the same scaled current density.

To calculate the difference in power output, the theoretical current density for the small and large area devices was divided by the theoretical current density for the reference cell. The resultant fraction was multiplied by the power density on the reference device of 50 mW cm^{-2} to calculate the actual power density.

Equation 2-2: Large area device current density ratio calculation.

$$\frac{Large\ Cell\ Current\ Density}{Reference\ Cell\ Current\ Density} = \frac{17.7}{19.7} = 0.898$$

$$0.898 \times 50\ mW\ cm^{-2} = 44.9 \approx 45\ mW\ cm^{-2}$$

Equation 2-3: Small area device current density ratio calculation.

$$\frac{Small\ Cell\ Current\ Density}{Reference\ Cell\ Current\ Density} = \frac{24.2}{19.7} = 1.228$$

$$1.228 \times 50\ mW\ cm^{-2} = 61.4 \approx 61\ mW\ cm^{-2}$$

It can be seen that when the reference device implies an irradiance of 50 mW cm^{-2} from the AM1.5 source, the actual irradiance is 61 mW cm^{-2} for the small area devices and 45 mW cm^{-2} for the large area devices. This goes some way to explaining the significant current density differences experienced between the large and small area devices. These power relationships can be used to scale the J_{sc} values for a given device and, by extension, the PCE values as PCE is directly proportional to J_{sc}.

A set of small and large area devices were fabricated for comparison, the transmittance of the CNT film was kept constant between these two sets as was the series of post fabrication treatments. The raw J_{sc} values are listed in Table 2-5. These J_{sc} values were then multiplied by 50/45 for the large devices and 50/61 for the small devices to scale the J_{sc} based on the calculated differences in actual irradiance.

Table 2-5: Measured J_{sc} values for large and small active area devices under 50 mW cm^{-2} spot size scaled based on power output difference with device size.

Device Type	*Measured J_{sc} (mA cm^{-2})*	*Scaling Factor*	*Adjusted J_{sc} (mA cm^{-2})*
Small device 1	12.586	50/61 = 0.819672	10.31639

Small device 2	12.793	50/61 = 0.819672	10.48607
Small device 3	12.636	50/61 = 0.819672	10.35738
Average Small Device	12.672	50/61 = 0.819672	10.38689
Large device 1	7.968	50/45 = 1.111111	8.853333
Large device 2	8.383	50/45 = 1.111111	9.314444
Large device 3	8.404	50/45 = 1.111111	9.337778
Average Large Device	8.252	50/45 = 1.111111	9.168889

After applying the scaling factor, as determined from the 2D current map of the spot area, the J_{sc} values are much closer than before adjustment. With the average difference decreasing from 4.42 mA cm^{-2} to 1.22 mA cm^{-2}. From these experiments it is clear that inhomogeneity of the AM1.5 light source is a significant contributor to the stark J_{sc} differences observed when the device active area is increased. However, this issue can be accounted for using a scaling factor.

2.2.2.2 Power Loss

There are additional causes for the difference in current density between the small and large active area devices other than the lamp spot inhomogeneity. Once cause is resistive power loss across the front contact of the devices. Both devices rely on the gold grid network across the front contact to transport charge carriers from the surface to be collected as the CNT film lacks the ability to transport charge carriers over long distances. This gold network won't perfectly transport charge carriers and any loss experienced across the metal will increase with distance. This is likely a reason for the drop in current density on the larger devices as the grid lines are five times larger in the 2.25 cm^2 devices. The power loss effect is measurable using Equation 2-4 and Equation 2-5. The equations show that power loss is proportional to the area and the current density.[99]

Equation 2-4: Power loss equation.

$$P_{loss}(Wcm^{-2}) = \frac{V(V) \times I(A)}{A(cm^2)} = \frac{R_s(\Omega) \times {I_{max}}^2(A^2)}{A(cm^2)} = R_s(\Omega) \times A(cm^2) \times {J_{max}}^2(A^2cm^{-4})$$

Equation 2-4 can be simplified as shown to give Equation 2-5

Equation 2-5: Simplified power loss equation, A is the active area of the device, J_{max} is the current density at the maximum power point, and R_{seies} is the series resistance.

$$P_{Loss} = R_{Series} \times A \times {J_{max}}^2$$

As discussed above, the AM1.5 source does not provide a homogeneous irradiance across the device area. Thus, this lamp spot could not be used to compare large devices to small devices to investigate power loss. Instead, both large and small area devices were fabricated and the JV characteristics were measured under room lighting. As a result of the low light intensity low current densities were observed. The JV curves produced by the small and large devices after a 2 % HF etch are shown in Figure 2-17.

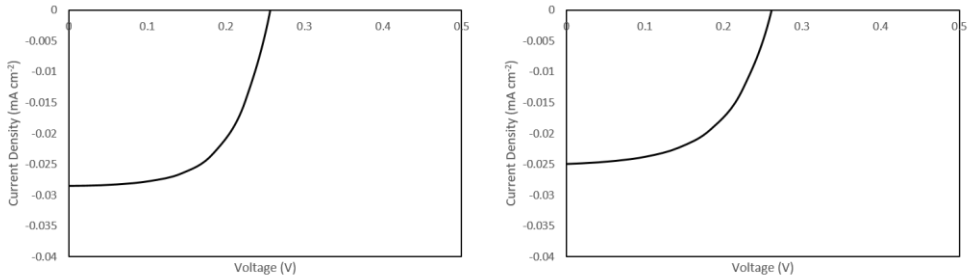

Figure 2-17: J/V Curves for Small device (Left) and Large device (Right) under roomlight illumination.

The large area devices produced a lower current density than the small area devices, although this difference was decreased after the HF etch. Initially, the J_{sc} of the small area device was 0.031 mA cm^{-2} but this decreased to 0.028 mA cm^{-2} after the etch. Conversely, the large area device produced a J_{sc} of 0.023 mA cm^{-2} which increased to 0.025 mA cm^{-2}. The J_{sc} values for the two devices in this case are much closer than when the same comparison is made under AM1.5 illumination (Table 2-5). This indicates that the use of room lighting over the solar simulation lamp has adjusted for the light intensity inhomogeneity discussed above. As both the R_{series} and the J_{max} can be determined from the J/V curves, the power loss per unit area can be calculated using Equation 2-5.

Table 2-6: Power loss per unit area calculations for small and large active area devices both as prepared and after treatment with 2 % HF.

	Current Density at Max Power (mA cm^{-2})	*Current Density at Max Power (A cm^{-2})*	*Current Density at Max Power Squared (A^2 cm^{-4})*	*Series Resistance (Ω)*	*Active Area (cm^2)*	***Power Loss (W cm^{-2})***
Silicon reference device	-0.0252	-2.52×10^{-5}	6.360×10^{-10}	1210	1	**7.70×10^{-7}**

Small device AP	-0.0235	-2.354×10^{-5}	5.542×10^{-10}	36800	0.09	**1.84×10^{-6}**
Small device 2 % HF	-0.0232	-2.321×10^{-5}	5.387×10^{-10}	20800	0.09	**1.01×10^{-6}**
Large device AP	-0.0163	-1.630×10^{-5}	2.656×10^{-10}	3190	2.25	**1.91×10^{-6}**
Large device 2 % HF	-0.0193	-1.934×10^{-5}	3.741×10^{-10}	1200	2.25	**1.01×10^{-6}**

Table 2-7: Power loss calculation from power loss per unit area and device area.

	Power Loss (W cm^{-2})	*Power Loss (W)*
Small device (0.09 cm^2) AP	1.84×10^{-6}	**1.65×10^{-7}**
Small device (0.09 cm^2) 2 % HF	1.01×10^{-6}	**9.08×10^{-8}**
Large device (2.25 cm^2) AP	1.91×10^{-6}	**4.29×10^{-6}**
Large device (2.25 cm^2) 2 % HF	1.01×10^{-6}	**2.27×10^{-6}**

Table 2-6 and Table 2-7 shows the data and calculated power loss per cm^2 for both sizes of device before and after etching with 2 % HF. It is apparent that the power loss per unit area is equivalent for both sizes of devices. This indicates that the drop in current experienced by the large area devices, even when the lamp spot inhomogeneity is taken into account, is caused by resistive power loss as it will clearly have a greater effect on larger area devices. It is unclear why the series resistance is so much higher for the small area devices. The series resistances are well below 1000 Ω when small area devices are measured under the AM1.5 light source. Additionally, when a J/V curve of the silicon reference device was produced under room lighting, the series resistance was calculated to be roughly 1200 Ω which is significantly higher than would be expected for this reference cell. When in room light, the reference device indicated a current of roughly 30 µA – 43 µA and thus a current density of 30 µA cm^{-2} – 43 µA cm^{-2}. This indicates that ideal devices of the same sizes as the small and large devices would produce currents of 2.7 µA – 3.9 µA for the small area device and 67.5 µA – 96.8 µA for the large area device. In actuality, the small device produced 2.52 µA – 2.79 µA and the large device produced 51.75 µA – 56.25 µA. This is expected as the Si/CNT heterojunction device will not produce current to the extent of ideal silicon devices. These small currents may be a reason for the high series resistances calculated, as the expected current output is significantly higher. Additionally, the room lighting cannot be assumed to have the same spectrum as the AM1.5 source thus, whilst we can determine the current per unit area (and thus the converted photons per unit area), we cannot be sure of the power/wavelength of the incident photons. To investigate the reason for the high series

resistance measurements, the silicon reference cell was measured at a series of different light intensities and the series resistance compared.

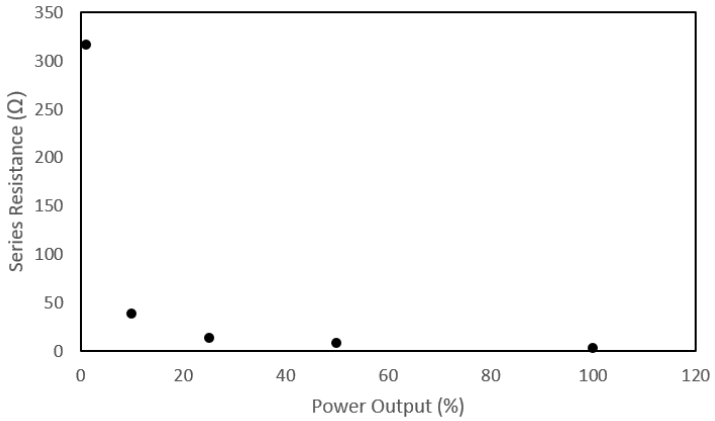

Figure 2-18: Plot of calculated series resistance vs power output of the AM1.5 source for the silicon reference cell.

Figure 2-18 shows that as the power output is decreased, i.e. the light intensity decreases, the series resistance increases logarithmically. The measured current for the 1 % data point was 0.327 mA on the reference device and thus this is still an order of magnitude higher than the current output from the room lights explaining the 1000 Ω order of the series resistance seen when the reference device J/V curve is produced under room lights. There also appears to be an increased effect with a decrease in active area as the small area devices produced significantly larger series resistances over the reference device and the large area devices (Table 2-6).

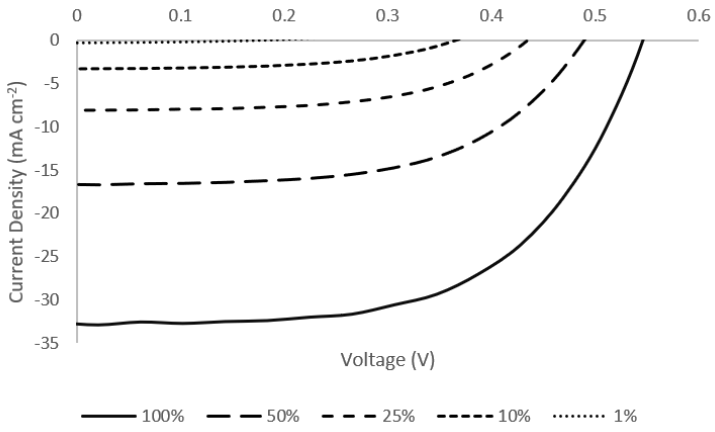

Figure 2-19: J/V curves for the silicon reference device at different power outputs.

Figure 2-19 shows the J/V curves for the reference device under different power outputs. The series resistance is calculated from the slope of the curve at the V_{oc} (where the line crosses the *x* axis). The

slope increases with a decrease in power output, supporting the data shown in Figure 2-18. This massive increase in sheet resistance with less intense light sources may indicate that the power loss equation cannot be performed on devices under room lighting, although the similarities in power loss per unit area seems to indicate that this is not an issue.

To offset the effect of the high series resistances when room lighting was used to illuminate the devices, a device of each active area size was measured under illumination from an incandescent globe light positioned approximately 20 cm above the device testing rig. This lamp at this height gave a current output from the reference cell of 5 mA, indicating the power output is roughly 15% of the ideal AM1.5 light spot. Table 2-8 shows the power loss data for lamp illuminated devices. It can be seen that, whilst the power loss calculations under room lighting gave the same results for large and small area devices, the power loss is significantly lower for smaller area devices. This indicates that the large area devices do suffer significantly compared to the small area devices in terms of resistive power loss.

Table 2-8: Power loss calculations for reference, small area and large area devices under lamp lighting.

	Current Density at Max Power (mA cm^{-2})	*Current Density at Max Power (A cm^{-2})*	*Current Density at Max Power Squared (A^2 cm^{-4})*	*Series Resistance (Ω)*	*Active Area (cm^2)*	*Power Loss (W cm^{-2})*
Silicon reference device	-4.046	-4.046 x 10^{-3}	1.637 x 10^{-5}	21.8	1	**3.57 x 10^{-4}**
Small device AP	-0.229	-2.29 x 10^{-4}	5.23 x 10^{-8}	285	0.09	**1.34 x 10^{-6}**
Small device 2 % HF	-0.113	-1.13 x 10^{-4}	1.266 x 10^{-8}	1280	0.09	**1.46 x 10^{-6}**
Large device AP	-3.69	-3.69 x 10^{-3}	1.36 x 10^{-5}	39.7	2.25	**1.215 x 10^{-3}**
Large device 2 % HF	-0.916	-9.16 x 10^{-4}	8.39 x 10^{-7}	185	2.25	**3.49 x 10^{-4}**

Any adjustment due to power loss across the front contact will be a more complex prospect than that achieved with the 2D map of the AM1.5 light spot.

Overall, from these experiments, it can be seen that the majority of the current density differential between large and small area devices is due to the inhomogeneous intensity of the AM1.5 light source. It was found that the current provided from the lamp is at a maximum in the centre and drops off towards the edges of the circle. In addition, certain areas of the lamp spot had lower current outputs

than other points at the equivalent distance from the centre. A 2D current output map of the lamp spot was used to calculate the difference in current output for different sized devices. It was determined from comparisons with a reference silicon device that at a supposed power output of 50 mW cm^{-2} (50% of the ideal output) small area devices experience a power output of 61 mW cm^{-2} whilst large area devices experience a power output of 45 mW cm^{-2}. This information allowed a scaling factor to be applied to J_{sc} measurements when testing large area devices. This scaling factor reduces the difference in J_{sc} between the large and small devices from 4.42 mA cm^{-2} to 1.22 mA cm^{-2}. It was suggested that the remaining difference may be due to a difference in power loss across the front of the device. The power loss was calculated in conditions in which the same illumination per unit area was achieved, to remove the effect of the inhomogeneous lamp spot. It was found that the power loss per unit area was virtually the same for both the small and large devices under low intensity illumination, which explains why this phenomenon will have a larger negative impact on the large devices as they have a larger area. However, the power loss per unit area was much lower for small area devices when both types of device were examined under increased illumination. This served to further indicate that resistive power loss has a more significant effect on large area devices than on small area devices. The difficulty in determining a constant comparison of power loss under a homogeneous light source made determining a corrective factor impossible at this time.

2.2.3 Incident Photon-to-electron Conversion Efficiency

Incident Photon-to-Electron Conversion Efficiency (IPCE) spectra were achieved using the same lamp as in the measurement of an illuminated J/V curve. The light was passed through an Oriel motorized filter wheel, model 74010, to a Newport bean splitter holder, model 78150. Output current data was measured using an Oriel Merlin radiometry system through an Oriel 70710 current pre-amplifier. The system was controlled, and data exported from TRACQ Basic computer software from Newport.

2.2.4 Thin Film Analysis

Thin films of either CNTs or interlayer materials were prepared and applied to the CNT/Si heterojunction solar device throughout the research in this thesis. As well as measuring the

photovoltaic properties affected by these elements a series of analysis techniques were used to probe for other thin film properties. The analysis methods used were near-identical regardless of thin film makeup.

CNT films were analysed using many methods to ascertain different properties of the nanotubes in question. Nanotube films attached to glass could be analysed for their chemical/electronic properties via UV-Visible absorbance spectroscopy, Raman spectroscopy, and 4-point probe sheet resistance measurements. Films attached to silicon were analysed for their physical properties via atomic force microscopy (AFM) and scanning electron microscopy (SEM). CNT films were attached to etched silicon substrates patterned with gold in order to produce CNT/Si heterojunction devices.

Interlayer materials were spin coated on to glass or silicon substrates and annealed as per the same conditions that were used to attach the films to device substrates. UV-Visible absorbance spectroscopy, AFM and SEM were used to determine thin film morphology and light absorbance properties.

2.2.4.1 Ultraviolet-Visible Spectrophotometry

Ultraviolet-Visible (UV/Vis) Spectrophotometry is a useful technique for analysing the Van Hove Singularities (VHS) in a SWCNT suspension or film. This technique is also useful for determining the lack of VHS in a DWCNT or MWCNT sample. UV/Vis spectrophotometry was performed on CNT films which had been attached to glass slides (generally via the heat/press method), thus allowing light to pass through the CNT film, unobstructed by the substrate. The wavelength range was 300 nm to 1100 nm and a clear section of the same glass slide was used as a background. As the concentration of a CNT or CNT/GO suspension was not accurately known after sonication and centrifuge treatment, UV/Vis spectral analysis was used to produce a calibration curve of CNT suspension volume vs film thickness (in terms of percentage light transmittance) for each new suspension.

UV/Vis spectrophotometry was also used to analyse thin interlayer films on glass in order to characterise the film and compare films produced with different spin coating or solvent parameters. Generally, the wavelength range was 300 nm to 800 nm for this application.

Two different UV/Vis spectrophotometers were used for this research: a Cary 60 UV/Vis spectrophotometer from Agilent and a Lambda 950 UV/Vis near infrared spectrophotometer from Perkin Elmer.

2.2.4.2 Four-Point Probe Sheet Resistivity Measurements

CNT film resistivity was analysed using a KeithLink four-point probe attached to a Keithlink Gwinstek data acquisition unit. For each experiment the probe was applied across the thin film in various orientations and five resistance measurements were taken per orientation. The raw data was passed through a Keithlink film resistivity measurement computer program to calculate a sheet resistance in Ω sq^{-1} for each measurement. These measurements were averaged together to give an overall sheet resistance measurement for the film.

2.2.4.3 Atomic Force Microscopy

Atomic force microscopy (AFM) was performed on CNT films on silicon to image the surface roughness and morphology of the films. AFM was also performed on solution processed interlayers on solar device substrates to image the morphology of the films. In addition, the thickness of the solution processed interlayers was measured using AFM by first manually scratching the film with a scalpel and imaging over the scratch with AFM. The scalpel did not damage the silicon substrate but sliced easily through the interlayer. This formed channels in the film, the height of which could be measured to determine the thickness of the film. AFM measurements were performed in air with a Bruker multimode 8 AFM with a Nanoscope V controller in standard tapping mode. The AFM probes used were silicon HQNSC15/ AlBS Mikromasch probes (nominal tip diameter and spring constant is 16 nm and 40 N m^{-1} respectively). Set-point, scan rate and gain values were chosen to optimize image quality. The AFM scanner was calibrated in x,y and z directions using silicon calibration grids (Bruker model numbers PG: 1 µm pitch, 110 nm depth and VGRP: 10 µm pitch, 180 nm depth). AFM topography

images have been flattened, and thickness and roughness measurements taken using Nanoscope Analysis 1.4.

2.2.4.4 Scanning Electron Microscopy

Scanning Electron Microscopy (SEM) was used to image CNT films on silicon to determine the film morphology and surface coverage. SEM was also used to image thin films of interlayer material on solar device substrates to ascertain film formation and surface coverage. In many cases, a smooth interlayer film was difficult to image under SEM as the surface appeared roughly homogeneous (as would a bare silicon surface). However, a good indication of a surface layer was found by damaging the interlayer with techniques that are not expected to damage silicon, such that the blemishes are visible under SEM. Two methods were used to this end, manual scratching (as described in Section 2.2.4.3) and burning of the interlayer film using a Raman laser. To achieve all SEM images, an Inspect FEI F50 SEM was used with beam spot size and high voltage adjusted to optimise image quality. The image resolution was generally 2048 x 1768 with an imaging speed of 30 µs.

2.2.4.5 Raman Microscopy

Raman spectra of the various nanotube types were obtained using a Witec Alpha R confocal Raman microscope. The laser used was a Nd:YAG 532 nm (2.33 eV) laser and the power used at the sample was less than 10 mW. A x40 magnification objective with a Numerical Aperture (NA) of 0.6. The data collected was single spectra with 10 spectra collected per sample at 5 different locations on each sample. The integration time was between 5 and 10 s with 3 accumulations per spectrum. The grating used has 600 grooves per mm, giving a resolution of 3 – 4 cm^{-1}. Polarised Raman spectroscopy was performed using a Horiba XploRA scientific confocal Raman microscope. The laser used was a Nd:YAG 532 nm laser and the power used at the sample was 1.2 mW. A x100 magnification objective was used. The data was collected at 25 locations in a 5 x 5 grid 2 spectra were collected per location with a 30 s integration time per spectrum. The grating used has 1200 grooves per mm.

CHAPTER 3 NANOTUBE WALL NUMBER EFFECTS

3.1 Publication

The work in this chapter was published in 2016 as per the following citation:

Grace, T., et al. (2016). "Investigating the Effect of Carbon Nanotube Diameter and Wall Number in Carbon Nanotube/Silicon Heterojunction Solar Cells." Nanomaterials **6**(3): 52.

3.2 Introduction

Research on the CNT/Si device architecture has been carried out with all three types of CNTs as defined by wall number (SWCNTs, DWCNTs and MWCNTs). However, there have been few comparative studies that looked at the effects of multiple types in one experiment. Jia *et al.*[83] published a comparative study in 2010 where they looked at all three CNT wall number types. It was determined that SWCNTs were superior to MWCNTs when low density films were used, and that the density (and thus optical transmittance) was a vitally important factor in achieving optimal PV properties. It was also found that devices with DWCNT films performed significantly better than devices with both SWCNT and MWCNT films. However, an issue in this work was that the DWCNT films were produced in a different way to the SWCNT and MWCNT films. The DWCNTs used were also more pristine and significantly longer tubes when compared to the SWCNTs and MWCNTs. As discussed in Section 1.2.7 the length of the CNTs used is a vital parameter when considering charge carrying performance, with films containing longer tubes able to avoid significant resistance losses due to tube-tube boundaries. Thus, it cannot be assumed that the double-walled nature of the DWCNTs used in the above study was the only factor in their improved PV performance in CNT/Si devices. It is apparent that a comparison between SWCNTs, DWCNTs, and MWCNTs where each nanotube type is prepared for use in CNT/Si devices in the same way remains to be explored.

3.3 Aims

1. To source CNT samples of different wall number and different diameter and create aqueous suspensions using the same solvent and processing conditions.
2. To then use these suspensions to create CNT films of equal transmittance and to use these films to produce CNT/Si solar devices to investigate the effect of wall number and CNT diameter on PV performance.

3.4 Results and Discussion

3.4.1 Sourcing the CNT samples

Five CNT samples were sourced for use in this experiment. These samples were specifically chosen to display a range of wall numbers and diameters whilst keeping the length of the tubes roughly

equivalent to avoid any confounding effects. The relevant parameters of the CNT samples chosen are shown in Table 3-1. Note that the parameters listed are all as defined by the supplier. It is probable that the average length of the CNTs would be reduced by the suspension forming process. Additionally, as the CNTs are suspended with the assistance of a surfactant and then centrifuged to remove non-suspended material including contaminants, the purity percentage is not critical as it will improve during processing.

Table 3-1: Relevant supplied parameters for sourced CNT species.

Sample Designation	*Supplied Diameter (nm)*	*Supplied Length (nm)*	*Purity (%)*
SWCNT – 1	1.4 – 1.5	500-1500	90
SWCNT – 2	0.8 – 1.2	100-1000	95
DWCNT – 1	2 – 4	<1500	>>60
DWCNT – 2	3.5	3000	90
MWCNT	9.5	1500	95

3.4.2 CNT suspension and film preparation

Each CNT sample was used to produce an aqueous CNT suspension as defined in Section 2.1.1**.** The CNTs were included at a concentration of 95 mg in 50 mL of an aqueous 1 % v/v Triton X-100 solution. Bath sonication method was performed in three 20 min sessions. Between each session the bath water was changed to keep the temperature near room temperature. Films were produced as defined in Section 2.1.2 using the 4-hole template. These films were used for Raman microscopy, UV-Visible spectrophotometry, SEM and to produce CNT/Si devices. It became apparent during experimentation that it is significantly more difficult to produce concentrated suspensions of DWCNTs when compared with SWCNTs, despite the addition of the same mass of dry nanotubes. It appears that the DWCNTs tend to remain bundled together to a much higher degree in suspension than the other CNT species used. MWCNTs appeared to form suspensions with comparable concentrations to SWCNTs.

3.4.3 SEM of CNT Films

SEM was used to analyse the physical morphology of the CNT films produced via vacuum filtration from suspension. The images are shown in Figure 3-1. It is apparent that the film produced from the DWCNT – 2 suspension did not form a homogeneous film, unlike the other samples. The DWCNTs formed large, coagulated clumps rather than thin, relatively flat, networks of CNTs and CNT bundles. This could be due to contaminants present in the suspension after centrifugation, a low concentration of DWCNTs present in suspension and/or a poorly formed suspension in general. Due to repeated poor film morphologies and surface coverages obtained from suspensions from sample DWCNT – 2, further work with this sample proved unfruitful and will not be discussed further in the rest of the chapter. A possible explanation for the difficulty with suspending the DWCNT – 2 sample at good concentration is their length. The DWCNT – 2 tubes were significantly longer than the other samples used, and this might have decreased their ability to form aqueous suspensions at high enough concentration to form homogeneous films when filtered. The DWCNT – 1 films also did not show a homogeneous surface coverage when compared with the SWCNT and MWCNT samples however this sample formed films with a preferable morphology over the DWCNT – 2 samples. This difficulty in forming good homogeneous films with DWCNT suspensions is likely due to the difficulties faced in forming stable, concentrated aqueous suspensions. Both the SWCNT and MWCNT films appear to be roughly equivalent in terms of forming films with good surface coverage and homogeneity. The circular anomalies prominently visible in the SWCNT – 1 film are from the vacuum filtration process where water has forced small pathways through the film. They are only visible in this film as it was thicker than the other films. Overall, it can be seen that good quality aqueous suspensions of both SWCNT samples, the DWCNT – 1 sample and the MWCNT sample were formed. These suspensions produced good homogeneous films with good surface coverage, which is important for incorporation in CNT/Si devices.

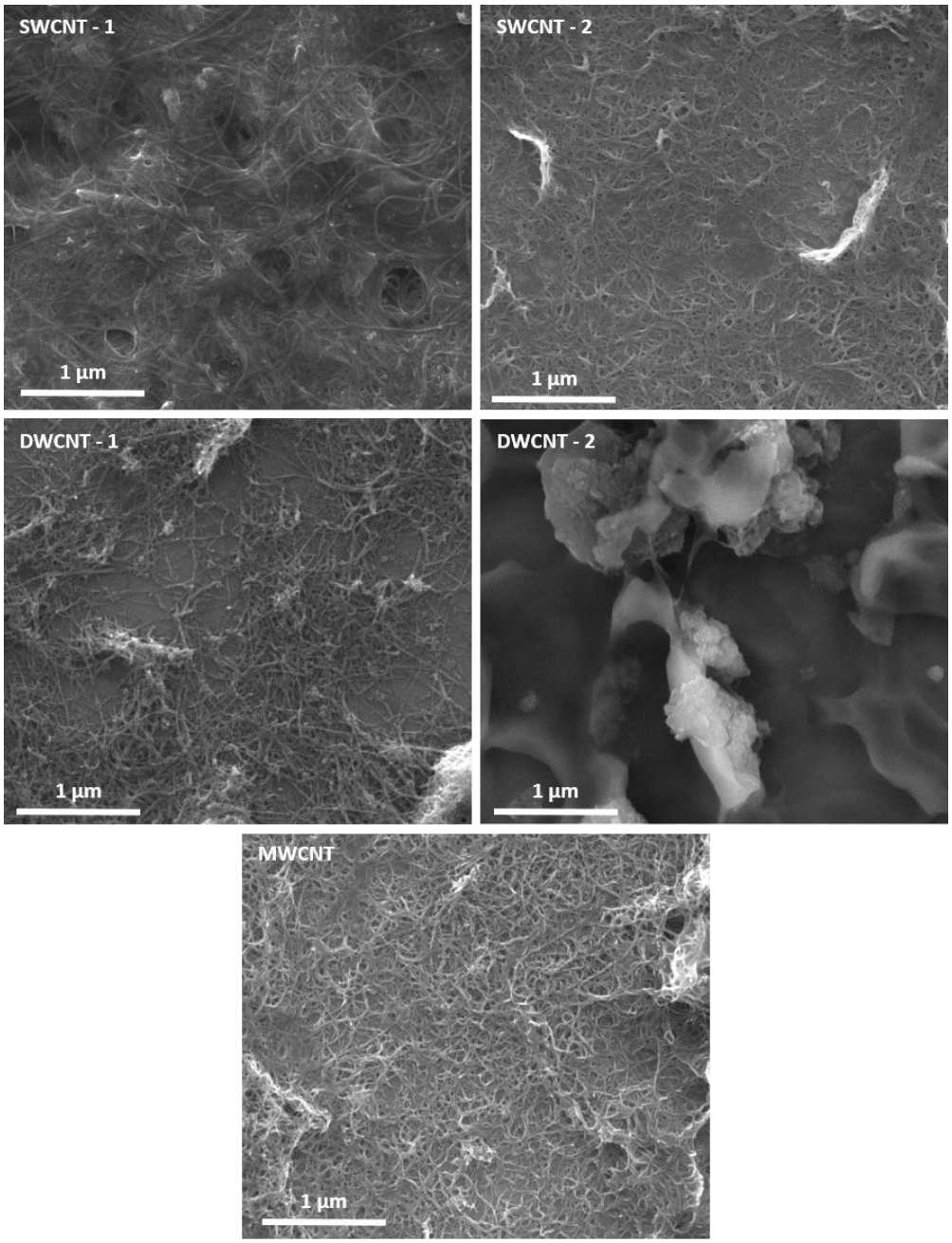

Figure 3-1: SEM images of CNT films produced from suspensions of different CNT samples.

3.4.4 Raman microscopy of CNT films

When imaged with Raman microscopy, CNTs display characteristic peaks at around 1580 cm^{-1} and 1350 cm^{-1}. These peaks are known as the G and D bands respectively, and they correspond to different types of carbon species. Highly ordered carbon species such as graphite, graphene or pristine CNTs are shown in the G band peak, whereas the D band is characteristic of disordered carbon species. Thus, a simple ratio of G band peak intensity to D band peak intensity can be used to describe the crystallinity of the CNTs in a given film.[175] Additionally, both SWCNTs and DWCNTs display radial

breathing mode (RBM) peaks between 100 cm^{-1} and 500 cm^{-1}. These are unique to the Raman spectra of these types of CNTs and can thus be considered direct evidence of their presence in a sample.[53, 175] Additionally, the precise RBM wavenumbers for a SWCNT or DWCNT sample can be used to calculate the diameter of the CNTs. Other peaks observed in Raman spectra of CNTs include the G' band, which is an overtone of the D band and is at around 2700 cm^{-1}, and a peak at 1550 cm^{-1} which is known as the Breit-Wigner-Fano (BWF) band and is attributed to metallic carbon species (for example m-SWCNTs).[53] The BWF peak is often observed as a shoulder on the G peak, due to their wavenumber proximity.

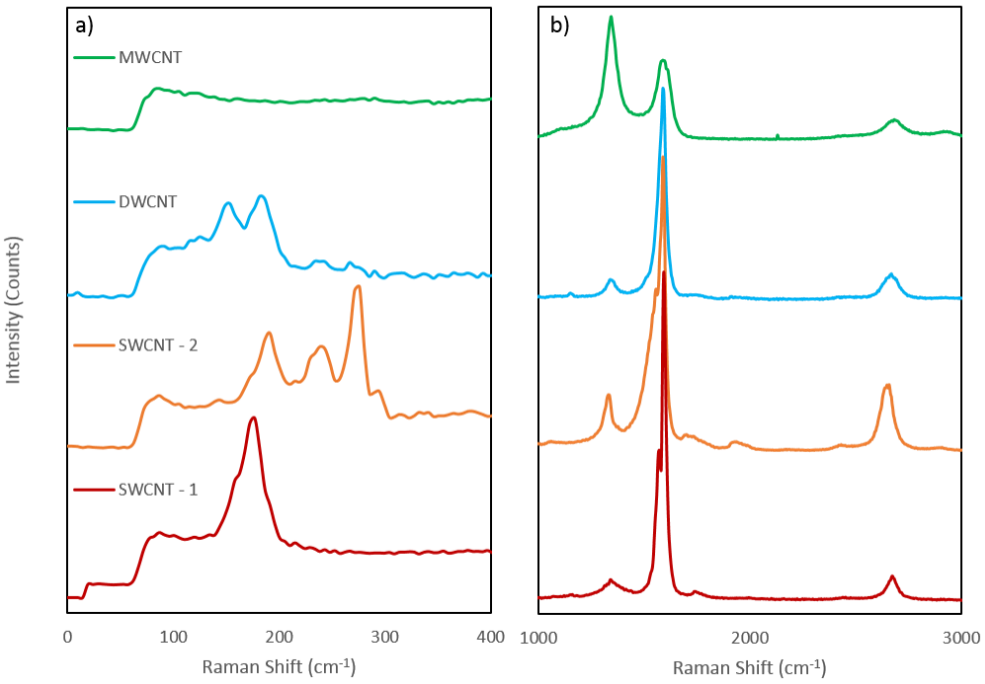

Figure 3-2: a) Low wavenumber region Raman spectra for all CNT species that formed viable films, showing the RBM region. b) High wavenumber region Raman spectra for all CNT species that formed viable films showing the D, BWF, G and G' bands from left to right. In both cases intensity values have been offset for easier viewing.

Figure 3-2 shows the Raman spectra for all CNT species that formed viable films. It is observable that there are no RBM peaks present in the MWCNT spectra (Figure 3-2 a)). This is expected, and is strong evidence that no SWCNT species is present in the MWCNT sample, as RBM peaks are an identifier for SWCNTs.[53] The characteristic G and D band peaks are observable for all samples, with the SWCNT and DWCNT samples presenting strong G band peaks relative to D band peaks and the MWCNT sample

presenting a stronger D band peak, with much similar peak heights for the G and D band peaks. The precise D/G ratios were calculated and are presented in Table 3-2.

Table 3-2: Calculated D/G ratios for each CNT sample that formed viable films.

	SWCNT – 1	*SWCNT – 2*	*DWCNT*	*MWCNT*
D/G Ratio	0.049	0.171	0.078	1.55

The SWCNT – 1 and the DWCNT samples exhibited very low D/G ratios, indicating a high level of order in the CNTs within the samples. The SWCNT – 2 sample showed a higher D/G ratio, indicating a higher level of disorder for these CNTs. The MWCNT sample gave a significantly higher D/G ratio to the other three CNT samples. This stark difference in D/G ratio for MWCNTs is expected and gives further proof that this sample solely consists of MWCNTs. There is a visible BWF shoulder on the G band peaks for both SWCNT samples, showing the presence of m-SWCNTs and thus indicating that an unsorted mix of chiral species are present. This is expected as the purchased CNT species were not of a particular chiral species and no chiral sorting was performed pre suspension.

The wavenumber at which the RBM peaks occur can be used to calculate the CNT diameter for SWCNTs as the RBM frequency is inversely proportional to the diameter of the CNTs.[53, 176] The wavenumber is related to the diameter via Equation 3-1.

Equation 3-1: Equation relating CNT diameter to RBM shift wavenumber, RBM shift is the wavenumbers of the RBM peaks, d_t is the nanotube diameter in nanometres, and A and B are constants.

$$RBM\ shift\ (cm^{-1}) = \frac{A}{d_t(nm)} + B$$

The constant A has an approximate value of 234 nm cm^{-1} determined from *ab initio* calculations and B is approximately 10 cm^{-1} which corrects the intertube interaction frequencies in SWCNT bundles.[176, 177] Equation 3-1 was applied to the RBM peak wavenumbers found from the Raman spectra of the SWCNT samples to calculate a CNT diameter. The RBM peaks for the DWCNT spectrum were also used to calculate a range of diameters for this sample, however a B value of 0 was used in this case as B is a correction specifically for intertube SWCNT interactions. In all cases, the calculated diameters were compared with the manufacturer supplied diameters as shown in Table 3-3.

Table 3-3: Calculation of CNT diameter from RBM Raman shift wavenumbers and comparison with manufacturer supplied diameter values.

Nanotube Sample	*RBM Raman Shift (cm^{-1})*	*Calculated Diameter (nm)*	*Supplied Diameter (nm)*
SWCNT – 1	177	1.40	1.4-1.5
SWCNT – 2	191, 239, 276	1.29, 1.02, .88	0.8-1.2
DWCNT Small Peaks	115, 125	2.03, 1.87	2-4
DWCNT Large Peaks	154, 186	1.52, 1.25	2-4

Table 3-3 shows the relevant values and calculated diameters. The calculated tube diameters show good agreement with the manufacturer supplied diameters for the SWCNT samples. The DWCNT diameter calculations seem to significantly differ from the manufacturer supplied diameter values. This can be explained, however, by assigning the visible RBM peaks to the inner DWCNT tubes as the interwall diameter difference is known to be 0.33 nm – 0.41 nm.[178, 179] To achieve a calculated diameter approaching 4 nm the RBM peak for the outer tubes would be at or below 117 cm^{-1}. The two small peaks at the left end of the Raman spectrum for the DWCNT sample are closer to this range and thus may be due to the outer tubes.

3.4.5 UV/Visible spectrophotometry of CNT films

UV/Visible spectrophotometry was used to investigate the properties of the different CNT samples in the visible and near IR ranges. Additionally, UV/Visible spectra are used to determine the thickness of a given set of CNT films in terms of light transmittance percentage (%T). UV/Vis spectra of films of each viable CNT sample are shown in Figure 3-3. It is expected that both the DWCNT and MWCNT films will produce a featureless spectrum with a slight increase in absorption as the wavelength decreases. UV/Visible spectra of SWCNT films will also display an increase but will be marked with several features due to the S_{11}, S_{22}, and M_{11} optical transitions between VHS.

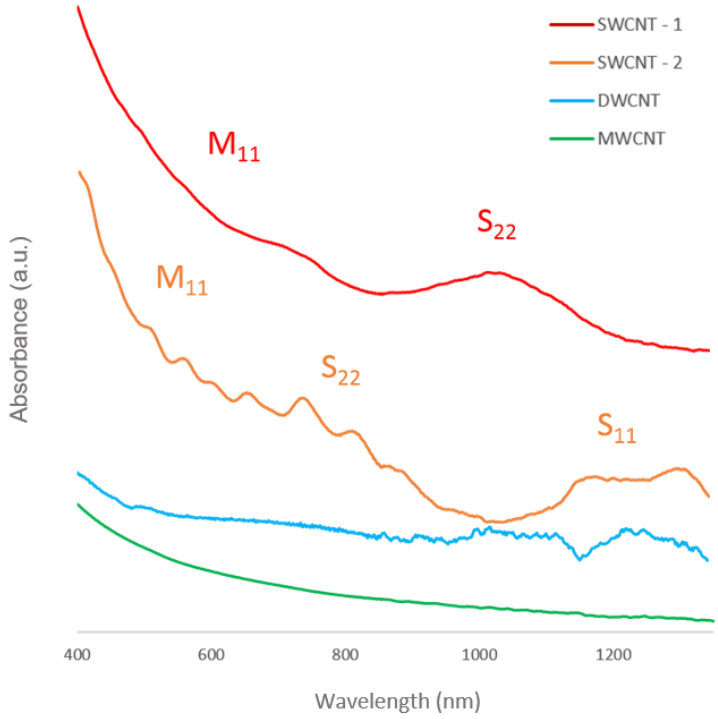

Figure 3-3: UV/Vis spectra of CNT films of all CNT types that formed viable homogeneous films. The absorption values on the y-axis have been offset to increase ease of viewing.

The spectra, in general, agree with expectations. The SWCNT – 1 spectrum displays a series of peaks from 810 nm – 1200 nm, which are due to the S_{22} transitions and a series of peaks from 450 nm – 800 nm due to M_{11} transitions. Meanwhile, the SWCNT – 2 spectrum displays peaks for three sets of transitions. S_{11} from 1100 nm – 1300 nm, S_{22} from 620 nm – 950 nm and M_{11} from 400 nm – 620 nm, although there is possibly some overlap between these transitional regions. Overall, these transitions show that SWCNTs are present in these samples and, likewise, the lack of these transitions in the DWCNT and MWCNT spectra show the absence of SWCNTs. The difference in transitional peak location between the SWCNT – 1 and SWCNT – 2 spectra is because of the presence of different chiral species between the two samples due to their different fabrication methods. Additionally, it is noticeable that the S_{11}, S_{22}, and M_{11} peaks are much more distinct for SWCNT – 2 than SWCNT – 1. This indicates that more distinct groupings of chiral species are present in SWCNT – 2 where as SWCNT – 1 consists of a broader range of chiral species with less specificity. MWCNTs in particular are not expected to display any absorbance features due to mixing of states between the CNT walls within the MWCNT.[24]

3.4.6 Transmittance Calibration and Sheet Resistance Film Measurements

A series of films with different suspension aliquot volume were created in order to determine the volume required to produce films with similar transmittance values, to accurately compare between samples. These samples were also measured for sheet resistance and an electrical to optical conductivity value calculated for each volume (Table 3-4). The σ_{dc}: σ_{OP} ratio is a figure used to compare thin conductive films by taking both their light transmittance (at 550 nm in this thesis) and their sheet resistance. The equation used is presented and derived here in Equation 3-2**.**

Equation 3-2: Equation for determinging the σ_{dc}: σ_{OP} ratio from sheet resistance (R_s) and light transmittance (T). μ_o is the free space permeability (4π x 10^{-7} N A^{-2}), and ε_0 is the free space permittivity (8.854 x 10^{-12} C^2 N^{-1} m^{-2}).[180]

$$\%T_{550} = (1 + \frac{1}{2R_s} * \sqrt{\frac{\mu_0}{\varepsilon_0}} * \frac{\sigma_{OP}(550)}{\sigma_{dc}})^{-2}$$

$$\frac{\sigma_{dc}}{\sigma_{OP}(550)} = \frac{1}{2R_s} * \frac{\sqrt{\frac{\mu_0}{\varepsilon_0}}}{T^{-1/2} - 1}$$

Table 3-4: Sheet resistance and direct current (DC) electrical to optical conductivity (σ_{DC}/σ_{OP}) as a function of thickness. σ_{DC}/σ_{OP} was calculated as per Hecht *et al.*[181]

Nanotube Type	*Volume of Suspension (mL)*	*% Transmittance (%)*	*Sheet Resistance (Ω sq^{-1})*	*σ_{dc}: σ_{OP} ratio*
SWCNT–1	0.5	82	4060	0.463
	1.0	74	1200	0.968
	1.5	88	690	1.575
	2.0	56	530	1.071
	2.5	59	390	1.615
SWCNT–2	0.5	57	2,380,000	0.000233
	1.0	85	4280	0.435
	1.5	64	4320	0.184
	2.0	65	2920	0.282
	2.5	57	2410	0.261
DWCNT–1	5.0	56	414,900	0.00125
	7.5	55	2550	0.212
	10.0	56	4260	0.129
	12.5	41	17,200	0.0187
MWCNT	1.0	62	4510	0.153
	1.5	72	4620	0.251
	2.0	65	4000	0.209
	2.5	52	2890	0.176
	3.0	52	3210	0.157

From the calibration performed above it is a clear there is a trend of decreasing sheet resistance with increasing volume (and increasing transmittance). This is due to an increase in the number of CNTs in the film which leads to the formation of a denser, more complete network. From the calibration data sets of films were created with transmittance values from 58 % to 65 %. These films were produced in sets of 4 with three films used for solar devices and one film used to calculate transmittance and sheet resistance measurements both as prepared and after treatment with dopant chemicals. The data for films used for PV devices is shown in Table 3-5.

Table 3-5: Average %T and sheet resistance data with treatment for each CNT sample that produced viable films.

Film type	*Transmittance (%)*	*As Prepared (Ω sq^{-1})*	*HCl Treatment 1 (Ω sq^{-1})*	*$SOCl_2$ Treatment (Ω sq^{-1})*	*HCl Treatment 2 (Ω sq^{-1})*	*σ_{dc}: σ_{OP} ratio*
SWCNT – 1	60	1440 ± 8.2%	951 ± 1.9%	693 ± 42%	543 ± 2.9%	0.268
SWCNT – 2	65	4070 ± 7.0%	3650 ± 2.6%	1880 ± 4.0%	2410 ± 12%	0.064
DWCNT	58	138000 ± 84%	4190 ± 39%	19600 ± 138%	2550 ± 38%	0.056
MWCNT	60	3340 ± 6.0%	3520 ± 6.0%	3020 ± 23%	2890 ± 27%	0.051

It is noticeable that the films produced from the DWCNT suspension display the highest sheet resistance along with the largest variation between measurements, although there was an overall trend of decreasing sheet resistance with doping. This is unexpected when transmittance is considered as the DWCNT films were the thickest and thus would be expected to have the best conductivity across the film due to a denser network of CNTs. The high error range for the DWCNT sheet resistance measurements shows the issues present with suspending and forming good, homogeneous films with DWCNTs. In general, the sheet resistance of the SWCNT and MWCNT films decreased with doping, indicating improved charge carrier transport. However, the SWCNT – 2 film increased with the final acid treatment, although the variation also increased, indicating that some areas of the film may still have decreased in sheet resistance. The doping chemicals had a lesser effect on the MWCNT films with an overall decrease of only 450 Ω sq^{-1}, this is likely because the dopant would only have an effect on the outer tube in a MWCNT and thus the inner tubes would be 'shielded' from the dopant and will not experience the conductivity improvement. Whilst this would also be true for DWCNTs, MWCNTs have a larger bulk to surface mass ratio and will thus experience more 'shielding'. In addition to this,

MWCNTs are overwhelmingly metallic in character due to the complex mixing of states between the walls (which can be individually described as SWCNTs with different chirality) and therefore there are no tube-tube energy barriers to be lowered by *p*-doping.[43] The σ_{dc}: σ_{OP} ratio showed that the SWCNT - 1 sample produced significantly better thin conductive films than the other samples, due to a significantly lower sheet resistance coupled with a similar transmittance at 550 nm. Overall, the lower sheet resistances in the SWCNT – 1 film with a similar amount of CNTs present (from similar transmittance) indicates that there is improved charge carrier transport present in films produced from the SWCNT – 1 sample.

3.4.7 Solar device Data

Films from the four CNT samples that were found to produce viable films were attached to standard small solar device substrates with no active area grid pattern, prepared as described in Section 2.1.5. The devices were tested as prepared, after a 2% HF etch, after thionyl chloride treatment and after a 2nd 2% HF etch.

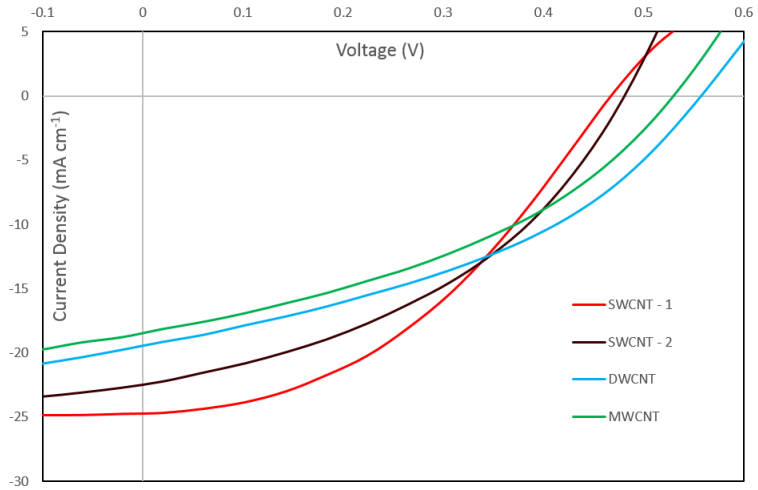

Figure 3-4: J/V curves for best performing devices for each CNT sample after the 2nd HF etch.

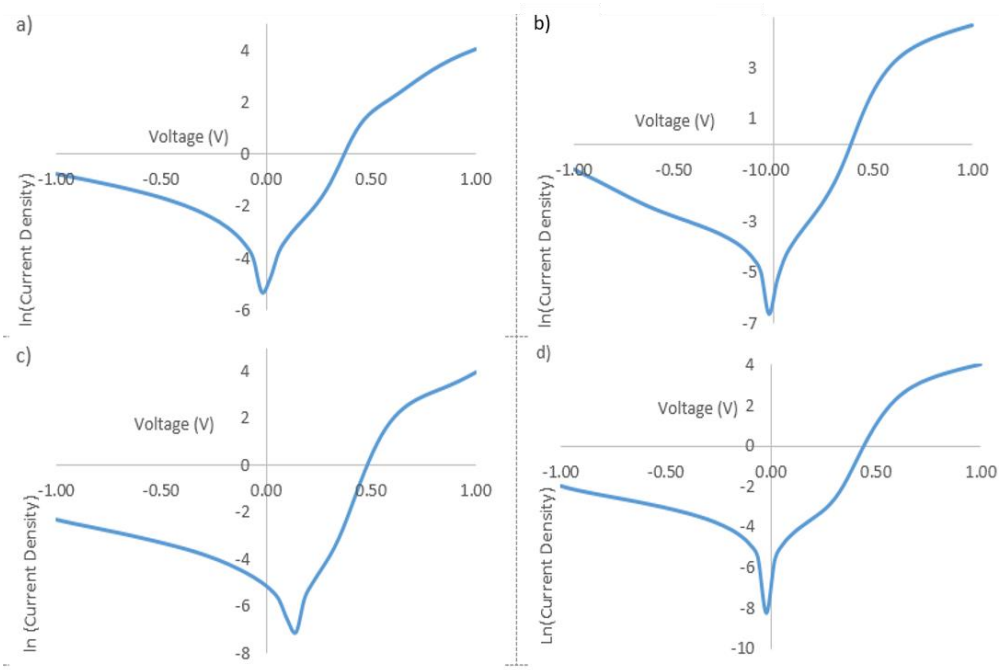

Figure 3-5: Log of current density versus voltage without illumination (Dark J/V curves) for devices for each viable CNT sample after the 2nd HF etch. a) SWCNT - 1, b) SWCNT - 2, c) DWCNT, and d) MWCNT.

Figure 3-4 and Figure 3-5 show J/V curves for the best performing devices for each viable CNT sample after the 2nd HF etch under illumination and in the dark, respectively. Both SWCNT samples display a similar curve shape, albeit with a higher J_{sc} for SWCNT – 1 and a higher V_{oc} for SWCNT – 2. Both the DWCNT and MWCNT samples produce a 'flatter' J/V curve, with a lower J_{sc} and a higher V_{oc}, with the DWCNT sample performing better than the MWCNT sample overall. This V_{oc} difference from SWCNT to DW/MWCNT samples is unexpected as the V_{oc} of the system is determined by the energy levels and should not be greatly affected by a change in CNT wall number. It is likely that the higher voltage is caused by a lower rate of charge carrier recombination for CNTs with more than one wall. The Dark J/V curves exhibit the same rough shape regardless of CNT wall number, with a significantly higher $\ln(J_{sc})$ for positive voltages. This is the ideal and expected situation as it indicates that the diode is functioning well in inhibiting electrical flow in the non-desired direction. All curves also displayed a bump in the positive voltage region, this shape is also expected and is useful for determining series and shunt resistances for the devices (Table 3-6).

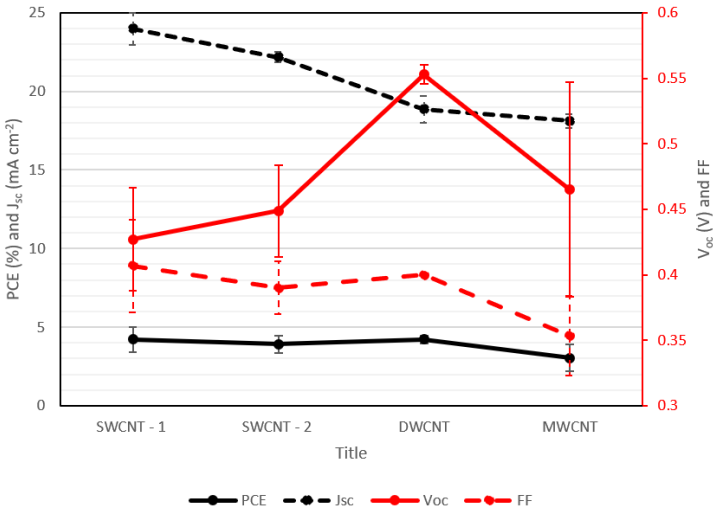

Figure 3-6: J/V properties for CNT/Si solar devices produced with all viable CNT samples after final treatment.

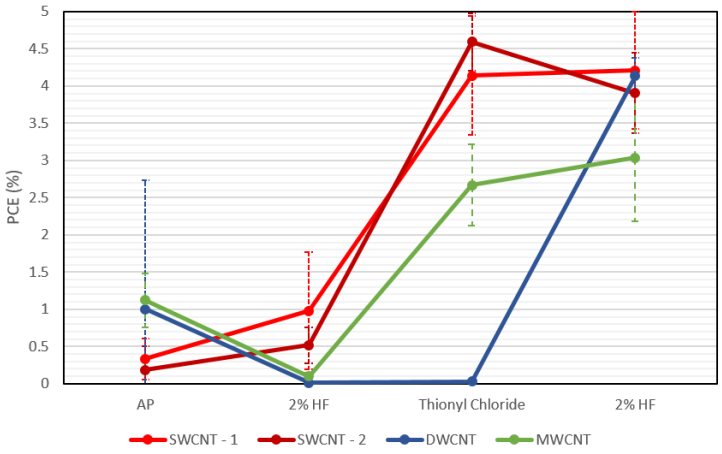

Figure 3-7: Average PCE values for each CNT type at different treatment stages.

Table 3-6: Numerical photovoltaic data for CNT/Si solar devices produced with all viable CNT samples. The data for the best performing devices is displayed in bold with the averages and standard deviation values given beneath in plain text.

	SWCNT – 1	*SWCNT – 2*	*DWCNT*	*MWCNT*
J_{SC} *(mA cm^{-2})*	**24.7;**	**22.5;**	**19.5;**	**18.4;**
	24 ± 4.3%	22.2 ± 1.5%	18.9 ± 4.5%	18.1 ± 2.5%
V_{OC} *(V)*	**0.468;**	**0.483;**	**0.58;**	**0.533;**
	0.427 ± 9.17%	0.449 ± 7.8%	0.553 ± 1.3%	0.465 ± 17.6%
FF	**0.41;**	**0.41;**	**0.40;**	**0.38;**
	0.41 ± 8.64%	0.39 ± 5.13%	0.40 ± 0.0%	0.35 ± 8.7%
PCE %	**4.79;**	**4.45;**	**4.31;**	**3.78;**
	4.21 ± 18.74%	3.90 ± 13.8%	4.14 ± 6.0%	3.03 ± 28.2%
R_{shunt} *(Ohm)*	**6.42 × 10^{3};**	**1.06 × 10^{3};**	**8.42 × 10^{2};**	**8.07 × 10^{2};**
	2.81 × 10^{3} ± 112%	7.91 × 10^{2} ± 30.2%	9.61 × 10^{2} ± 17.5%	6.65 × 10^{2} ± 24.8%
R_{series} *(Ohm)*	**1.21 × 10^{2};**	**1.11 × 10^{2};**	**1.44 × 10^{2};**	**1.64 × 10^{2};**
	1.08 × 10^{2} ± 16.3%	1.12 × 10^{2}± 9.4%	1.57 × 10^{2} ± 11.3%	1.68 × 10^{2} ± 2.1%
Diode Ideality	**2.37;**	**1.98;**	**1.67;**	**1.94;**
	3.27 ± 23.96%	1.95 ± 16.4%	1.93 ± 19.3%	2.75 ± 33.2%
J_{SAT} *(mA cm^{-2})*	**2.20 × 10^{-3};**	**4.64 × 10^{-4};**	**1.35 × 10^{-5};**	**1.31 × 10^{-4};**
	2.45 × 10^{-1} ± 106%	1.81 × 10^{-3} ± 145%	1.26 × 10^{-4} ± 126%	1.39 × 10^{-1} ± 171%

Film Transmittance (%)	60	65	58	60
Final Sheet Resistance of Film (Ω sq^{-1})	543 ± 2.9%	2410 ± 12%	2550 ± 38%	2890 ± 27%

Figure 3-6 and Table 3-6 display numerical photovoltaic data for a range of important parameters. A good shape comparison can be seen in the plot displaying the fundamental J/V curve properties (Figure 3-6). By the 2nd 2% HF etch the best device PCE values ranged from 3.78 % for the MWCNT sample to 4.79 % for the SWCNT – 1 sample. The large difference between the MWCNT device performance and the other three nanotube types is significant considering the care taken to control other differences between devices. Overall, devices produced with SWCNT – 1 films performed the best in terms of PCE, FF, and J_{sc}. It is surprising that these devices were out performed in terms of V_{oc} by the DWCNT and MWCNT samples. This difference can be attributed to the higher reverse saturation current (J_{sat}) for these samples. A smaller J_{sat} indicates that less current is flowing in the undesired direction in the device. The relationship between J_{sat} and V_{oc} is shown in Figure 3-8. It is notable that the average J_{sat} values possess very high error bars due to the large range of J_{sat} values in each batch of devices. Figure 3-7 displays the average PCE for each CNT type at each stage of post-fabrication treatment. This clearly displays the significant improvement the CNT/Si device receives from doping. Additionally, it is also clear that devices with MWCNT films initially perform at the same level as devices with DWCNT films (and above devices with SWCNT films) but do not experience the same level of improvement from doping as seen with SWCNT and DWCNT films. This supports the results shown in Table 3-5 where it was seen that the sheet resistance of MWCNT films does not decrease to the same extent as SWCNT and DWCNT films after doping. The origin of the significant increase in PCE for the DWCNT sample from the $SOCl_2$ doping step to the 2nd 2% HF etch is unknown. As $SOCl_2$ is a *p*-type dopant, it is expected that the PCE will improve due to increasing conductivity and lowering the CNT fermi level relative to the silicon. The 2% HF effect may be due to acid digestion of non-DWCNT

impurities (up to 40% weight in the starting material (Table 3-1)) resulting in a better contact between DWCNTs and the silicon layer.

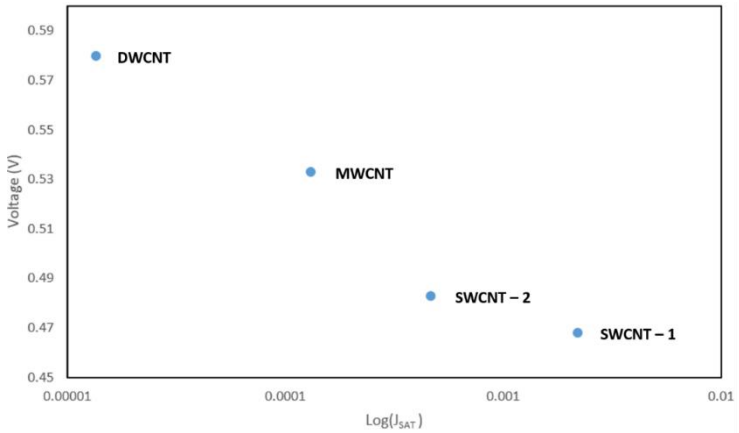

Figure 3-8: A plot of the relationship between reverse saturation current (J_{sat}) and open circuit voltage (V_{oc}) for the best performing devices for each viable sample.

Jia *et al*.[83] determined that the optical and conductive properties of a CNT film (σ_{dc}: σ_{OP} ratio when combined) are the most important parameter for CNT/Si device performance. Thus, it is important to compare the device results in Table 3-6 with the σ_{dc}: σ_{OP} ratio calculations in Table 3-5. The σ_{dc}: σ_{OP} ratio was highest for the SWCNT – 1 sample, which would explain why this sample gave the best J_{sc} and PCE performance. The SWCNT – 2, DWCNT and MWCNT samples all showed similar σ_{dc}: σ_{OP} ratios with SWCNT – 2 being the highest and the DWCNT and MWCNT samples being roughly equivalent. This compares well with the J_{sc} data, which was superior for the SWCNT – 2 devices then the DWCNT devices, then the MWCNT devices (when SWCNT – 1 devices are ignored). Although, overall there is no consistent trend between σ_{dc}: σ_{OP} ratio and J_{sc} visible (Figure 3-9). The device PCE results do not follow the same trend due to superior V_{oc} data for the DWCNT and MWCNT devices compared to the two SWCNT type devices.

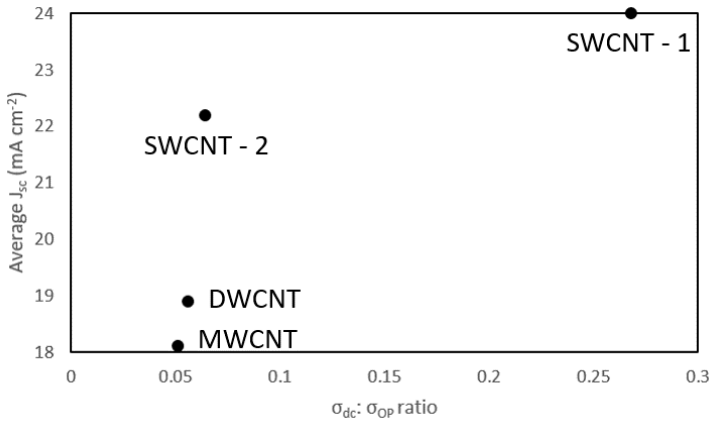

Figure 3-9: Plot of σ_{dc}: σ_{OP} ratio vs average J_{sc}.

The improved PCE values seen in the SWCNT samples over the DWCNT and MWCNT samples can be partially understood by observing the difference between the R_{shunt} and R_{series} values obtained. The R_{series} value describes resistances impeding current flow through the desired circuit and thus will ideally be very low. Conversely the R_{shunt} value describes resistances impeding current flow through undesired paths or 'short-cuts' in the device and will ideally be at least an order of magnitude higher than the R_{series} value for a given device. The difference between the average R_{shunt} and R_{series} values for each viable CNT type is shown in Figure 3-10. It can be seen that SWCNT – 1 films gave the best $R_{shunt} – R_{series}$ separation, although all types showed a difference of at least 500 Ω and each sample displayed a resistance difference of at least 3 orders of magnitude.

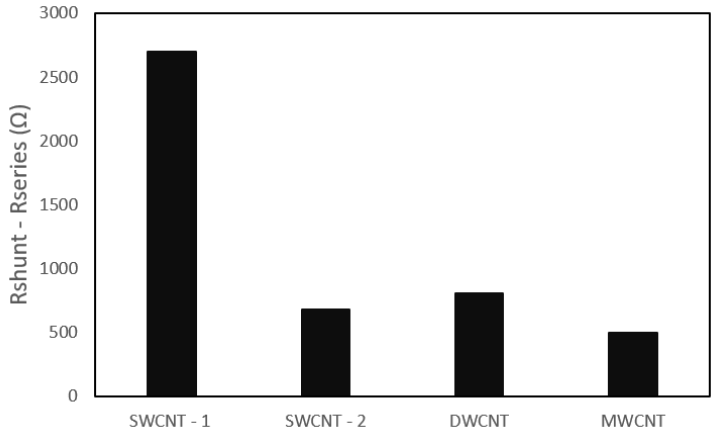

Figure 3-10: Difference between average shunt and series resistances for different viable nanotube types.

The SWCNT – 1 sample devices produced higher diode ideality values on average, indicating that these devices were performing less ideally than for the other samples. This could be indicative of poorer CNT/Si contact in the devices for this sample.

Overall, the SWCNT samples performed better than the other types, with SWCNT – 1 devices performing better than SWCNT – 2 devices. This is expected from analysing the sheet resistance measurements on films for each sample, as the SWCNT films exhibited lower resistances after final treatment. This is probably due to better morphology of the SWCNT films compared to the DWCNT films. Although there is some work to suggest that DWCNTs conduct charge better than other wall number types.[182] The poorer film performance in this study is likely traceable to the difficulty in forming suspensions as concentrated and homogeneous as the other wall number types, due to the lower purity of the DWCNT sample used for device fabrication. The MWCNT sample showed a good film morphology and overall good sheet resistances and device performance post-fabrication. However, the devices did not improve with doping to the same extent as the SWCNT samples.

3.5 Conclusions

Suspensions of each nanotube type were produced under the same solvent and processing conditions and films were produced with roughly equivalent transmittance. This allowed an unambiguous comparison to be made between different nanotube wall number types in CNT/Si devices.

It was observed that, although one SWCNT sample performed at a higher PCE than the other samples, both SWCNT samples and the DWCNT sample produced similar PCE values as each other, with a difference of less than 0.5 % between the three samples. SWCNT films produced better J_{sc} values, whilst DWCNT and MWCNT films displayed higher V_{oc} values. Fill factor values were found to be similar across the board, with SWCNT – 1 films producing better R_{shunt} to R_{series} ratios. Sheet resistance measurements showed that MWCNT films did not respond to chemical doping to the same extent as other samples, due to outer tube shielding. The results of this study indicate that, when variables

other than nanotube type are controlled, large diameter single-walled carbon nanotube films provide the best performance in CNT/Si devices.

CHAPTER 4 ALIGNED-SMOOTH CNT FILMS

4.1 Introduction

The morphology of the CNT films used in CNT/Si devices is of the utmost importance when it comes to their photocurrent production. When films are produced via standard vacuum filtration (Section 2.1.2), they are homogeneous on the macroscale. On the micro/nano scale, however, the films are highly disordered and form a complex network of nanotubes, with many holes and clumps distributed across the film. Holes in the film are a problem for device performance, as they are areas in which there is no CNT/Si junction. They introduce variations in the depletion region and the overall CNT/Si contact area is reduced. Additionally, disfigurements in the film will retard the film's ability to efficiently transport charge carriers across the film from the CNT/SI heterojunction to the gold top contact.

Whilst the presence of holes in the film can be reduced by producing a thicker film, this leads to its own problems. A thicker film will reduce the amount of light incident on the silicon layer of the device, lowering photocurrent production. It is important, therefore, to look for methods to improve the microscale morphology of the CNT film and to improve the smoothness of the film to create more CNT/Si junctions in a given area. One such option is to focus on orienting the CNTs within the film to produce aligned films. Aligned CNT films do not suffer the same hole issues and provide an overall better coverage over the silicon. Many methods have been suggested and implemented for forming smooth, aligned CNT films such as: physical shearing from highly concentrated CNT suspensions,[95, 96, 148, 149] physical shearing of dry CNT films,[183, 184] growth of upright CNTs followed by vertical collapse,[151, 185] drawing from highly aligned arrays,[154] deposition of aligned CNTs using Langmuir-Blodgett[186]or Langmuir-Schaefer[187] deposition, horizontal growth on a patterned substrate,[153] and self-assembly of CNTs from evaporation of suspension,[155, 157] drop-casting,[156] and deposition on a slide pulled from solution.[158] This chapter looks at a simple, novel method to produce flat, aligned CNT films over a large area through the use of ultra-slow filtration, first examined by He *et al*.[188]

Vacuum filtration is a common method for forming randomly aligned and rough CNT films, thanks to the simplicity and ease of application. The idea behind slow filtration for smoother, aligned CNT films is that, in suspension, the CNTs will naturally align within the fluid, and a slow deposition process will allow this alignment to be maintained in the produced film. Additionally, vacuum filtration can form rough pores in the CNT networks due to the solvent being rapidly pulled through the film. A slow filtration process will eliminate this issue and will thus lead to the formation of smoother films. For CNT alignment to occur three conditions must be satisfied.

1. The surfactant concentration must be below the critical micelle concentration (CMC).
2. The CNT concentration must be below a threshold value.
3. The filtration process must be controlled at a low speed.[188]

The alignment of the CNTs in suspension is driven by electrostatic interactions between anisometric particles in a colloidal solution as investigated by Onsager,[189] Song *et al.* determined that long MWCNTs form a lyotropic liquid crystalline phase[190] and Engel *et al.* used this property to form rows of aligned CNTs via solvent evaporation.[157]

4.2 Aim

1. To use a slow filtration technique to produce aligned SWCNT films
2. To analyse the morphological and conductivity differences between films made with the standard vacuum filtration method and the slow filtration method.
3. To observe and analyse any differences in device performance between CNT/Si devices consisting of slow filtered films and fast filtered films.

4.3 Slow Filtration Rate

The films in the work by He *et al.*[188] were produced using a filtration rate of around 1 – 2 mL hr^{-1} or 0.017 – 0.033 mL min^{-1} using very low concentration suspensions of CNTs. In order to replicate the slow rate a PTFE filtration membrane was selected with a pore size of 0.1 µm. The initial experiments were performed with purified arc-discharge SWCNTs (the type used in other experiments in this

thesis) suspended in a 1 % SDS suspension. The CNT concentration was 0.5 mg mL^{-1} for this experiment. The 1 % SDS solution was bath sonicated for 10 minutes and the suspension was tip sonicated after CNT addition and centrifuged as detailed in Section 2.1.1. The suspension was then diluted with water at a ratio of 1:10.

It was important to ensure that the SDS concentration was below the critical micelle concentration (CMC) to ensure that the SDS properly assists in suspending the SWCNTs.[188] The CMC of SDS is 8.2 mM.[191] A 1% SDS solution is 0.1 g of SDS in 10 mL of water.

$$number\ of\ moles_{SDS} = \frac{mass_{SDS}}{Molar\ Mass_{SDS}} = \frac{0.1\ g}{288.372\ g\ mol^{-1}} = 0.00035\ moles$$

$$Concentration_{SDS} = \frac{number\ of\ moles_{SDS}}{Volume} = \frac{0.00035\ moles}{0.010\ L} = 0.035\ mol\ L^{-1} = 35\ mmol\ L^{-1}$$

$$Diluted\ 1{:}10$$

$$35\ mmol\ L^{-1} * \frac{1}{10} = 3.5\ mmol\ L^{-1}$$

Thus, it was confirmed that, once diluted 10-fold for filtration, the concentration of the SDS was below the CMC.

10 mL of the resultant diluted SWCNT suspension was filtered with a low vacuum and the rate of volume loss measured vs time passed.

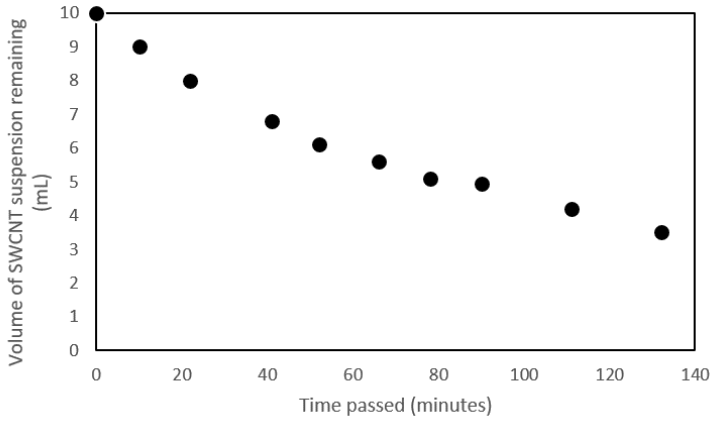

Figure 4-1: Volume of solution remaining vs time passed for initial SWCNT suspension.

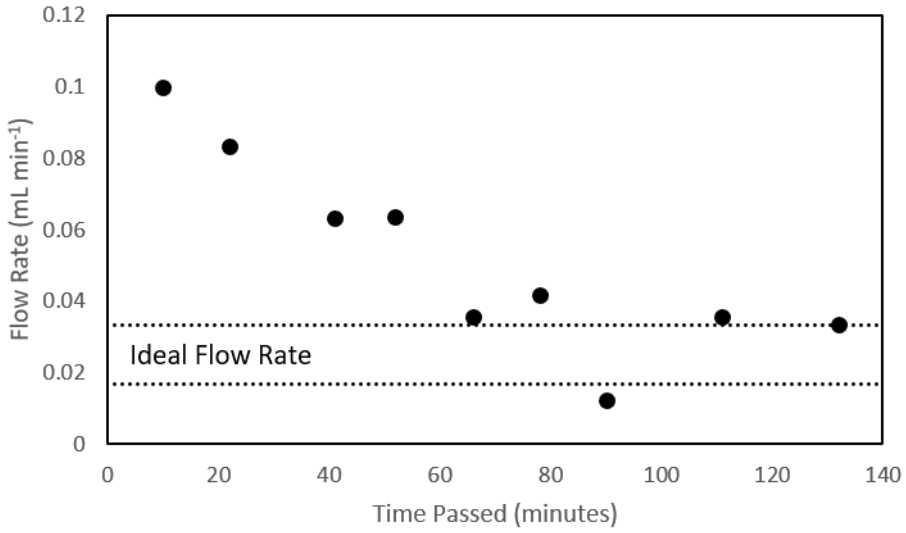

Figure 4-2: Flow rate for initial SWCNT suspension. The dotted lines indicate the flow rate range from He *et al*. in mL min^{-1}.

As can be seen in Figure 4-1 and Figure 4-2, the flow rate was initially faster than desired with approximately 4 mL of the solution passing through the membrane in the first hour of filtration. It can also be observed that the flow rate decreased as more solution was filtered. This is expected as over the course of the filtration the membrane will be covered by more SWCNTs and this will retard filtration. In the above case the filtration slowed significantly after the first few hours. This is likely due to the build-up of CNTs on the filtration membrane as this will retard the ability for solution to pass through the membrane.

New suspensions were made at concentrations of 0.2 mg mL^{-1} for 3 different samples: Arc-discharge SWCNTs, HiPCO SWCNTs, and MWCNTs in 1 % SDS solutions. 500 µL aliquots of these suspensions were filtered slowly in a 10 mL aqueous solution on to small pore PTFE filter membranes with the flow rate recorded and SEM and AFM images of the films obtained. The wrinkle patterns visible in Figure 4-3 are due to the wetting of the membranes prior to filtration. The wrinkles are due to areas of differing CNT film thickness. Additionally, a comparison film was formed under normal 'fast' filtration conditions. The wrinkles are much less apparent in the fast filtered film, indicating that the pressure exerted by the applied vacuum is strong enough to overcome the membrane patterns caused by wetting.

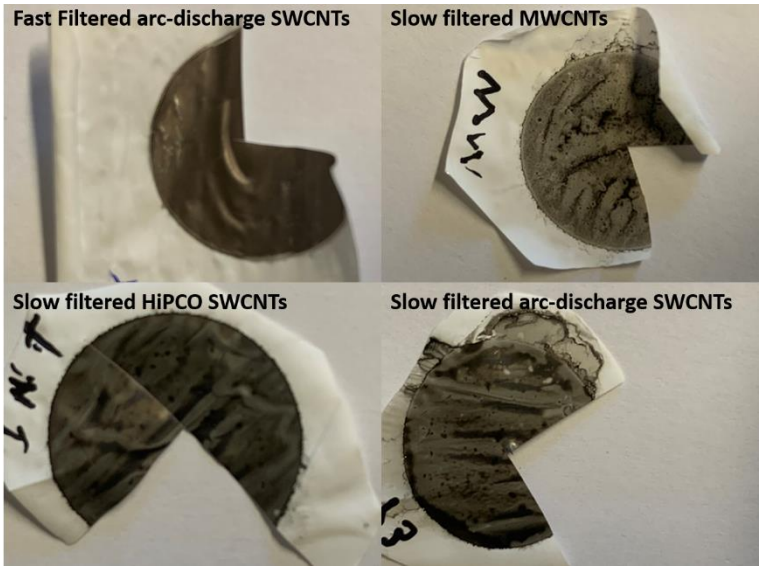

Figure 4-3: Images of finished filtration membranes.

There was a clear macroscale difference in film morphology between fast filtered and slow filtered films. The slow filtered films were much more effected than the fast film by the wrinkled phenomenon in the membranes. It was also apparent that these films are very thick and would likely be unsuitable for device usage.

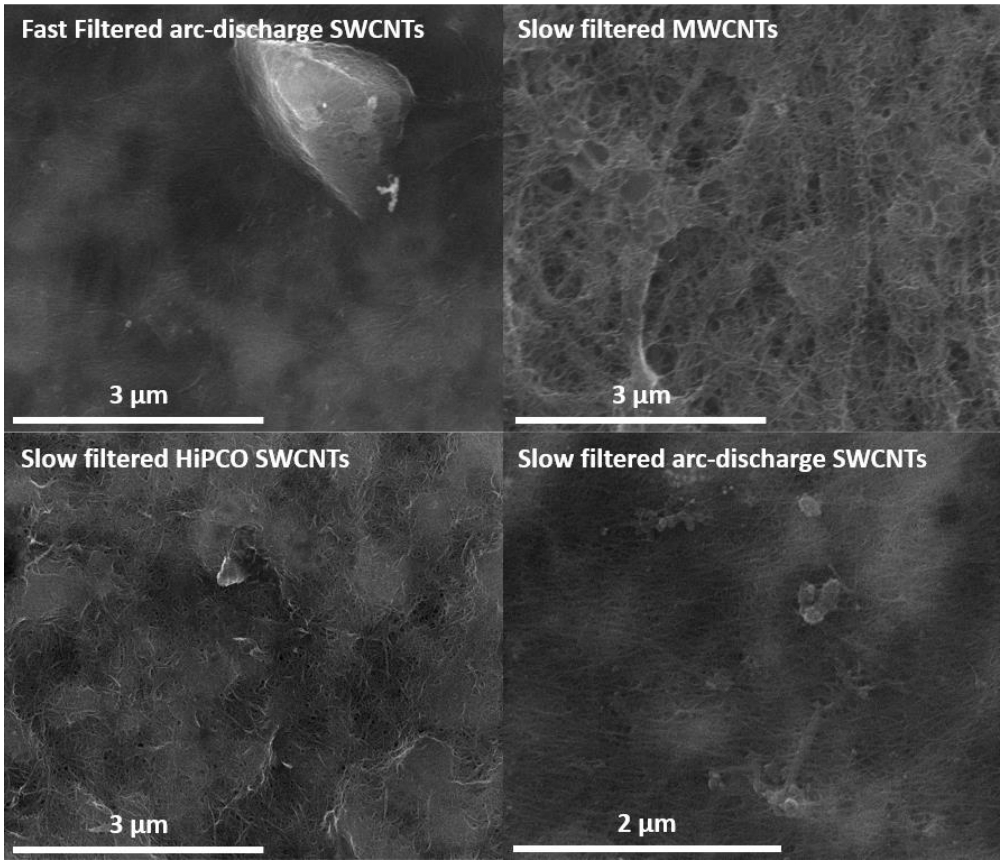

Figure 4-4: SEM images of fast and slow filtered CNT films.

Figure 4-4 shows the microscale structure of the slow and fast filtered CNT films. No alignment is visible at all in the MWCNT and HiPCO SWCNT samples and, though some degree of alignment may be visible in the slow filtered arc-discharge SWCNT sample the film does not visually differ greatly from the fast filtered arc-discharge SWCNT sample.

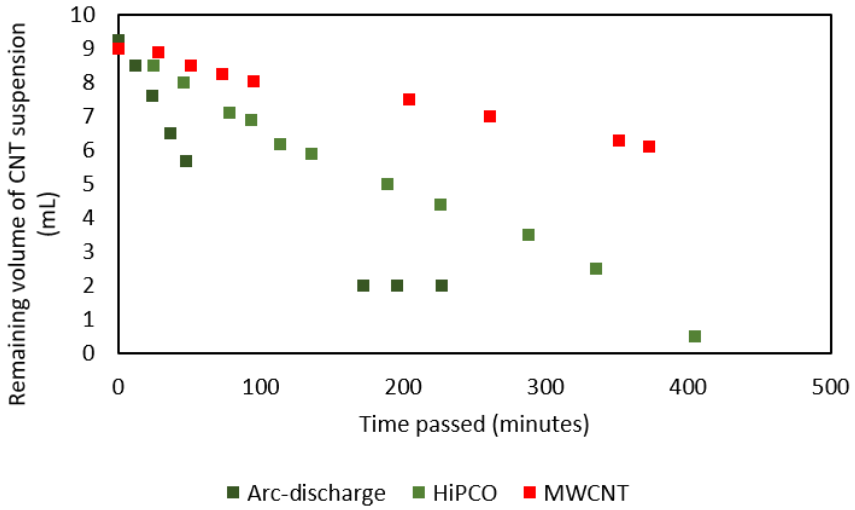

Figure 4-5: Volume loss with time for gravity filtration of 100 µL aliquots of CNT samples diluted up to 10 mL with water.

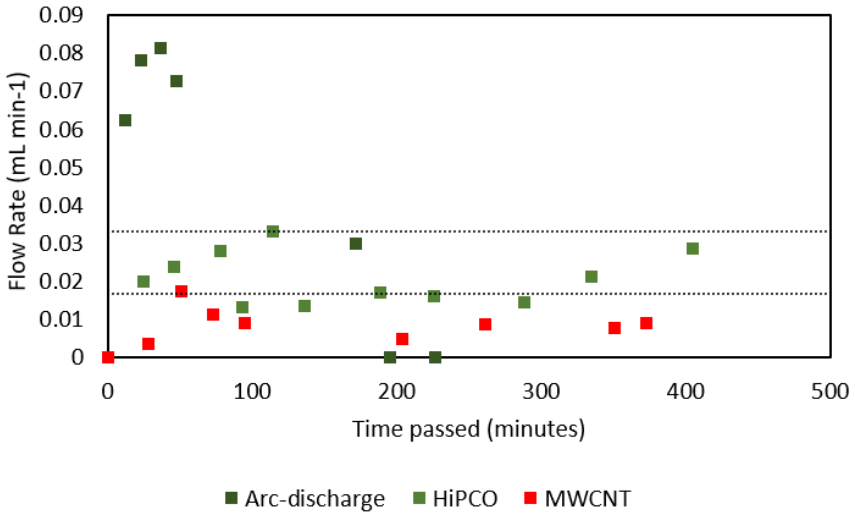

Figure 4-6: Flow rates for gravity filtration of 100 µL aliquots of CNT samples diluted up to 10 mL with water. Horizontal lines indicate the optimum flow rate as published by He *et al*.[188]

It is apparent that there is a large difference in flow rates between the different CNT types. Both the HiPCO and MWCNT samples appear to filter at the desired rate of 1-2 mL hr^{-1} however the arc-discharge sample filtered much faster. Overall, there was no obvious alignment and the films produced were all much thicker than films that would be used in CNT/SI devices. As such, the volume of suspension filtered was reduced to 100 µL for the next experiments in diluted up to 10 mL with

purified water. Additionally, a small volume of water was filtered through the setup under vacuum prior to the gravity filtering of the CNT suspension. This served to flatten the filter paper and prevent the ridges that were seen previously.

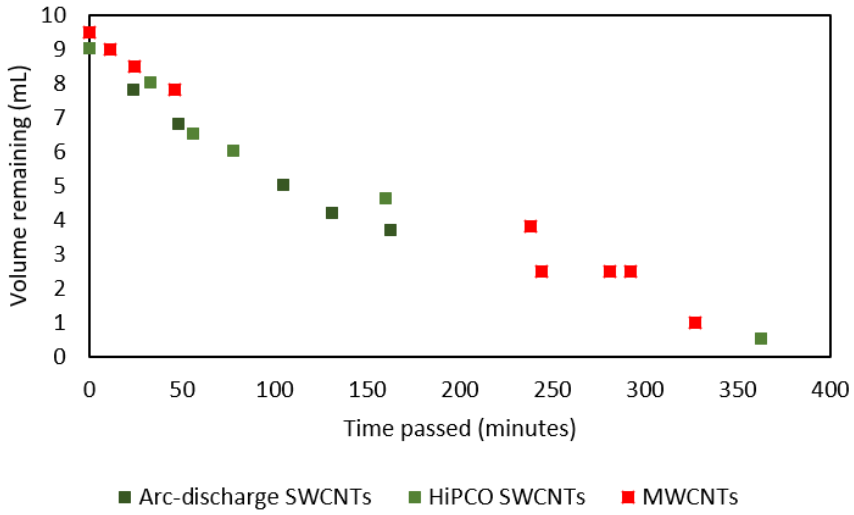

Figure 4-7: Volume loss with time for gravity filtration of 100 µL aliquots of CNT samples diluted up to 10 mL with water following brief water filtration under vacuum.

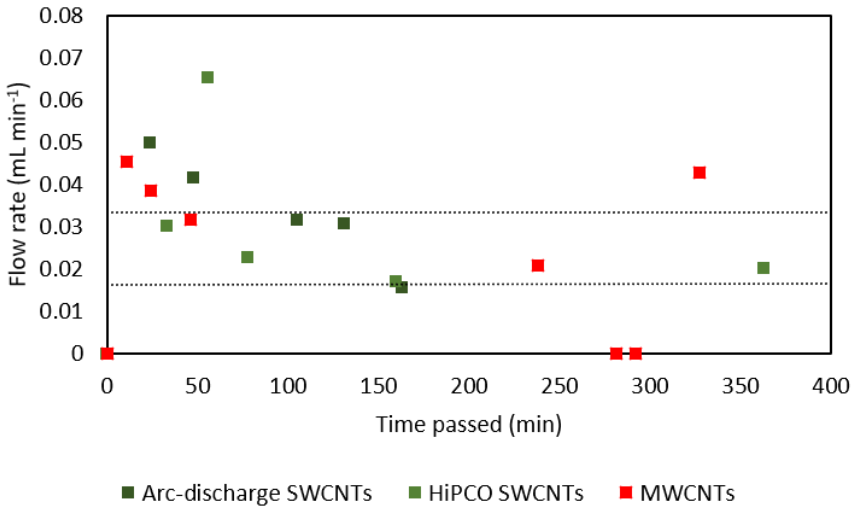

Figure 4-8: Flow rates for gravity filtration of 100 µL aliquots of CNT samples diluted up to 10 mL with water following brief water filtration under vacuum. An outlier data point of 0.22 mL min^{-1} in the MWCNT flow rate has been excluded. Horizontal lines indicate the optimum flow rate as published by He *et al*.[188]

Figure 4-7 and Figure 4-8 show the flow rates for smaller aliquots of suspension following a brief vacuum filtration of water to flatten the paper. The flow rate appears to be roughly equivalent for all three CNT types. The overall rates are faster for the HiPCO SWCNT and MWCNT samples whilst the rate has decreased for the arc-discharge SWCNT sample. The increase in flow rate for the HiPCO SWCNT and MWCNT samples was likely due to passing through a small volume of water prior to

filtering the CNT suspensions. The reduction in flow rate for the arc-discharge SWCNT sample suggests an issue in the previous filtration. In each case, however, the flow rate was still higher than the 1 – 2 mL hr^{-1} desired rate.

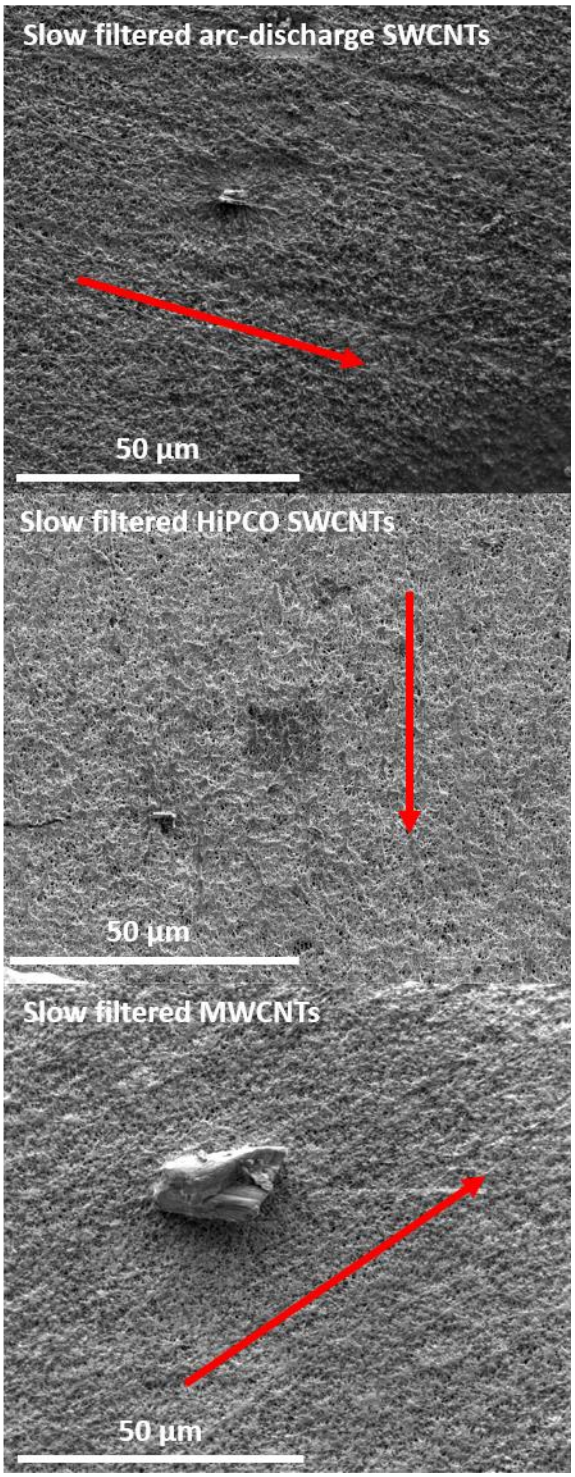

Figure 4-9: SEM images of slow filtered CNT films. Red arrows show the direction of possible CNT alignment present.

The SEM images of the slow filtered films with a smaller aliquot of suspension (Figure 4-9) show more promise than those obtained previously. There is a clear trend of directionality visible in the arc-discharge SWCNT film (top left to bottom right) and the MWCNT film (top right to bottom left). There is no trend as obvious in the HiPCO SWCNT film although there could be directionality from the top of the image to the bottom. The possible directionality highlighted in Figure 4-9 was determined from visual observation of the images. Secondly, the films all appear to be relatively flat and homogeneous on the microscale imaged here, this is vastly different to the films on the macro scale where they are far from homogeneous.

Figure 4-10: Optical images of slow filtered films.

Figure 4-10 shows the macroscale inhomogeneity of CNT films filtered under gravity. These represent a common problem observed for all slow filtered films. As can be seen, the dark regions of higher CNT concentration are smaller in area to the lighter regions, as such, for solar device application and future imaging, the lighter areas were used as more small films could be cut from this area and the transmittance and film conductivity could be more reliably calculated. The films produced by He *et al.*[188] were visually homogeneous across the whole film. The likely reason for this is that in their research a low, controlled vacuum was applied, where as in these experiments, gravity was used as the bias to push the CNT suspension through the membrane.

4.4 Volume Dependence

A series of volumes of arc-discharge and HiPCO SWCNTs were filtered, both fast and slow, to determine the effect of SWCNT concentration on film morphology. In each case, the volume shown was diluted up to 10 mL with water before filtration commenced. Additionally, for these and future experiments, the filtration membranes were changed to cellulose ester membranes with a pore size of 0.1 µm in an attempt to decrease the flow rate. Figure 4-11 and Figure 4-12 show the change in volume and hence flow rate for three different CNT types with the new membranes. The flow rates plots all show a peak within the first hour ranging from 0.01 mL min^{-1} to 0.025 mL min^{-1} which then decreased to at or below 1 mL hr^{-1} (0.0167 mL min^{-2}) by the 120 min mark. Thus, the change in membrane successfully reduced the flow rate of CNT suspension filtration to the desired value.

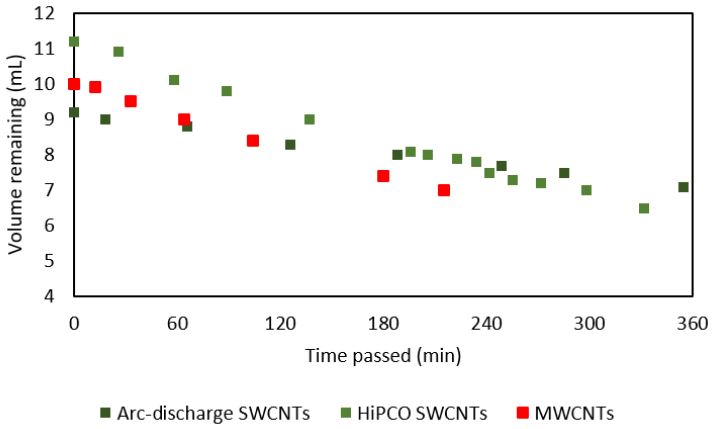

Figure 4-11: Volume loss with time for gravity filtration of 100 µL aliquots of CNT samples diluted up to 10 mL with water when using new cellulose 0.1 µm pore membranes.

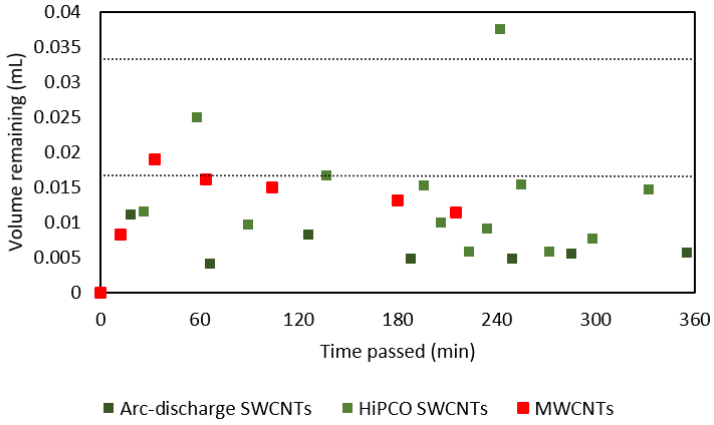

Figure 4-12: Flow rates for gravity filtration of 100 µL aliquots of CNT samples diluted up to 10 mL with water when using new cellulose 0.1 um pore membranes. Horizontal lines indicate the optimum flow rate as published by He *et al*.[188]

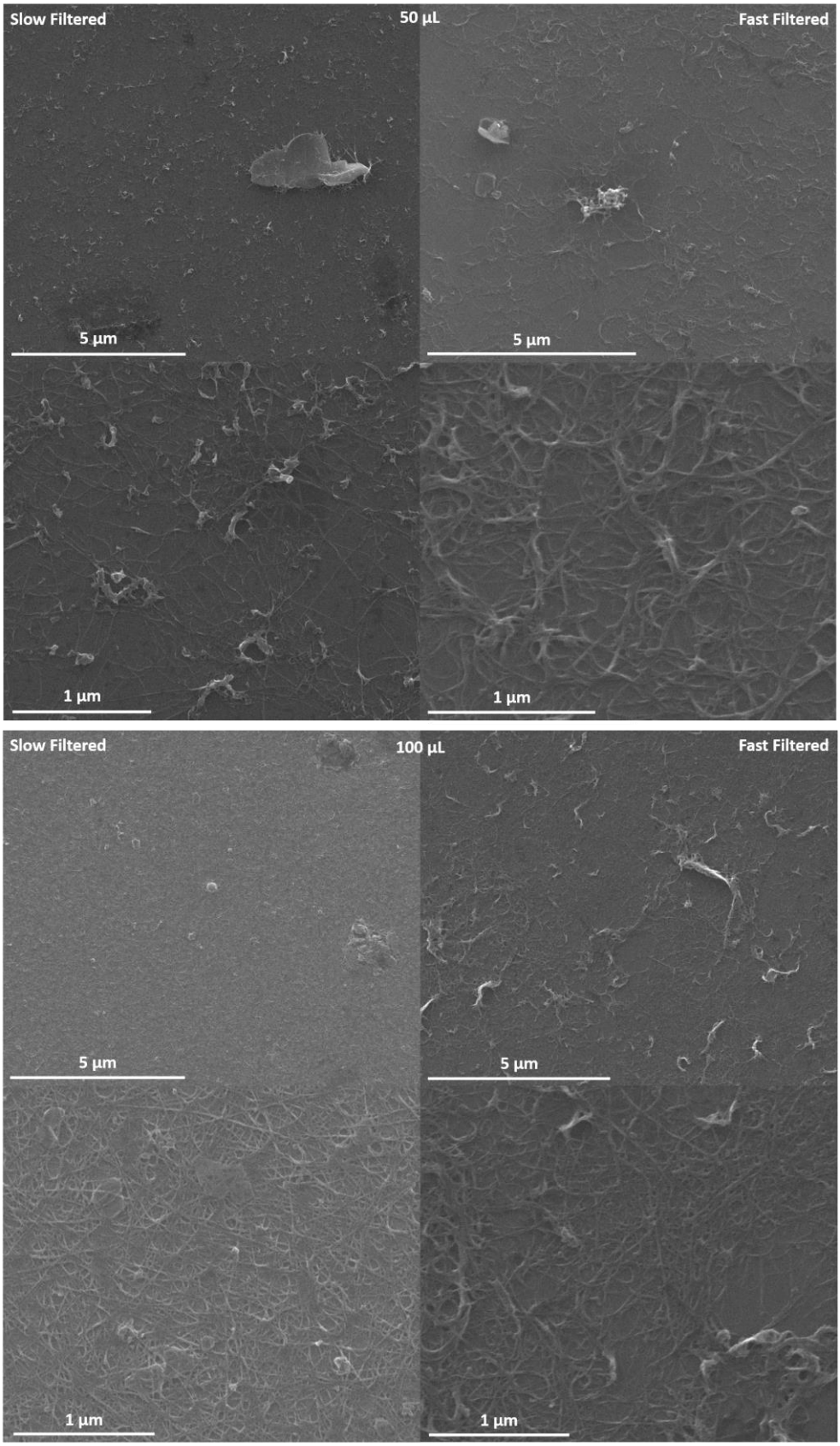
Slow Filtered
50 µL
Fast Filtered
5 µm
5 µm
1 µm
1 µm
Slow Filtered
100 µL
Fast Filtered
5 µm
5 µm
1 µm
1 µm

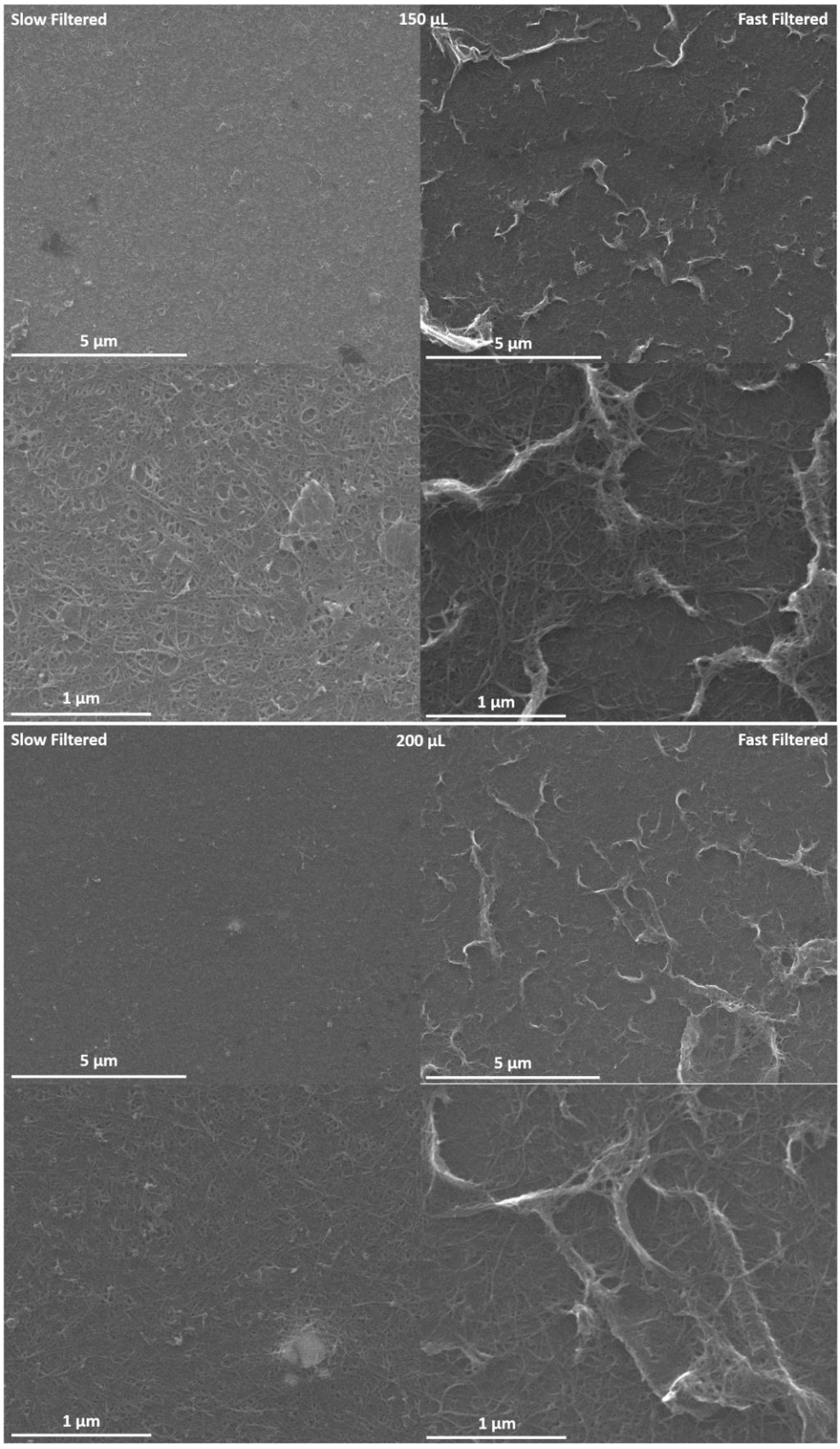

Figure 4-13: SEM images of arc-discharge SWCNTs filtered quickly and slowly at different volumes

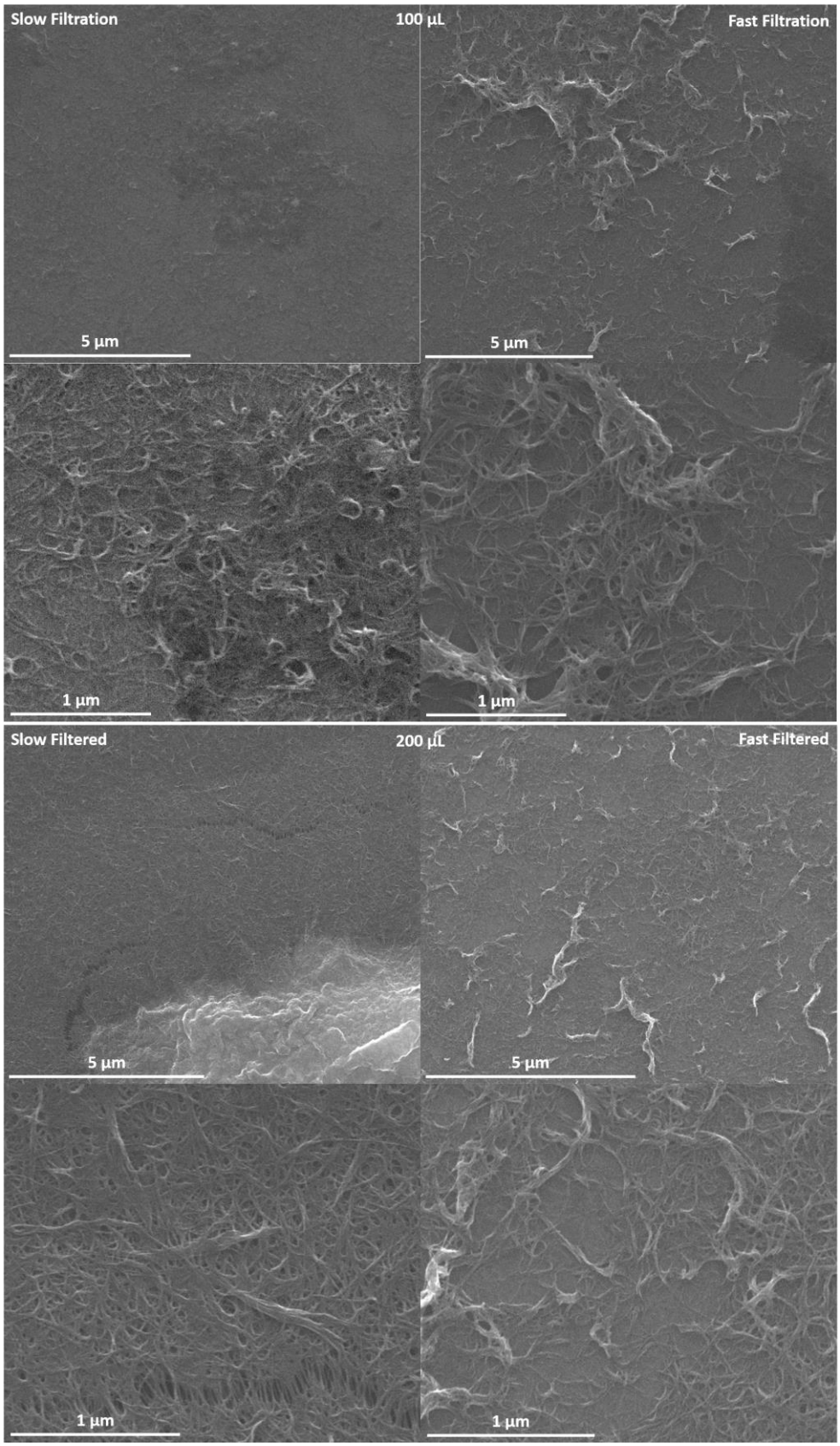
Slow Filtration
100 µL
Fast Filtration
5 µm
5 µm
1 µm
1 µm
Slow Filtered
200 µL
Fast Filtered
5 µm
5 µm
1 µm
1 µm

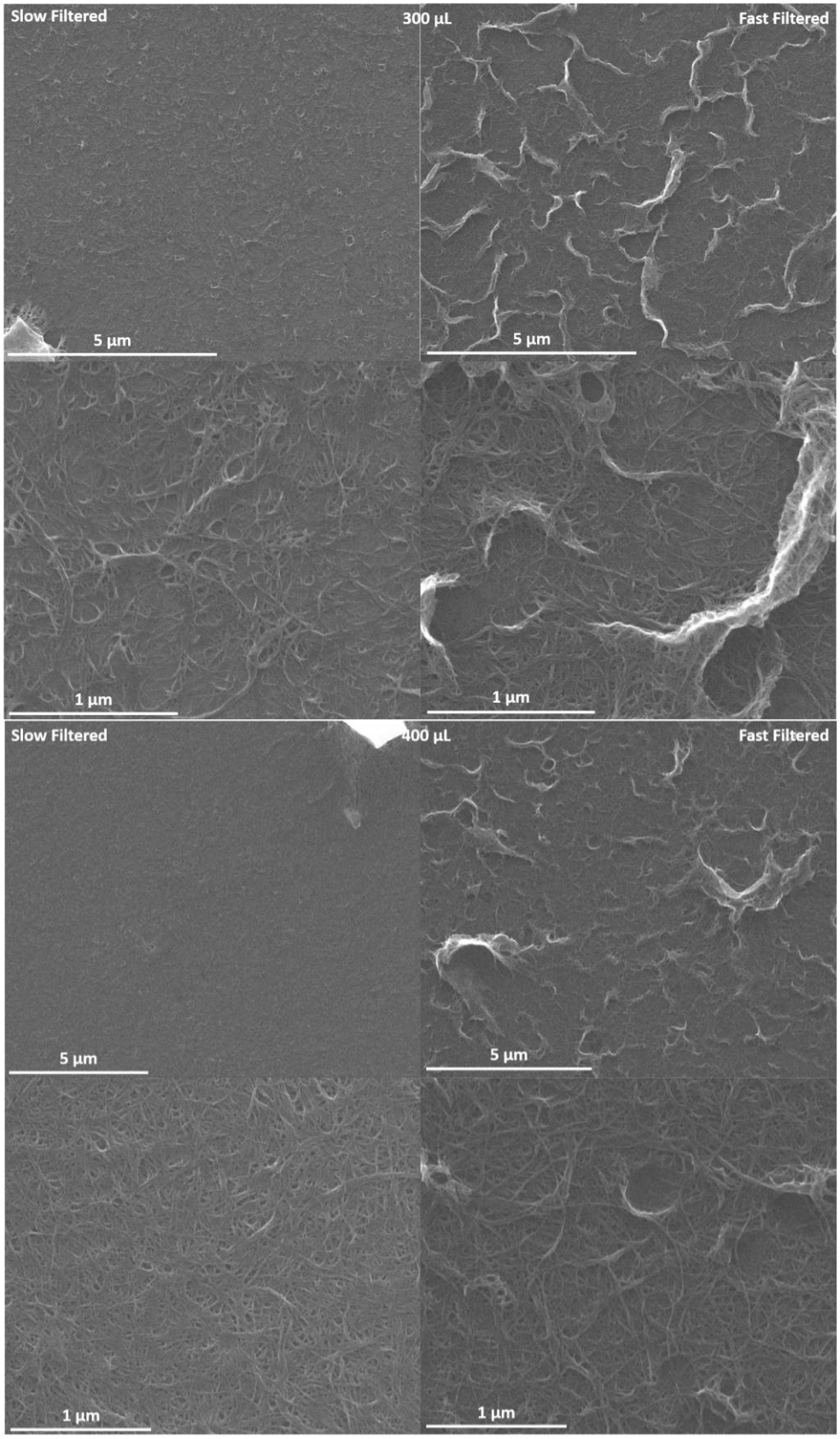

Figure 4-14: SEM images of HiPCO SWCNTs filtered quickly and slowly at different volumes.

Figure 4-13 and

Figure 4-14 show the microscale morphology of SWCNT films fabricated with both slow and fast filtration at different volumes. The only change visible with increasing SWCNT suspension volume (and thus SWCNT concentration) is an improvement in surface coverage, with clear gaps visible in the films at lower concentration and full SWCNT coverage observed at higher concentrations. It is clear that directional SWCNT alignment was not achieved in any of the samples with the SWCNTs exhibiting random orientations in all of the slow and fast filtered samples. However, a stark difference is observed in film roughness with slow filtration when compared to fast filtration. Large buckled SWCNT regions are seen in the fast filtered films whereas these are not present in the slow filtered films. From this alone, it is likely that slow filtered films are preferable for use in CNT/Si devices, as smoother films will provide a better contact between the SWCNT film and the silicon substrate.

4.5 Slow vs Fast Filtration Solar Device Data

Slow and fast filtered films of arc-discharge SWCNTs were produced from 400 µL aliquots in 10mL of water and were attached to the standard circular device substrate (active area 0.071 cm^2) (Section 2.1.5). For the fast filtered films, the film areas were homogeneous on the macro scale and thus any area of the films could be used in CNT/Si devices. As discussed above, slow filtered films are not homogeneous on the macroscale and thus it is important to keep consistent which areas of a film are chosen for solar device usage. All slow filtered films have a small area of high CNT density and a larger area with a much lower density, for solar device applications the high SWCNT density area was never used in order to keep the devices as consistent as possible.

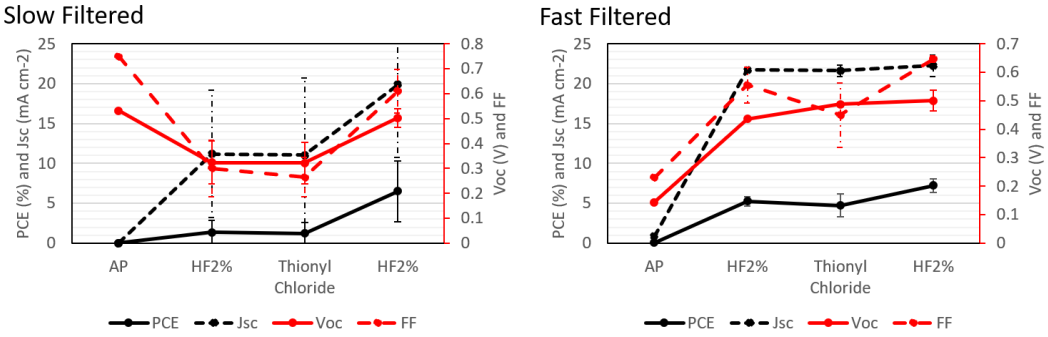

Figure 4-15: J/V properties for devices with 400 µL aliquot slow and fast filtered arc-discharge SWCNT films.

It is apparent that, on average, the devices with fast filtered films outperform those with slow filtered films with an average PCE of 7.21% vs 6.51% although this includes a low performing 2.26% device in the slow filtered batch. Without this outlier device the slow filtered films average rises to 8.64% albeit from only 2 cells. To address the large offset between devices in the slow filtered samples a further set of 3 devices were fabricated and tested.

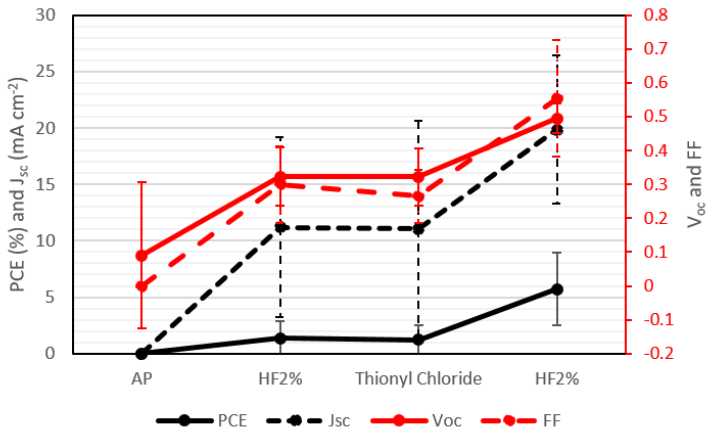

Figure 4-16: J/V properties for additional devices with slow filtered 400 µL films additional devices.

The additional set of devices did not serve to improve the stability of the average PCE, with one device failing to produce a photocurrent and two other devices of 6.51 % and 2.25 %. If the top performing 3 devices from the slow and fast sample sets are averaged the slow filtered films outperform the fast filtered films with an average of 7.93 % to 7.21 % however it is important to acknowledge the existence of several poorer performing devices in the slow filtered film sets. The full sets of device data after final 2 % HF etch can be seen in Table 4-1. It is noticeable that, for most parameters, the slow filtered devices best performance was superior than or equal to the best performance of the fast filtered devices. However, in every case (except shunt resistance) the variation between individual data points was greater for the devices with slow filtered films. The high variability between devices produced with slow filtered SWCNT films is likely due to the macroscale inhomogeneity of the films (Figure 4-10).

Table 4-1: Solar device data for fast filtered and slow filtered films, bold text is the best-recorded result with the average and standard deviation in brackets.

	Fast Filtered Films	*Slow Gravity Filtered Films*
PCE (%)	**8.06** (7.21 ± 0.84)	**9.64** (5.71 ± 3.24)

J_{sc} *(mA cm^{-2})*	**24.76** (22.26 ± 1.33)	**27.46** (19.84 ± 6.55)
V_{oc} *(V)*	**0.532** (0.501 ± 0.038)	**0.532** (0.495 ± 0.044)
FF	**0.66** (0.647 ± 0.012)	**0.67** (0.554 ± 0.172)
Ideality	**2.34** (2.53 ± 0.26)	**2.40** (2.89 ± 0.71)
Saturated Current Density (mA cm^{-2})	**0.00198** (0.005 ± 0.003)	**0.0008** (0.025 ± 0.033)
Series Resistance (Ω)	**51.4** (53 ± 1.66)	**50.5** (128 ± 115)
Shunt Resistance (Ω)	**25300** (10456 ± 12857)	**17200** (7665 ± 6775)

4.6 400 µL Slow vs Fast Filtration Film Data

It is important to determine the light transmittance of the slow filtered films vs the fast filtered films as this is a crucial parameter that has a significant effect on device performance. Both sets of films were produced with the same volume from the same SWCNT suspension, however as the slow filtered films are known to produce non-homogeneous films it cannot be assumed that both fast and slow filtration setups will produce films of equal transmittance. A sample film of both filtration rates was used to produce a UV-Vis spectrum and a transmittance value calculated from an average of the transmittance at 400 nm and 850 nm. The slow filtered film had a transmittance of 78.5 % whilst the fast filtered film had a much lower value of 51.2 %. This is a significant observation as this large of a difference in transmittance would be expected to give a large PCE difference. It is thus apparent that there is a difference in the light transmittance vs film conductivity for SWCNT films produced via slow filtration. To further observe this difference the sheet resistance for both sets of films was measured and plotted here as Figure 4-17.

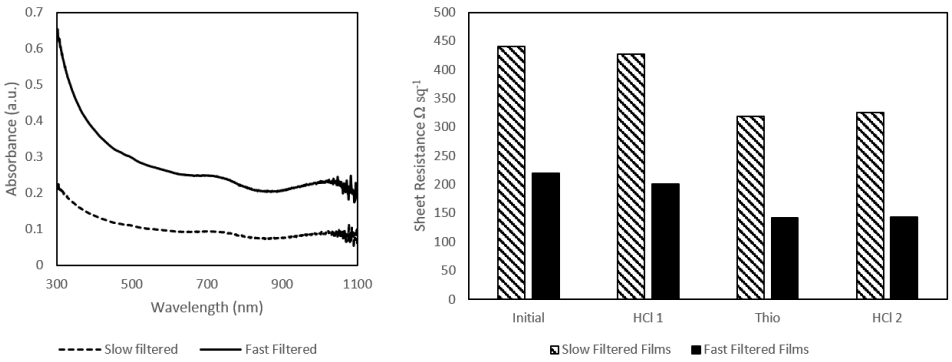

Figure 4-17: UV/Visible spectra and sheet resistance comparison for slow vs fast filtered SWCNT films.

The slow filtered films used for solar devices let through 30 % more light than the fast filtered films but have twice the sheet resistance. Together, the sheet resistance and transmittance can be combined to produce a ratio of DC electrical conductivity (σ_{dc}) and optical conductivity (σ_{OP}). This ratio is a good way to directly compare thin SWCNT films with differing resistance and transmittance properties.[181, 192] The ratio is defined relative to the transmittance as shown in Equation 4-1 and this equation can be rearranged to directly give the σ_{dc}: σ_{OP} ratio with an experimental transmittance at 550 nm and an experimental sheet resistance (Equation 4-1), both of which have been achieved for the slow and fast arc-discharge SWCNT films.

Equation 4-1: σ_{dc}: σ_{OP} ratio equation.

$$\%T_{550} = (1 + \frac{1}{2R_s} * \sqrt{\frac{\mu_0}{\varepsilon_0}} * \frac{\sigma_{OP}(550)}{\sigma_{dc}})^{-2}$$

$$\frac{\sigma_{dc}}{\sigma_{OP}(550)} = \frac{1}{2R_s} * \frac{\sqrt{\frac{\mu_0}{\varepsilon_0}}}{T^{-1/2} - 1}$$

Where T is transmittance at 550 nm in this case, R_s is the sheet resistance, μ_0 ($4\pi \times 10^{-7}$ N A^{-2}) is the free space permeability and ε_0 (8.854×10^{-12} C^2 N^{-1} m^{-2}) is the free space permittivity. From Equation 4-1 it can be seen that a high σ_{dc}: σ_{OP} ratio will be produced for a film with low sheet resistance and high light transmittance. Thus, a higher σ_{dc}: σ_{OP} ratio indicates a more optimal film for use in a CNT/Si device.[180]

Table 4-2: σ_{dc}: σ_{OP} ratio calculations for slow and fast films used in solar device production.

Treatment Point	T_{550}	*Sheet Resistance Slow Filtered (Ω)*	*DC/OP Slow Filtered*	T_{550}	*Sheet Resistance Fast Filtered (Ω)*	*DC/OP Fast Filtered*
As Prepared	0.79	440	**0.379425**	0.53	220	**0.621004**
HCl 1	0.79	427	**0.390997**	0.53	200	**0.682166**
Thionyl Chloride	0.79	319	**0.524073**	0.53	142	**0.962568**
HCl 2	0.79	325	**0.513056**	0.53	143	**0.95487**

Table 4-2 shows that the σ_{dc}: σ_{OP} ratio increases with treatment, indicating an improvement in overall film performance. This is expected as the treatment improves the film conductivity, the thionyl chloride doping also removes the VHS transitions visible in the 600 – 800 nm regions of the spectrum and thus reduces light absorbance (increasing transmittance). Overall, the table also shows that the σ_{dc}: σ_{OP} is higher for the fast filtered films than for the slow filtered films. This indicates that the fast filtered films are superior for CNT/Si use as their lower sheet resistance outweighs their increased light absorbance. In Section 4.7 slow and fast filtered films with similar transmittance values will be compared.

As observed from SEM images (Figure 4-13 and Figure 4-14) the fast filtered films appeared much rougher on the microscale than slow filtered films. The smoother a SWCNT film, the better contact it will make with the silicon surface and will thus lead to an increase in photocurrent production. The roughness of the film was analysed using AFM. Two areas on a film of each filtration type were imaged by AFM and the images are shown in Figure 4-18. Additionally, the root mean square average height deviation (R_q) and the arithmetic average of the surface height deviations (R_a) were taken from the

image and are shown here in Table 4-3, together these are quantitative measurements of the roughness of the film.

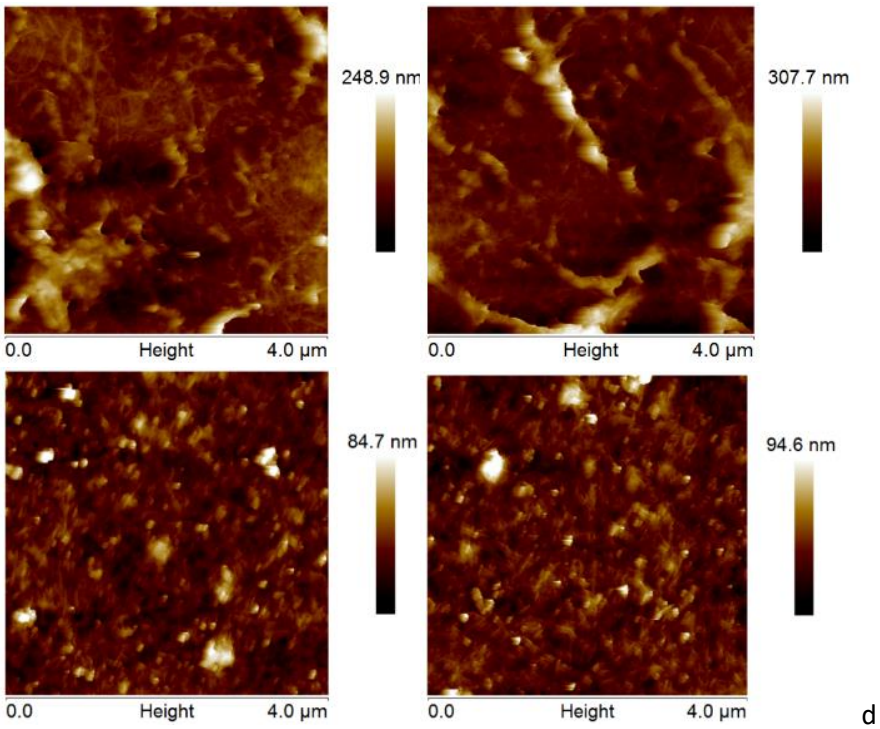

Figure 4-18: AFM images for fast (top row) and slow (bottom row) filtered films formed from 400 µL aliquots of arc-discharge SWCNT suspension.

Table 4-3: Quantitative AFM roughness data for fast and slow filtered films formed from 400 µL aliquots of arc-discharge SWCNT suspension.

	Image Z Range (nm)	*Image Rq (nm)*	*Image Ra (nm)*
Fast Film Spot 1	248.9	31.6	23.3
Fast Film Spot 2	307.7	40.1	28.9
Average	**278.3**	**35.85**	**26.1**
Slow Film Spot 1	84.7	10.7	7.54
Slow Film Spot 2	94.6	11.6	8.25
Average	**89.65**	**11.15**	**7.90**

Both the AFM images themselves and the quantitative roughness data and Z-Range demonstrate clearly that the slow filtered films are significantly flatter than fast filtered films. The R_q values and R_a values for fast filtered film were both 3 – 4 times higher than the slow filtered film. Additionally, the Z-Range was also roughly 3 times higher. By observing the AFM images themselves, large ridges can be seen in the fast filtered film which dwarf the highest of 'mounds' visible in the slow filtered film. These ridges are a product of the turbulent water flow caused by the vacuum filtration method and are the cause of the higher Z-range, R_q, and R_a values.

4.7 500 µL Films for Solar device Application

In order to gain more data for a better σ_{dc}: σ_{OP} ratio comparison films were filtered from a new arc-discharge SWCNT suspension. A larger volume of 500 µL was used but thinner films were produced as the new suspension was less concentrated than that used previously. As per the 400 µL case the slow filtered films were again inhomogeneous on the macroscale and thus the obviously thicker region was avoided when sections were cut for solar device usage. An attempt was made to produce slow and fast filtered films of roughly equivalent transmittance.

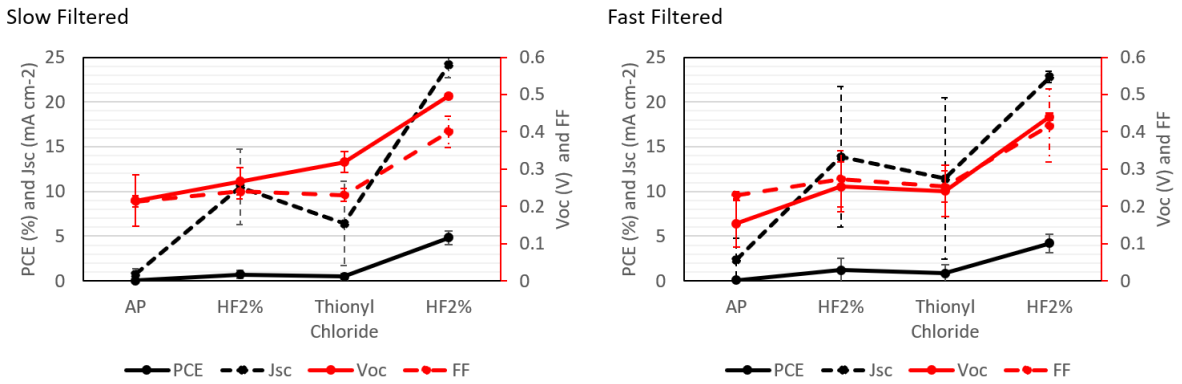

Figure 4-19: J/V properties for devices with slow and fast filtered SWCNT films from 500 µL aliquots.

Figure 4-19 shows that both sets of devices have the same maximum PCE of around 5.4%. In this case, however, the slow filtered films produced a higher average PCE, with a higher average Jsc, and V_{oc}, but a lower average FF.

Table 4-4: Device data for fast and slow filtered films formed from 500 µL aliquots of CNT suspension.

	Fast Filtered Films	*Slow Gravity Filtered Films*
PCE (%)	**5.38** (4.21 ± 1.01)	**5.39** (4.86 ± 0.76)
J_{sc} *(mA cm^{-2})*	**23.47** (22.77 ± 0.62)	**25.21** (24.17 ± 1.47)
V_{oc} *(V)*	**0.451** (0.440 ± 0.009)	**0.501** (0.497 ± 0.0064)
FF	**0.53** (0.417 ± 0.098)	**0.43 (**0.40 ± 0.042)
Ideality	**3.72** (3.82 ± 0.16)	**2.03** (2.74 ± 0.92)
Saturated Current Density (mA cm^{-2})	**0.0950** (0.143 ± 0.046)	**0.00068** (0.0087 ± 0.013)
Series Resistance (Ω)	**13.3** (113 ± 34.2)	**103** (259 ± 254)
Shunt Resistance (Ω)	**2820** (1482 ± 1172)	**41300** (14360 ± 23331)

4.8 500 µL Film Analysis

As per the films used previously, the slow filtered film segments used for solar device application were thinner than the fast filtered films. UV-Vis analysis of the two types of film was used to calculate the average transmittance between the transmittance at 400 nm and the transmittance at 850 nm. There was some variance between the films and so two films were used in each case. The fast filtered films were found to be between 85 % and 95 % and the slower filtered films were from 95 % to 97 %. It is expected that this difference in thickness for the faster films accounts for the variance in device performance with these films. It is expected that when the transmittance of the CNT films approaches 90% and above that the devices will decline in performance as the ability of super thin films to transfer current is poor as the CNT network becomes patchy as thickness decreases. This explains the high variability in PCE for devices with fast filtered films (Table 4-4) but it is surprising to see that the devices with slow filtered films performed well and with low variation considering that they all had transmittances above 90 %. The sheet resistance values for these films were all an order of magnitude higher than that used previously. In addition, the values were much more varied with values on the order of x 10^6 Ω were occasionally reported. These issues are all likely due to how thin the films were, thinner films will conduct poorly compared to thick films and will have more charge gaps and holes

throughout the network. The outlying data points were removed when average sheet resistance was calculated. The sheet resistance and transmittance measurements were combined to produce σ_{dc}: σ_{OP} ratios for the slow and fast filtered films to allow for a better comparison.

Table 4-5: σ_{dc}:σ_{OP} ratio calculations for slow and fast filtered films of similar %T. Sheet resistance values calculated after a thionyl chloride dope.

	$\%T_{(450-800)}$	*$\%T_{(550)}$*	*Sheet resistance after thionyl chloride doping (Ω)*	*σ_{dc}: σ_{OP} ratio*
Slow Films	95%	95.3	2240 ± 1760	0.081953
Slow Films	97%	97.9	2870 ± 930	0.064665
Fast Films	85%	84.7	3930 ± 960	0.043994
Fast Films	95%	97.9	4300 ± 151	0.043187

Table 4-5 shows a different result to Table 4-2, with the slow-filtered films producing higher σ_{dc}: σ_{OP} ratios than the fast-filtered films. Both fast-filtered films produced σ_{dc}: σ_{OP} ratios significantly lower than the thicker fast-filtered films in Table 4-2. This indicates that the slow filtered films were superior thin conductive films to the fast filtered films. Thus, it appears that when the SWCNT films produced are very thin (>90 %T) slow filtered films outperform fast filtered films.

4.9 Polarised Raman Spectroscopy

In the work by He *et al.*[188] polarised Raman spectroscopy was used to quantify the degree of alignment within slow filtered SWCNT films. By varying the polarisation of the incident laser and the detector between horizontal and vertical, the intensity of the characteristic SWCNT peaks would vary wildly depending on whether the laser/detector were polarised perpendicular or parallel to the CNT alignment direction. This technique was attempted with one slow filtered SWCNT film and one fast filtered SWCNT film. However, the Raman setup used was unable to polarise the incident laser vertically. Thus, the incident laser polarisation was kept horizontally polarised. Three spectra were taken with a non polarised, horizontally polarised, and vertically polarised detector. This compromise meant that a quantitative measurement of film alignment could not be determined, but a qualitative observation of the change in peak intensity with polarisation could be performed. It was observed

that the spectra would shift significantly in intensity when repeated scans at the same location were performed. To account for this 25 spectra were produced and averaged over a 5 x 5 grid with each spectra produced from two separate scans. An averaged spectrum was produced for the slow filtered film and the fast filtered film. Additionally a spectrum was produced for the slow filtered film turned 45° to see the effect of changing any possible alignment plane relative to the detector polarisation plane.

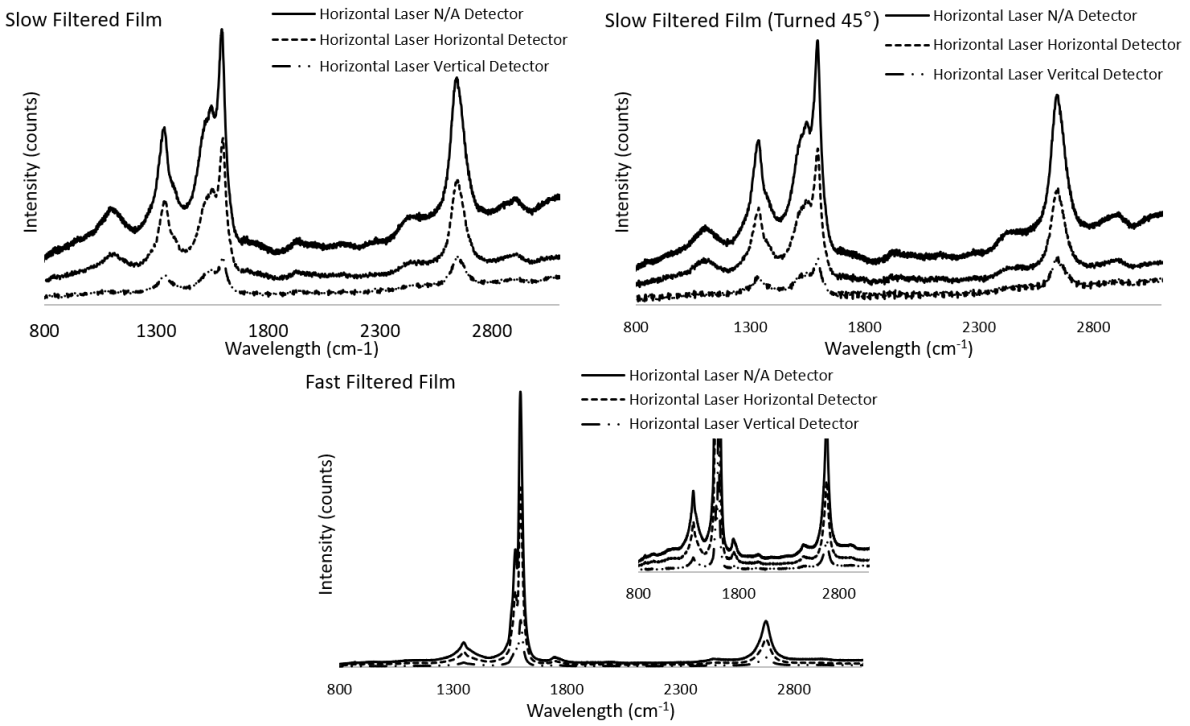

Figure 4-20: Raman spectra with different detector polarisation for slow filtered and fast filtered films. These spectra show the characteristic D (1340 cm^{-1}), G (1600 cm^{-1}), and G' (2700 cm^{-1}) peaks for SWCNTs.[53, 175]

Figure 4-20 shows the Raman spectra of both films with different polarisations. As well as the characteristic D, G, and G' peaks, smaller peaks are visible at around 1000 cm^{-1}, 2400 cm^{-1}, and 2900 cm^{-1}. The 2400 cm^{-1} peak may be due to highly oriented pyrolytic graphene, which displays a small peak at 2400 cm^{-1},[193] whilst the 2900 cm^{-1} peak may be due to a G + D peak.[194] The presence of these peaks indicates that there are graphene-like structures in the SWCNT film. Glass microscope slides display a peak at a little over 1000 cm^{-1} when a 532 nm laser is used[195] (as was used here) thus this peak is likely caused by the glass substrates. Glass can also show a small peak at 2400 cm^{-1} which may also be the cause of the 2400 cm^{-1} peak in Figure 4-20. The relative difference in intensity

between the slow filtered and fast filtered spectra is due to the difference in film thickness. The peak intensity of the slow filtered SWCNT film changes significantly with polarisation, as expected from He *et al*.[188]. However, there is also a significant drop in peak intensity observed for the fast filtered SWCNT film. To quantify the peak intensity change, the ratios between peak heights for the non polarised spectra and the peak heights for polarised spectra were calculated and tabulated in Table 4-6.

Table 4-6: G and D peak intensities for each polarisation method for each film. The ratios were calculated compared to the peak with no detector polarisation.

	Slow Filtered			*Slow Filtered (45°)*			*Fast Filtered*		
Detector Polarisation	Non Polarised	Horizontal	Vertical	Non Polarised	Horizontal	Vertical	Non Polarised	Horizontal	Vertical
G Peak Counts	241	143	40.9	230	133	38.9	3270	2120	539
G Peak Ratio	1	**0.593**	**0.170**	1	**0.578**	**0.169**	1	**0.647**	**0.165**
D Peak Counts	155	91.5	26.7	143	85.3	26.0	276	166	48.9
D Peak Ratio	1	**0.589**	**0.172**	1	**0.596**	**0.182**	1	**0.603**	**0.178**

Table 4-6 clearly shows that the relative peak intensities for different detector polarisation were virtually identical for the slow filtered and fast filtered SWCNT films. This indicates that either there is no difference in SWCNT alignment between the films or that the polarisation changes performed were not able to distinguish SWCNT alignment. SEM images of slow filtered CNT films vs fast filtered CNT films did not show clear alignment in slow filtered films (Figure 4-13 and Figure 4-14) so it is most likely that there is little alignment for the slow filtered SWCNT film.

4.10 Conclusion

It was determined that the slow filtration method could produce CNT films which were well organised on the microscale when compared to regular CNT filtration methods. Although there was no clear and consistent improvement in CNT alignment using slow filtration, this improvement produced films that were smoother and more highly organised on the microscale. However, on the macroscale, films produced via the slow filtration method were less organised than with standard filtration methods with small areas of high CNT density surrounded by larger areas of low CNT density. Fast filtered films,

on the other hand were homogeneous on the macro-scale to the naked eye. It is conceivable that some degree of stirring during gravity filtration would help to alleviate this issue. However, this also may decrease the benefits seen on the microscale for slow filtration as it could disrupt the natural ordering of the CNTs in suspension. Alternatively, the use of a controllable low vacuum system instead of gravity filtration may lead to improved macroscale homogeneity.

It was seen that, slow filtered SWCNT films did allow for the production of CNT/Si devices that performed at a similar level despite a thinner film (increased transmittance) being applied. This indicates that the smooth nature of the films allows for an improved CNT-Si contact and improved charge production and extraction capability despite a thinner film being used. The slow filtered SWCNT films were found to produce superior σ_{dc}: σ_{OP} ratios at high transmittance (> 90 %), indicating that very thin slow filtered SWCNT films are superior thin conductive films to very thin fast filtered SWCNT films.

CHAPTER 5 LARGE ACTIVE AREA DEVICES FABRICATION AND OPTIMISATION

5.1 Introduction

An important consideration for the CNT/Si heterojunction device design is that, in the vast majority of research, very small active areas are used, with most being below 1 cm^2.[14] In particular, the best published PCE for this device design was produced with an exceptionally tiny active area of less than 1 mm^2.[14, 16] Whilst small area devices are useful for determining the mechanisms behind the device and experimenting with architectural differences, it is important to examine the effect of scaling up the device active area to a point that could be applied in industry. Some work has been done on scaling up the active area over the past few years. Work done by Xu *et al*.[135] fabricating devices with active areas in excess of 2 cm^2 with thick lines of CNTs crossing the device to assist in photocurrent extraction whilst Li *et al.*[99] used silver nanowires on their upscaled active area devices. The work in this chapter will see the active area of the device increased from 0.09 cm^2 to 2.25 cm^2. The increased active area device will be fabricated and tested both with and without a top surface grid to assist in photocurrent extraction. The limitations imposed by the increase in area will be probed and a new back contact will be formulated compared to that previously used by this research group. Additionally, modifications to the top contact and the use of a new filtration membrane will be investigated. Some of the issues with a larger active area have already been investigated in Section 2.2.2.

5.2 Design

The initial large area device design consisted of a simple upscaling of the same design principle used in the previous chapters. The active area shape was changed from a circle to a square to make more efficient use of the silicon wafer, as the wafers were cut with a straight-line diamond cutter. The active area of the design was 1.5 cm × 1.5 cm giving an active area of 2.25 cm^2. This is three orders of magnitude larger than the devices previously discussed in this thesis, which had an area of 0.074 cm^2. These devices were fabricated following the same process and silicon wafers as previously used (Section 2.1.5). Fabricating the larger active area devices was simple as there was no change required

to the photolithographic recipe. However, the large area devices were produced on the wafer scale and a mask aligner was used to expose the photoresist rather than a UV torch (Section 2.1.5.1).

It was assumed that the sheet resistance of the CNT film would have a significantly increased effect on the performance of the CNT/Si solar device as the active area is increased, given the film would be required to transport charge carriers across a larger distance. Thus, it was decided that a metallic grid across the front contact of the large active area device would be required to assist in charge carrier removal by decreasing the transport distance of the CNTs alone. The design of the gold grid system on CNT/Si devices was rigorously tested with small active areas (0.04 cm^2 – 0.09 cm^2).[136] The optimal grid line, width, and pitch found for a square 0.09 cm^2 device were taken and applied to the 2.25 cm^2 design. It is worth stating that, as devices with larger areas will produce more current the optimal grid parameters will be different. However, they are a good starting point. In all, two new designs were produced, one with and one without a top contact grid network. The grid design consisted of lines with a thickness of 40 µm, spaced evenly at 520 µm apart (Figure 5-1). Overall, this grid array produced a device structure consisting of 676 squares of 540 × 540 μm^2, 25 squares of 540 × 400 μm^2, 25 squares of 460 × 540 μm^2, and 1 square of 460 × 400 μm^2. The total active area of the devices was 2.25 cm^2 including grid lines. The exposed silicon area of the devices (total active area – gold grid area) was 2.089 cm^2. However, convention dictates that the total area including the grid design be used when calculating device properties.

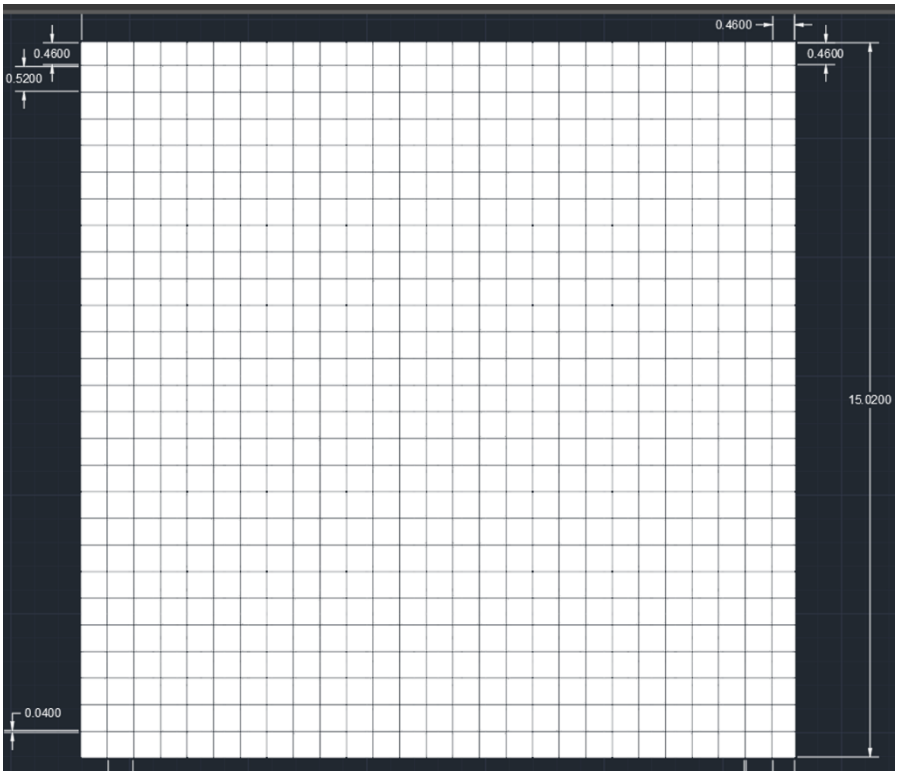

Figure 5-1: Schematic of the large active area device design. White areas are silicon and blue lines are gold grid lines, all measurements are in mm.

In addition to scaling up the silicon/gold substrate, the CNT film had to also be increased in size to cover the larger active area. The vacuum filtration set up easily accommodated an increased template size. Initially, a square film template of 2 cm × 2 cm was made to fit over the 1.5 cm × 1.5 cm active area. A square film was used to reduce the amount of CNTs that would be required to make each film. However, the square film proved difficult to align on device substrates when flotation attachment was performed (Section 2.1.3.2). Thus, the square film was replaced by a circular template with a diameter of 2.5 cm as a circular film could cover the active area regardless of orientation. The main issue encountered with using larger area films is that the structural integrity of the film decreases as the area increases. Additionally, the larger area increased the likelihood of air bubbles forming under the film during heat/press attachment. These air bubbles could lead to ruptures in the film, forming small holes. In order to decrease the likelihood of these events, films were fabricated with transmittances between 50 % and 60 % (instead of the optimal 70 %) as this increased the lateral strength of the film. The flotation attachment method significantly reduced the chance of trapped air bubbles forming. However, the lateral strength of the film was still important to avoid ripping during solvent transfer.

Films produced with a transmittance of 70 % or higher were prone to rip apart when the solvent was changed from acetone to water as this step confers a large amount of kinetic energy to the film. The flotation attachment method requires CNT suspensions with graphene oxide (GO) added at a ratio of 2.25:1 CNT:GO. For the remainder of this thesis all films were produced from CNT/GO suspensions.

An effort was made, during large active area device experimentation, to optimise and standerdise various aspects of the device fabrication process. The next three sections cover the design and implementation of an alternative back contact, the optimization of the thickness of the front contact and the optimization of the time allowed for silicon oxide growth post BOE etching.

5.3 New Back Contact Design

For the small area devices studied in Chapters 3 and 4, the back contact was created by manually scratching the pre-grown 100 nm oxide from the back of the silicon wafer using a diamond tipped scribe. A gallium-indium eutectic (eGaIn) was applied to form a contact between the exposed silicon and a steel plate to form the back contact. This method worked well on the small area devices but did introduce some variability into device performance. Additionally, the eGaIn had adhesive properties which was useful to hold the substrate and steel together. This adhesive effect was less pronounced on the large area devices as the amount of eGaIn required to stick the larger substrate to the steel increased. Additionally, due to the higher aspect ratio of length and width to height of the large area silicon substrates the manual scratching step was no longer as viable. The brittle nature of the <100> silicon wafers used gave the devices a tendency to snap due to the force applied by the diamond-tipped scribe. Additionally, the previously used back contact did not lend itself well to large scale production as each substrate had to be individually scored with the diamond-tipped scribe. The eGaIn/steel devices were also multi part where as substrates with the new back contact were one piece. These issues, coupled with the poor reproducibility of the manual scratching step, lead to the design of a new, more uniformly applicable back contact.

The new back contact formation method proposed was to fully etch the 100 nm oxide off the back of the wafer using buffered oxide etch (BOE: 9:1 ammonium fluoride: hydrofluoric acid) and thermally evaporate a layer of aluminium followed by an annealing step. Aluminium was chosen for the back contact as this has been used in similar cell research, first by Li *et al*.[96] and by other groups since.[14, 76, 103, 196, 197] Aluminium is preferable in this case over a Cr/Au layer (as is used on the front contact) as devices with Cr/Au back contacts have been shown to have significantly degraded FF at illuminations around 1 Sun.[14] In addition, it is known from research in silicon solar cells that SiO_2/Al as a rear contact reflects near-bandgap photons, improving the light absorption in the silicon.[198] This back-contact design allowed substrates to be prepared for CNT film attachment on the wafer scale, reducing processing time. It is worth noting that the difference in oxide removal carried out on the back of the silicon could affect charge carrier extraction. The BOE etch removes the entirety (or close to) of the 100 nm silicon oxide layer on the back of the wafer, where-as the manual scratch removes a vastly smaller amount of oxide. The loss of a greater amount of the surface passivating oxide layer may serve to increase the amount of carrier recombination due to dangling bonds, contaminants and lattice mismatch.[14] Increased recombination may lead to reductions in V_{oc}, J_{sc}, and FF,[14] although these effects were not observed in previous reports.[95, 98, 199] To address this, an experiment was performed where silicon wafers were left in atmosphere for different time periods after etching to determine the effect of the growth of a thin, atmospheric silicon oxide layer. In addition to this, the annealing temperature and time were varied between 250 ˚C and 300 ˚C and 25 min and 30 min respectively. The annealing step is important as it allows a thin Al_2O_3 layer to grow between the Al and Si, passivating the silicon surface.[14, 198] This is achieved at low temperatures (for metal annealing) hence the decision to use 250 ˚C and 300 ˚C temperatures.[14] A 250 °C annealing temperature has been previously used for aluminium back contacts in CNT/Si devices by Harris *et al*.[98] Lastly, the importance of a gold capping layer (as protection against aluminium oxidation) was investigated.

The change in back contact material is not expected to have much effect on the operation of the devices in terms of energy levels. The work function of eGaIn is 4.1 eV – 4.2 eV[200] compared to the work function of aluminium of approximately 4.25 eV.[201] This is compared to the work function of the phosphorous doped silicon of 4.26 eV (Resistivity 1 -5 Ω cm, carrier density 6 x 10^{15} – 1 x 10^{15} cm^{-3}).

To investigate the effect of the thickness of the silicon oxide layer between the silicon substrate and the evaporated aluminium contact 3 batches of 6 devices were fabricated (in all examples in this work the device architecture consisted of an active area of 1.5 cm × 1.5 cm - 2.25 cm^2 with no top contact grid network unless otherwise specified). Each batch had the rear oxide removed and was left in atmospheric conditions for 15 min, 40 min, or 70 min before being stored in a nitrogen environment. The back side of the silicon wafer was then coated with a layer of aluminium 250 nm thick and a 25 nm thick layer of gold before being annealed for 30 minutes at 300 ˚C. The devices from each batch were compared to determine the effect of silicon oxide regrowth.

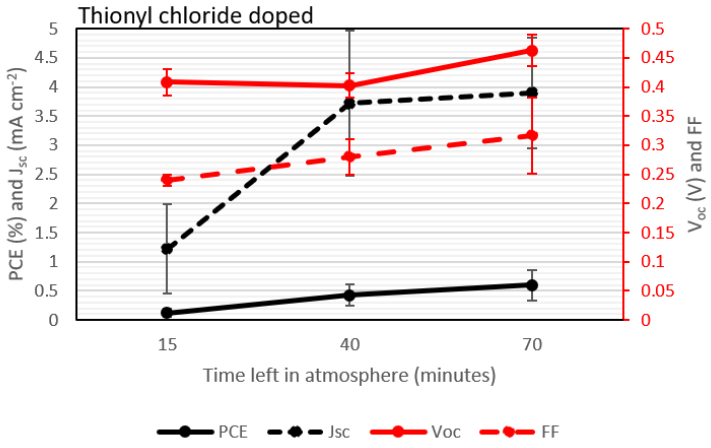

Figure 5-2: J/V properties for large area devices with different time periods between BOE etch and Al layer evaporation.

Figure 5-2 shows the averaged device data for each batch of devices after thionyl chloride doping. It is apparent that the device efficiency improves with oxide regrowth time, with the longest exposed samples producing the highest efficiencies. The trends seen for each of the parameters show an increase with oxide growth time, with the J_{sc} displaying a sharp increase from 15 to 40 minutes and the V_{oc} increasing from 40 to 70 mins. Overall, the data shows that the improved efficiency of the 70 mins samples is likely due to a combination of improvement in, J_{SC}, V_{oc}, and FF. This indicates that the

presence of a silicon oxide layer is beneficial to the device performance. This may indicate that the silicon oxide layer is required to passivate the surface prior to aluminium coating. Additionally, the improvement may be due to improved adhesion between the aluminium layer and the silicon as, it is known that evaporated aluminium will form an interphase consisting of Al-O-Si bonds which results in strong adhesion[202] and thus may improve surface passivation. Surface passivation in this case refers to the removal of dangling bonds on the surface of the silicon which create additional energy levels which assist in carrier recombination.[203] Thus, passivation lowers recombination at the surface and improves device properties PCE and J_{sc} values are low when compared to the small area device due to the use of device substrates with no top metal grid in this experiment.

As the PCE of the devices in Figure 5-2 was still rising at the longest oxide regrowth time the experiment was performed again, this time with no 15 min data point but with a larger range from 40 min to 180 min. For this experiment and for the following two experiments (Figure 5-3, Figure 5-9, and Figure 5-11) titanium was used as the adhesion layer between the silicon and the gold layer on the front contact of the devices. The reason for this was a temporary lack of chromium. The titanium was expected to function similarly to the chromium and, as the same material was used across the following experiments a comparative study was still valid. However, it became apparent that the heating needed to anneal the aluminium back contact damaged the titanium and caused ruptures in the gold top contact which served to decrease the consistency between devices. These ruptures became noticeable during wet chemical treatment as some areas of the gold pattern became ‘bubbly’ and sections of the gold would occasionally come loose from the device surface during the final 2 % HF treatments.

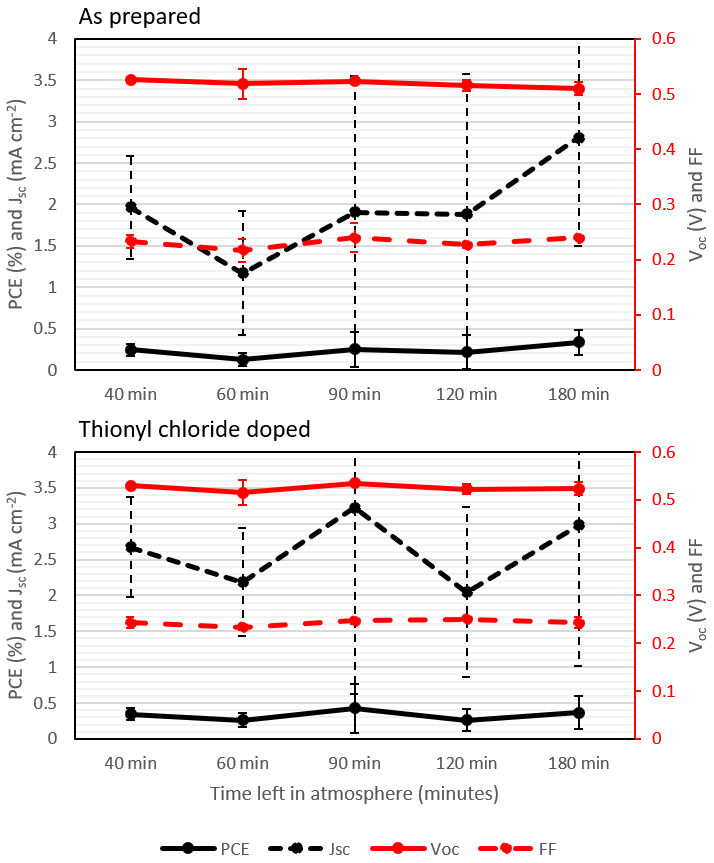

Figure 5-3: J/V properties for large area devices with extended back contact oxide regrowth times.

Figure 5-3 shows the device data for an extended range of oxide regrowth times. Prior to thionyl chloride doping, there appears to be an increase in PCE with time due to an increase in J_{sc}. However, the values from the 90 min to 180 min data points are all within error value of each other. After doping, the trend flattens out with a local maximum visible at the 90 min mark, although these values are within error value of each other. There is also a slight peak in the V_{oc} visible for the 90 min devices with this point roughly 0.01 V higher than the 60 min, 120 min, and 180 min devices.

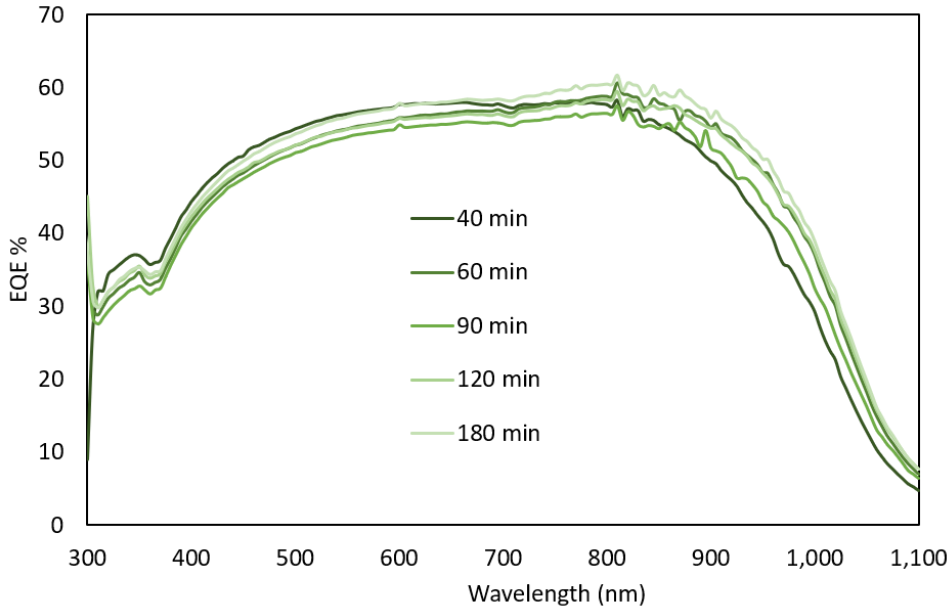

Figure 5-4: EQE data for the best performing device for each back-contact oxide regrowth time.

Whilst the devices were illuminated from the front side, IPCE data with different back contact oxide thickness (Figure 5-4) is still important to consider. This is because the absorption of light through silicon decreases significantly at higher wavelengths (Figure 5-5).[127] The light that passes through the silicon can be reflected at the back contact and be absorbed in the silicon as it passes back through. Figure 5-4 shows that there was a change in photon absorption at higher wavelengths with a change in regrowth time. The 40 min sample displayed the highest EQE % up until around 600 nm. There is then a relatively sharp drop in IPCE compared to the other samples. By around 900 nm the 40 mins sample is roughly 5% less than the 180 min sample and roughly 10 % less by around 950 nm. The EQE values at 900 nm were plotted against oxide regrowth time to observe any trend present.

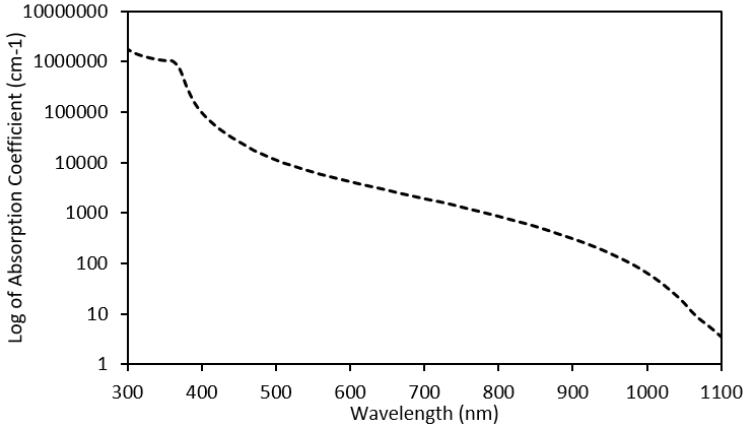

Figure 5-5: Absorption Spectrum of Silicon.[127]

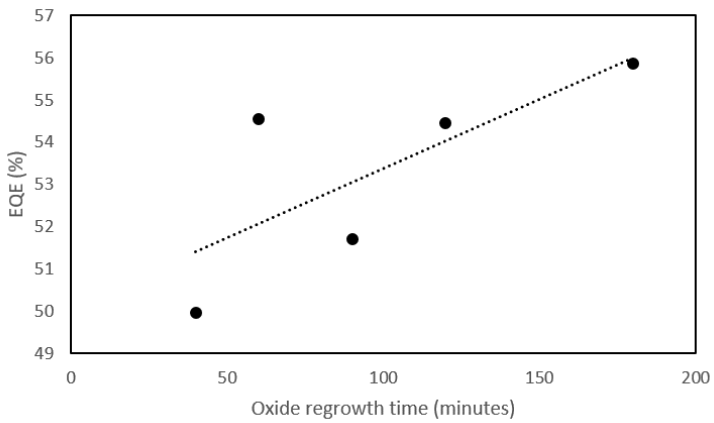

Figure 5-6: EQE at 900 nm plotted against back contact oxide regrowth time. With a linear trend line fitted.

Figure 5-6 shows an upward trend in EQE with increasing oxide regrowth time. This indicates that, as silicon oxide thickness increases on the back contact, an increasing number of high wavelength photons are reflected back into the silicon to be absorbed to produce excitons. Whilst the linear trend only has an R^2 value of 0.56 there is a clear upward trend in EQE with increasing oxide regrowth time.

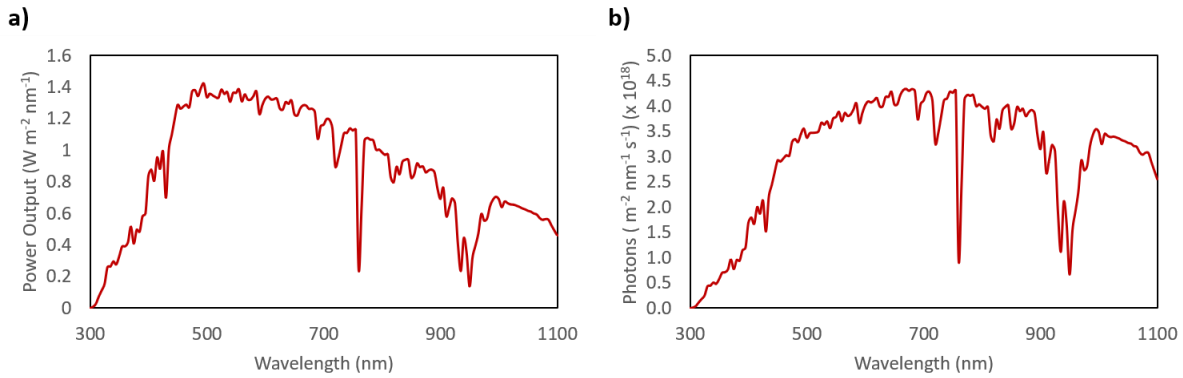

Figure 5-7: The AM 1.5 solar intensity spectrum in terms of: a) power, and b) photons.[127, 204]

The EQE data shown in Figure 5-4 is based on a light that gives equal intensity at different wavelengths. The solar spectrum is not homogeneous across wavelengths as can be seen in Figure 5-7**.** Thus, certain regions of the EQE spectrum are more important as they correspond to regions of higher intensity in the solar spectrum. The solar spectrum in Figure 5-7 a) is the general form and is a function of power per unit area per nm versus wavelength. However, this is not useful for comparing with solar EQE data as, provided they are absorbed, each photon will produce one exciton, regardless of power. Thus, the plot was converted to be a function of photon count versus wavelength by dividing the power output

by the energy of the photon at each wavelength (Figure 5-7 b). The EQE values were multiplied by the solar intensity in terms of photon count (Figure 5-7 b) from 300 nm – 1100 nm.

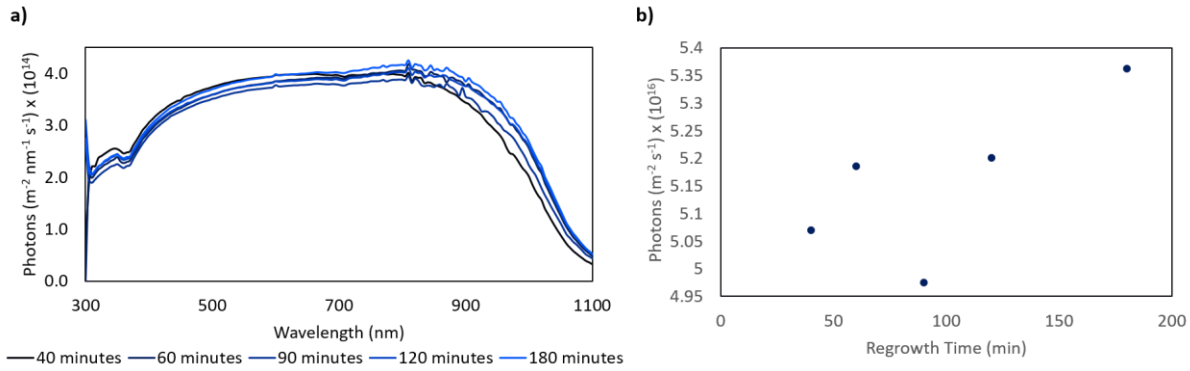

Figure 5-8: a) EQE data multiplied by solar photon intensity for each regrowth time, b) total photon count per m² per s for each regrowth time.

Figure 5-8 a) shows that the solar photon intensity spectrum multiplied by EQE closely matches the EQE spectra for each regrowth time. Thus, whilst the 40 min sample absorbs the most photons from 300 nm to 600 nm, it also absorbs the least from 800 nm to 1100 nm. The total photons per m^2 per s was summed for each time sample and plotted in Figure 5-8 b). This plot shows that the total number of photons per m^2 per s was between 5 x 10^{16} photons m^{-2} s^{-1} and 5.4 x 10^{16} m^{-2} s^{-1} with the lowest point being the 90 min sample and the highest being the 180 min sample. The 40 min sample, which displayed the most varied spectrum in Figure 5-8 a), did not absorb significantly more, or less, photons per m^2 per s than the other samples. Overall, there is little difference between the samples in terms of photon absorption per m^2 per s.

From the data presented here, it is apparent that there is little significant difference in performance with the regrowth times tested. Morita *et al*. investigated the growth rate of silicon oxide in ambient conditions and determined that a 2 Å - 3 Å jump in thickness occurs between 200 min and 1000 min. However, before this jump the oxide thickness is relatively stable at 2 Å.[205] Thus, the lack of large differences between device performance at the times measured may be because the oxide thickness change is negligible. It is assumed that with longer regrowth times a decrease in device performance would be seen as the oxide thickness would increase enough to reduce current flow.

90 min was chosen for use in future devices in this thesis. This was to ensure a long enough time to ensure a SiO_x layer was present whilst not being so long as to disrupt overall manufacturing time. Additionally, the average PCE of devices with a 90 min regrowth time was higher than the average PCEs for the shorter regrowth times and there was a slight downwards trend in V_{oc} from the 90 min point.

5.3.1 Gold cap on aluminium contact.

The use of a gold capping layer to prevent significant aluminium oxidation during device processing was investigated. To investigate the effect of a 25 nm gold capping layer on the aluminium back contact an experiment was performed in which 4 batches of 3 devices were produced from the same wafer either with or without this layer. One batch of each of these pairs was annealed at 300 ˚C for 30 min and the other was annealed at 250 ˚C for 25 min. These devices were tested as per the above experiments.

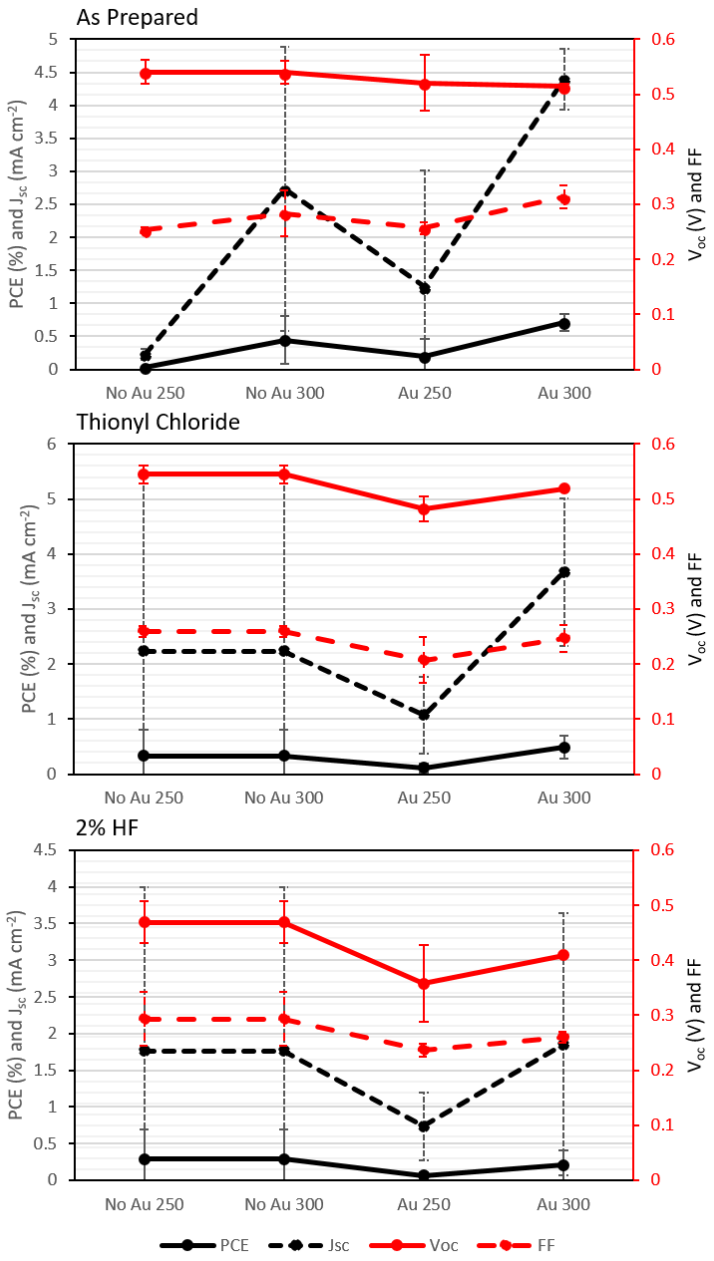

Figure 5-9: J/V properties for comparison between gold layer and annealing times at three different treatment stages.

Figure 5-9 shows the averaged device data for the three devices in each batch. The general performance of the devices decreases with treatment, as too does the J_{sc} consistency between devices, especially for the two batches with no gold layer producing very high error margins when the devices were averaged. This degradation in consistency is due to the issues based around the titanium adhesion layer as discussed for Figure 5-3.

As all the devices were produced from the same substrate and the V_{oc} and FF properties seem largely unaffected, it was concluded that the data still provides a useful comparison. There are some

important trends to observe. Firstly, the devices with no gold layer generally produced higher open circuit voltages, especially after the treatment steps. Based on previous reports, It is highly likely that alloying of the gold and aluminium layers is occurring at the interface even prior to annealing.[206] Belser determined that the minimum alloy temperature for two evaporated layers of aluminium and gold was 90 °C although they also state that alloying had occurred in samples not exposed to heat and possibly during the deposition process itself.[206] Weaver and Brown investigated the diffusion of atoms in gold-aluminium layers and determined that the time of diffusion for a 70 nm gold layer was roughly 100 min at 84 °C and also determined that the time of diffusion for a 262 nm gold film was 15 hr at the same temperature but only 4 min at 164 °C. Thus, at 250 °C – 300 °C for a 25 nm thick film it can be expected that diffusion will occur. The diffusion is characterised by a change in light reflectivity as phase boundaries within the layers move due to the formation and growth of an Au_2Al layer. However, the presence of other Au_xAl_y alloys is expected but in small amounts.[207] This explains visual observations of the Al/Au film rapidly changing colour as annealing began. In aluminium films with no gold cap it is expected that a 1.5 nm – 2 nm layer of aluminium oxide (Al_2O_3) virtually instantaneously once exposed to oxygen.[208] Thus, it is clear that for both structures (with or without a gold cap) the electrical structure is not as simple as Au/Al/Si or Al/Si as there will be other materials present. The superior V_{oc} of devices with no gold cap indicates that the Al/Si structure is preferable.

A higher annealing temperature is favourable for good device results, particularly for the devices with a gold cap. This may be because the annealing step helps to restructure the crystal lattice of the metal which is important as the evaporation deposition step likely does not create a highly ordered crystal structure. Semaltianos found that slowly evaporated aluminium films (the films in this thesis were evaporated at a slow rate of approximately 2 Å s^{-1}) consist of a grainy structure and the size of the grains increase with film thickness.[209] Additionally, the increase in annealing temperature may serve to better passivate the silicon at the Al/Si interface and thus prevent recombination.[14]

It is difficult from this data to ascertain which recipe is optimal for use in future production due to the large variations in some data points. However, it seems that the higher temperature anneal is preferable. It also appears that no gold cap is required as the V_{oc} and FF are higher (especially post treatment) than those samples with a gold cap. Although the average J_{sc} is highest for the gold capped 300 ˚C, the error bars show that the highest J_{sc} values were achieved with individual non-capped devices. Thus, for future experiments, a 300 ˚C anneal for 30 minutes was performed and no gold cap was added. Interestingly, after thionyl chloride wet treatment discoloration of the aluminium film is observable whereas the same discolouration is lessened or not visible at all with the gold layer in place see Figure 5-10.

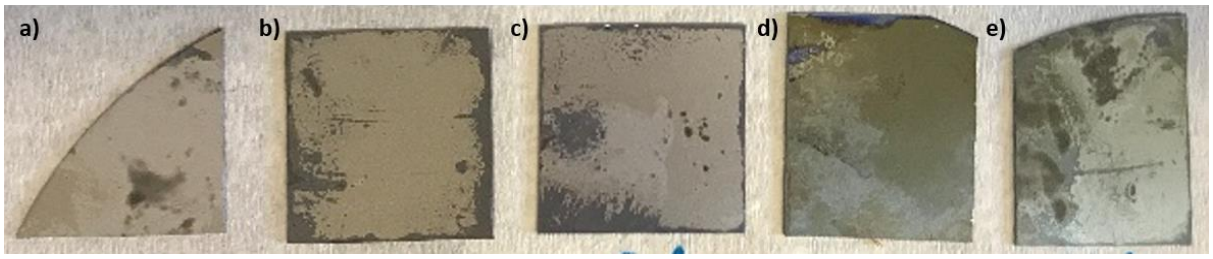

Figure 5-10: Back metal contacts: a) aluminium layer before chemical treatment, b) aluminium layer 250 degree annealing after thionyl chloride chemical treatment, c) aluminium film annealed at 300 degrees after thionyl chloride chemical treatment, d) aluminium/gold film annealed at 250 degrees after chemical treatment, and e) aluminium/gold film annealed at 300 degrees after chemical treatment.

In order to directly compare devices with fully oxide etched, evaporated aluminium back contacts and devices with scratched oxide, eGaIn/steel back contacts, three devices were made with the same architecture. Note, the wafer used in this experiment had experienced the same titanium adhesion layer issues as discussed for Figure 5-3 and Figure 5-9. However, as no annealing step was required when the eGaIn/Steel back contact was used the gold bubbling effect was not observed. Thus, the data in Figure 5-11 is more consistent.

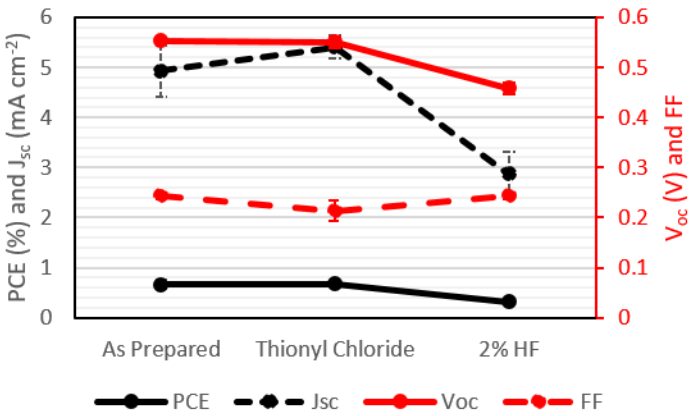

Figure 5-11: J/V properties for individual devices and overall average for devices with a manually scratched/eGaIn/steel contact.

Overall, the properties are similar to those of the devices with an aluminium back contact, indicating that there are no losses in performance, to offset the gains in fabrication time and consistency that the aluminium method brings. The best performing device from this batch had a PCE of 0.76 % where as the best performing aluminium device was 0.82 %. Whilst the J_{sc} values achieved for the eGaIn/Steel devices are higher than the averages in the aluminium back contact experiment (an average of 5.41 mA cm^{-2} after $SOCl_2$ doping compared to an average of 3.25 mA cm^{-2} after doping), they are approximately the same as the best performing aluminium device (5.99 mA cm^{-2}). Thus, it seems unlikely that there is a significant J_{sc} difference between the back-contact designs, when the variation issue due to the titanium adhesion layer is considered.

5.3.2 Light Source Power with different back contact architectures

The AM1.5 light source used throughout this thesis does not provide a spot size large enough to cover the entire active area of the large area CNT/Si heterojunction device at the same intensity as was used for small area cells previously in this thesis (100 mW cm^{-2}). For the previous experiments in this chapter the light source was raised to produce a larger spot size. However, this led to a lower intensity. For the back-contact comparative studies the decrease in power caused by the lower intensity light source was not adjusted for as a comparison between devices was all that was required. To further analyse the optimal spot size for large device analysis a set of devices were tested, with treatment, at a range of power output percentages in increments of 10 % from 10 % to 100 %, three types of back contact were also used in this experiment, aluminium, aluminium with gold, and eGaIn/steel.

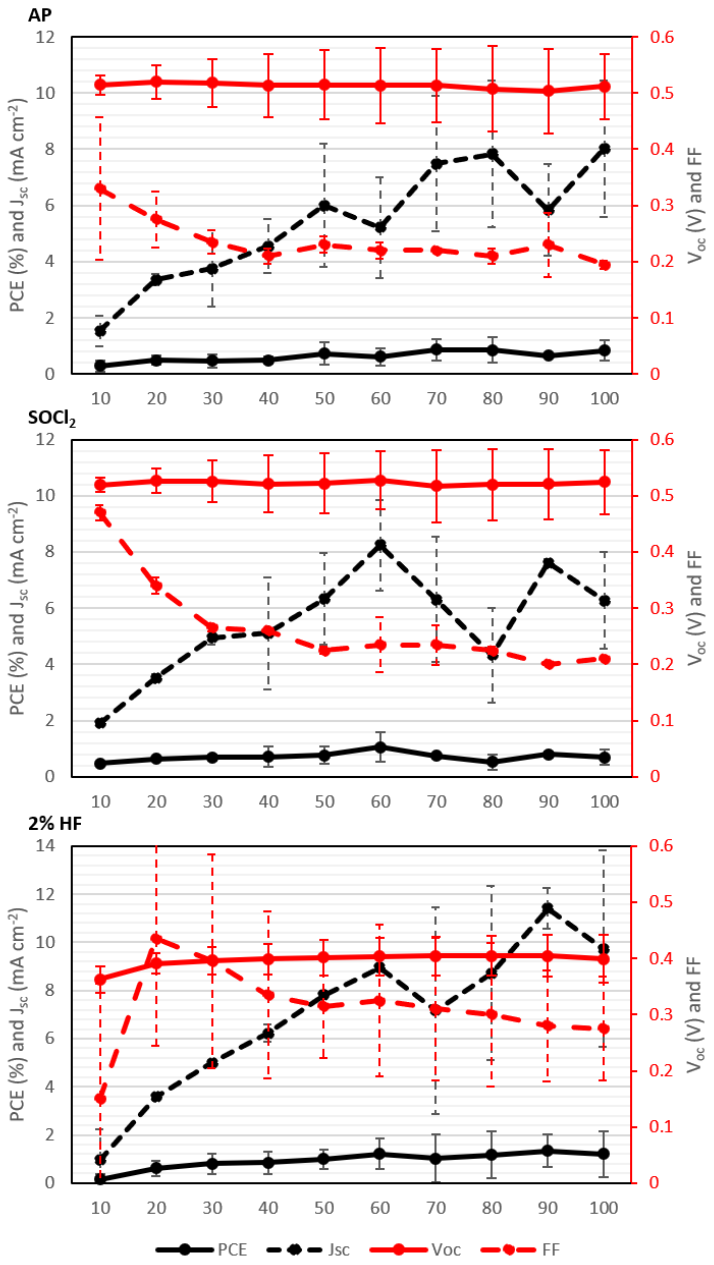

Figure 5-12: J/V properties with treatment for devices with evaporated aluminium back contact

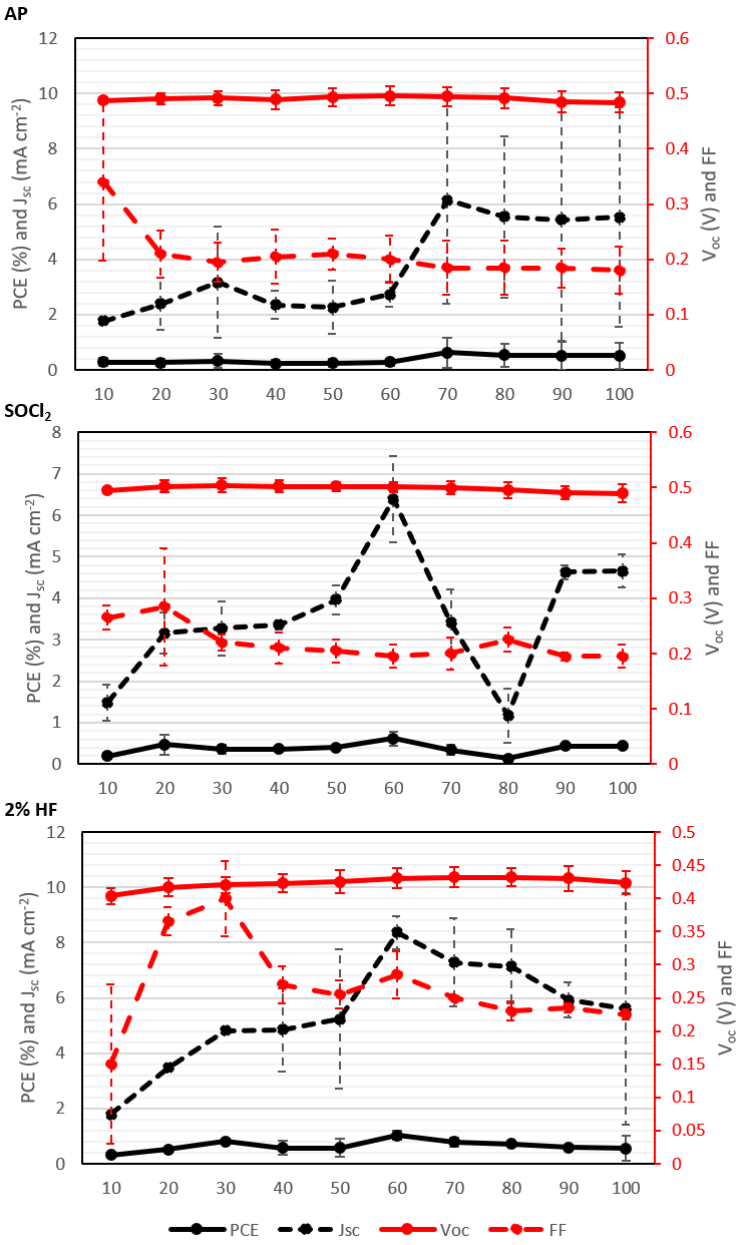

Figure 5-13: J/V properties with treatment for devices with evaporated aluminium contact with gold cap.

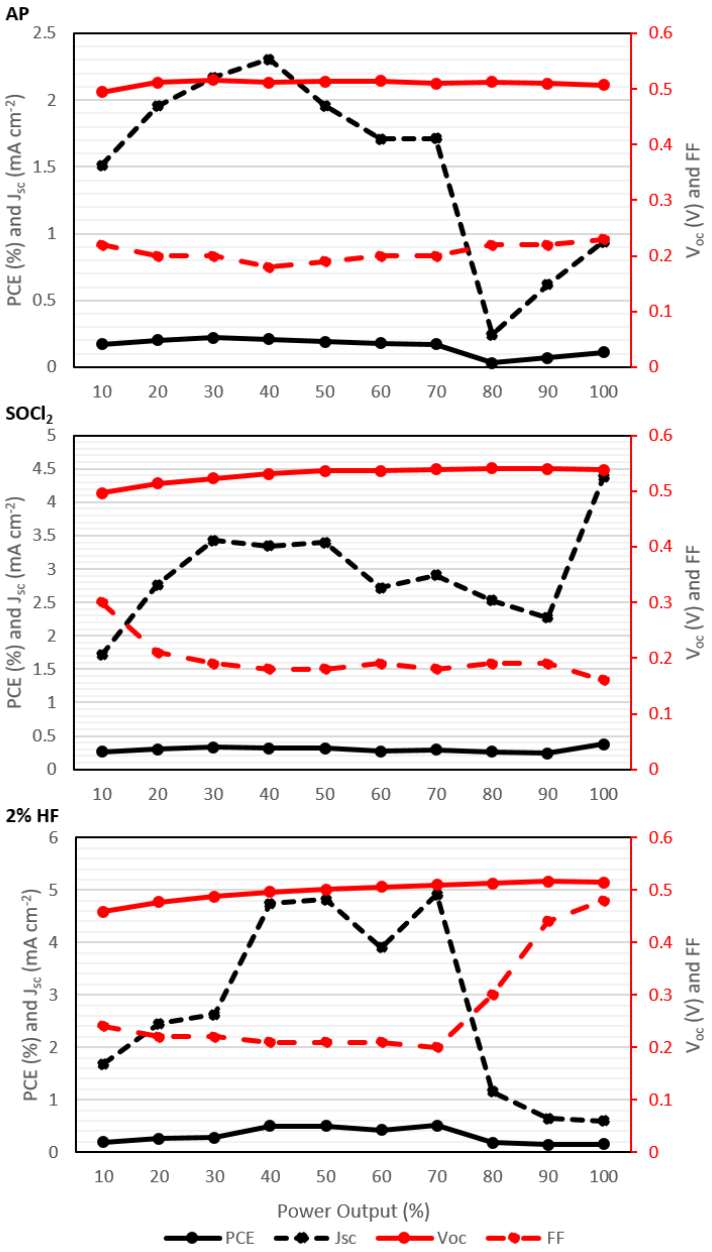

Figure 5-14: J/V properties with treatment for devices with an eGaIn/Steel back contact.

In general, from Figure 5-12, Figure 5-13, and Figure 5-14 a trend is observed for the PCE of a given device to increase with increasing light intensity, which is expected as an increase in photon incidence should correlate with an increase in photocurrent production. However, the increase stops at a point and tends to plateau at higher intensities. The reason for this is that at the higher intensities (around 70 %) the spot size is too small to cover the whole active area. Thus, whilst the covered areas benefit from an increase in photon intensity, uncovered areas will produce negligible current as only room lighting and stray light from the fringes of the lamp illuminated them. In the aluminium backed cases

this plateau appears to begin around the 60 % - 70 % point which corresponds visually with the point at which parts of the active area are no longer illuminated. In the case with an eGaIn/steel back contact (Figure 5-14), the plateau appears to occur earlier at around 40 % - 50 %. Followed by a decrease in performance up to 90 % and then a sudden increase at 100 %. It is notable that the sharpest decrease (from left to right) is from 70 % - 90 % which corresponds with the intensities at which the active area is not completely illuminated.

As is the case for most device data, the trend in PCE is often due to a trend in J_{sc}, with the J_{sc} increasing with light intensity in these experiments. For the devices with aluminium back contacts (Figure 5-13) the FF decreased with an increase in intensity. This indicates that, as more photocurrent was generated, the devices struggled to deal with it as efficiently. This increased charge carrier recombination at higher injection levels was most likely due to the lack of a grid pattern on the front contact. In all three back contact designs the FF dropped to a plateau of roughly between 0.2 and 0.3. The exception to this trend occurred with the eGaIn/steel back contact sample, where a significant increase in FF was observed at high intensity (80 % -100 %) after the 2 % HF etch. There was very little change in V_{oc} with increasing light intensity, suggesting that the Fermi level has been un-pinned from the injection level on the back junction and thus the assumed Al_2O_3 layer present between the aluminium film and the silicon has effectively passivated the surface.

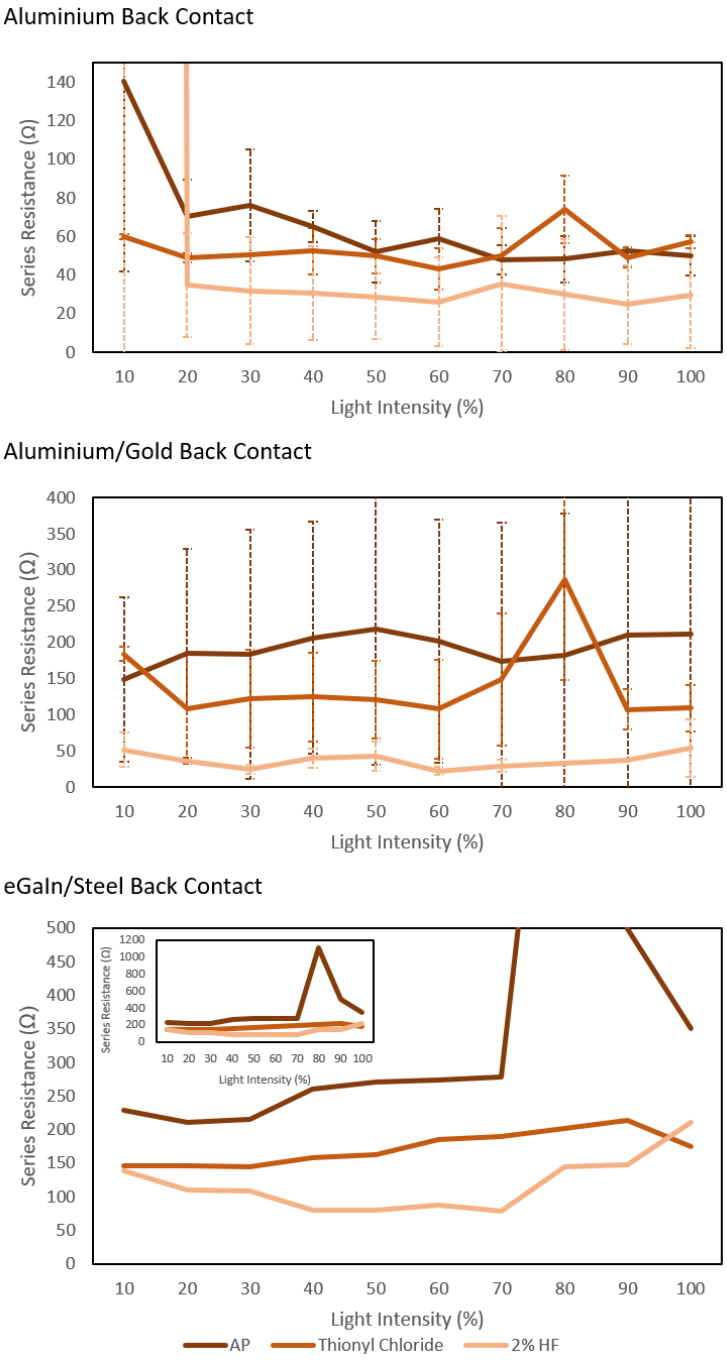

Figure 5-15: Series resistance for devices with different back contacts at a range of light intensities for each treatment step.

Figure 5-15 shows that there was a decrease in sheet resistance with $SOCl_2$ doping and 2% HF treatment. There is no clear trend in sheet resistance with light intensity.

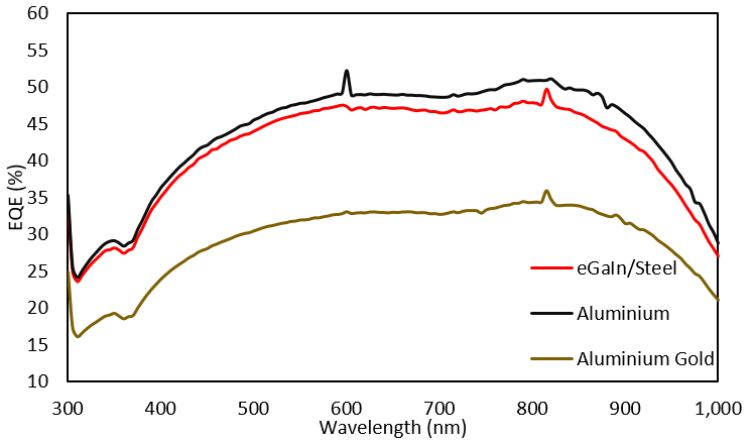

Figure 5-16: EQE spectra for three back contact architectures.

Figure 5-16 shows EQE data for each back contact design and appears to show similar shaped spectrum. However, it is difficult to compare the aluminium with gold cap spectrum as it is lower than the other two. To better compare the spectral shape the aluminium gold spectrum was offset to be at a similar level to the other two.

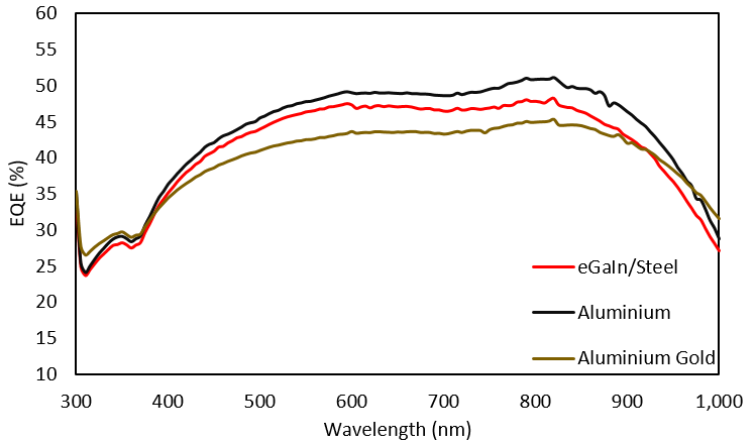

Figure 5-17: EQE spectra for three back contact architectures with the aluminium gold spectrum offset to compare shapes. Three outlier points have also been corrected.

By offsetting the aluminium gold spectrum Figure 5-17 shows a clear difference in shape between the eGaIn/steel and aluminium back contacts, and the aluminium gold back contact at higher wavelengths (800 nm – 1000 nm). Indicating that the presence of the gold capping layer is reflecting more light back through the substrate than the other two.

From the data shown it was deduced that both an aluminium back contact and an aluminium back contact with a thin gold cap are viable alternatives to the eGaIn/steel approach. However, most data showed a preference towards the design with no gold cap and, as the addition of the gold cap adds

processing time, complexity, and cost, it was decided to continue with a 300 nm aluminium back contact with a 30 min 300 ˚C anneal.

5.4 Top Contact Grid

In the experiment comparing device performance with and without a front grid the reduced intensity was adjusted for by multiplying by $\frac{100(\%)}{Power\ Output(\%)}$ where the power output was roughly 70 % in this case.

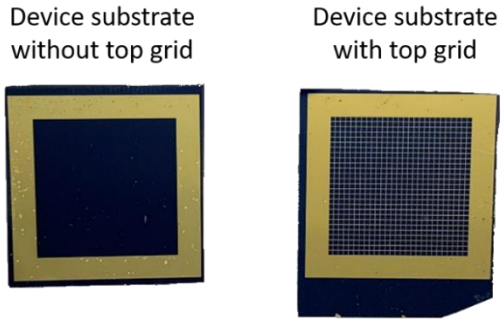

Figure 5-18: Optical images of device substrates with and without a top contact grid.

Up until this point large area devices were used with no front grid pattern. Whilst these devices allow for comparative studies to be done, the individual devices perform significantly worse than the small area devices. The large area devices displayed low PCE values barely exceeding 1 % which was largely attributable to J_{sc} results of less than 5 mA cm^{-2} compared to the expected small area J_{sc} of above 20 mA cm^{-2}. It is expected that the addition of the top contact grid pattern (see Figure 5-18) will enhance the performance of the large area CNT/Si device, as it will assist the CNT film in transporting charge carriers from the heterojunction to be collected. Although it is also worth noting that the addition of a grid will impact the actual area of CNT/Si heterojunction that can be illuminated by the AM1.5 source.

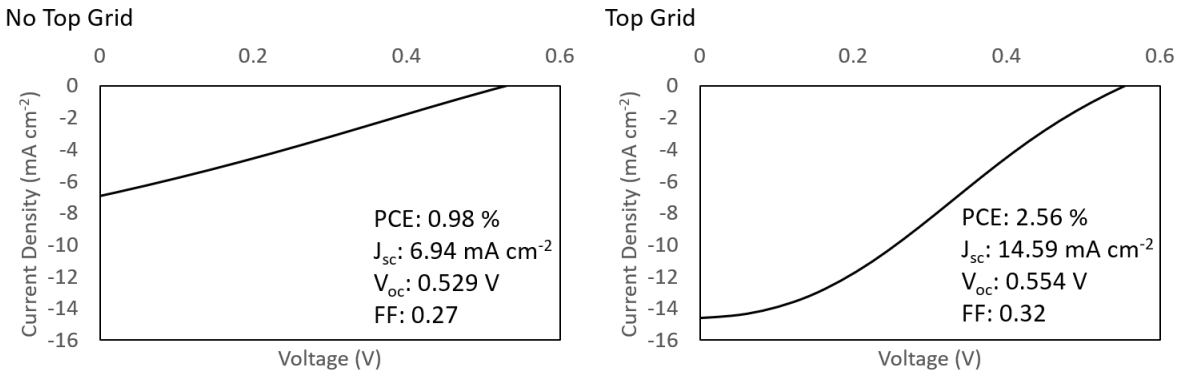

Figure 5-19: Initial device results with and without a top contact grid after thionyl chloride doping and a 2% HF etch. Note that these experiments were performed with a lower functioning lamp giving approximately 70% of the expected power.

It is clear from Figure 5-19 that the addition of the metal grid on the front contact of the device gives significantly better performance than with an open front. The PCE was roughly 2.5 times higher for the device with a grid pattern. This was due, in part, to a slight increase in V_{oc} and an 18 % increase in FF. However, the most significant change was in J_{sc} which more than doubled after the use of a top contact grid lattice. This is expected as the grid will assist the CNT film in transporting charge carriers and thus, will increase the amount of extracted charge carriers. Additionally, it was found that on some occasions the 2 % HF etch would lead to areas of the CNT film breaking from the surface on devices with no top contact grid. It was expected that this was due to the removal of the supporting oxide, reducing the CNT film contact with the substrate. This did not occur on the small area devices or on the large area devices with a grid lattice as the CNT film retained significant substrate contact thanks to the smaller areas it had to cover in between the grid lines. The accidental exfoliation of the CNT film from large area devices with no grid pattern allowed a comparison between large area devices with no grid with either a full CNT coverage or a CNT film with a large hole in the centre (see Figure 5-20). The devices that have large holes in the CNT/GO film in the centre of the active area do not perform significantly worse than devices with the film relatively intact. The parameters in Figure 5-20 are low in general as the performance of these devices suffered once the 2 % HF etch was performed, and it was this treatment step that caused the exfoliation of sections of the CNT film. The lack of obvious difference in performance with large areas of the CNT film missing from the active area

indicates that the majority of the produced charge carriers are not being collected with no grid lattice present.

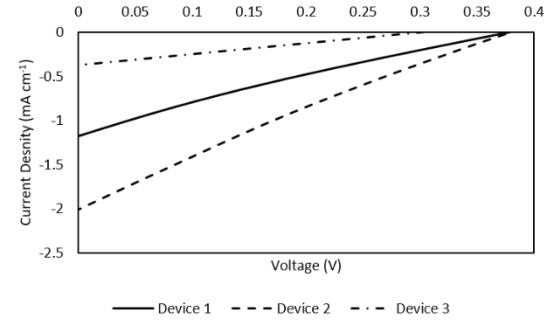

Device 1	Device 2	Device 3
PCE: 0.1	PCE: 0.17	PCE: 0.03
J_{sc}: 1.18	J_{sc}: 2.01	J_{sc}: 0.37
V_{oc}: 0.378	V_{oc}: 0.380	V_{oc}: 0.302
FF: 0.22	FF: 0.22	FF: 0.25

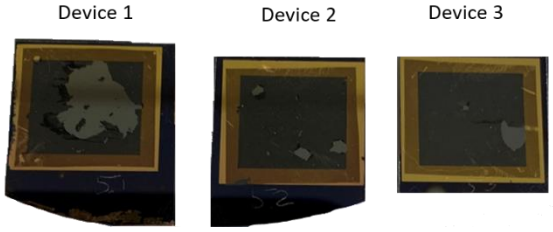

Figure 5-20: J/V curves and parameters for three large area cells with no top contact grid. With optical images of the devices measured.

5.4.1 Top Contact Grid Optimisation

As stated in Section 5.2, the parameters for the grid design were based on optimal parameters for devices with an area of 0.09 cm^2 and thus it cannot be assumed that the same parameters are optimal for the 2.25 cm^2 devices. It is important to optimise the top contact but varying the width of the grid lines and the grid line spacing as well as comparing the performance of a gridded design with a 'fingers' design experimentally would all require the production of new photolithographic masks. However, the height of the metal grid could easily be adjusted during the sputter deposition of the layers. A top contact of 5 nm chromium with 145 nm gold was previously used as the top contact in the CNT/Si heterojunction device design. It was thought that this top contact might be too thin to properly transport current across the device to be collected, as the large devices would be expected to produce higher raw current due to the increase in active area. There are downsides to increasing the grid thickness. The CNT film is assumed to sit flat across the entirety of the front contact, but there is a region between the top edge of each gridline where the CNT film slopes down to the silicon (Figure

5-21). Thus, an increase in gold thickness may reduce the overall CNT/Si intimate contact area. However, the uncontacted silicon is not an issue provided it is not wider than the diffusion length near the silicon surface. Also, the stretching required by the CNT film to reach the silicon with higher grid lines may reduce the ability of the film to transport charge carriers. Lastly, as the metal grid increases in thickness the ability for acetone to remove the AZ-1518 photoresist from under the chromium/gold layer was reduced. This led to an increase in processing time and an increase in poorly formed substrates without full Cr/Au exfoliation from the active area.

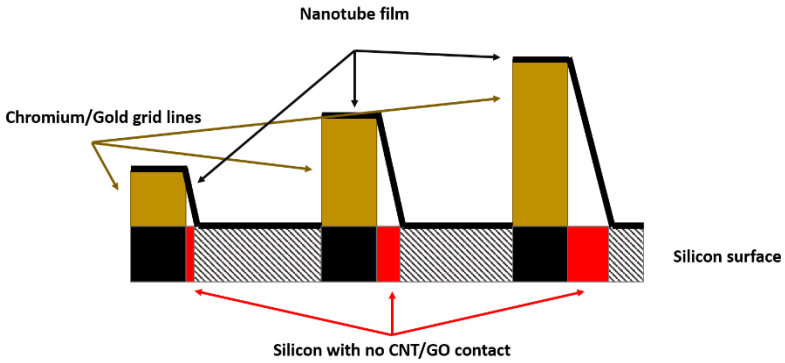

Figure 5-21: Schematic demonstrating the loss of CNT/Si contact area expected with an increase in grid height. Note this image is not to scale; the actual distance between the grid lines is three orders of magnitude larger than the grid height.

There exists an optimal front metal contact thickness where the benefits of enhanced charge carrier transport are maxed out compared to the detriments from a stretched CNT film and reduced photon intensity. To find this optimal point a series of devices were fabricated with different top contact thicknesses, 150 nm (the previous norm), 305 nm, 450 nm, 600 nm and 750 nm. In each case the full thickness of the layer is distributed between 5 nm of chromium and x nm of gold where x + 5 equals the full thickness. J/V curves for each batch of devices were collected at 100 mW cm^{-2} (100% intensity) and at 50 mW cm^{-2} (50% intensity) to account for the issues with spot size coverage. At the thickest value (5 nm Cr + 745 nm Au) there was a noticeable increase in difficulty in exfoliating the metal from areas coated with photoresist after sputtering. Some areas of gold could not be removed from the wafer even with extended periods of soaking in acetone. This indicates that the thickness of the metal had increased to the point where diffusion of acetone through the layer was heavily impeded.

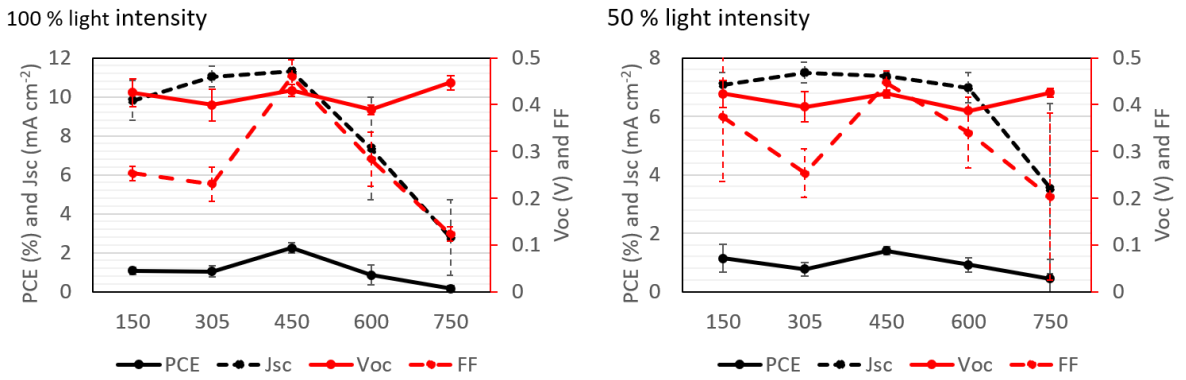

Figure 5-22: J/V properties for devices with different top contact thicknesses at different input power.

It is clear from Figure 5-22 that an optimal thickness for the large area device exists at 5 nm Cr plus 445 nm Au. In Figure 5-22 there is a clear tail off in performance as the thickness is increased from this point, with very poor device results recorded at the thickest level. At the thinner heights, there is a less clear trend, with the 50 % intensity data indicating that the 150 nm devices could reach the same PCE heights as the 450 nm devices, albeit with a significantly higher variance. The 100 % intensity data (Figure 5-22) shows a clearer peak at 450, with a virtually flat trend before this peak. It is interesting that such variance could exist between measurements when the same devices were used to produce the J/V curves at each intensity. This is likely due to a dependency on which part of the outer top metal contact was contacted by the probe during measurement. This phenomenon was discovered and analysed and is shown in this chapter in Section 5.8.

In Figure 5-22 a departure is seen from previous device property break downs as the parameter that most resembles the PCE vs front contact thickness is the FF in this case, rather than the J_{sc}. It is apparent that the major reason behind the superiority of the 450 nm samples is a significantly better FF. This indicates that devices with a 450 nm front contact experienced less charge carrier recombination than at other thicknesses. There is also a similar trend noticeable with the J_{sc} values although this trend is more gradual than for the FF or PCE. The J_{sc} was found to increase slightly from 150 nm to 450 nm and then deteriorate much more rapidly as the front contact thickness was increased from 450 nm. In general, larger error bars are also observed in the 600 nm and 750 nm samples, indicating a loss of consistency at these thicknesses. The V_{oc}, on the other hand was found

to remain relatively stable, but with a 'zig-zag' pattern, with peaks at 150 nm, 450 nm, and 750 nm and troughs at 305 nm and 600 nm. The highest V_{oc} values were recorded at the 750 nm point. Overall, however, the data suggests that thick top contacts above 450 nm lead to significant deterioration in device properties and also to an increase in manufacturing difficulty due to the need for acetone to pass through the metal contact to reach the photoresist. A thickness of 450 nm was found to give optimal performance and thus this thickness was used in future experiments.

In order to observe how the gold grid lines form as the thickness (and sputter time and heat absorption) increased, AFM images were taken of device substrates with each of the thicknesses used in the above device data experiments. Three-dimensional computer images were produced using the data for each front metal height are shown in Figure 5-23.

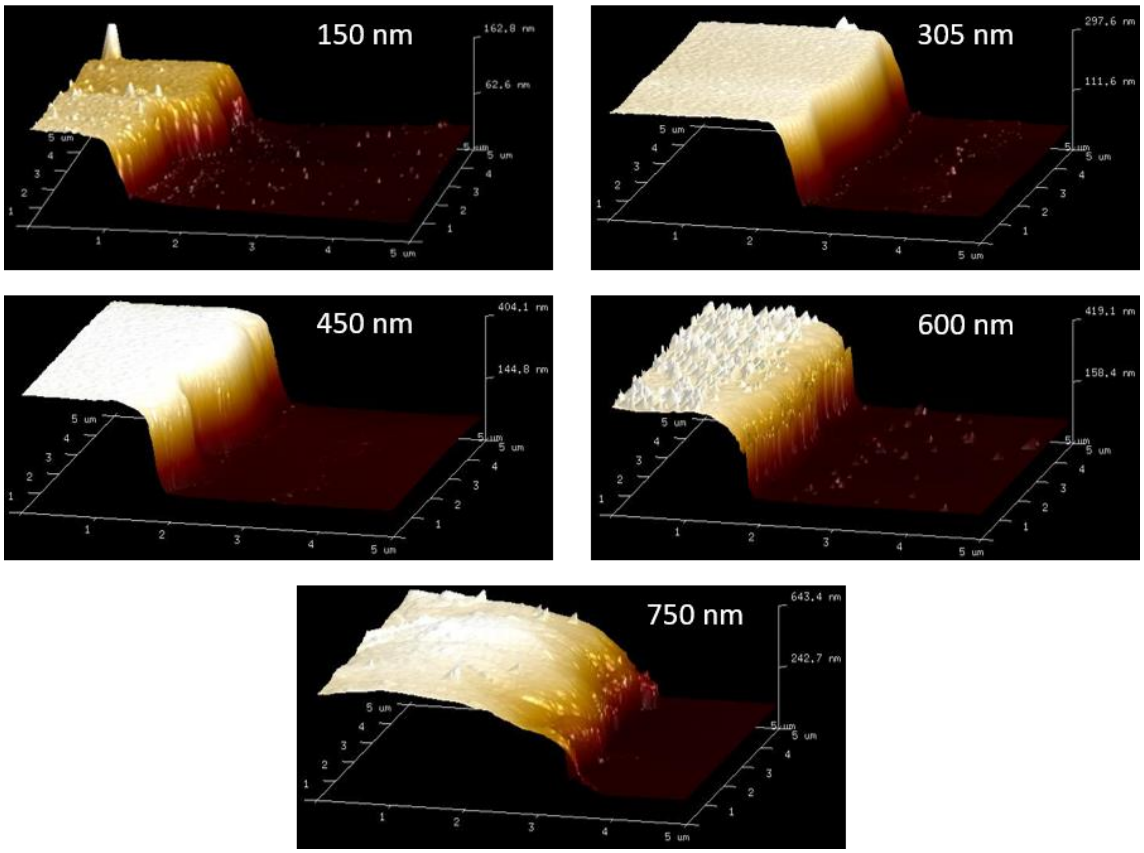

Figure 5-23: Three dimensional CGIs of increasing top metal grid thickness.

The AFM data shows that the grid lines for the 150 nm to 600 nm samples are relatively straight, with variations of significantly less than a micrometre present along the length. The surface of the lines is generally flat, and a sharp cliff is observed in most cases. There is some roughness present on the

edges of the grid lines which is due to the lift off method used to form the gold pattern. When the photoresist was dissolved, it pulled the metal above off with it. Thus, 'ripping' occurred at the junction on the microscale. The major exception to these observations is the 750 nm case. It is apparent that when the metal reaches this thickness the morphology changes drastically, the surface of the line is significantly rougher than the other four thicknesses and tapers for roughly 1.5 µm before the cliff edge rather than forming a sharp edge. Cross-sectional data was obtained from the AFM images for each metal height, this data is shown in Figure 5-24, Figure 5-25, and Figure 5-26.

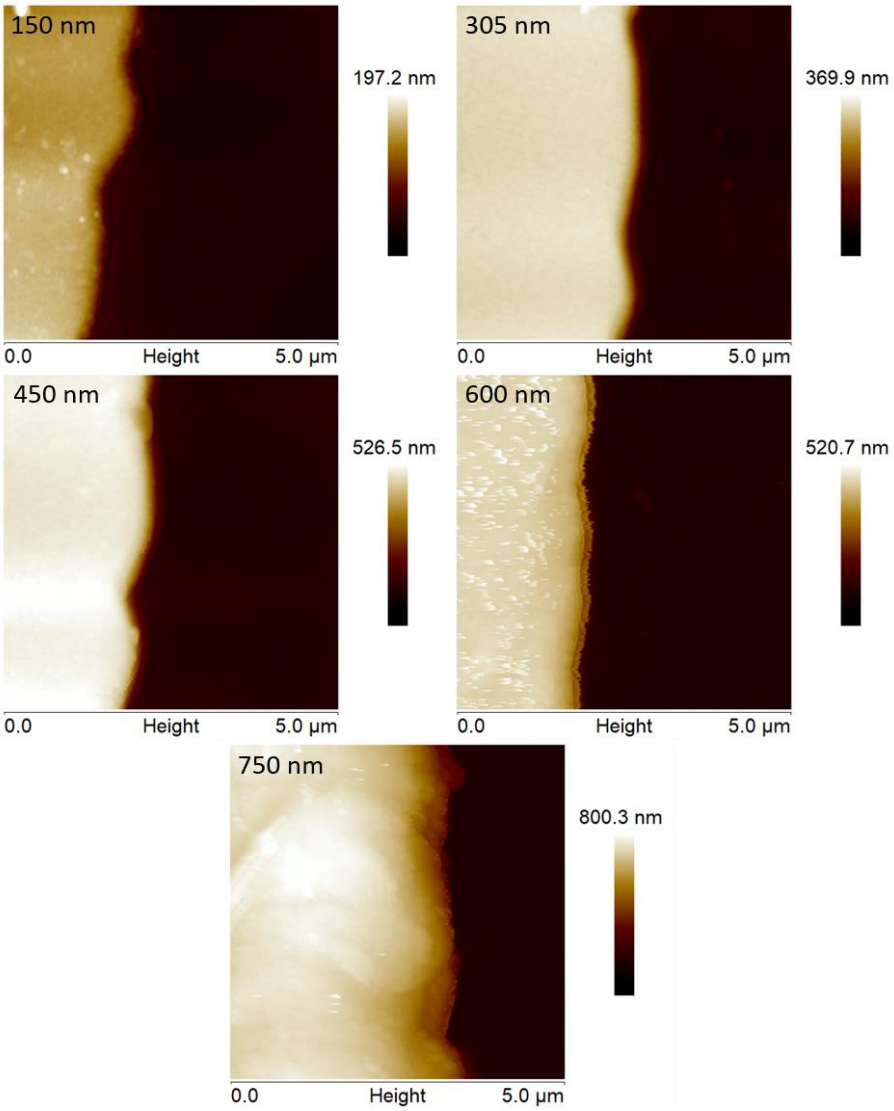

Figure 5-24: AFM height maps of differing gold thickness.

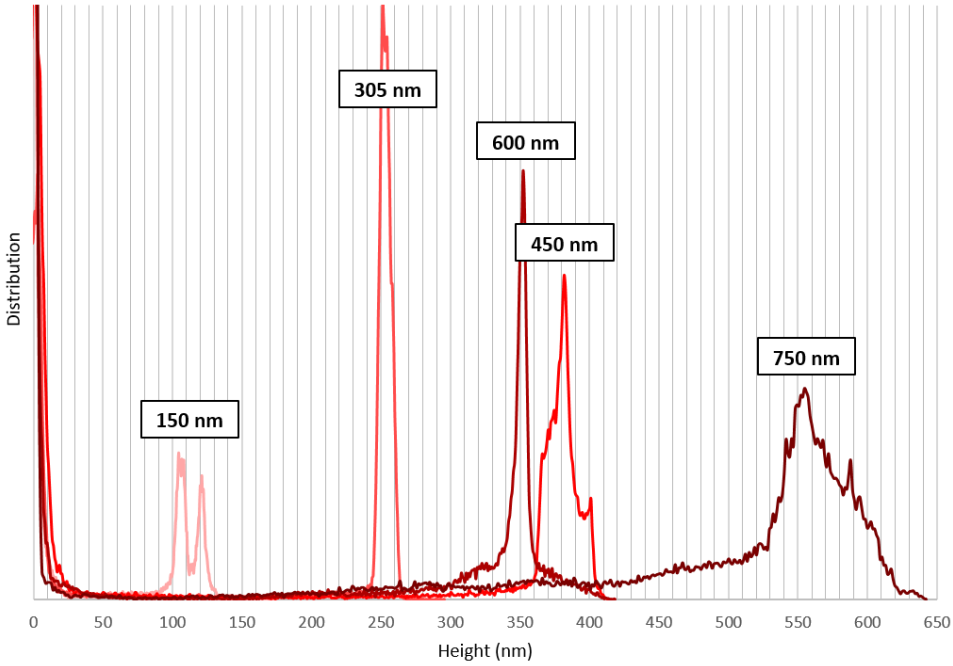

Figure 5-25: Height distribution plots from AFM images of different top contact heights. The y-axis displays the percentage count for each height. The labels represent the input metal thickness.

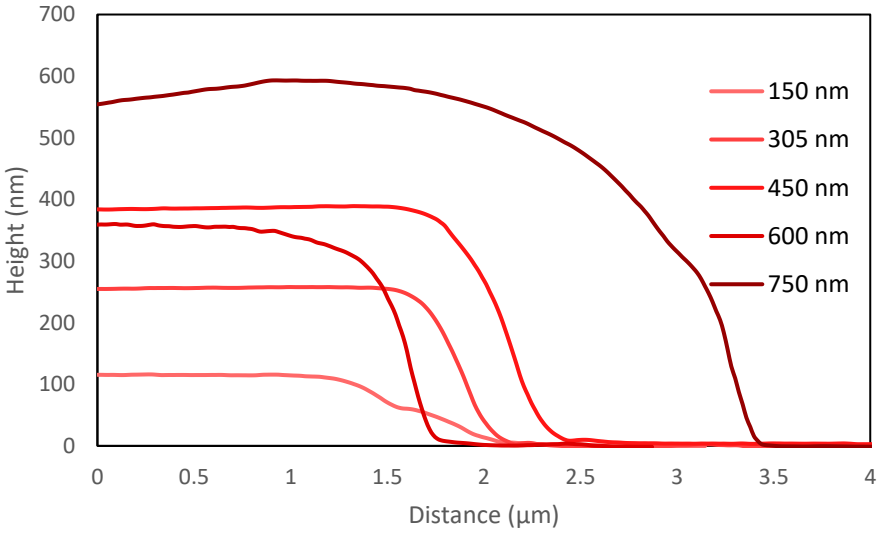

Figure 5-26: Cross-section of AFM images from differing front metal layer thicknesses.

Figure 5-25 and Figure 5-26 show that the metal thickness increases as is expected but there are two notable issues. The most severe is that the height of the metal in the 600 nm sample is significantly lower than can be expected. The other issue is that none of the height profiles are at the height expected to have been formed from the sputter coating, with each of the measurements being roughly 50 nm lower than expected (with the exception of the 600 nm sample). There are a few possible explanations for this. The most likely cause is due to non-homogeneity in the sputtering process across

a large surface. It is known that the sputtered metal thickness is at its maximum in the centre of the target and will decrease radially outwards from there. This is observable for small area device wafers when coated with 150 nm of metal as there is a distinct colour difference between the gold in the centre and a bronze colour on the fringes. Whilst the large area devices are not formed as close to the edge of the wafer as the small area devices it is very likely that there is still some tail off from the centre to the edges. Another possible explanation is that the metal 'lift-off' process caused by dissolving the photoresist layer exfoliates the top surface of the metal grid near the edges, although the relative sharpness of the edges would seem to indicate that this is not the case. Additionally, a calibration issue with the quartz crystal microbalance, used to determine metal thickness in the sputter coater, may be a factor.

5.5 Top Surface Silicon Oxide Growth Optimisation

The pre-grown 100 nm SiO_x layer on the surface of the substrates is removed via a BOE etch prior to CNT film attachment. However, heating, water contact, and air exposure during post-etch processing will lead to regrowth of SiO_x between the substrate and the CNT film. It has been shown in previous research[210] that the presence of an ultra-thin oxide layer is optimal for ideal solar device performance as it passivates the surface, reducing the recombination rate. Thus, control of the oxide layer is important to investigate. Prior to this experiment the device substrates were left in atmosphere for 30 min to allow a thin atmospheric oxide to grow and prevent the growth of further oxide due to CNT attachment and other post etching processing. However, differences in ambient temperature and humidity will cause the oxide to grow at different speeds, thus a new method was trialled. In this method, a droplet of H_2O_2 was placed on the silicon surface immediately after BOE etching was completed and allowed to sit for 5 s before washing with DI water. The purpose of the H_2O_2 is to cause rapid oxide growth to take place and protect the surface from further oxide growth in the same way as allowing oxide growth in air but in more controlled conditions. All devices tested in this section have a top contact grid.

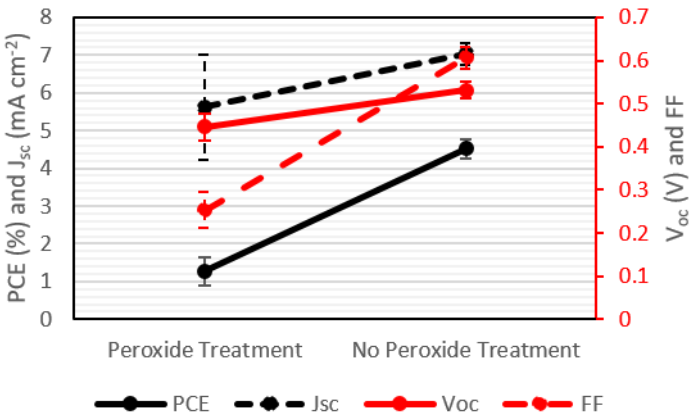

Figure 5-27: J/V properties for CNT/PEDOT:PSS/Si devices when either treated with an H_2O_2 droplet or left in air for 30 minutes with no post fabrication processing applied.

Figure 5-27 shows that the use of H_2O_2 to treat the etched silicon surface serves to significantly damage the performance of CNT/PEDOT:PSS/Si devices compared to simple air exposure (The PEDOT:PSS was used as a hole-transporting interlayer (Section 6.2)). Thus, for the later experiments an H_2O_2 post etching treatment was not applied. The degradation in performance may be due to the growth of an oxide layer thick enough to impede the CNT/Si heterojunction, however in devices sets treated with H_2O_2 future 2% HF etches were not found to significantly increase device performance so this is unlikely. Alternatively, the H_2O_2 treatment may be growing a SiO_x layer which is highly disordered, and this may be interfering with the CNT/Si junction.

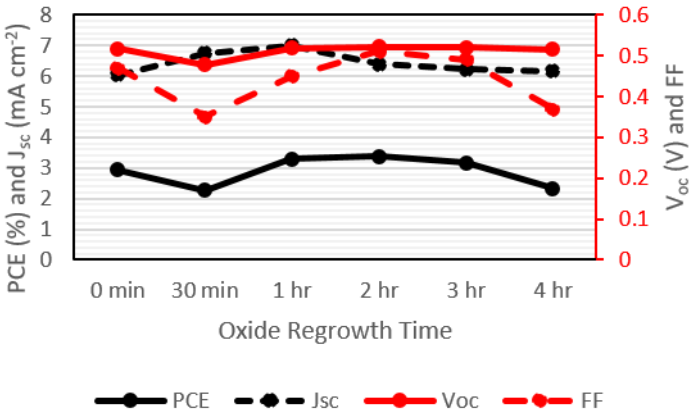

Figure 5-28: J/V properties for large area devices with a PEDOT:PSS interlayer after different regrowth times.

Figure 5-28 shows performance for devices left in air after BOE etching of the 100 nm SiO_x layer for different time intervals. There is a peak in PCE around the 1 hr – 2 hr mark with a decrease in PCE for time intervals higher than this. The 30 min device displays a significantly lower PCE than the other

samples, this appears to be due to a lower V_{oc} and FF. The V_{oc} in particular is noteworthy as this parameter is relatively consistent for the other samples tested. There is a peak in the J_{sc} trend for the 1 hr sample and a peak in the FF trend for the 2 hr sample, explaining why these two devices produced the highest PCE results. Oxide layer growth on silicon in air is known to exhibit a stepwise growth pattern with a step occurring above 200 min in air until around 1000 min in air.[205] This explains the drop in performance from the 3 hr device to the 4 hr device as the oxide layer has begun to thicken. As the oxide is expected to stay at a constant thickness from 1 min of exposure up to this step it is surprising that there is also a notable difference between the 0 min – 30 min – and 1 hr devices. Although it seems apparent that the 30 min sample suffered due to a lower V_{oc}.

5.6 Application of a Chromium Top Contact Cap

The addition of a thin cap of chromium applied on top of the gold layer (thus giving a Cr-Au-Cr sandwich design) could assist in the CNT/front contact interface and improve charge carrier extraction and thus current production. To analyse this, a set of devices were produced with a 5 nm Cr – 445 nm Au – 5 nm Cr top contact grid and tested at 50 % and 100 % intensity. The data is shown Figure 5-29.

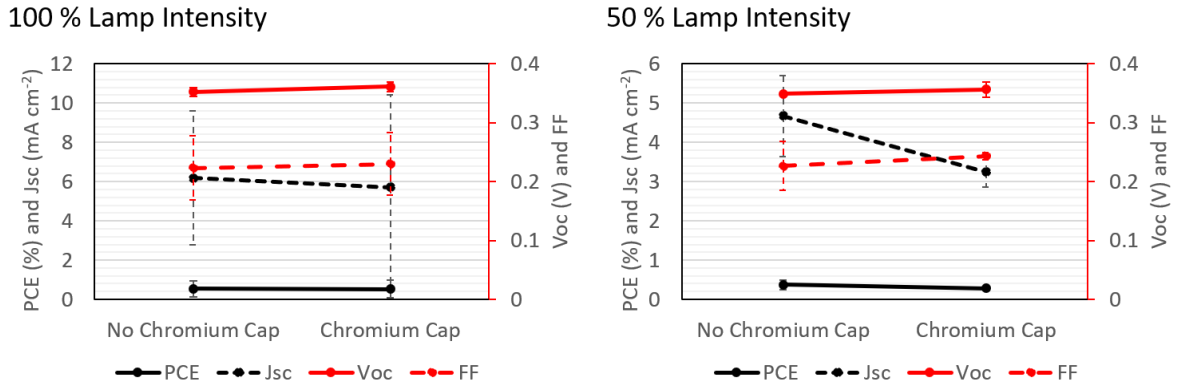

Figure 5-29: J/V properties for devices with and without a 5 nm chromium cap on the top gold contact.

Figure 5-29 shows J/V data for devices with and without a 5 nm chromium cap on the top gold contact. There was a large amount of inconsistency in J_{sc} and FF at 100 % lamp intensity. This issue is lessened somewhat at 50 % intensity. There is, as expected, a clear decrease in J_{sc} and PCE at reduced intensity, whilst the V_{oc} and FF remain relatively stable. It is also notable that these devices performed poorly when compared to the 450 nm data set from the previous experiment. This inability for a new set of

devices to match a previous set of devices is not uncommon when researching this device design and shows the importance of comparing devices directly with other devices produced concurrently rather than across a range of time. A possible reason behind this change could be a drift in the transmittance of the CNT films used between experiments. With these issues noted it is still apparent that, in terms of PCE, devices with no chromium cap perform slightly better. This is due to a clear drop in J_{sc} in the 50% intensity plot, outside the error bar range. Conversely, there is an increase in V_{oc} and FF with the chromium cap present.

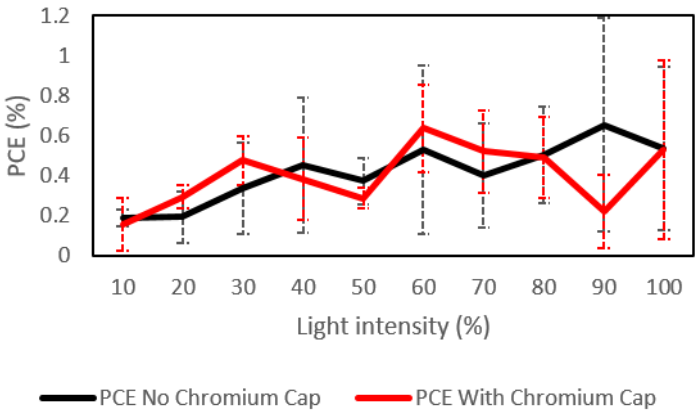

Figure 5-30: Average PCE values for devices with and without a 5 nm chromium cap at a range of light intensities.

Figure 5-30 shows the PCE of both device designs with increasing light intensity. Apart from the expected increase in PCE with increasing intensity (up until 60 % - 70 % where the spot size is insufficient to illuminate the entire device active area) it is clear that there is no definite preferred design, with the differences in J_{sc}, V_{oc}, and FF combining to give roughly equivalent PCE values. Thus, no significant and notable improvement to PCE is gained from the addition of a 5 nm chromium cap, whilst the J_{sc} experiences a drop and the V_{oc} and FF experience slight rises. In light of this a chromium cap was not applied for future large area devices.

5.7 Use of Alumina Filtration Membranes for SWCNT Film Fabrication

It was suggested that the use of alumina filtration membranes over the standard cellulose ester membranes could lead to improvement in CNT/Si device performance as the alumina filters had smaller pores and were flatter overall than the cellulose ester filters. This would be expected to lead to flatter CNT films, which could lead to an improvement in the CNT/Si device due to an increase in

CNT/Si contact area, as discussed in Chapter 4. CNT films on alumina filters are produced in the same way as with cellulose ester films (Section 2.1.2), however, the heat/press attachment method (Section 2.1.3.1) could not be used as acetone would not dissolve the alumina filters. Film flotation (Section 2.1.3.3) was more viable as the alumina can be dissolved in a solution bath of 3 M NaOH. In order to determine the effect of both the different film attachment techniques and the change in filtration membrane three sets of devices were prepared to be tested: a cellulose ester set attached via the heat/press method, a cellulose ester set attached via film flotation in acetone then water and an alumina set attached via film flotation in NaOH then water. In all these cases the solvent was removed and replaced with the next solvent rather than moving the film between solvent baths. As discussed in section 5.2 Design circular template membranes were used for all three sets.

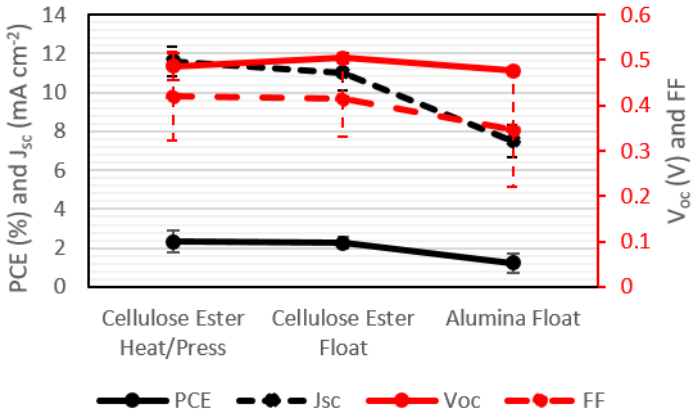

Figure 5-31: J/V properties for devices produced with different filter membranes and different attachment methods.

Figure 5-31 shows that, whilst the attachment method did not seem to cause much difference in device performance, the films prepared on alumina membranes demonstrated poorer performance across the board. It is notable that the two cellulose ester cases are not exactly the same. The films attached via heat/press gave a lower average V_{oc} (albeit only a difference of roughly 0.02 V) and a higher average J_{sc} (again, a difference of less than 1 mA cm^{-2}) however in general they performed similarly enough to be considered equivalent. Meanwhile the films filtered on alumina membranes produced lower J_{sc} , V_{oc}, and FF values than both cellulose ester samples, with no error bar overlap present in the J_{sc} cases or in the V_{oc} case when compared to floated cellulose produced films (although, again the difference in V_{oc} is slight). Thus, the move to alumina filtration membranes with the same

CNT suspension volume produces devices with significantly lower current output and thus lower performance.

However, as the alumina filtration membrane is expected to change the morphology of the CNT film, it should not be assumed that the same volume of CNT suspension will produce films with the same transmittance when the filter medium is changed. In fact, when films were created to test this, it was found that, whilst the films filtered on cellulose ester gave a 53 % light transmittance value, the films filtered on alumina gave a 38 % light transmittance value. Thus, there is a significant difference in photon blocking between the two film sets. To address this, thinner films were produced which tested at the much more favourable value of 60 % light transmittance. These films were applied to substrates and tested as with the above devices.

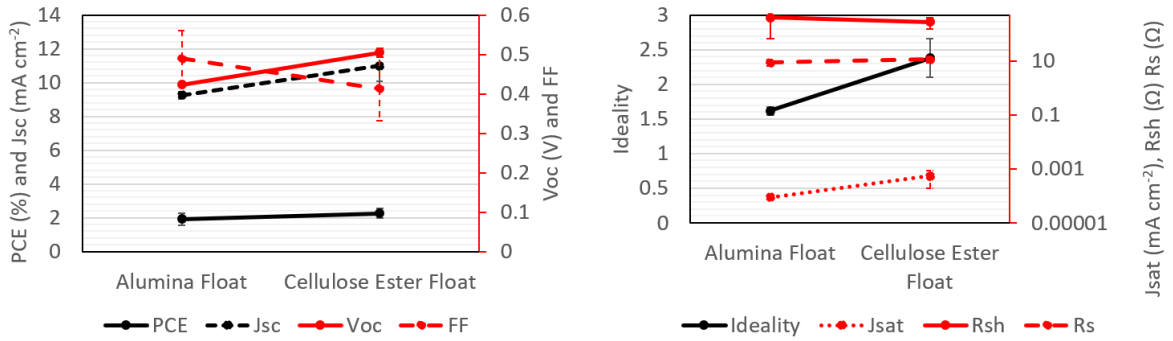

Figure 5-32: J/V properties for cells with CNT films formed on alumina filters or cellulose ester filters with similar transmittance values.

Figure 5-32 displays the combined data for devices produced with either alumina filtered films or cellulose ester films with equivalent transmittance. In this comparison, both sets were assembled using the film flotation approach. Whilst it is again apparent that the alumina filtered films produce devices with lower performance (PCE) than cellulose ester filtered films, it is noticeable that they are not inferior in all departments. The alumina filtered films perform worse than the cellulose ester filtered films in terms of both V_{oc} and J_{sc} and it is this that gives rise to the inferior average PCE results. However, the alumina filtered films produced better FF values than the cellulose ester films. In addition, Figure 5-31 b) shows that the films produced from alumina filtration produce devices with superior diode properties than those produced with cellulose ester filtration. With the alumina devices

exhibiting an average ideality closer to 1, a lower J_{sat} by roughly an order of magnitude and a higher R_{sh} coupled with a lower R_s which is the ideal situation. Overall, the photovoltaic performance of a device is most heavily gauged by the PCE value and thus the cellulose ester films performed better with films of equivalent transmittance.

SEM and AFM analysis were also performed on the alumina filtered films to investigate whether the expected improvements in film smoothness were achieved.

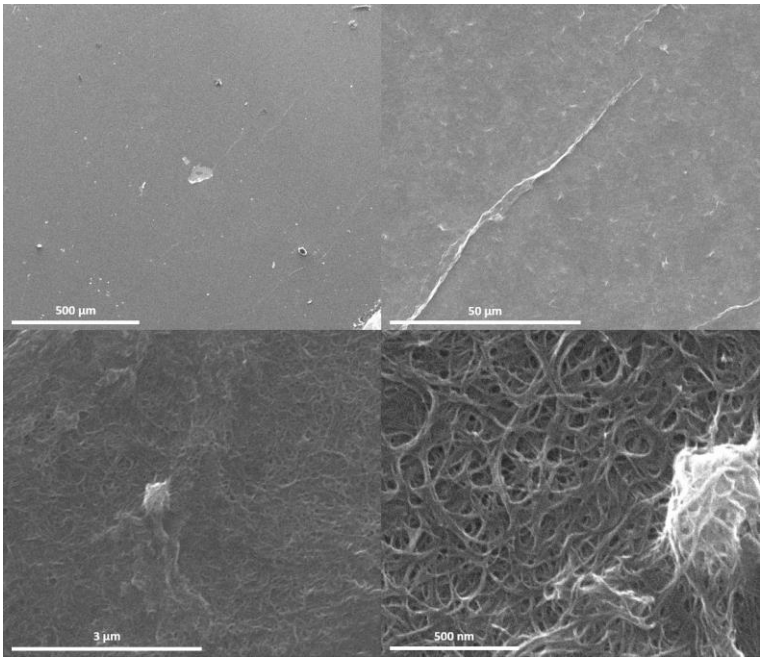

Figure 5-33: CSE filtered films under SEM at different magnifications.

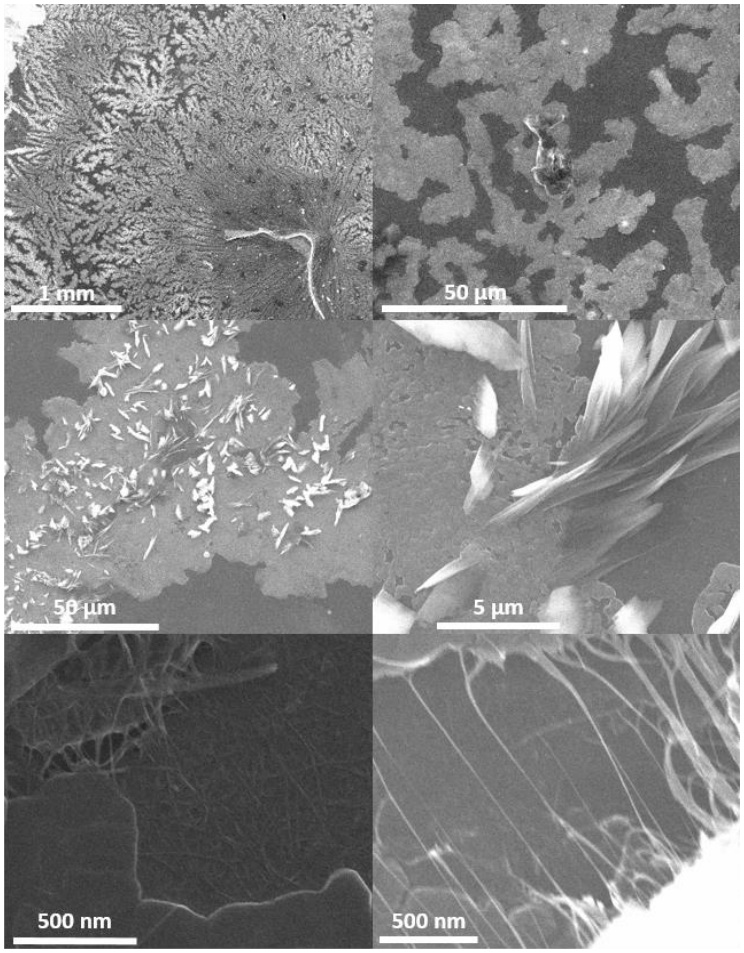

Figure 5-34: Alumina filtered films under SEM at different magnifications. Showing white 'crystal' structures.

Figure 5-33 and Figure 5-34 display SEM images of a CNT film produced via filtration on a cellulose ester membrane (Figure 5-33) or an alumina membrane (Figure 5-34). The film produced via cellulose ester filtration appears as expected for CNT films produced under the same conditions, consisting of a flat sheet of CNTs/CNT bundles which appears less homogeneous as the magnification level is increased. The CNT film produced via alumina filtration has a more variability. At low magnifications the film appears to consist of large bright mats of tubes separated by darker areas, when the magnification is increased it was observed that the areas in between and under the mats consisted of a film of CNTs which appeared roughly equivalent to the films seen under cellulose ester filtration (bottom left image Figure 5-34) although this film could be flatter. Meanwhile, the higher mats above this film appear to also consist of a CNT matrix, as shown by the bottom right image in Figure 5-34 where CNTs/CNT bundles can be seen stretching between two bright areas. Additionally, there are also large amounts of white 'crystal' structures visible at medium magnifications, these may be

alumina crystals which have remained undissolved during the repeated NaOH baths. The large bright structures above the CNT film and seen with bridging CNTs/CNT bundles may also, be alumina flakes remaining after the NaOH bath. Overall these SEM images are somewhat inconclusive in determining how the morphology of the CNT film is affected with different filtration membranes due to the presence of large, unknown structures in the CNT films produced by filtration on alumina, obscuring the CNT film from being imaged.

In order to examine the effect of a change in bath pH on the crystal structures observed in Figure 5-34, a new alumina filtered film was dissolved in a 3M NaOH bath. The bath was diluted to around a pH of 7 as previously and a piece of the film was attached to silicon at this point. Then the bath pH was decreased to 4 with the addition of neat HCl and another piece of the film was attached immediately. The rest of the film was then left in the pH 4 bath overnight and another piece was attached to silicon following this. All three pieces of the same film were imaged using SEM.

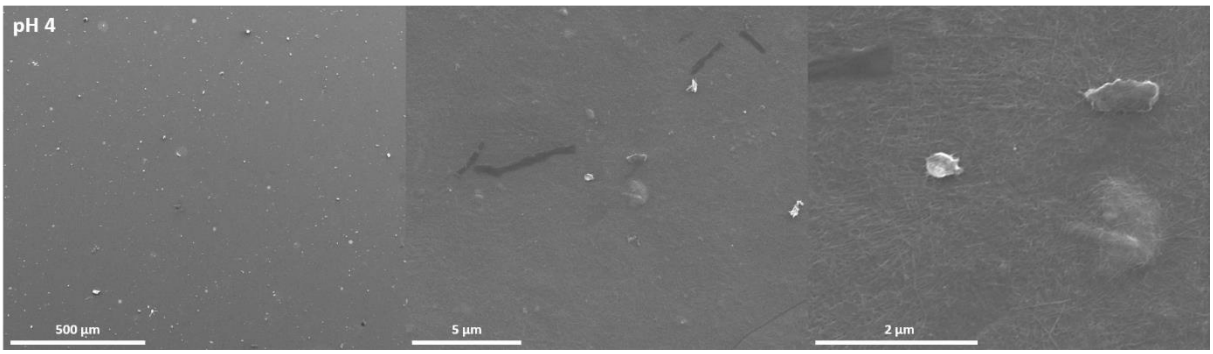

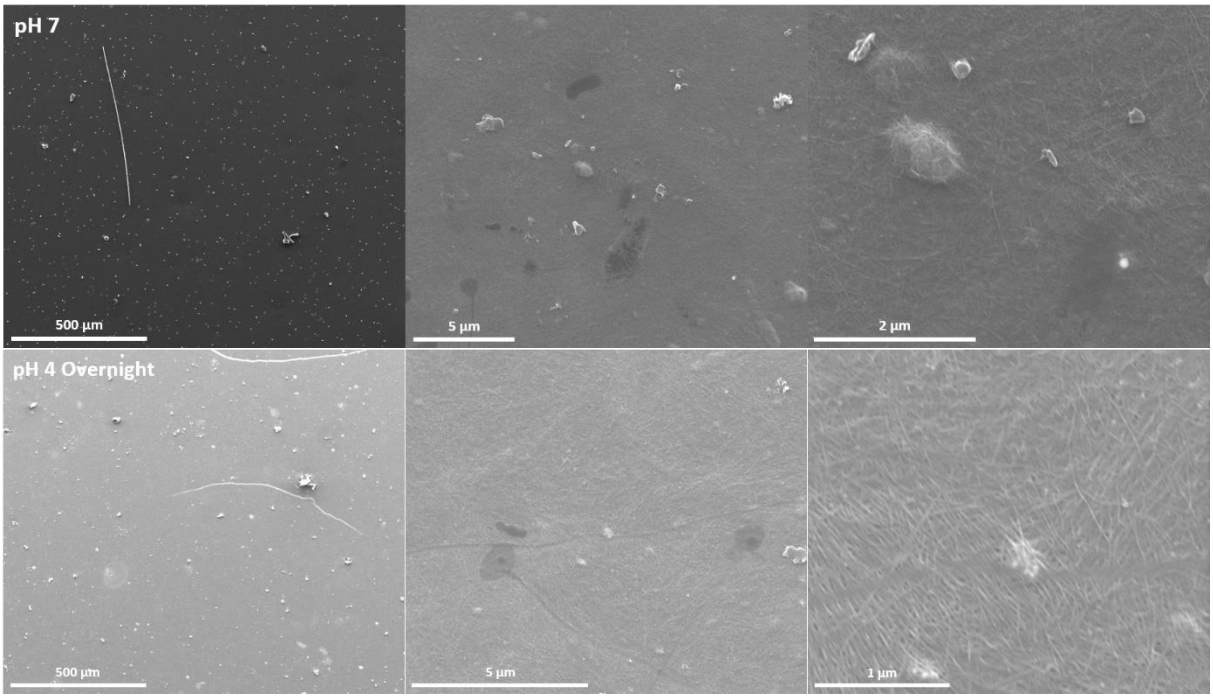

Figure 5-35: Alumina filtered films floated in water baths at different pH.

Figure 5-35 shows SEM images of different pieces of the same alumina filtered SEM film floated in different pH conditions. There is very little visual difference present between the three film pieces. Additionally, there is no sign of the large shard structures seen in Figure 5-34. Instead, large, flat, homogeneous CNT mats are visible with the occasional small bright lumps present. These may be smaller versions of the shards from before although these are present on all film pieces and may simply be contaminant particles from the air. The films imaged in Figure 5-35 were left in the NaOH bath for a longer period of time than the films in Figure 5-34. This extended time in the bath may have assisted in completely dissolving the alumina membrane and thus be the reason that there are no shard structures visible in Figure 5-35. AFM height maps were also produced for CNT films filtered onto cellulose ester membranes and alumina membranes both from basic or acidic bath flotation.

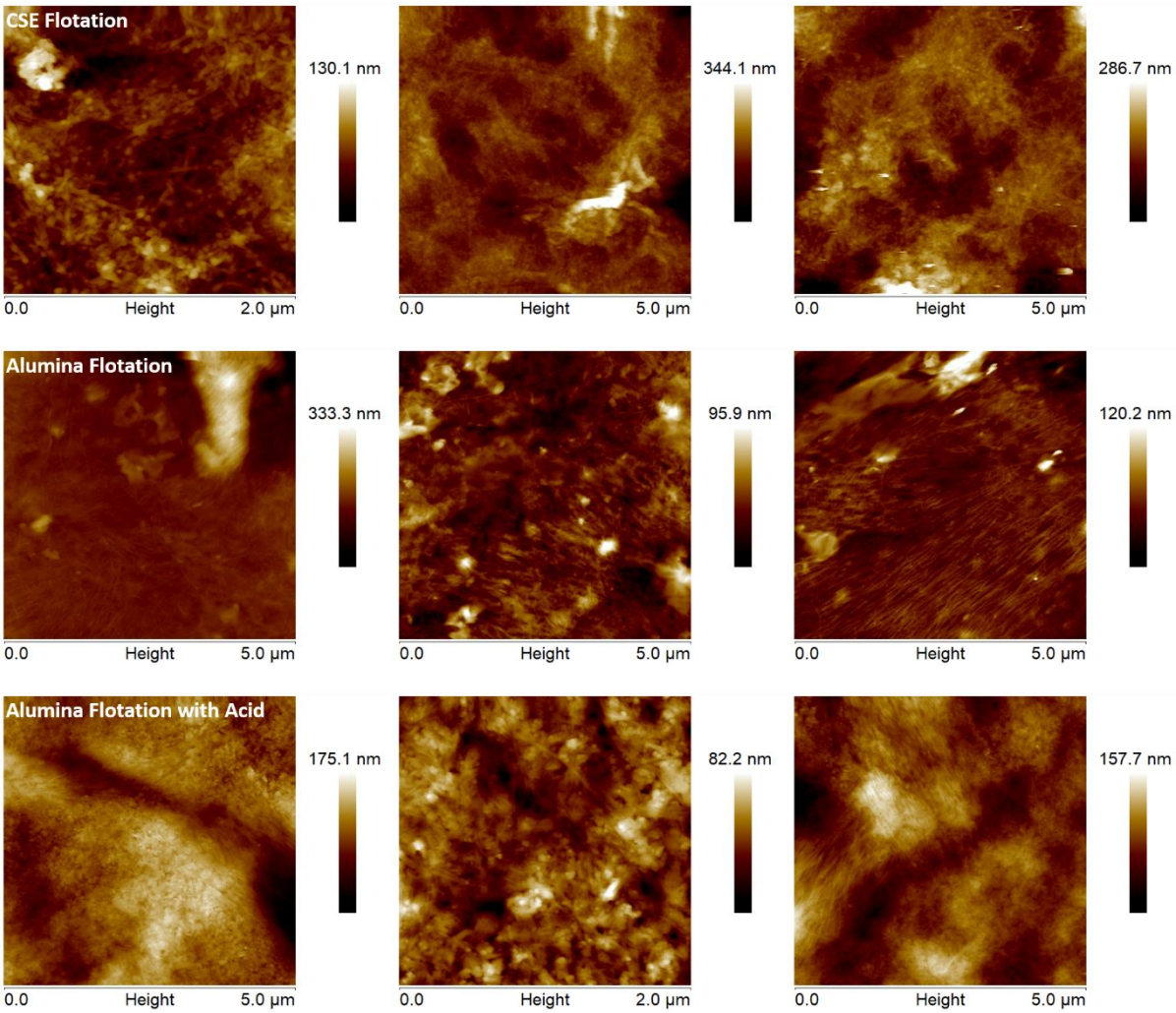

Figure 5-36: AFM images of SWCNT films filtered on CSE or alumina membranes.

The AFM data shows that complex CNT networks are present in all film cases. There is, again, no evidence of the large shards seen in Figure 5-34. There are some small bright spots present in one of the alumina filtered films at pH 7 but these are also visible in some case for the other two film types/conditions. Overall, the data suggests that there is little difference in terms of film formation between the two filter types. Although the Z axis ranges seem to suggest that the alumina filtered films are, in general, smoother than the cellulose ester filtered films. In order to further analyse this, the same roughness indicators were determined for these AFM images as were used in Chapter 4**.**

Table 5-1: Film roughness data for films filtered on CSE and alumina membranes.

Filter Membrane	*Figure 5-36 Image (From Left to right)*	*Image Z Range (nm)*	*Image Rq (nm)*	*Image Ra (nm)*
CSE	1	130.1	17.2	13.3
	2	344.1	39.1	27.7
	3	286.7	37.0	28.1

Alumina	1	333.3	35.6	20.8
	2	95.9	12.6	9.53
	3	120.2	13.3	9.07
Alumina with acid	1	175.1	23.9	18.5
	2	82.2	11.4	8.98
	3	157.7	21.0	16.4

Table 5-1 shows the film roughness measurements for the different SWCNT films, determined as per Section 4.6, where R_q is the root mean square average height deviation, and R_a is the arithmetic average of the surface height deviations. There is an amount of variation observed for each film type, with the CSE R_q value varying from 17.2 nm to 39.1 nm, and the alumina films varying from 13.3 nm to 35.6 nm and 11.4 nm to 23.9 nm for neutral and acid treated films respectively. For the CSE and acid treated alumina films this variation can be explained by considering the area imaged. The outlier points exhibiting lower Z range, R_q, and R_a for both of these sample sets correspond to AFM images with an area of 2 x 2 μm^2 instead of 5 x 5 μm^2. There is no such area variation present in the alumina filtered samples with no acid treatment. However, there is a high feature present in the top right corner of the image, which likely gave the increased roughness values. The values for the 5 x 5 µm images were averaged so as to better observe the difference between films.

Table 5-2: Average film roughness data for SWCNT films filtered on CSE and alumina membranes.

Filter Membrane	*Image Z Range (nm)*	*Image Rq (nm)*	*Image Ra (nm)*
Cellulose Ester	315.4	38.1	27.9
Alumina	183.1	20.5	13.1
Alumina with acid	166.4	22.5	17.5

Table 5-2 shows that there is a clear difference in the roughness quotients R_q and R_a as well as the Z range for the alumina films compared to the CSE film. The difference is less severe than that seen between slow and fast filtered films in Chapter 4. However, it is still clear that filtering on to alumina membranes does give a decrease in film roughness. The decrease in film roughness did not give an improvement in device performance in this study.

Overall, it was decided that future research with the CNT/Si large area device in this thesis would continue to use cellulose ester membranes over the alumina membranes. The reasons for this are two-fold. Firstly, it was not apparent that the change in membrane from cellulose ester to alumina gave improvement in device performance. In fact, it seemed that there was a decrease in current production and device voltage, despite an apparent improvement in device diode properties. Secondly, the alumina membranes come with significant problems in terms of CNT film processing and device fabrication. The cellulose ester membranes are flexible (like paper) and this allows them to be easily separated from the template membrane and the filtration apparatus. Contrary to this, the alumina membranes are rigid and brittle. This leads to significant difficulties in separation from the Parafilm template and the filtration setup. Their brittle nature meant that almost any flex experienced by the alumina membrane would lead to cracking along the length of the membrane. These cracks would cause ruptures in the CNT film formed on the membrane and the film would drift apart at these cracks once the alumina was dissolved in the 3 M NaOH bath. Whilst this may not be problematic for small area films templates where there are gaps between each film, it is problematic for the large area films as they take up the majority of the membrane area. Thus, the film would be damaged, if not outright destroyed, by almost any cracking experienced by the alumina filters. Whilst this processing difficulty could be avoided by continuous use and fabrication of multiple films to replace any damaged ones it was not preferable, especially when no significant device performance gains were observed when CNT films filtered on alumina were used.

5.8 Effect of Top Electrode Contact Placement

When large area devices were being tested it was observed that performance was more inconsistent than expected in small area devices. Moving the contact probe on the top gold layer to different areas could lead to drastic changes in the J/V curve produced for a given large area device. It appears that the gold layer was not acting as a perfect conductor across the area it covers or there would be no effect caused by moving the probe.

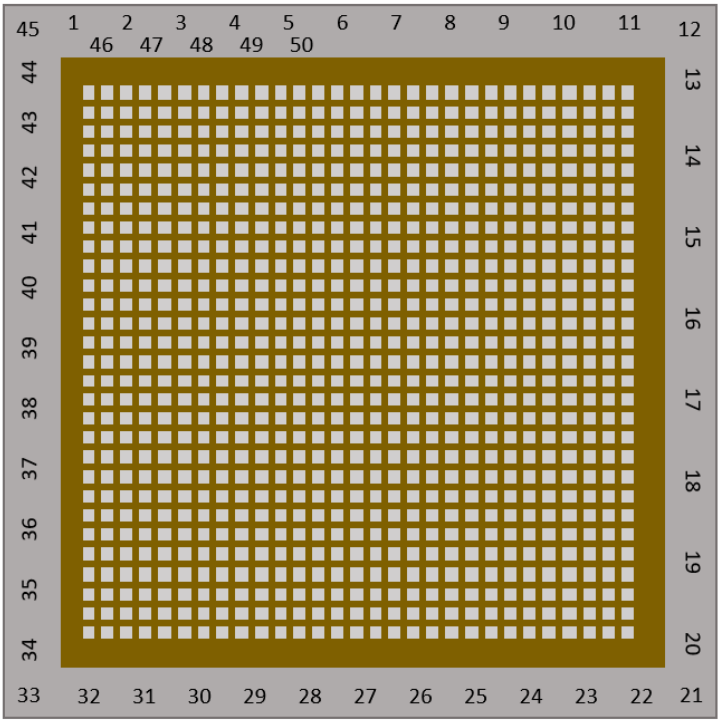

Figure 5-37: Diagram of contact positions used to produce Figure 5-38.

This phenomenon was investigated by taking a large area device and measuring the J/V curve for a series of places along each edge. Roughly 10 – 12 measurements were taken along each side and a measurement was taken on each corner, the distance between each measurement point was roughly 1.5 mm (see Figure 5-37). Additionally, the measurements were continued half way along the edge that was measured first after the device had been fully circumnavigated.

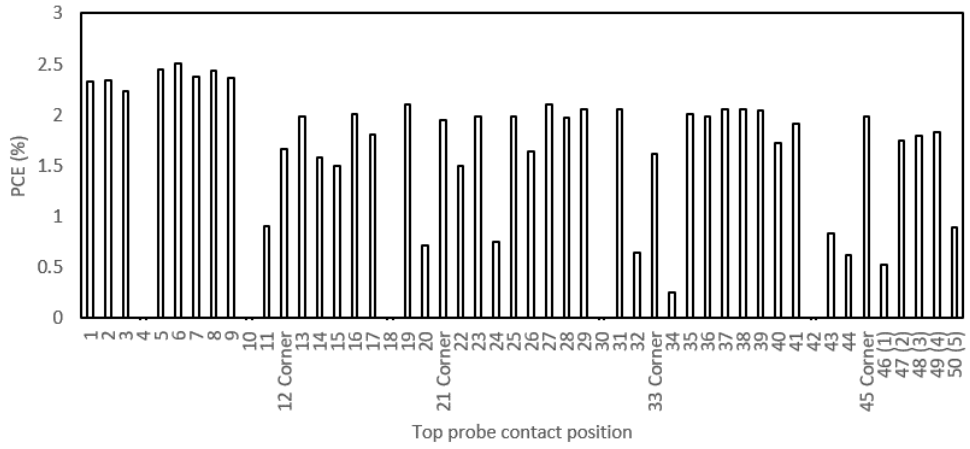

Figure 5-38: PCE measurements for one large area device for different top contact probe position.

Figure 5-38 displays the PCE recorded at different probe locations. The position clearly had a strong effect on device performance. However, there is a notable plateau visible at around 2 % (although this plateau may be slightly higher for the first nine measurements). As the majority of the points tested

produced a PCE similar to this plateau, it was assumed that the majority of probe positions will give a good representation of the device properties. The positions where no PCE data point seems visible are areas where a 'short' occurred, in that the current linearly changed with voltage and the current was 0 mA cm^{-2} at 0 V, this is also a phenomenon occasionally seen with the large area devices, however repeated testing can surpass this. It is also observable that the performance of the device decreases on the second pass of the first tested side. This may be due to limited data points, or possibly due to a decreased effect of the dopant chemicals used due the roughly 10 min between the first test and the last or regrowth of the SiO_x layer between the Si and CNT parts of the heterojunction. Although this is unexpected in such a short time frame. Overall, whilst the inconsistent nature of the top contact appears to be a problem for the device, a simple work around was devised. For future experiments with the large area device, 5 measurements were taken in succession, one in (roughly) the centre of each side and one on a corner and the best performing (in terms of PCE) J/V curve and associated data was used to analyse the device. As there are no PCE results significantly above the plateau in Figure 5-38 taking the highest PCE of multiple measurements will likely give a good approximation of the device performance.

5.9 Conclusions

The CNT/Si heterojunction device was found to be scalable, with a simple increase in active area still producing a functioning device. However, it was found that the J_{sc} decreased significantly as the active area size was increased. A new back contact architecture consisting of a 300 nm aluminium layer was fabricated and found to be a preferable contact to the previous eGaIn/steel contact. A grid lattice was formed on the top contact of the device and this gave a significant improvement in performance as the grid lines assisted the CNT film in transporting charge carriers. The thickness of this top contact was varied, and an optimal thickness of 5 nm Cr + 445 nm Au was determined. Hydrogen peroxide was tested as a possible control for the thickness of the interfacial oxide on the top surface but was found to reduce device performance.

The use of alumina membranes over cellulose ester membranes was investigated as it was expected that these would give smoother CNT films, although it was found that these films gave reduced device performance, despite being smoother and producing a better diode. Although these filters were not continued with in this thesis, they may prove to be an interesting area for further research. Finally, a problematic change in device performance based on contact position was examined and it was determined that producing several J/V curves at various points around each device and taking the best performing measurement was a good way to circumvent the problem.

CHAPTER 6 LARGE ACTIVE AREA DEVICES HETEROJUNCTION OPTIMISATION

In order to further enhance the performance of the large area CNT/Si heterojunction device, a series of five interlayers (materials that sit between the substrate and the CNT film) were trialled. The interlayers will be discussed in three sections.

1. The commonly used polymer interlayers PEDOT:PSS and PANI
2. Two metal compounds CuSCN and MoO_x
3. A novel organic interlayer material.

In each of these sections the aims are:

1. To investigate the film morphology of the interlayer(s) and determine optimal parameters to form a good film.
2. To incorporate the interlayer(s) in large area devices and compare performance with devices to no interlayer.
3. To determine an optimal film thickness for use in the large area device.

6.1 CNT/GO Film Conductivity

Two different doping chemicals are used to improve the conductivity properties of the CNT/GO films used in the CNT/Si heterojunction devices. Each dopant chemical was applied to CNT/GO films attached to glass and the conductivity compared to demonstrate the improvement expected from the application of these dopants to the CNT/GO film in a CNT/Si device.

Note: All films in this chapter will be CNT/GO films as flotation attachment was used in all cases.

Table 6-1: Sheet resistance of CNT/GO films with and without doping.

Doping Type	*Sheet Resistance Before Doping (Ω)*	*Sheet Resistance After Doping (Ω)*	*Improvement (%)*
Aqueous $AuCl_3$	580 ± 5	199 ± 7	69
$SOCl_2$ Contact	842 ± 47	216 ± 4	74
$SOCl_2$ 2 min Vapour	850 ± 24	292 ± 6	66

Table 6-1 shows the change in sheet resistance with various doping techniques. Note that two different $SOCl_2$ doping techniques are shown. This was because direct contact with $SOCl_2$ was expected

to damage the interlayer materials examined in this chapter. The vapour technique is described in section 2.1.8.1 and the data is included separately here to investigate the difference between direct contact doping and vapour doping. The sheet resistance of the large area CNT/GO films analysed decreases significantly for each dopant. The largest decrease was due to direct contact $SOCl_2$ doping. The vapour $SOCl_2$ doping gave the least improvement, however all three gave improvements within 8 % of each other. Interestingly, the variation decreased with doping for both $SOCl_2$ samples. The initial sheet resistance for the $SOCl_2$ doped samples was higher than that of the $AuCl_3$ doped sample. This is likely because the films were thicker for the $AuCl_3$ doping. Film thickness has a significant impact on sheet resistance.

6.2 PEDOT:PSS and PANI Interlayers

6.2.1 Introduction

Two conductive polymer interlayers were selected for application in the large CNT/Si heterojunction devices, poly(3,4-ethylenedioxythiophene) polystyrene sulfonate (PEDOT:PSS) and polyaniline (PANI). These polymers were selected for two reasons. They require simple processing techniques to apply to the CNT/Si device and they have been used previously in research on smaller active area CNT/Si heterojunction devices. As both of these polymers have previously given improvements in device performance,[128, 131] it can be assumed that they will similarly improve the large area device. Figure 6-1 shows energy level diagrams for the three device designs investigated in this section. Both PEDOT:PSS and PANI have been applied to silicon substrates to form solar devices in their own right. Acid doped PANI films were formed on silicon to produce a heterojunction, however they gave poor performance due to lateral resistance across the PANI film.[129] PEDOT:PSS layers were formed on amorphous silicon films on crystalline silicon to produce photoactive heterojunctions which gave performances of 2.1 % at an optimal thickness of 110 nm.[211] More recently, silicon nanowire/PEDOT:PSS junctions have been fabricated, with improved conductivity and thus, improved device performance.[212, 213] A significant limiting factor in these devices is the poor lateral conductivity of PANI and PEDOT:PSS. Tune *et al*.[128] and Yu *et al.*[131] have shown that these

polymers can be incorporated between the silicon substrate and the CNT film in the CNT/Si device, where they improve device performance by improving the depletion region.[131] Doped PANI and PEDOT:PSS are both good hole conductors and thus assist the heterojunction in separating excitons.[129, 213]

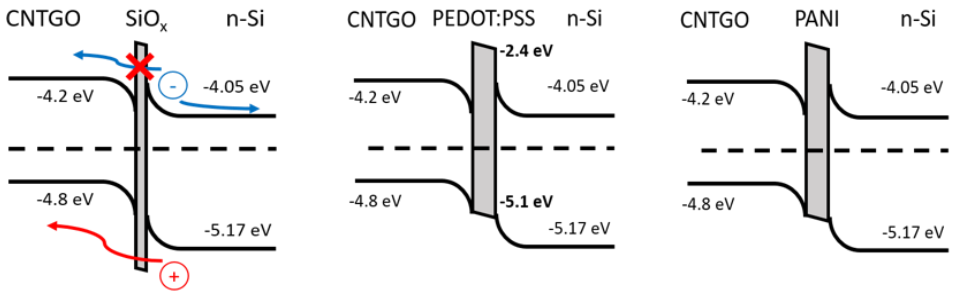

Figure 6-1: Energy diagrams for a device with no interlayer, a device with a PEDOT:PSS interlayer and a device with a PANI interlayer, the energy levels of PANI vary dependent on the oxidation state of the film and thus no numerical energy levels are stated here.[214]

6.2.2 PEDOT:PSS Film Characterisation

In the following experiments, PEDOT:PSS films on glass were imaged with UV/Visible spectrophotometry to compare film formation via relative intensities of their characteristic peaks. Different solution volume and spin speeds were used and the difference in spectrum investigated. Alternate deposition methods were also trialled: A bulk method where the entire solution aliquot was pipetted onto the substrate once spinning had commenced or a dropwise method where droplets of the solution aliquot were dropped onto the substrate with a brief wait in between (Figure 6-2).

For the following experiments, the PEDOT:PSS preparation was changed from a 1:10 dilution with water to a 1:5 dilution with IPA. This was to create a less hydrophilic solution to enhance attachment to silicon substrates and glass slides for testing. The glass slides used in this experiment were cleaned by sonicating in aqueous detergent solution followed by an IPA solution and dried in an oven. Stable PEDOT:PSS films were formed on the glass slides and were found to be unaffected by a water bath. This is an important property to consider as the interlayers have to be submerged in a water bath to pick up the CNT/GO film when attaching via flotation.

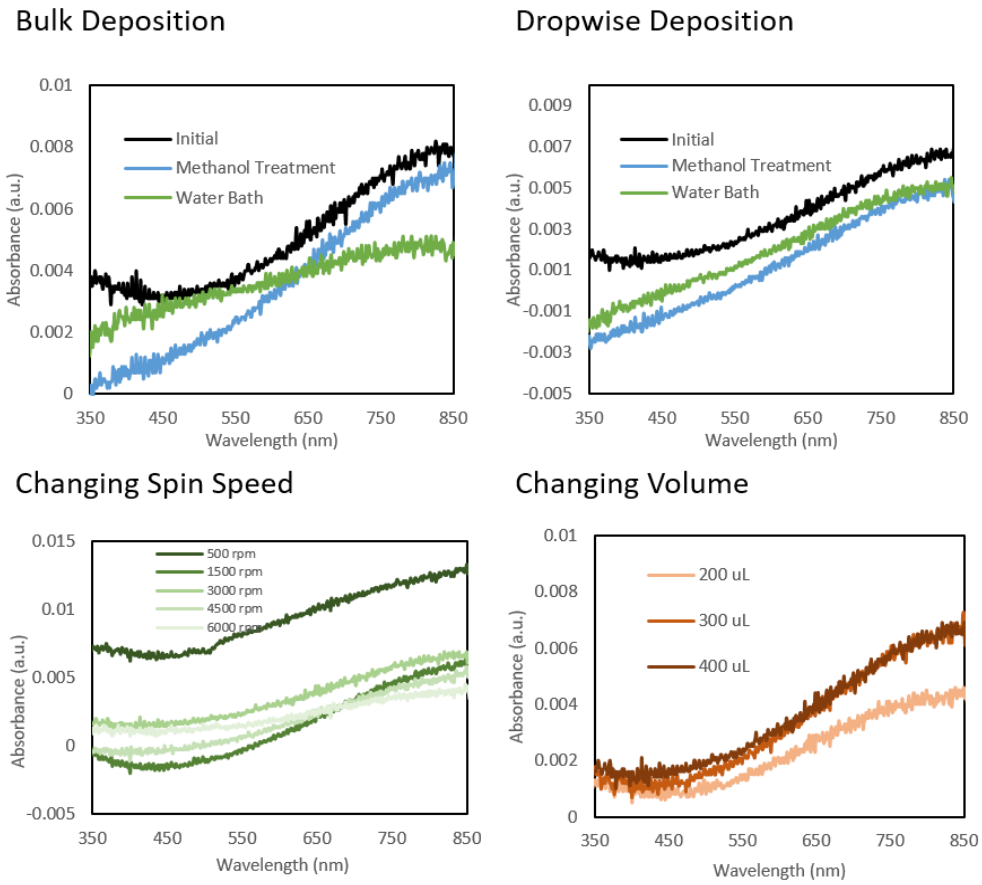

Figure 6-2: UV/Visible spectrophotometric spectra for PEDOT:PSS films produced on glass slides. The top two graphs show films produced using bulk (left) and dropwise (right) deposition and changes due to post fabrication chemical baths.

Figure 6-2 shows a rise at the edge of the spectral range (850 nm) with a trough also visible at around 440 nm. Ideally, the spectra would continue beyond 850 nm but large amounts of noise and error in the range above 850 nm meant that this could not be achieved. The large amount of noise is due to the low absorbance values caused by the thin nature of the films imaged. There is little difference between a bulk solvent attachment process and a dropwise attachment process. However, the spectrum lost its shape somewhat when the bulk deposited film was exposed to a water bath whereas the dropwise film was seemingly unaffected. It is interesting to note that the 10 min methanol bath (used to remove water from the PEDOT:PSS film) appeared to decrease the sharpness of the trough, moving it past the lower edge of the spectrum. The bottom left plot in Figure 6-2 shows changes in spectra caused by changes in spin speed. At 500 rpm, the shape is different from the norm. When the PEDOT:PSS was spun at 500 rpm it was clear, visually, that a thin film was not formed properly, indicating that this speed is too slow for correct film formation. Initially, it is not clear what effect

further spin speed changes have on the film formation as the 850 nm peak for the 1500 rpm sample is lower than the 3000 rpm sample, yet the peak height decreases from there. However, by taking the difference between the 850 nm peak and the baseline at around 450 nm a number could be found to describe the relative peak intensity to some degree.

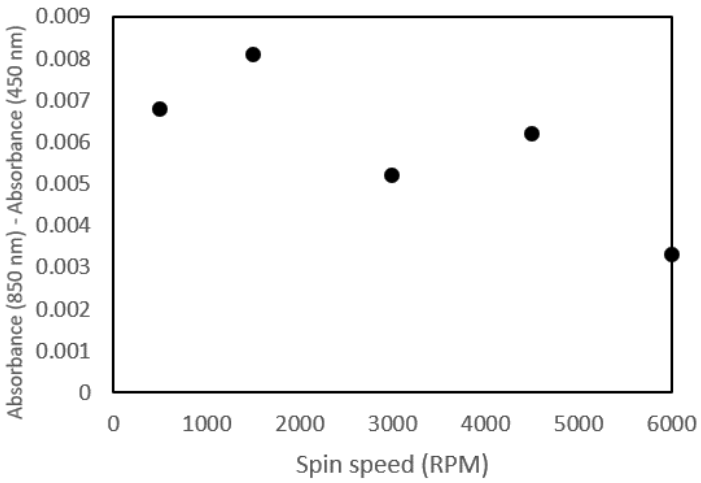

Figure 6-3: Relative peak absorbance difference for different spin speeds.

Figure 6-3 shows a plot of relative peak height (peak absorbance at 850 nm minus baseline absorbance at 450 nm) for the different spin speed samples. It is clear that there is a general downward trend, indicating that the spectra become flatter as the spin speed is increased. This indicates that the films decrease in thickness with an increase in spin speed. It was also visible in Figure 6-2 that a change in volume has little effect on film formation between 300 µL and 400 µL, however a large decrease in 850 nm peak height is seen when the volume is dropped to 200 µL. This indicates that the higher volumes are required to give optimal film formation.

Additionally, PEDOT:PSS films on glass were exposed two dopant chemicals commonly used in CNT/Si heterojunction devices: gold chloride ($AuCl_3$) and thionyl chloride ($SOCl_2$). The UV/Visible spectra of these films were compared with spectra taken before chemical exposure. Note that $SOCl_2$ doping was accomplished via a 2 min vapour exposure and not direct contact to avoid dissolving the polymer.

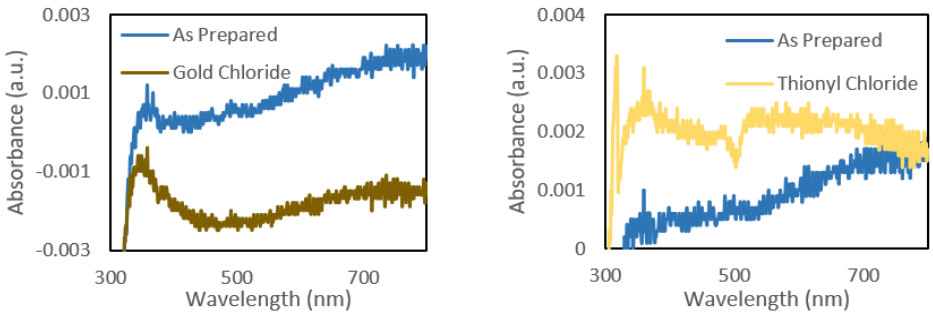

Figure 6-4: UV/Visible spectra of PEDOT:PSS films as prepared and after exposure to the chemical dopants $AuCl_3$ (Left) and $SOCl_2$ (Right). Films were spun at 3000 rpm from a 400 µL aliquot deposited dropwise.

Both dopant chemicals have an effect on the UV/Visible spectra of PEDOT:PSS films (Figure 6-4) however the effect was more significant when the films were exposed to $SOCl_2$.There was a slight drift to the left for the peak when exposed to $AuCl_3$. It was difficult to determine the effect of $SOCl_2$ on the PEDOT:PSS film as the spectrum was dominated by noise.

6.2.3 PANI Film Characterisation

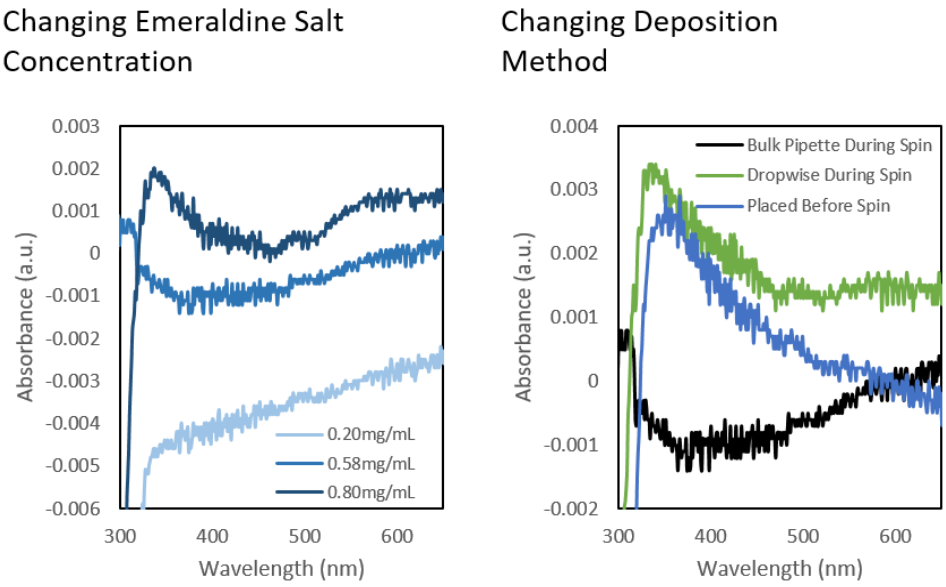

Figure 6-5: UV/Visible spectra of initial PANI films on glass. Spun at 3000 rpm from s 500 µL aliquot deposited dropwise for the LHS plot.

Initially, the PANI films were produced using a concentration of 0.58 mg mL^{-1}, as stated by Yu *et al.*[131] This concentration is compared with both a higher concentration of 0.80 mg mL^{-1} and a lower concentration of 0.20 mg mL^{-1}. A comparison was performed between three different deposition techniques: bulk and dropwise (as above for PEDOT:PSS) and a third method where the PANI aliquot was placed on the substrate prior to spinning. Figure 6-5 shows the UV/Visible spectra produced from these two comparisons. The UV/Visible spectra for different emeraldine salt concentration shows that

the lower concentrations are too low to give a clear peak. However, the 0.80 mg mL^{-1} spectrum displayed a more distinct peak at around 580 nm – 600 nm. The concentration was increased to 1.0 mg mL^{-1} and a volume of 500 µL was spun dropwise (as this method gave the best spectral shape in Figure 6-5) to form a more distinct peak shape.

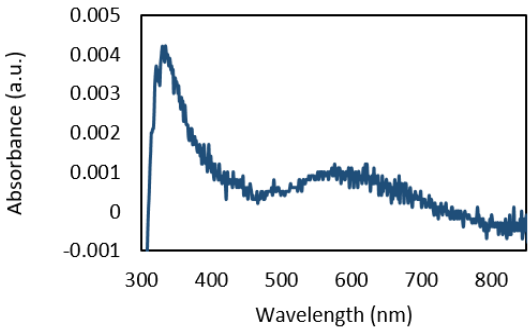

Figure 6-6: UV/Visible spectrum for a 500 µL aliquot of 1.0 mg mL^{-1} spun dropwise at 3000 rpm.

Figure 6-6 shows that at the higher concentration of 1.0 mg mL^{-1} provides a clear peak at around 590 nm and a trough from 800 to 850 nm. A similar spin speed experiment to that performed with PEDOT:PSS was performed with 500 µL aliquots of this concentration of PANI spun dropwise.

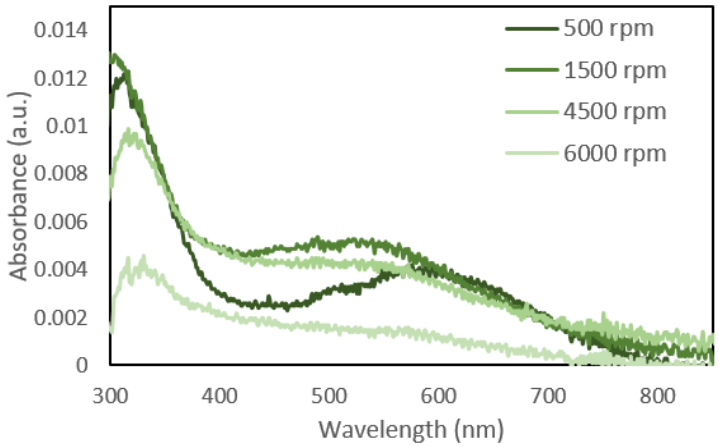

Figure 6-7: UV/Visible spectra of PANI films spun dropwise at different speeds from 500 µL aliquots of 1.0 mg mL^{-1} concentration solution.

Figure 6-7 shows the effect of different spin speed on the UV/Visible spectrum of PANI films. The 500 rpm spectrum has a different shape than the other three spin speed spectra. This is similar to the difference observed for PEDOT:PSS (Figure 6-2). Aside from this, it is noticeable that the characteristic peak drops in intensity relative to the rest of the spectra as the spin speed increases, indicating that the film thickness decreased with an increase in spin speed similarly to PEDOT:PSS. Figure 6-8 shows

a PANI plot of relative peak height similar to Figure 6-3. The decrease in peak height relative to the background is clear as the points decrease with spin speed. The 4500 rpm and 6000 rpm samples have negative differences as the background was rising towards the lower wavelength end of the spectrum and thus the absorbance is higher at 420 nm than at 546 nm.

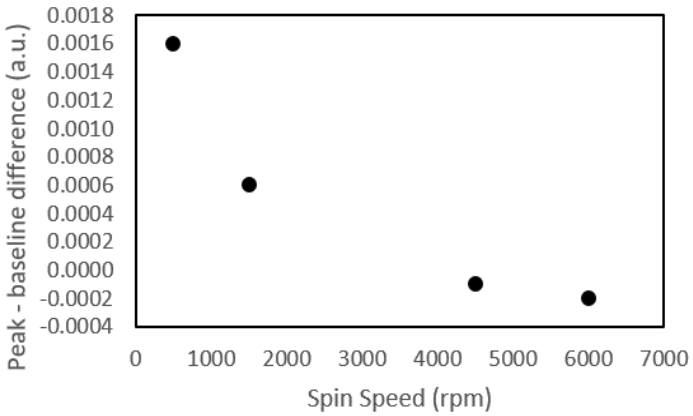

Figure 6-8: Peak - baseline absorbance difference vs spin speed. The peak wavelength was 546 nm with the baseline at 420 nm for the 1500, 4500, and 6000 rpm samples. The peak and baseline were 600 nm and 450 nm for the 500 rpm sample.

As for PEDOT:PSS films, UV/Visible spectra of PANI films was taken before and after treatment with $AuCl_3$ and $SOCl_2$.

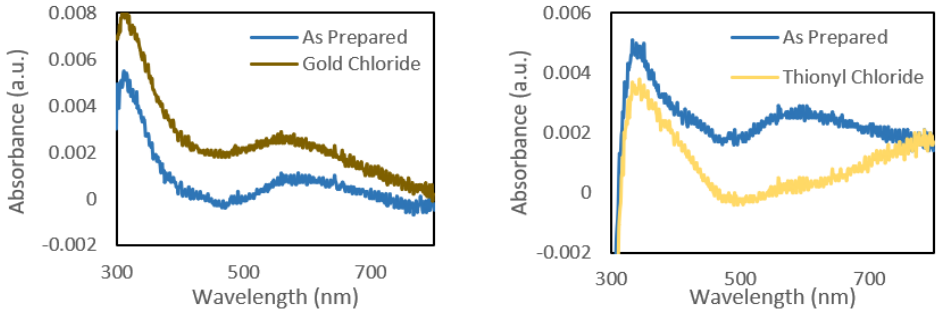

Figure 6-9: UV/Visible spectra of PANI films before and after exposure to $AuCl_3$ (Left) and $SOCl_2$ (Right). Films were spun at 3000 rpm from a 500 µL aliquot deposited dropwise.

Both dopants had an effect on the spectra of PANI films (Figure 6-9). Similar to PEDOT:PSS, the peak shifted slightly to the left after $AuCl_3$ exposure. The $SOCl_2$ had a much more significant effect, with the PANI peak shifting from around 550 nm – 600 nm to beyond 750 nm.

6.2.4 AFM and SEM Images

6.2.4.1 AFM Images of PEDOT:PSS Films

AFM analysis was used to determine the thickness of the polymer layers. The probe was scanned across the scratches in the films, taking height measurements at both the surface of the polymer film and the silicon substrate underneath. Thus, an accurate height of the polymer films could be determined, a relationship between spin speed and film thickness, and an optimal thickness for CNT/Si device implementation determined. Two plots representing film thickness are presented for each AFM height map in this chapter. A set of three cross-sectional line graphs are produced from lines across the film. The data for these lines is offset to allow all three lines to be presented on the same plot. The amount of offset is indicated for each plot. The second plot is a height distribution plot in which the percentage of pixels on the height map that correspond to each height is presented. The advantage of the cross-sectional line graphs is that specific areas on the film can be investigated for height. However, the lines may not represent the entire height map. The height distribution plot takes the entire height map into account and will thus represent the entire sample. However, this plot is more likely to be affected by particles of anomalous height and the inherent feedback mechanism of AFM imaging causing areas on either side of high contaminant particles to appear lower. An example of this phenomenon is seen in Figure 6-10 on the 6000 rpm height map.

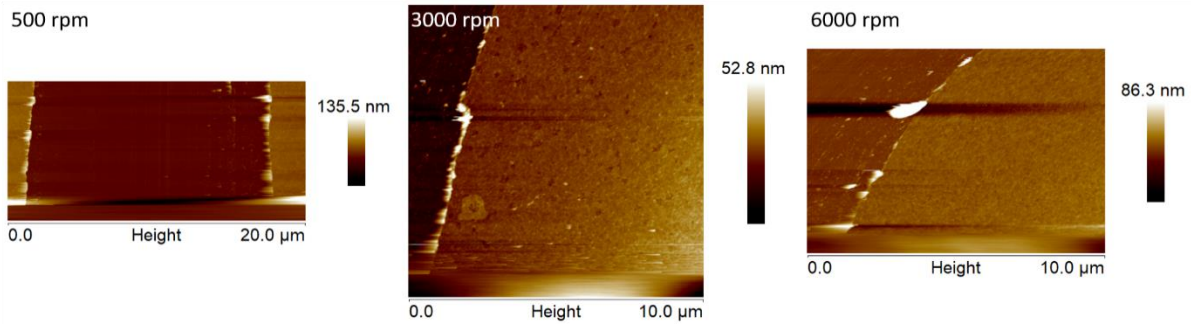

Figure 6-10: AFM height maps of PEDOT:PSS films spun dropwise from 400 µL aliquots at various spin speeds.

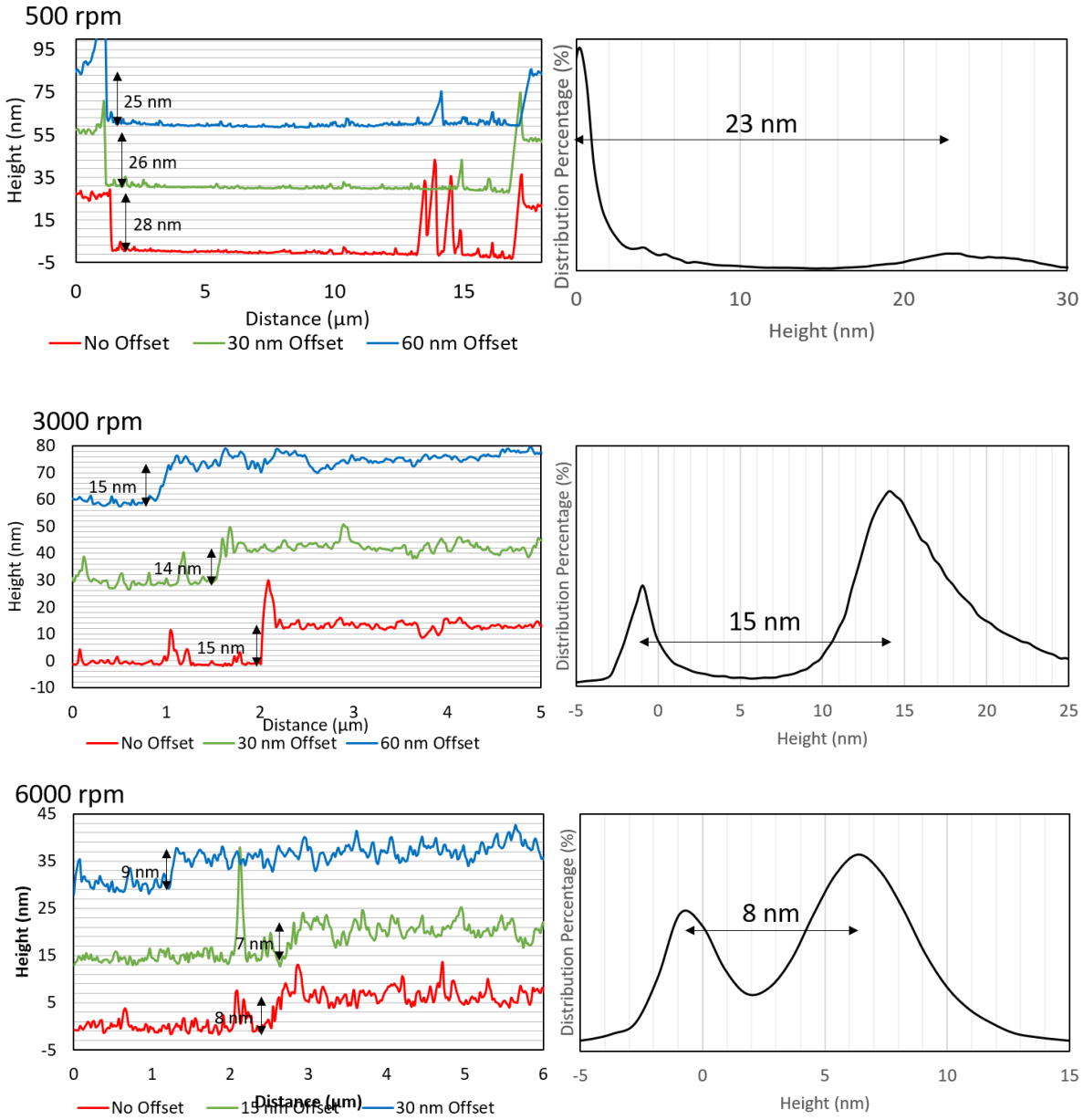

Figure 6-11: Cross sectional and height distribution data for PEDOT:PSS films at different spin speeds.

From the cross sectional AFM data for PEDOT:PSS films, Figure 6-10 and Figure 6-11, the height of the layer can be determined. There is a clear trend of decreasing film thickness with increasing spin speed. The film height was around 17 nm at a spin speed of 500 rpm, around 13 nm at 3000 rpm and around 8 nm at 6000 rpm.

6.2.4.2 SEM Images of PEDOT:PSS Films

SEM images were taken of PEDOT:PSS films at different spin rates. An issue with SEM imaging of thin films is that, unless they exhibit a degree of surface roughness, their presence can often be hard to detect as they will appear visually similar to a bare substrate. Thus, it was decided to manually damage

the film via light scratching with a scalpel. The scalpel will remove any polymer layer present on the surface but will have no effect on the much denser silicon underneath. Thus, the scratches will appear under SEM, allowing the film to be observed. These scratches were also applied for film thickness determination in AFM (Section 6.2.4.1).

As mentioned previously, the dilution solvent for the PEDOT:PSS was changed from water to IPA. This was done in order to provide better, more homogenous attachment of the PEDOT:PSS to the silicon surface. To demonstrate this improvement SEM images were taken of PEDOT:PSS films produced from a 1:10 water dilution and compared with images taken of PEDOT:PSS films produced from a 1:1 IPA dilution.

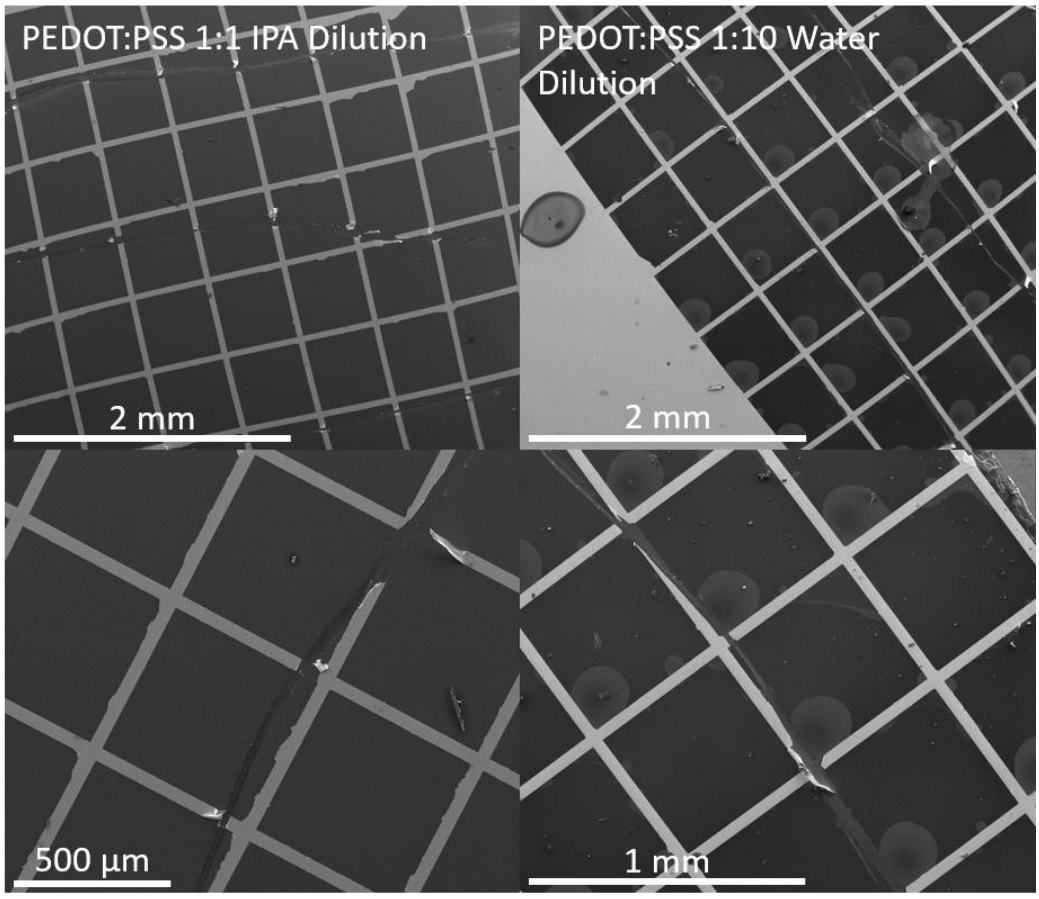

Figure 6-12: SEM images of PEDOT:PSS films on silicon/gold substrates. Films were spun dropwise from 400 µL aliquots at 3000 rpm.

Figure 6-12 shows PEDOT:PSS films produced from a 1:1 IPA dilution and from a 1:10 water dilution. It is obvious that the IPA diluted sample gave a much smoother, more homogenous film than the 1:10 water dilution. The images of 1:10 water diluted films show large blobs in the corners of most of the

grid squares, whereas the 1:5 IPA diluted films were smooth, homogenous films. PEDOT:PSS films were produced at different spin speeds and are shown in Figure 6-16.

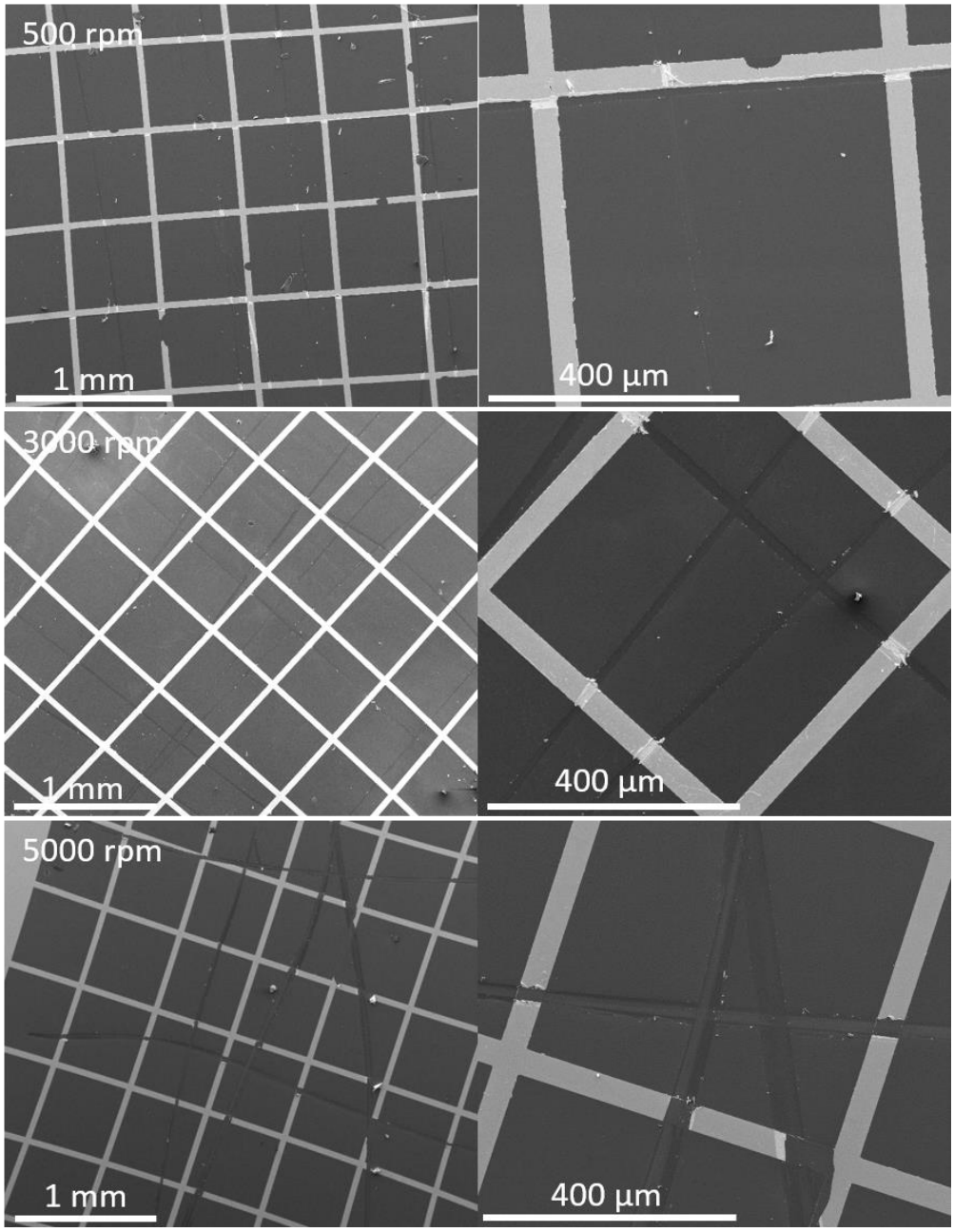

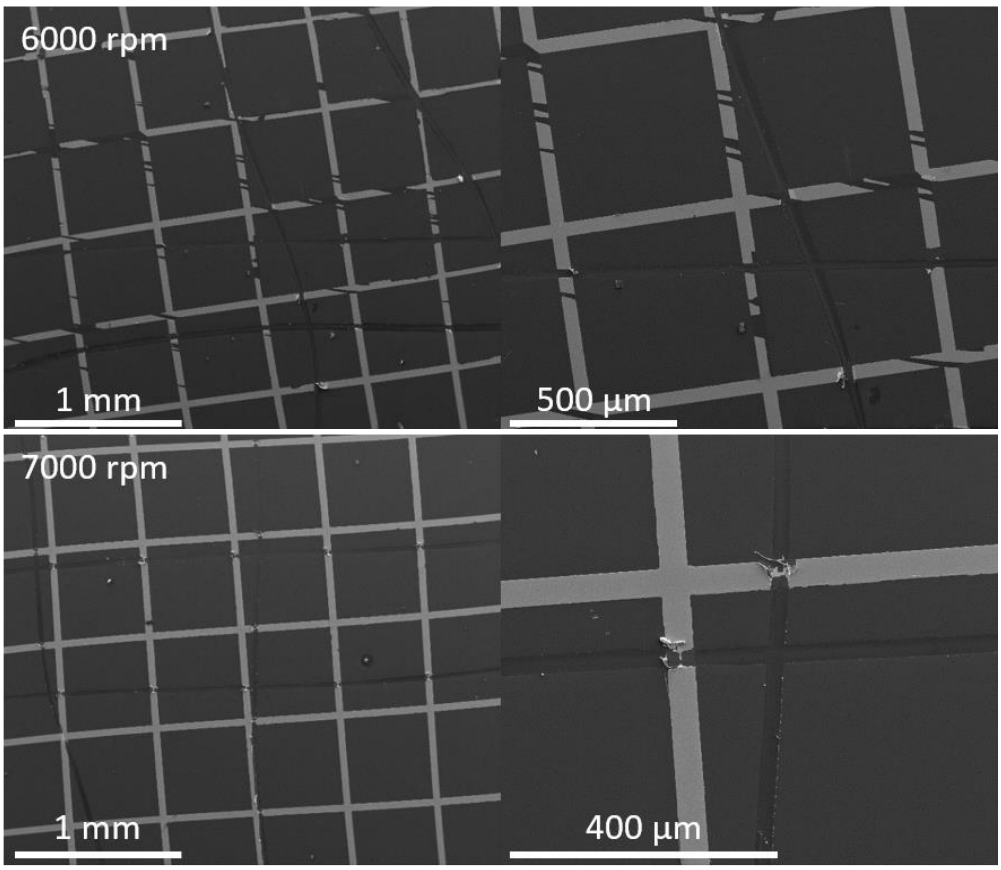

Figure 6-13: PEDOT:PSS films spun from 400 µL aliquots dropwise at various spin speeds.

The difference in spin speed makes no difference in the aspects of film morphology that can be observed with SEM imaging. In all cases the films appear smooth and homogenous. Some holes, likely caused by air bubbles trapped during spin coating, are visible in the close-up 7000 rpm image, but these defects seem rare. Note that in the 6000 rpm images there is significant damage to the gold grid lines present. This was because the silicon/gold substrates used for SEM/AFM imaging often were not perfectly formed. The substrates that had no obvious defects in the grid pattern were reserved for device fabrication. Thus, it is common to see defects in the grid network in SEM imaged samples.

6.2.4.3 AFM Images of PANI Films

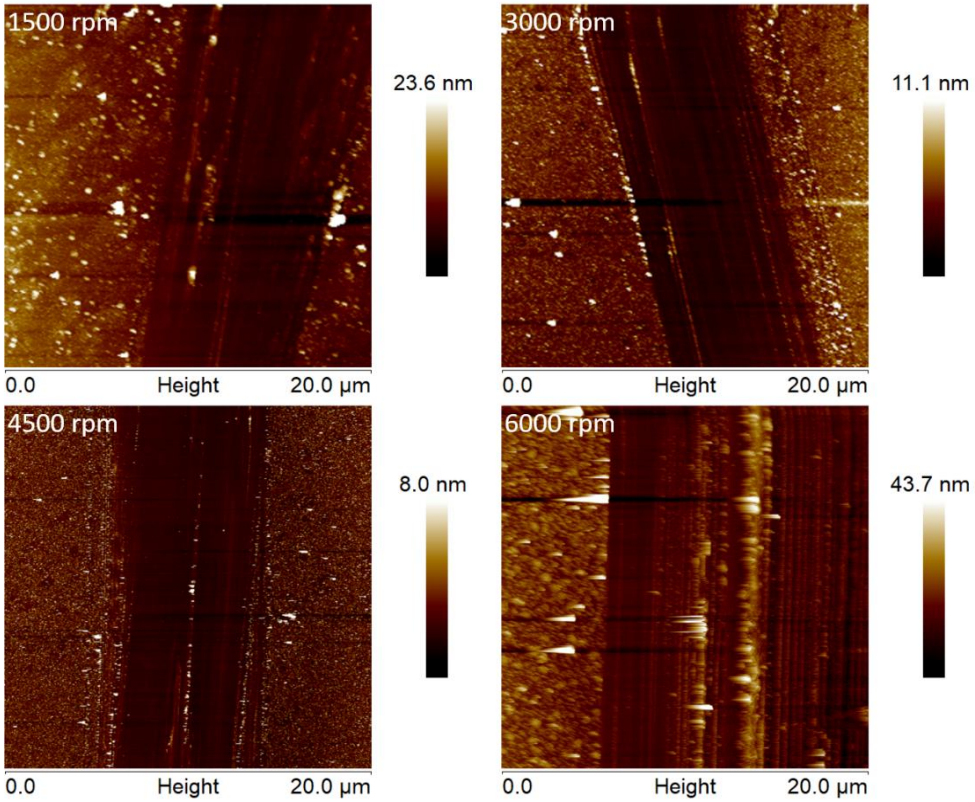

Figure 6-14: AFM height maps of PANI films at spun dropwise from 500 µL aliquots from 1.0 mg mL^{-1} solution at different spin speeds

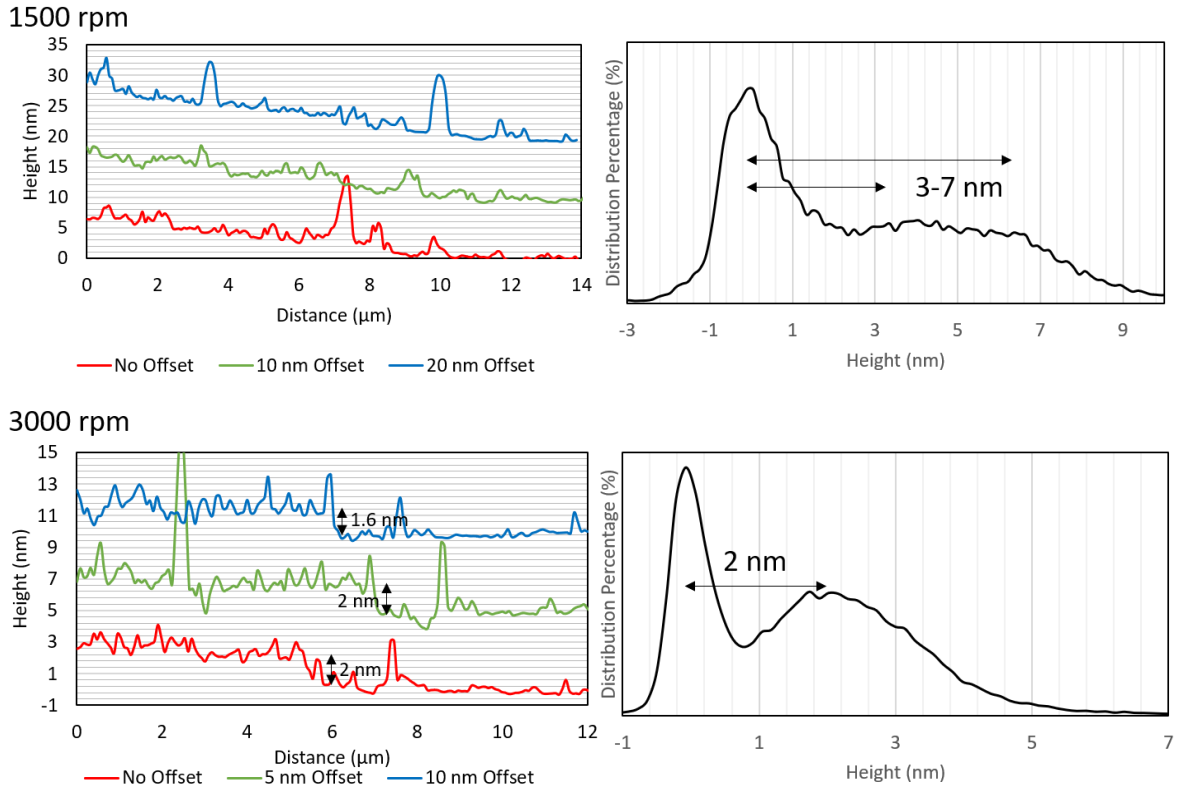

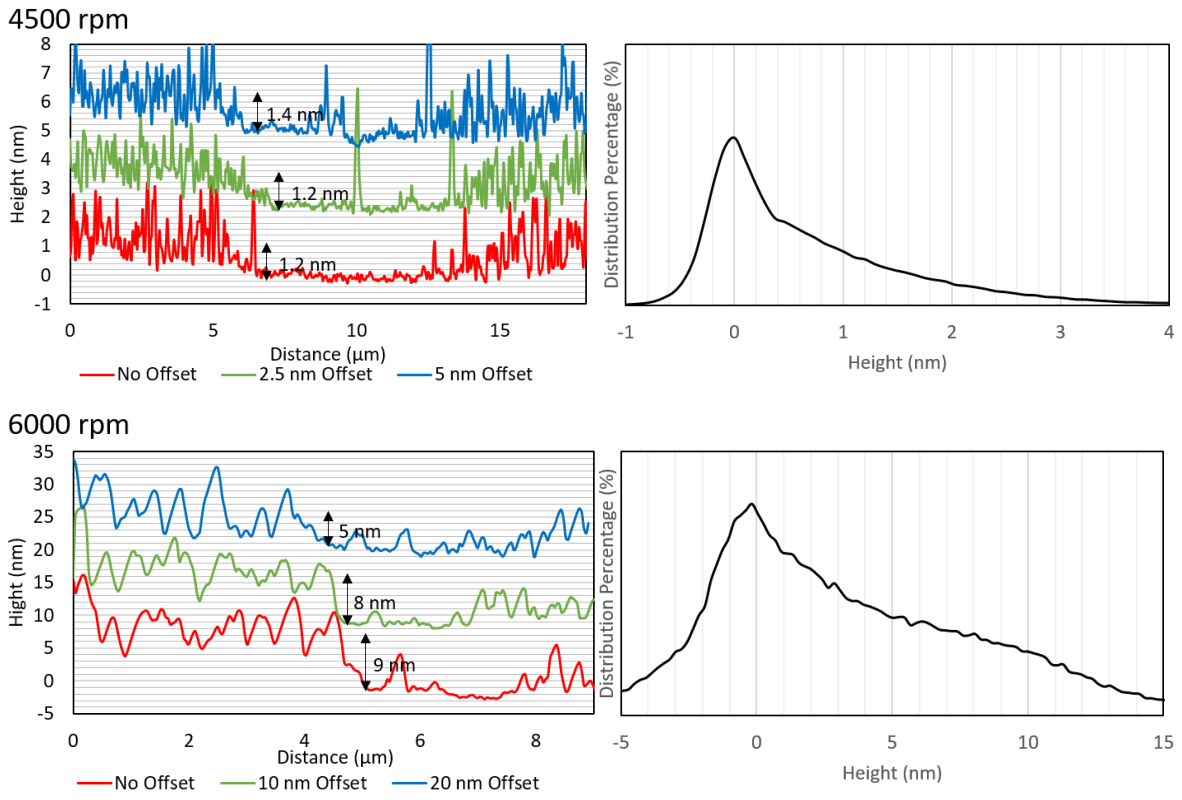

Figure 6-15: Cross-sectional line graphs and height distribution plots from AFM height maps of PANI films at different spin speeds.

Figure 6-14 and Figure 6-15 display the AFM maps and cross-sectional data of PANI films formed at different spin speeds. The cross-sectional line graphs for the 1500 rpm film show no clear cliff, which makes it difficult to determine a film thickness from this alone. The height distribution plot gives a thickness of 3 nm to 7 nm due to a broad height distribution after the clear peak at 0 nm. The height distribution plot for the 3000 rpm sample gave a film thickness of 2 nm, with a more distinct film height peak than the 1500 rpm sample. For the two higher spin speeds the height distribution plots were not useful as they displayed gradual downward curves after the 0 nm peak rather than a corresponding film height peak. This was due to the nonhomogeneous nature of the PANI films, which is also visible in the AFM height maps (Figure 6-14). The cross-sectional line graphs allow the edges themselves to be specifically probed and thus, gave a better indication of the film thickness. The 3000 rpm sample was roughly 2 nm thick, whilst the 4500 rpm sample was roughly 1.2 nm thick. This shows a trend of decreasing film thickness with increasing spin speed. The 6000 rpm sample does not fit this trend, showing a film thickness of 5 – 9 nm. The high variances in the 4500 rpm and 6000 rpm samples,

coupled with large amounts of noise in the 4500 rpm sample and unresolved film height peaks in the height distribution plots, suggests that these films consisted more of islands of PANI on the surface, than homogeneous films. However, the AFM height maps Figure 6-14 are visually similar for all spin speeds, suggesting that the four films are similar in lack of homogeneity.

6.2.4.4 SEM Images of PANI Films

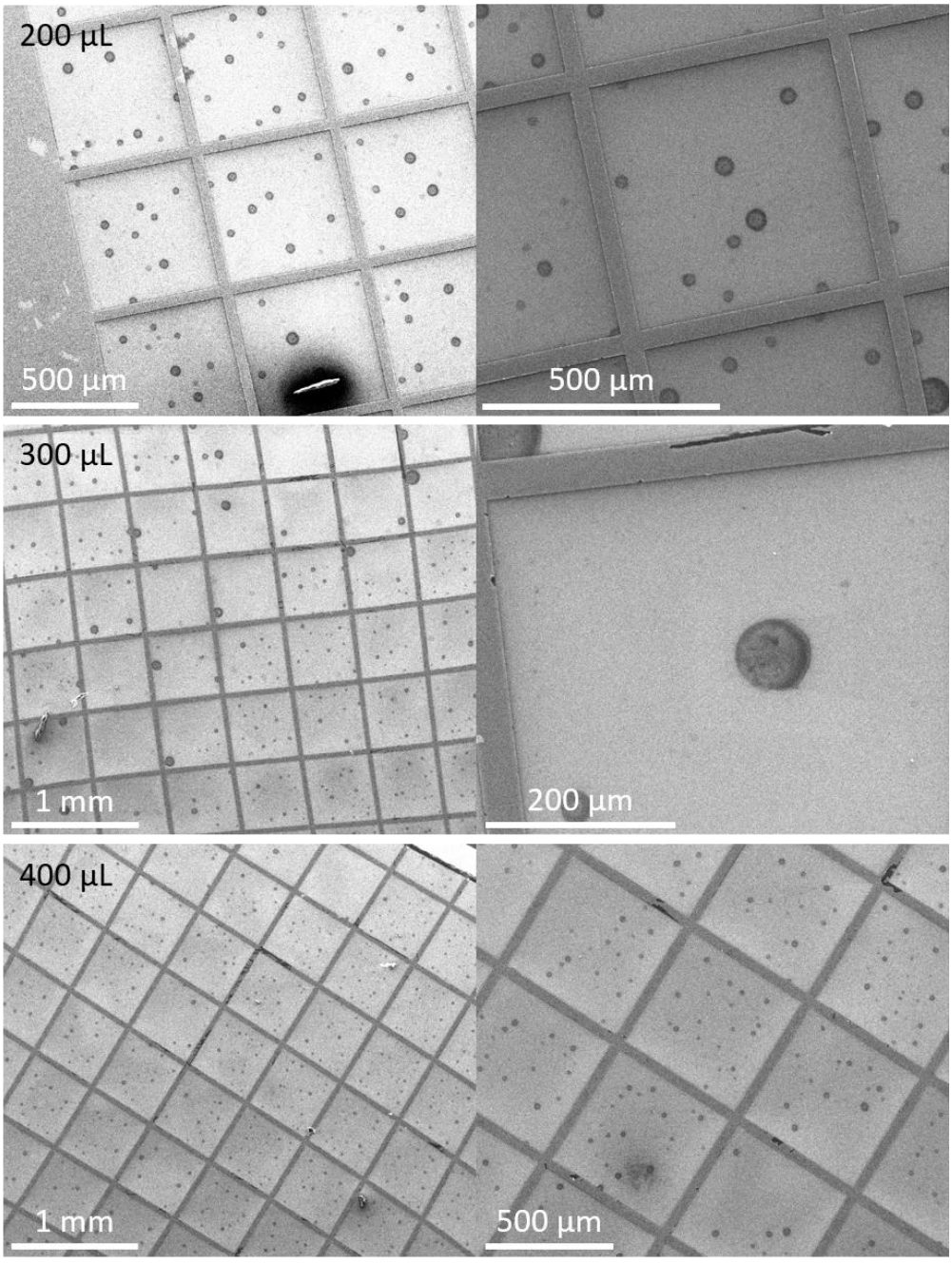

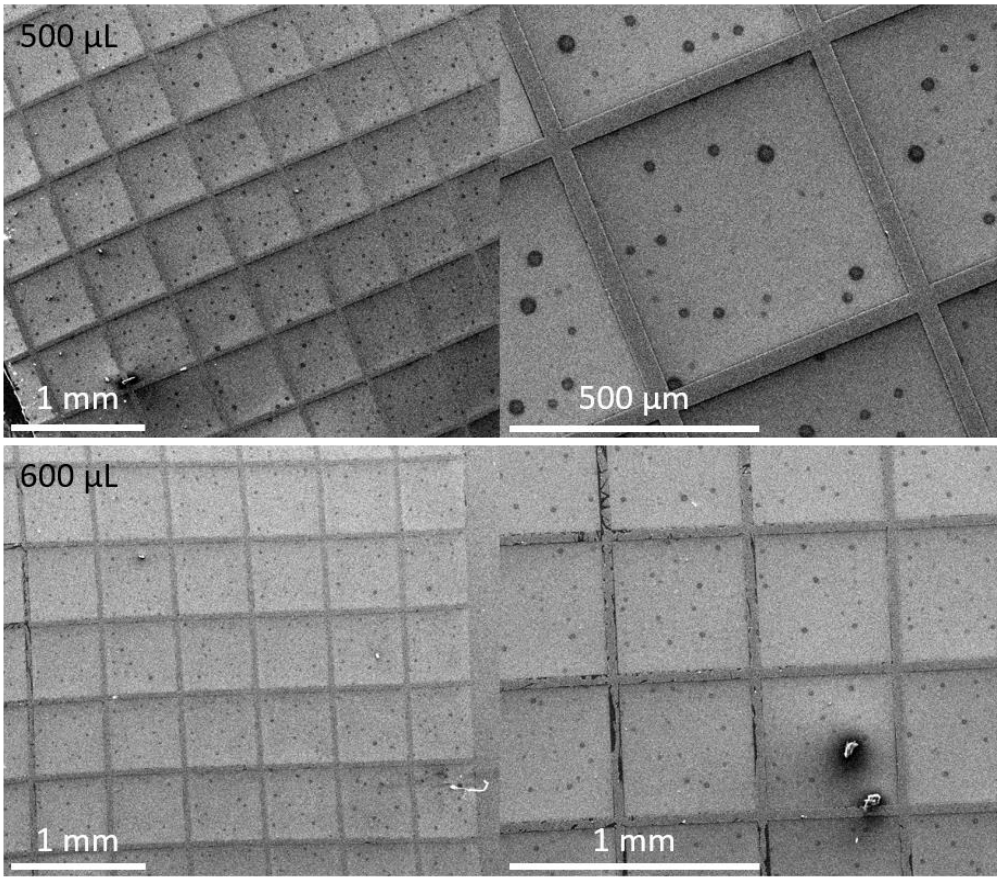

Figure 6-16: SEM images of PANI films spun at 3000 rpm from different aliquot volumes deposited dropwise.

Initially, SEM images were taken of PANI films formed with different polymer solution volume. The most important aspect of these images (Figure 6-16) is that these films are not as smooth and homogenous as the PEDOT:PSS films shown in Figure 6-13. There are many holes present in the films, with little difference observable with changing aliquot volume.

6.2.5 Solar Device Data

6.2.5.1 PEDOT:PSS Devices with Varied Solution Volume

The initial experiments involved varying the volume of applied polymer solution during spin coating. In the small area devices a few drops was all that was required for a film,[131] but for a larger area it was assumed that a higher volume was required. To ascertain the optimal volume for each polymer, a range of volumes were used to fabricate sets of devices and the J/V curves recorded and the properties averaged for each volume. The devices were tested as prepared and after treatment with aqueous gold chloride.

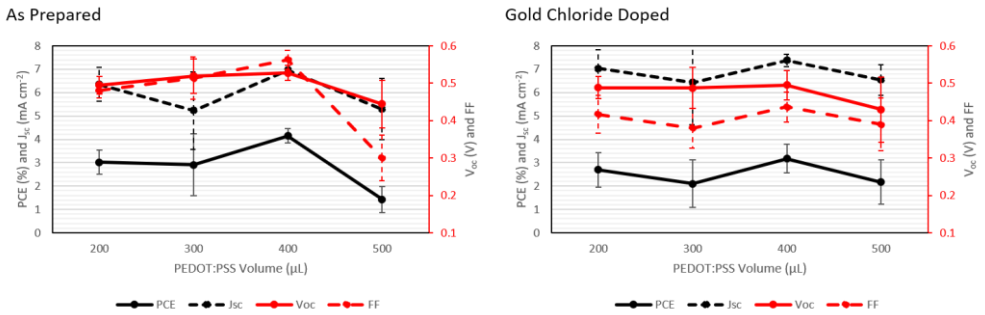

Figure 6-17: J/V properties for devices with different PEDOT:PSS solution volume, spun at 3000 rpm for 30 s.

The PEDOT:PSS data in Figure 6-17 shows a general trend of increasing PCE with the applied volume of polymer solution (diluted 1:10 with water) until at the 500 µL data point when a significant drop in PCE was observed. It is noticeable that for the first three volume data points the PCE decreased when a gold chloride chemical dope was applied. In general, this trend is common for PEDOT:PSS where the as prepared sample performance is superior to the performance after doping. The large error bars visible on some of the data points are due to individual poorly performing devices, when the worst performing device from each set was removed the trend of increasing PCE with volume up to 400 µL was even more apparent. The same trend is observed for the J_{sc},, whilst the V_{oc} and FF display a clearer trend without a dip in performance at the 300 µL point. The significant drop in PCE at the 500 µL data point is due to a significant drop in FF. The average V_{oc} and J_{sc} are also lower at this point, but the drop in FF is much more severe. This FF drop is recovered somewhat with doping with aqueous gold chloride however the FF of the other data points decreased with doping.

6.2.5.2 PANI Devices with Varied Solution Volume

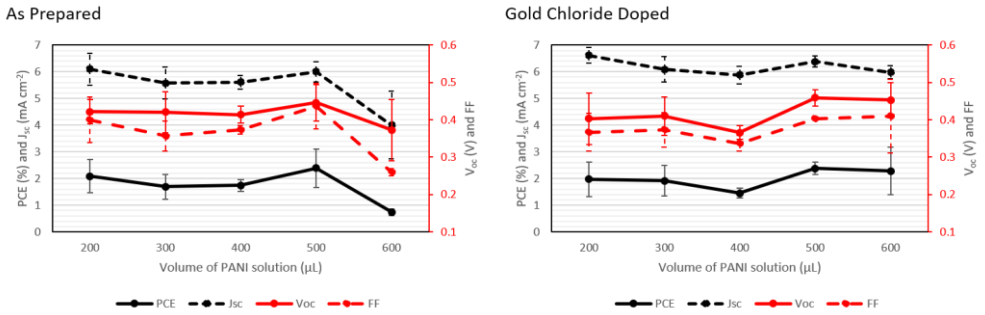

Figure 6-18: J/V properties of devices prepared with different volumes of PANI solution, spun at 3000 rpm for 30 s.

The PCE data for different PANI solution volume (Figure 6-18) displays a less clear trend than that observed from PEDOT:PSS. There is a slight trend downwards in performance from 200 µL to 300 µL followed by an upwards trend from 400 µL to 500 µL. Whilst the gold chloride doping does not lead

to a significant performance drop, as seen in the PEDOT:PSS samples, it does not seem to give much improvement either, with the notable exception of the 600 µL data point. Once again, the lowest PCE data point (600 µL) corresponds to a significant drop in FF which is then recovered with aqueous gold chloride doping.

Overall, the PANI devices showed a lower performance than the PEDOT:PSS devices. Although, the two sets cannot be directly compared as the substrate preparation regime was different between the sets. For the PEDOT:PSS set the substrates were cleaned with a water – ethanol – acetone rinse cycle and the devices were left in air for 30 min after BOE etching to encourage a thin atmospheric oxide to grow. For the PANI set, the substrates were cleaned via sonication in a water – IPA – ethanol cycle and the devices were treated with H_2O_2 for 5 s after BOE etch to grow a thin passivating oxide layer. It was later shown that this second regime leads to poorer device results than the former regime (Section 5.5). Thus, in order to analyse the performance of the interlayers the PEDOT:PSS devices and the PANI devices must be compared with concurrently produced devices with no interlayer following the same cleaning regime. For the PEDOT:PSS case, devices with no interlayer were fabricated and found to produce an average PCE of 2.89 % ± 0.40 after gold chloride treatment. As can be seen in Figure 6-17, the best performing PEDOT:PSS devices at 400 µL produced an average PCE of 3.17 % ± 0.61. For the PANI case, devices with no interlayer were fabricated and found to produce an average PCE of 1.94 % ± 0.38 after gold chloride treatment. As can be seen in Figure 6-18, the best performing PANI devices at 500 µL and 600 µL produced an average PCE of 2.37 % ± 0.23 after gold chloride and an average PCE of 2.28 % ± 0.89 after gold chloride respectively. Additionally, both sets of devices at the higher two volumes produced one device over 3 %. Overall, this shows that when the change in cleaning regime is taken into account, both PEDOT:PSS and PANI give significant improvement in device performance when compared to devices with no interlayer. The full comparison between devices with and without interlayers is shown in Figure 6-19.

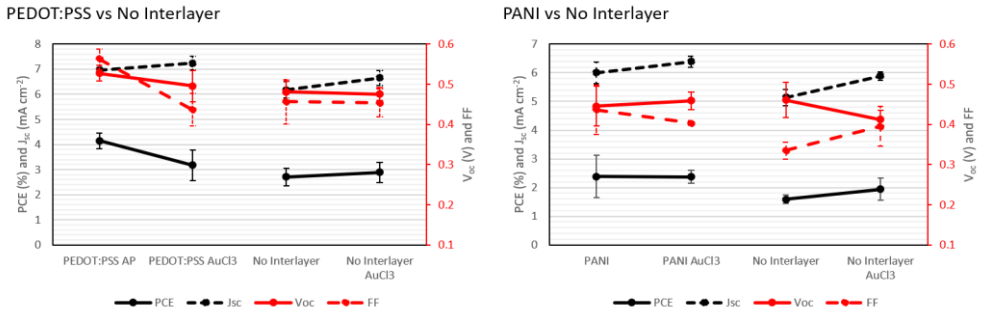

Figure 6-19: J/V properties of devices with PEDOT:PSS or PANI interlayers and concurrently produced devices with no interlayer.

The optimal volume as determined from the above data was 400 µL for the PEDOT:PSS solution due to the peak in PCE at this volume. For PANI the optimal volume was determined to be 500 µL as this was the lower volume of the two highest performing volumes. Figure 6-19 shows that at these optimal volumes, both PEDOT:PSS and PANI serve to improve device performance due to improvements in J_{sc} and FF. Additionally, doping with gold chloride serves to improve device consistency for devices with PANI interlayers but leads to significant deterioration in FF, and thus PCE, for devices with PEDOT:PSS interlayers.

6.2.5.3 PEDOT:PSS and PANI Devices with Varied Spin Speed

CNT/Si heterojunction solar devices were fabricated with PEDOT:PSS and PANI films at different spin speeds to investigate the effect different film thicknesses had on device performance.

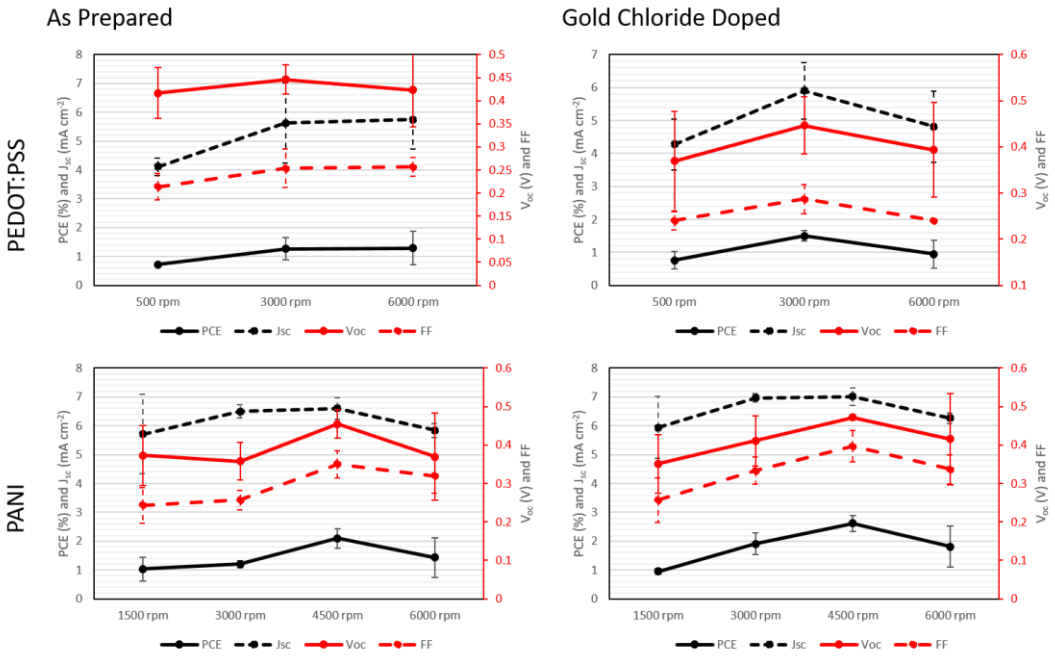

Figure 6-20: J/V properties of devices with PEDOT:PSS (top) and PANI (bottom) at different spin speeds before and after $AuCl_3$ doping.

Figure 6-20 shows the device performance trend with polymer spin speed for both PEDOT:PSS and PANI films. It is clear that spin speed (and thus film thickness) had a significant effect on device performance. In both cases an optimal spin speed was identified, 3000 rpm for PEDOT:PSS and 4500 rpm for PANI. For these samples the PCE values for devices with PEDOT:PSS are significantly lower than that observed in the initial experiment (Figure 6-17). This was due to the same cleaning regime problems as described for the PANI devices in Figure 6-18, including the post BOE etch H_2O_2 treatment. The film thickness had an effect on all three device parameters presented in Figure 6-20. With increases and decreases in J_{sc}, V_{oc}, and FF contributing to the PCE trend with spin speed.

From the device data in Figure 6-20 and the height data in Figure 6-11 it is apparent that the optimal film thickness for PEDOT:PSS is around 13 nm. This is compared to Yu *et al.* who achieved significant performance improvement on small area CNT/Si devices with PEDOT:PSS films around 5 nm thick.[131] This thickness is significantly lower than that used in Si/PEDOT:PSS devices where the PEDOT:PSS film can be 110 nm[211], 200 nm[212] or 2.65 µm thick.[213] Although, for the last reference the PEDOT:PSS was covering an array of nanowires and thus the distance between wires was more important than the thickness of the layer.[213]

The optimal spin speed for PANI films was determined to be 4500 rpm (Figure 6-20). The AFM height data (Figure 6-14) suggested that the film thickness at this spin speed was > 2 nm. However, the large amount of variation in the AFM height data for PANI films calls this into question. It is clear that the thickness of the PANI film is likely > 5 nm at least, with a spin speed of 4500 rpm. This is similar to the research by Yu *et al*. which showed an improvement in CNT/Si device performance with PANI films of around 5 nm thick.[131]

From the above data optimal film attachment conditions were determined to produce the best performing devices. In order to reconcile the data in Figure 6-20 with Figure 6-17 and Figure 6-18

devices were produced under these optimal conditions but using the former washing regime and with a 30 minute wait in air rather than a H_2O_2 treatment.

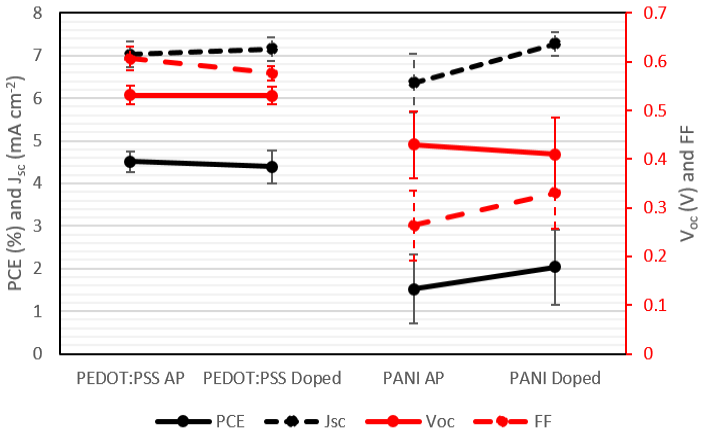

Figure 6-21: J/V properties for devices with optimal PEDOT:PSS and PANI films with a 30 minute wait instead of an H_2O_2 treatment. PEDOT:PSS devices were doped with $SOCl_2$ and PANI devices with $AuCl_3$.

In the PEDOT:PSS case the devices as prepared performed with an average PCE of 4.51 % ± 0.25 with a decrease in performance following doping and 2% HF etching as was observed for other PEDOT:PSS devices. For devices with a PANI interlayer the devices improved with gold chloride treatment up to an average PCE of 2.03 % ± 0.89. It is apparent that reverting to the original substrate cleaning and preparation method PEDOT:PSS devices are improved to the high performing values as originally seen in Figure 6-17. However, this was not the case with PANI, with the new set of devices performing worse than the previous two experiments seen here (Figure 6-18 and Figure 6-20). This data is shown in Figure 6-30 at the end of section 6.1.

6.2.5.4 PANI (DMF) Devices

It was apparent that the PANI suspension was not forming homogeneous surface coatings to the same extent as PEDOT:PSS. In general, the films formed were much thinner and rougher, especially at higher spin speeds. An explanation of this could be that the PANI solution is not properly wetting the substrate. It became apparent during experimentation that interlayers dissolved in more hydrophobic solvents formed much better layers than those in hydrophilic solvents. Hence the improvement in surface coverage when the PEDOT:PSS solvent was changed from water to IPA. The PANI used thus far consisted of emeraldine salts dissolved in a hydrophilic 80 % acetic acid solution. Previously, PANI

has also been applied to the CNT/Si heterojunction solar device by dissolving the same salts in the hydrophobic dimethylformamide (DMF).[128] Thus, PANI suspensions prepared in this fashion was also applied to large area devices. An issue with using DMF is that an acid dopant is required,[128] previously the 80 % acetic acid solvent was acting as both a dopant and solvent. In order to dope the PANI, drops of 2 % HCl solution were added during spin coating in between each drop of PANI solution. The effect of this was measured using UV/Visible spectrophotometry.

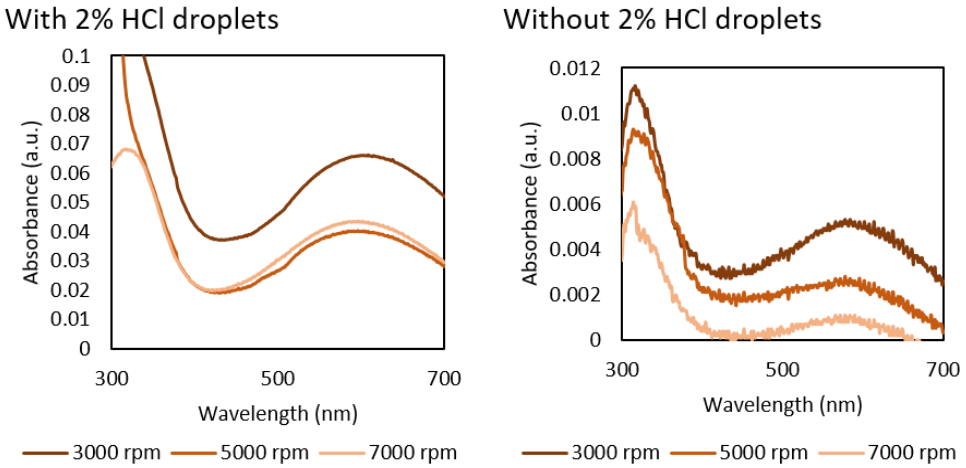

Figure 6-22: UV/Visible spectra of PANI films produced from 500 µL aliquots of a DMF solution at different spin speeds.

Figure 6-22 shows an additional effect of the acid droplets. The addition of the acid droplets causes a much stronger absorbance signal from the formed PANI layer. This may be indicative of thicker, more homogenous film formation although it is unclear why the addition of aqueous acid droplets would have this effect.

When PANI films from DMF suspension were spin coated onto glass substrates the colour was blue. This was unexpected as the PANI films spun from 80 % acetic acid suspension were green. It was observed that the colour of the PANI films from DMF suspension changed during the 2 hr annealing step. After annealing, the PANI films spun from DMF suspension were the same green colour as the as-spun films from 80 % acetic acid suspension. To characterise this, films were spun from both suspensions and imaged prior to annealing. The spectra in Figure 6-23 shows a clear difference in peak position, explaining the observed colour difference.

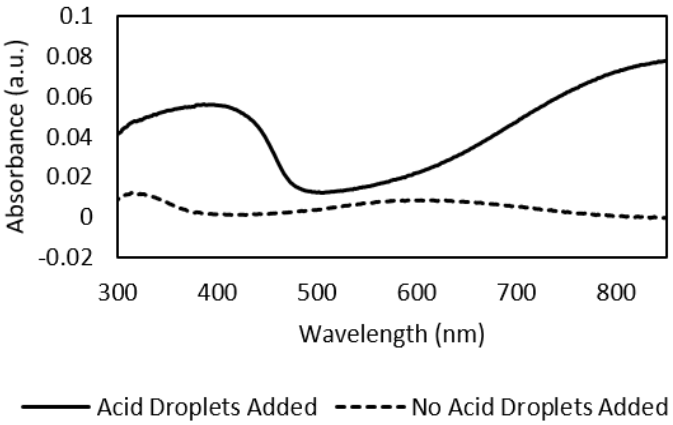

Figure 6-23: UV/Visible spectra of PANI films formed from DMF solution with and without acid droplets with no annealing.

It appears that the addition of the acid droplets causes a different spectral shape than that shown for PANI films produced from 80 % acetic acid suspension, although these were not observed to change colour during the annealing step. The PANI films shown to have improved CNT/Si device performance previously displayed a UV/Visible peak before the 700 nm point.[128] Thus, the change to green is consistent with previous reports.

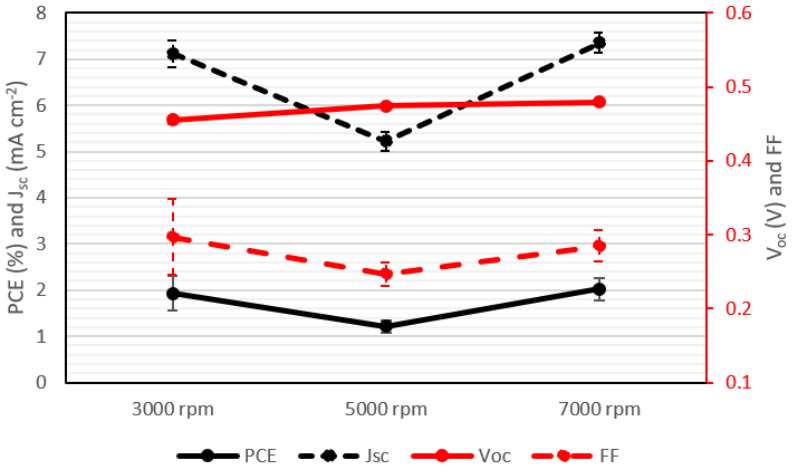

Figure 6-24: J/V properties of devices produced with PANI films from DMF solution at different spin speed after a thionyl chloride vapour dope.

Figure 6-24 shows average PCE data for devices produced with PANI films spun from DMF solutions at different spin speeds. These devices were doped with thionyl chloride vapour instead of aqueous gold chloride solution. It is notable that there seems to be little spin speed dependency on device performance. The devices with films produced at 5000 rpm performed worse than both the 3000 rpm and 7000 rpm samples, this was due to a significantly lower average J_{sc} (5.22 ± 0.20 mA cm^{-2} compared

with 7.12 ± 0.29 mA cm^{-2} (3000 rpm) and 7.35 ± 0.21 mA cm^{-2} (7000 rpm)) and lower average FF (0.25 ± 0.02 compared with 0.30 ± 0.05 (3000 rpm) and 0.29 ± 0.02 (7000 rpm)). Overall, the PCE values achieved for devices with PANI films spun from DMF solution are not significant improvements over those seen with PANI films spun from 80 % acetic acid solutions.

6.2.5.4.1 SEM Images of PANI (DMF) Films

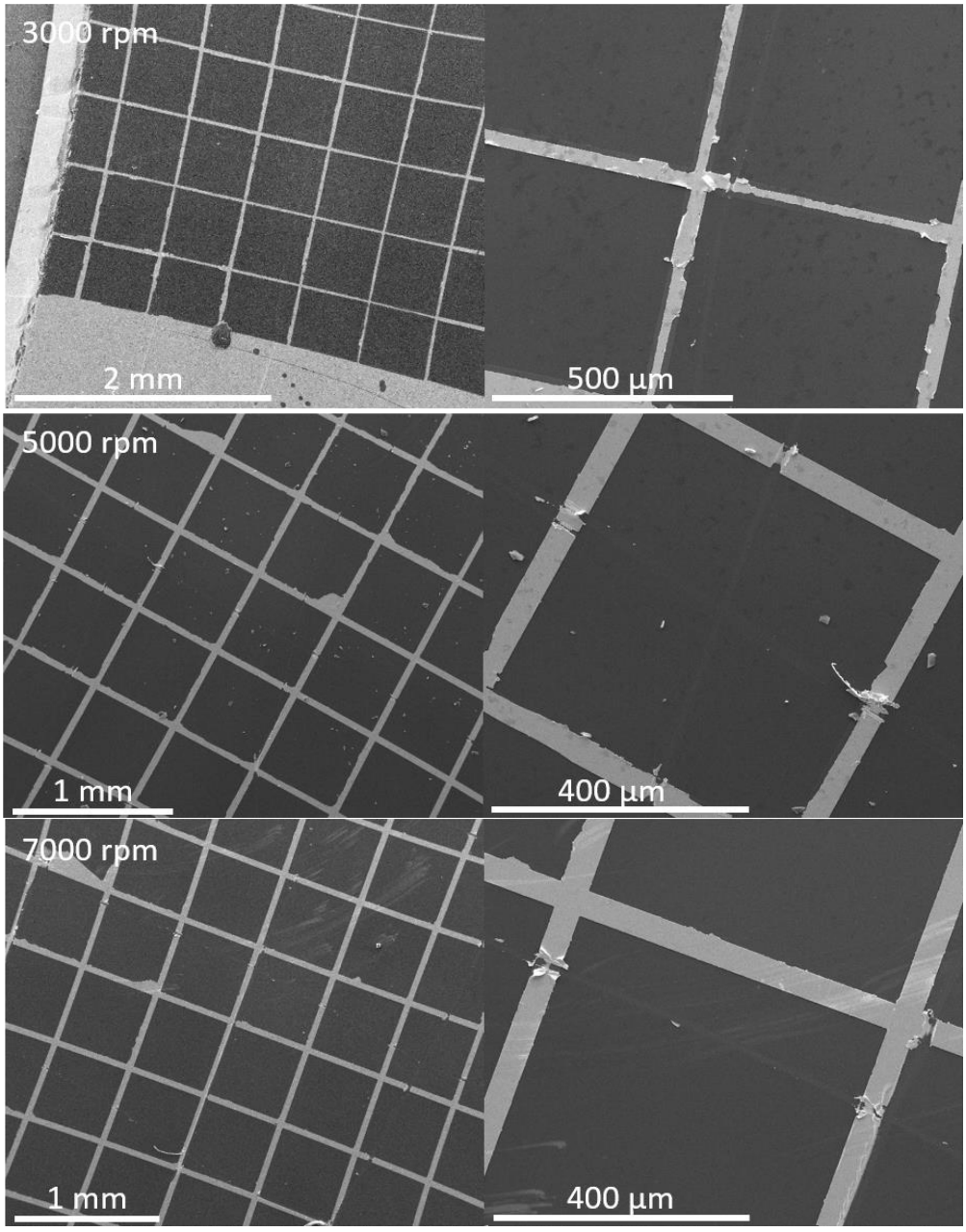

Figure 6-25: SEM images of PANI films spun from 500 µL aliquots of DMF suspension at different spin speeds.

The SEM images of PANI films spun from DMF at different spin speeds are shown in Figure 6-25. At slower speeds of 3000 and 5000 rpm blotchy dark patches are visible on the film, indicating that a non-homogenous film has been formed. These dark patches are not visible on the 7000 rpm film.

6.2.5.4.2 AFM Images of PANI (DMF) Films

AFM height maps were taken of PANI films spun from DMF to determine the thickness of the films as previously discussed.

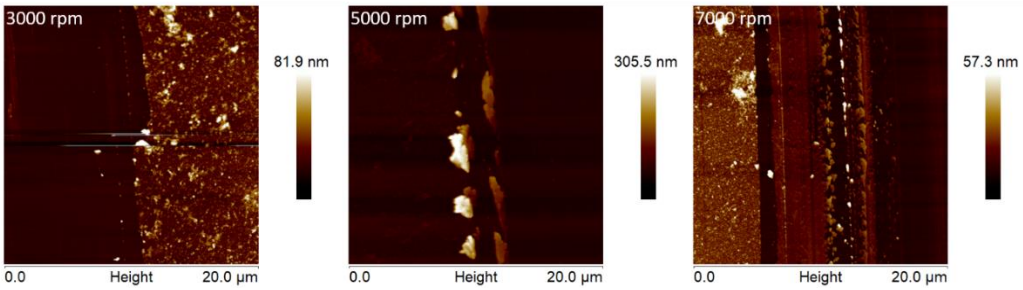

Figure 6-26: AFM height maps of PANI films spun from DMF at different spin speeds.

From the AFM height maps alone (Figure 6-26) it can be seen that the PANI films still appear 'speckled' similar to films formed from 80% acetic acid suspension (Figure 6-14) and do not appear to have formed smooth, homogenous films.

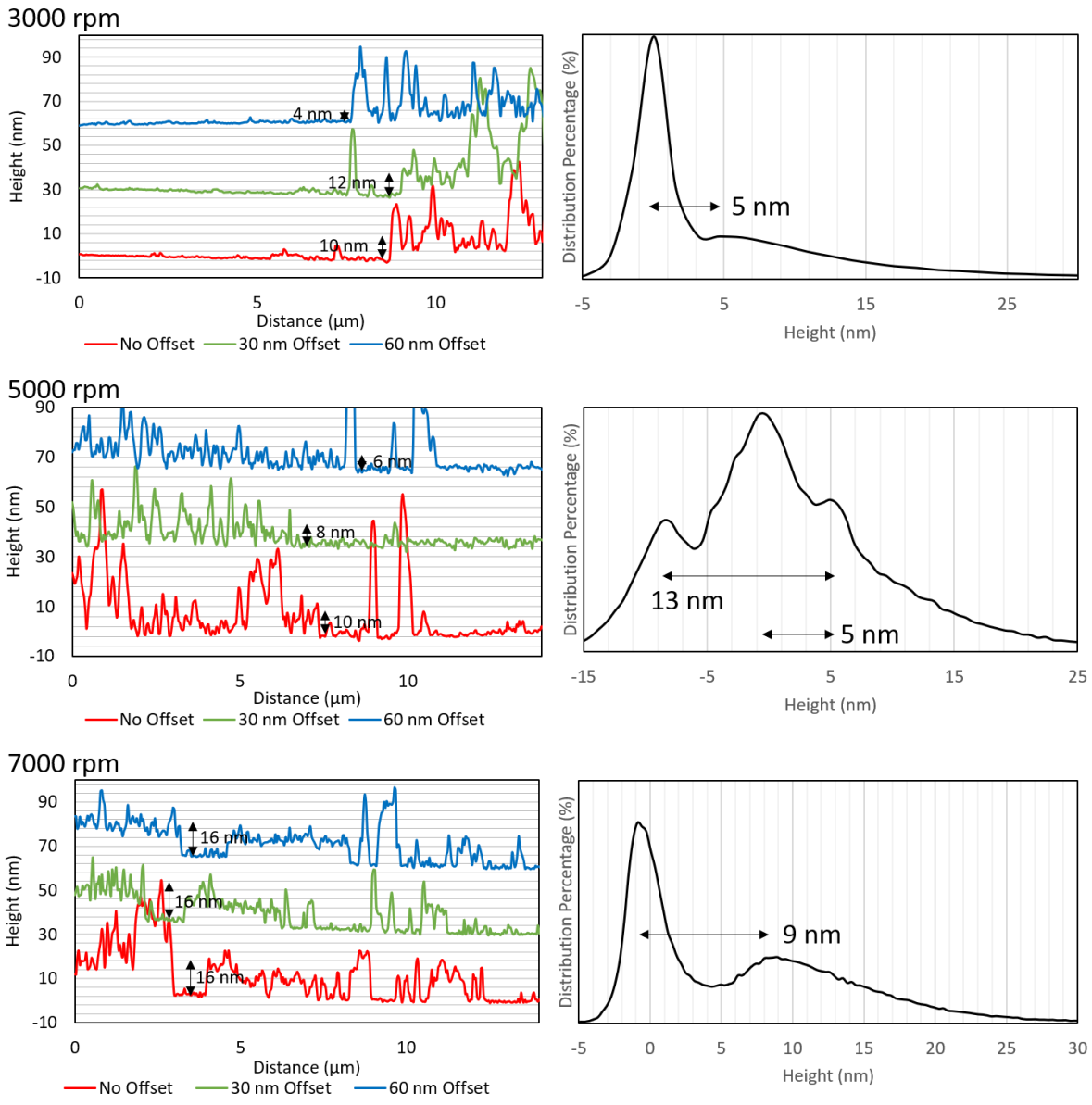

Figure 6-27: AFM cross sectional height data for PANI films spun from DMF at different spin speeds. From top to bottom: 3000 rpm, 5000 rpm, and 7000 rpm.

The PANI films spun from DMF suspension do not form films with superior homogeneity to those spun from 80% acetic acid suspension (Figure 6-15). Figure 6-27 shows that there is, again, little consistency within height measurements for the most part. The 3000 rpm sample height distribution suggests a film height of 5 nm, however the broad peak and cross-sectional line graphs indicate the film was up to at least 12 nm in thickness in some regions. The 5000 rpm sample gave significantly noisy line graphs and appeared to consist of three distinct height areas according to the height distribution. The film height is likely a similar range to the 3000 rpm sample. The 7000 rpm sample gave the most resolved plots however the height distribution graph gave a film height of 9 nm, whereas the line graphs suggest

a height of 16 nm. There is no clear trend of height with spin speed. From the data here it is not clear why the 5000 rpm devices performed poorly compared to the 3000 rpm and 7000 rpm devices. It is apparent that PANI films spun from DMF are thicker than those spun from 80% acetic acid (Figure 6-15).

6.2.5.5 Devices without CNT/GO Films

To determine the performance of the interlayers, separate from CNT effects, devices were fabricated with no CNT/GO film applied. They were tested both with and without a 5 nm top coating of gold as a surface conducting film. The gold cap was formed by sputter coating after interlayer attachment and the edges of the devices were covered to prevent any gold contact with the aluminium back contact.

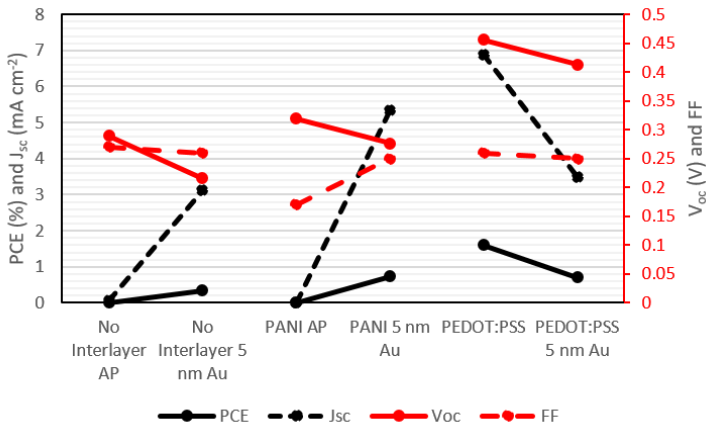

Figure 6-28: J/V properties for devices with PANI, PEDO:PSS, or no interlayer before and after a 5 nm gold film was attached

The device data in Figure 6-28 shows that the general device performance is worse than that of devices with a CNT/GO film with a PCE high of 1.6 %. Both the device with no interlayer and the device with a PANI interlayer display a significant increase in J_{sc} after the gold layer was attached, indicating that without this film the device is poor at extracting charge carriers. Conversely, the PEDOT:PSS device showed a significant decrease in J_{sc} when the gold cap was applied, indicating a decrease in charge carrier production/extraction. This is likely due to a decrease in the amount of light getting to the silicon surface, due to the gold layer. For all devices, the V_{oc} decreased with the attachment of a thin gold layer, indicating why a CNT/GO film is preferable. There was little change in FF for the device with no interlayer and the PEDOT:PSS device. However, an increase was seen for the device with a PANI

interlayer. Overall, the PEDOT:PSS device displayed the best performance, yet it was lower than that seen from CNT/Si, CNT/PANI/Si and CNT/PEDOT:PSS/Si devices. This indicates that the device improvement seen from the addition of PEDOT:PSS and PANI requires the CNT/GO film to form well performing devices.

In order to compare the properties of a thin gold cap with a CNT/GO film both designs were analysed with UV/Visible spectrophotometry and the sheet resistance was calculated using a 4-point probe with associated software.

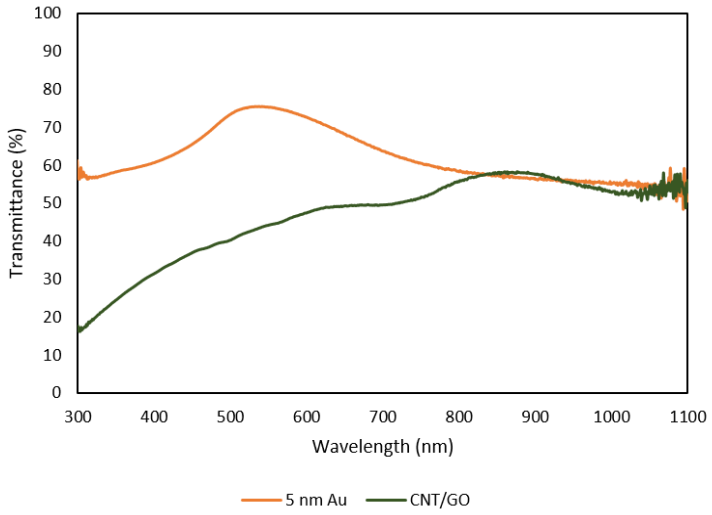

Figure 6-29: UV/Visible spectra for 5 nm gold films and for a CNT/GO film with a transmittance of 45 %.

Table 6-2: Sheet resistance data for doped and undoped CNT/GO film and a 5 nm gold cap.

Material	*Sheet Resistance (Ω sq^{-1})*
CNTGO	**423**
CNTGO $AuCl_3$	**133**
5 nm Au	**23**

Table 6-2 shows that even a thin gold cap provides a more favourable sheet resistance than a doped CNT/GO film with an order of magnitude difference observed. This indicates that a gold capping layer will perform better than a CNT/GO film when it comes to transporting separated charge carriers from the silicon to the gold top contact, however this does not take into account the ability for a thin gold/silicon junction to separate charge carriers to the same degree as a CNT/silicon junction. The UV/Visible spectra in Figure 6-29 demonstrate that the thin gold films were superior in terms of light

transmittance to the CNT/GO film measured. Note that the CNT/GO films used in the final devices for each section in this chapter had higher transmittance values than that shown in Figure 6-29.

6.2.5.6 Final Devices with Low Transmittance Films

The final experiment for all interlayers was to fabricate devices with the optimal interlayer formation parameters and test on devices with a 2% HF etch – $SOCl_2$ Vapour – 2% HF etch treatment pattern. In addition, the CNT/GO films used were significantly thinner than those used for the previous experiments. The transmittance of the new films was 65 % to 69 %, at least 15 % higher than previously used. The move from aqueous $AuCl_3$ to $SOCl_2$ as the doping chemical was due to continual tests on multiple designs of devices with little consistent improvement observed from aqueous $AuCl_3$. Devices with no interlayer were fabricated to compare the dopant chemicals and it was found that $SOCl_2$ was a superior dopant. $SOCl_2$ vapour was used instead of directly applying the chemical to the device as $SOCl_2$ is an aggressive organic solvent.

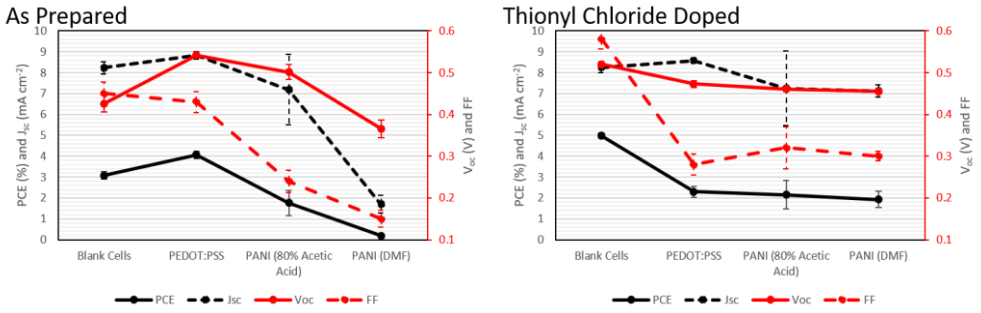

Figure 6-30: J/V properties for final devices with optimal interlayer parameters and thinner CNT/GO films.

Figure 6-30 shows device performance for devices with different interlayers before and after $SOCl_2$ doping with thinner CNT/GO films. The devices with no interlayer significantly outperform those with interlayers after $SOCl_2$. However, it can be seen that the devices with PEDOT:PSS outperform all other devices before any treatment is performed. Note that the final 2% HF etch data is not shown as this step caused a reduction in PCE for all devices. It was surprising that the PANI devices performed more poorly than the devices with no interlayer as the initial results in this experiment showed that PANI films could give performance improvement (Figure 6-18). The main reason for this is likely be the inability for PANI suspensions to form smooth, homogenous films on the silicon/gold substrates (Figure 6-14, Figure 6-15, and Figure 6-16). Meanwhile, the PEDOT:PSS was shown to form smooth

films with controllable thickness (Figure 6-10, Figure 6-11, and Figure 6-12). Thus, it is understandable why these devices would perform better than the PANI cells. The main reason for the significant difference between devices with no interlayer and PANI devices is that the performance of the devices with no interlayer has increased significantly from those in Figure 6-19. Due to the thinner CNT/GO films used.

6.3.6 PEDOT:PSS and PANI Interlayer Conclusions

It was found that both PEDOT:PSS and PANI interlayers can improve the performance of the large area CNT/Si heterojunction device. Devices with a PEDOT:PSS interlayer were found to give significant improvement to devices prior to chemical doping. However, this improvement decayed with doping as the performance of devices with PEDOT:PSS decreased whilst the performance of devices with no interlayer increased. Optimal deposition solution volumes and spin speeds were determined from a combination of UV/Visible photospectrometry, SEM, AFM, and device testing. The effectiveness of PANI as an interlayer was inconsistent, with later devices failing to give better performance than devices with no interlayer. The reason for this was likely due to poor film formation on the large area substrates. The use of DMF as an alternative PANI solvent was investigated but was not found to solve the problem.

6.3 Copper Thiocynanate and Molybdenum Oxide Interlayers

6.3.1 Introduction

Metal oxide films have been shown to improve the performance of CNT/Si heterojunction devices. Molybdenum oxide (MoO_x) in particular gave the current best performing CNT/Si device (17 %).[16] The MoO_x was applied via thermal evaporation of MoO_3 and was placed between the CNT film and the Au top contact.[16] In this thesis, an alternate method of applying MoO_x was investigated. An IPA suspension of MoO_x was spun on substrates to form a thin MoO_x layer in more ambient conditions than those required for thermal evaporation. For the device design used in this thesis, placing an interlayer on the substrate prior to CNT/GO film attachment meant the interlayer was present at both

the CNT/Si interface and the CNT/Au interface. MoO_x has also been observed to improve device properties by acting as a light trapping layer.[16] This will also be investigated in this chapter.

Additionally, copper thiocyanate (CuSCN) was also investigated as a novel interlayer material in the CNT/Si device. CuSCN is a molecular semiconductor with a wide bandgap (>3.4 eV), good hole transport characteristics, and high optical transparency.[174, 215] CuSCN has been incorporated in a range of solar devices, including organic PVs and perovskite solar cells,[174] as well as in thin-film transistors and inverter circuits.[216, 217] It has also been shown to be preferable to PEDOT:PSS as a hole transport layer in organic bulk heterojunction solar cells.[218] These properties are the reason why CuSCN was tested as an interlayer in the CNT/Si heterojunction device.

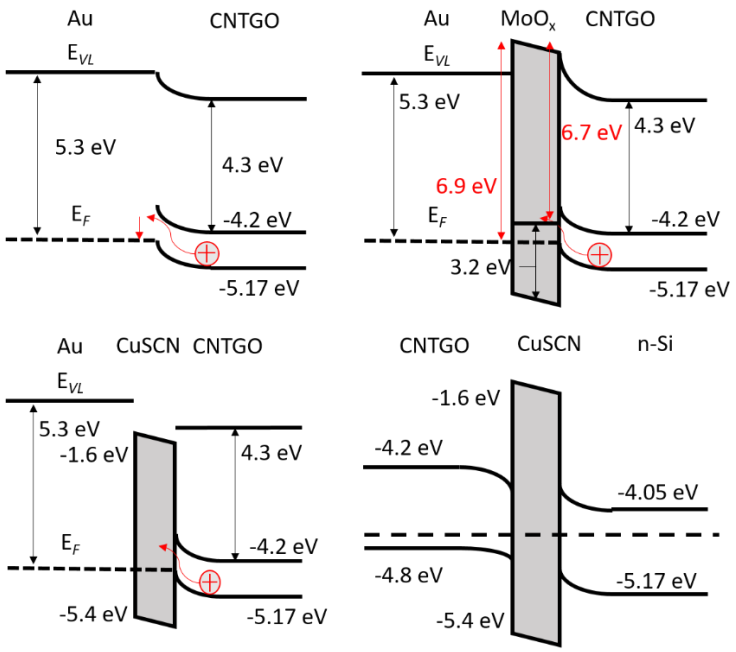

Figure 6-31: Energy diagrams of the Au/CNT junction with and without MoO_x or CuSCN interlayers and the CNT/Si junction with a CuSCN interlayer.[16, 174]

6.3.2 Molybdenum Oxide Film Characterisation

As with the PEDOT:PSS and PANI layers, UV/Visible spectra of films spun on glass were used to investigate the effects of different spin parameters on film formation. Additionally, they were used to investigate the effect of different chemical dopants on the interlayer material. Firstly, for MoO_x the deposition method was varied, followed by the volume of solution, followed by the spin speed. The difference in absorbance between a characteristic peak at around 740 nm and the baseline at around

540 nm was calculated to give a relative peak height. This was plotted against the varied parameters to give an idea of the effect of the parameter on spectral shape.

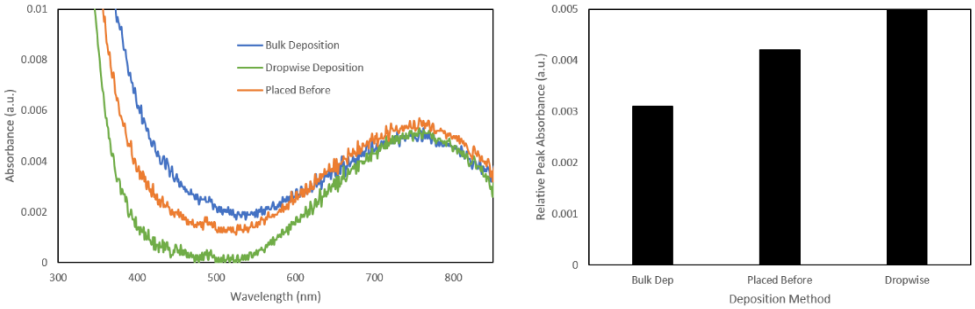

Figure 6-32: UV/Visible spectra and relative peak absorbance plots for a variation of solvent deposition method. For each experiment 500 µL of solution was spun at 2500 rpm for 60 seconds.

Figure 6-32 shows that, as with previous interlayer experiments, it is apparent that a dropwise method is the most desirable as this gives the most distinct peak.

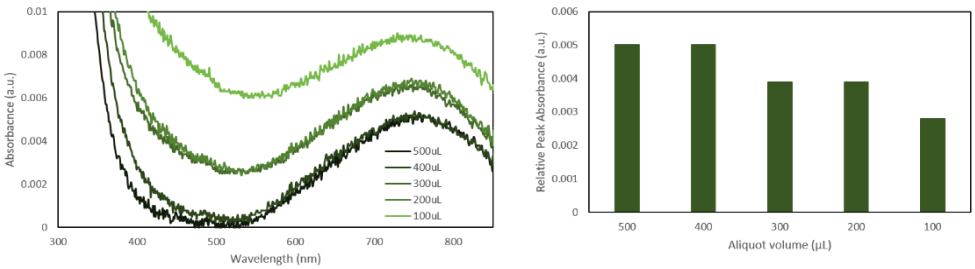

Figure 6-33: UV/Visible spectra and relative peak absorbance plots for a variation of deposition aliquot. For each experiment the solution was applied dropwise during a 60 second spin at 2500 rpm.

The size of the solution aliquot deposited was varied from 100 µL to 500 µL and the UV/Visible spectra are shown in Figure 6-33. For these spectra the importance of the relative peak height comparison is highlighted as the base line absorbance is shifted as the volume decreased. It is noticeable from the relative peak height with change in volume plot (Figure 6-33) that the absorbance difference between 740 nm and 540 nm was equivalent for spectra with similar absorbance baselines. A trend is visible of peak height decreasing as the aliquot volume is decreased. These results will be compared with solar device results obtained with MoO_x interlayers of different volume.

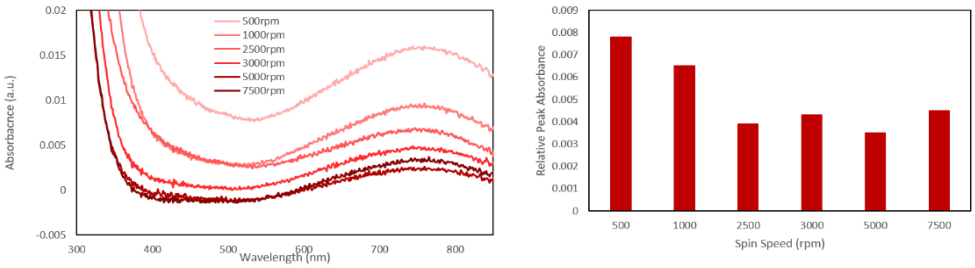

Figure 6-34: UV/Visible spectra and relative peak absorbance plots for a variety of spin speeds. For each experiment 200 µL of solution was applied dropwise and the samples were spun for 60 seconds.

Figure 6-34 shows the variation in UV/Visible spectra for films spun at different speeds. Again, the relative peak absorbance plot is necessary to avoid the complicating effects of different baselines. There is a trend visible for the 500 rpm, 1000 rpm, and 2500 rpm samples of decreasing relative peak height. From the 2500 rpm sample onwards the relative height plateaus. The downward trend is expected as this indicates that higher spin speed forms thinner films.

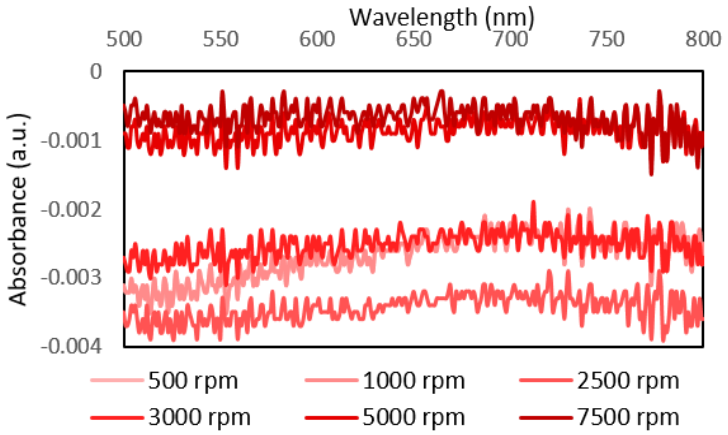

Figure 6-35: UV/Visible spectra of MoO_x films spun at different speeds after dunking in a water bath.

An issue was encountered when the MoO_x films on glass were being treated with various chemicals. It was observed that the visible blue colouring on the glass slides after MoO_x coating was completely absent after the slides were dunked in water. To confirm this, UV/Visible spectra were produced of the MoO_x films after dunking in a water bath for a period of less than a minute. Figure 6-35 shows clearly that the spectral shape observed in other spectra (Figure 6-33 and Figure 6-34) is completely absent and only flat, noisy spectra are visible. This is a concern as the CNT/GO films are floated in a water bath in order to be attached to the silicon/gold substrates. Additionally, all post-fabrication chemical treatments except $SOCl_2$ doping are done with aqueous solvents (HF and $AuCl_3$). It was apparent that a different CNT/GO film attachment method had to be found and chemical doping other

than by $SOCl_2$ had to be avoided. In order to find a solvent bath that will not damage the MoO_x film a series of films were produced on glass slides and were then dunked in solvent baths of four solvents: Water at pH 4, water at pH 12, acetone, and IPA.

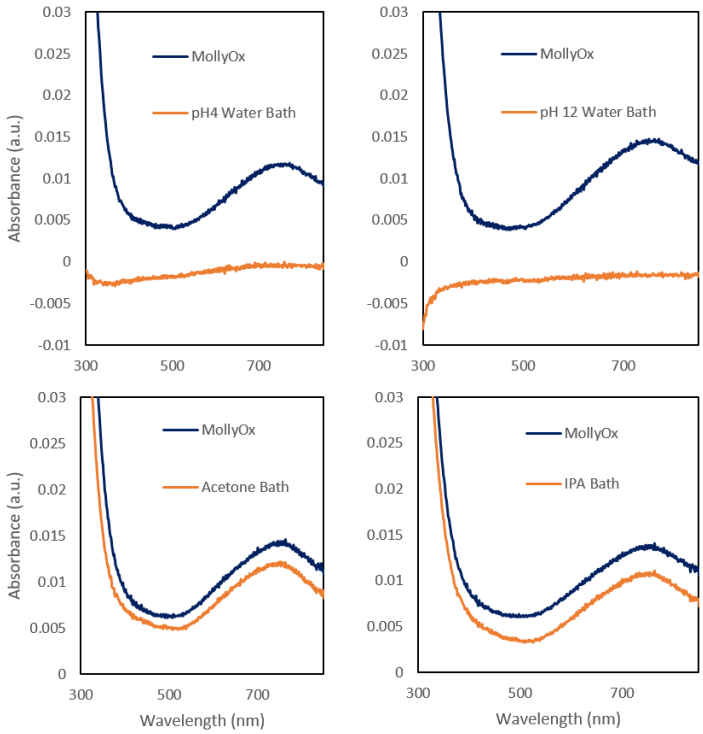

Figure 6-36: UV/Visible spectra of MoO_x films on glass before and after dunking in various solvents.

Figure 6-36 shows that a change in water pH to acidic or basic does not affect its ability to completely remove any MoO_x film present on glass. However, both acetone and IPA do not appear to damage the films significantly. In both cases, overall absorbance decreased after solvent bath dunking but, crucially, the spectral shape was maintained, with a peak at around 750 nm and a baseline at around 500 nm. An acetone bath was used to dissolve the MCE paper on which the CNT/GO suspension has been filtered prior to floating the CNT/GO films in the water bath. Therefore, for substrates coated in MoO_x CNT/GO film attachment was performed directly from the acetone bath rather than after transferring the film to a water bath.

The MoO_x films were annealed for 30 min at 80 ˚C directly after spin coating. This is a lower temperature than for any other annealed interlayer in this research (PEDOT:PSS and PANI were annealed at 140 ˚C , CuSCN was annealed at 100 ˚C). Thus, it was considered that a higher annealing

temperature could be used to strengthen the attachment of the MoO_x to the substrate and protect it from aqueous solvents. The annealing temperature was increased to 400 ˚C and UV/Visible spectra were taken both after higher temperature annealing and after a subsequent water bath. Note that the melting point of MoO_3 is 795 ˚C[219] so the chances of melting the MoO_x layer are low.

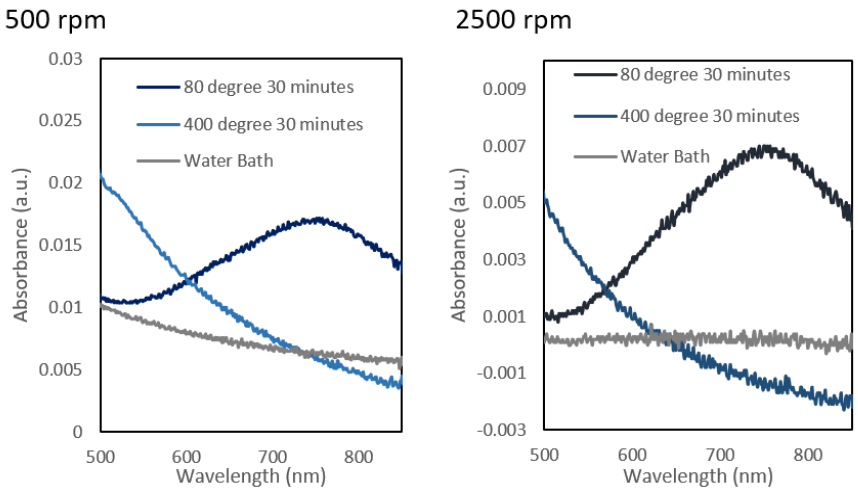

Figure 6-37: UV/Visible spectra of MoO_x films formed at different spin speeds after an 80 ˚C anneal, a 400 ˚C anneal and a water bath.

Figure 6-37 shows that a 400 ˚C anneal does nothing to protect a film formed at a spin speed of 2500 rpm. With a flat zero absorbance line present after the water bath. It appears that a film spun at 500 rpm might be slightly protected after a 400 ˚C anneal with a slope present in the spectra after water bath, although this rise may be due to the glass background which rises sharply at wavelengths below 500 nm. It is also apparent that the higher temperature anneal changes the absorbance spectra of the MoO_x layer significantly from that of an 80 ˚C annealed film. This corresponded with visible observations where the blue tinge on the glass present after the 80 ˚C anneal was no longer present after the 400 ˚C anneal, and the glass surface simply appeared cloudy. The peak at 740 – 750 nm is absent and a general upward trend in absorbance with lower wavelength is observed. Thus, even if the 400 ˚C anneal did succeed in protecting the MoO_x layer, the change in absorbance spectra, and thus photoelectrical properties, may have an impact on performance in the CNT/Si device.

6.3.3 Copper Thioncyanate Film Formation

In the study by Wijeyasinghe *et al*.[174] two solvents were used to prepare solid CuSCN for coating, aqueous ammonia (NH_3(aq)) and diethyl sulphite (DeS). They found that $NH_{3(aq)}$ was the preferred

solvent as devices with CuSCN layers spun from an $NH_{3(aq)}$ solution performed favourably compared to devices with CuSCN layers spun from DeS solution. This was due to high purity and exemplary film structure exhibited by CuSCN layers spun from NH_3(aq) solution compared to CuSCN layers spun from DeS or PEDOT:PSS films.[174] Thus, NH_3(aq) was initially used as the solvent for CuSCN film deposition on the device substrates. However, it soon became apparent that $NH_{3(aq)}$ does not wet the substrate sufficiently to form a homogeneous film when spin coated. The solvent would instead bundle into the corners of the grid squares. This was visible from optical observation and confirmed by SEM imaging (Figure 6-38)

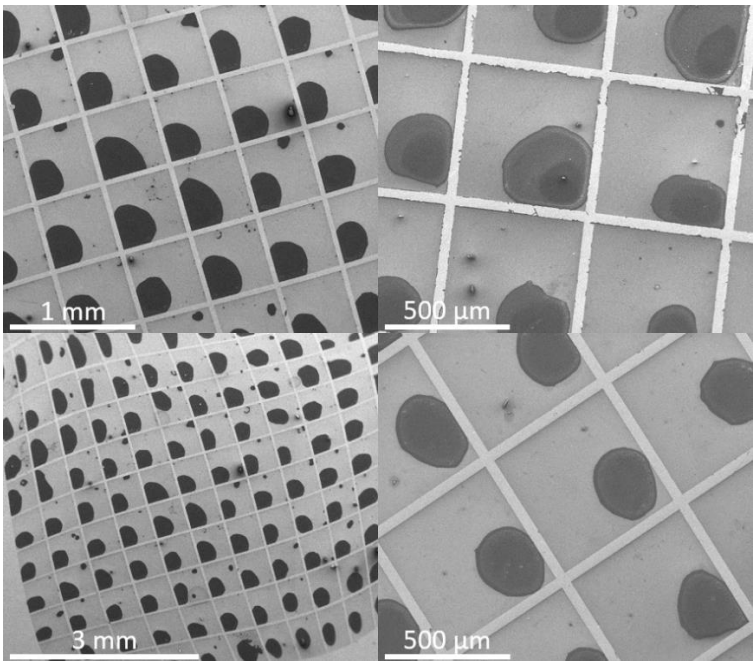

Figure 6-38: SEM images of CuSCN films spun from NH_3(aq) solution, showing the bundling effect caused by poor surface wetting.

As an alternative to spin coating, CuSCN suspended in $NH_{3(aq)}$ solution was poured onto a silicon/gold substrate and left to allow the solvent to evaporate. The result was a substrate covered with blue crystal structures.

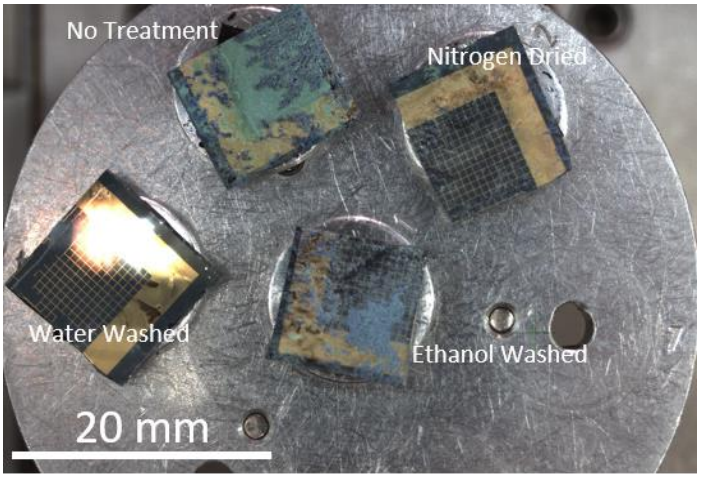

Figure 6-39: Optical image of substrate left in CuSCN NH_3(aq) solution until evaporation was complete. Each quarter substrate has been treated in a different way post bath treatment.

After CuSCN deposition from NH_3(aq) evaporation, the substrate was cut into quarters and each quarter was treated to remove the large surface structures that had grown during solvent evaporation (see Figure 6-39). A wash with ethanol removed the largest growths but the substrate was still covered in some areas by darker blue smaller crystals. Blowing the substrate with nitrogen served to remove all the large visible crystals but left a mottled looking surface. A 10 min bath sonication treatment in a beaker with water removed the large growths and left a much cleaner looking surface than the nitrogen blowing. Each quarter was imaged under SEM.

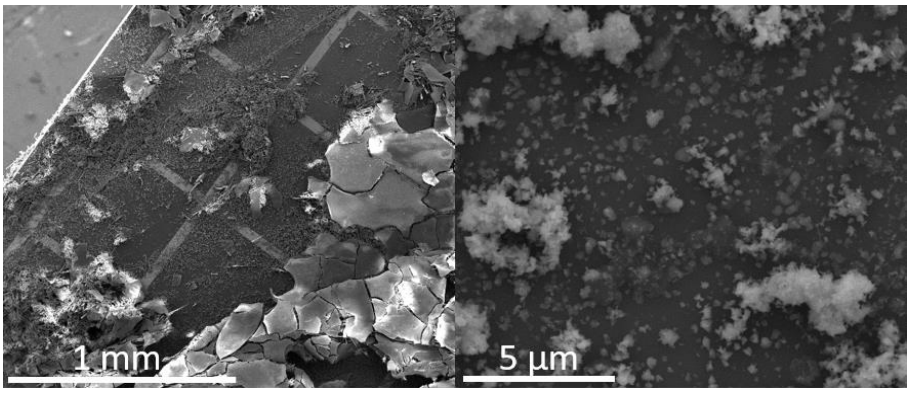

Figure 6-40: SEM images of substrate quarter with deposited CuSCN crystals after no post treatment.

With no post crystal deposition treatment, large crystal structures are visible on the surface. It was observed that these growths changed in brightness over extended SEM imaging, indicating that they were experiencing charging from the electron beam. At enhanced zoom levels small crystal pieces are visible on the substrate.

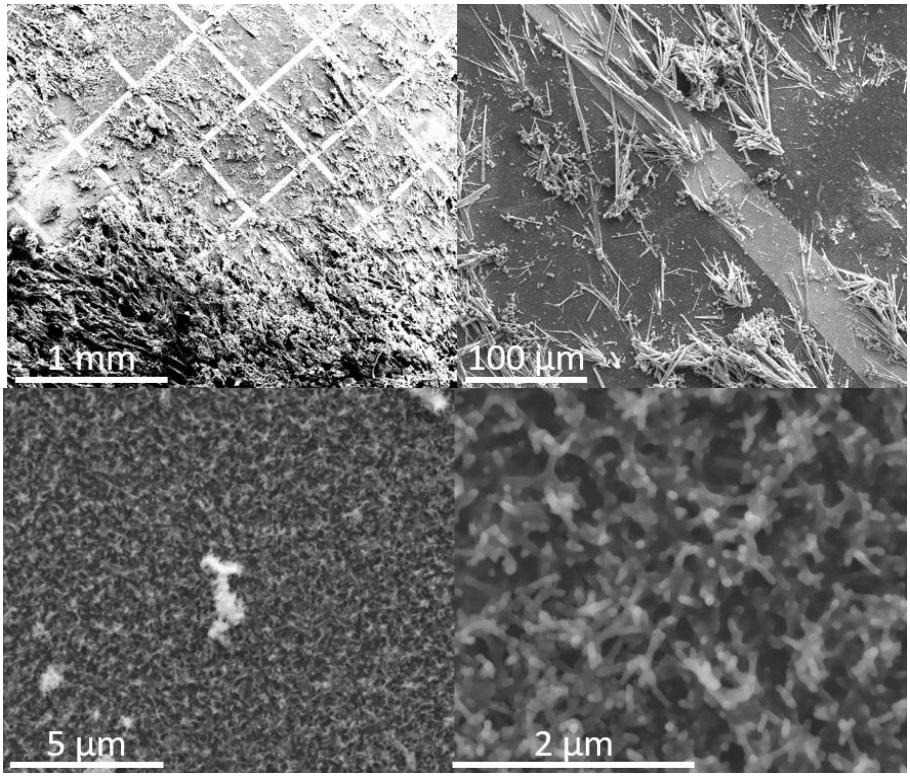

Figure 6-41: SEM images of substrate quarter with deposited CuSCN crystals after ethanol washing.

After ethanol washing (Figure 6-41) the large, flat crystal structures are no longer present on the surface, however jagged smaller crystals are plentiful. At enhanced zoom levels a thin, relatively homogeneous, layer of smaller structures was visible coating the silicon underneath the larger crystal formations.

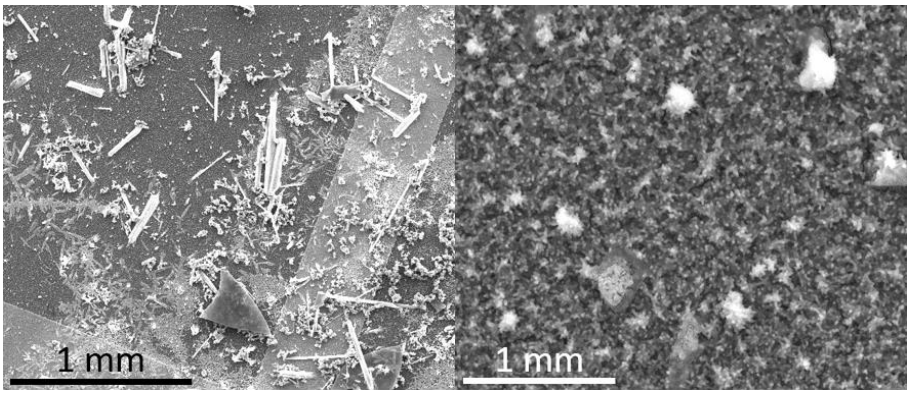

Figure 6-42: SEM images of substrate quarter with deposited CuSCN crystals after blowing with nitrogen gas.

Blowing the substrate quarter with nitrogen gas was more effective than ethanol at removing the larger crystal structures (those visible optically), however, Figure 6-42 makes it clear that the smaller jagged shapes are still present after blowing with nitrogen. It is likely these structures are the cause

of the mottled look on this substrate quarter when viewed optically (Figure 6-39). The same underlying film of smaller crystal growths is also visible on this sample.

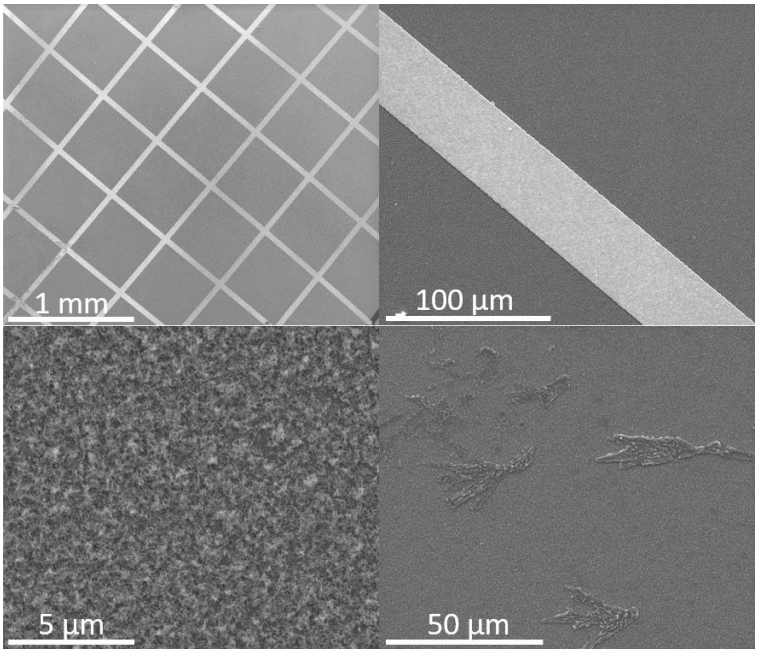

Figure 6-43: SEM images of substrate quarter with deposited CuSCN crystals after bath sonication in water.

The substrate appeared substantially different under SEM when sonicated in water (Figure 6-43). The large crystal structures are completely gone and all that is left is the thin underlayer of smaller CuSCN crystals. Thus, a simple sonic bath in water is sufficient to remove the excess crystal structures and leave a thin, relatively homogeneous, crystalline CuSCN layer on the surface of the silicon/gold substrate. This crystal layer was imaged using AFM to determine its height and roughness.

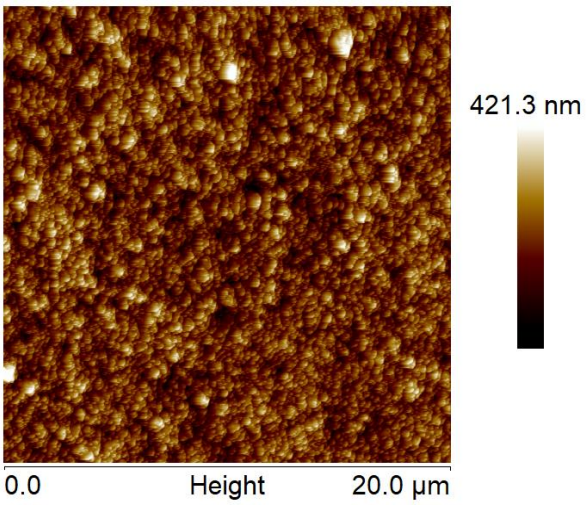

Figure 6-44: AFM height map of CuSCN crystal deposition from $NH_{3(aq)}$ solution.

Figure 6-44 shows an AFM height map of the CuSCN crystal layer visible on the substrates after sonication in a water bath. Whilst the crystal layer was small compared to the large crystals visible under SEM, this layer is still significantly thicker than the other interlayers formed from spin coating. The height scale is 421.3 nm, the image Z range is 598 nm, and the Rq and Ra values are 60.9 nm and 48.4 nm respectively. These are high values (when compared with CNT film roughness measurements (Table 4-3) and thus it can be seen that this crystal layer is both very tall and very rough, casting doubt as to whether it can be a suitable thin interlayer.

It was necessary to fabricate a thin, homogeneous CuSCN layer in order to determine its effectiveness in the CNT/Si heterojunction device. Thus, CuSCN solutions were prepared in DeS (the alternate solvent used by Wijeyasinghe *et al.*[120]) and spin coated onto glass slides and silicon/gold substrates for analysis. From simply viewing the substrates it was clear that this solution had no problem in fully wetting the glass and silicon/gold substrates and formed a thin film across the surface.

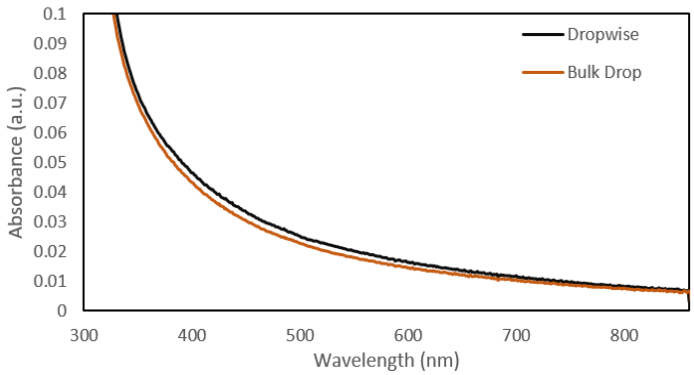

Figure 6-45: UV/Visible spectra of CuSCN films produced from DeS suspension spun at 2500 rpm from 500 µL aliquots.

As can be seen in Figure 6-45, the spectrum of a CuSCN film spun from DeS did not have any characteristic peaks in the range observable on a glass slide. This matched the observable colour of the film which was a dull yellow-brown tone. In comparison, the CuSCN $NH_{3(aq)}$ solution was a deep blue colour and the crystals that were formed from it were various shades of blue. There was not much observable difference in spectra when the deposition method was changed. A dropwise method was used for future film formation as this has was preferred with the other interlayers.

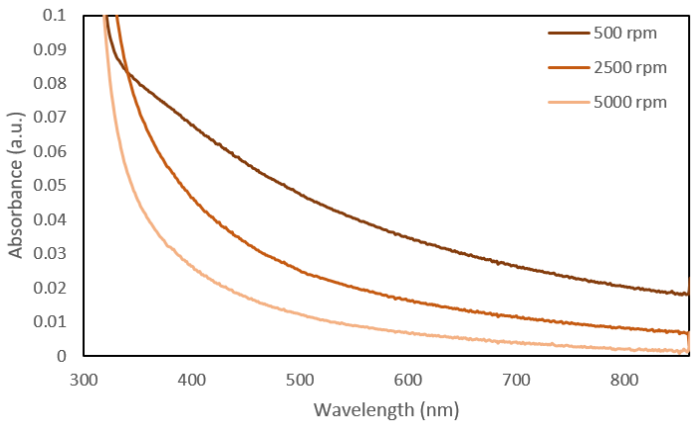

Figure 6-46: UV/Visible spectra of CuSCN films produced from DeS suspension spun from 500 µL aliquots with a dropwise deposition.

A decrease in UV/Visible absorbance is seen when the spin speed is increased (Figure 6-46). This matches the other interlayers, with slower spin speeds producing thicker, and thus more light absorbent films. The absence of a local maximum to characterise the change in absorbance with spin speed makes the CuSCN films difficult to categorise compared to the other interlayer materials. However, at 500 rpm the spectrum has a different shape, with a much flatter curve present from ~350 nm to 800 nm. This indicates that at sufficiently low spin speeds the morphology of the film is affected compared to when the spin speed is increased. This matches the other interlayers, where the 500 rpm films were different in morphology than at higher spin speeds.

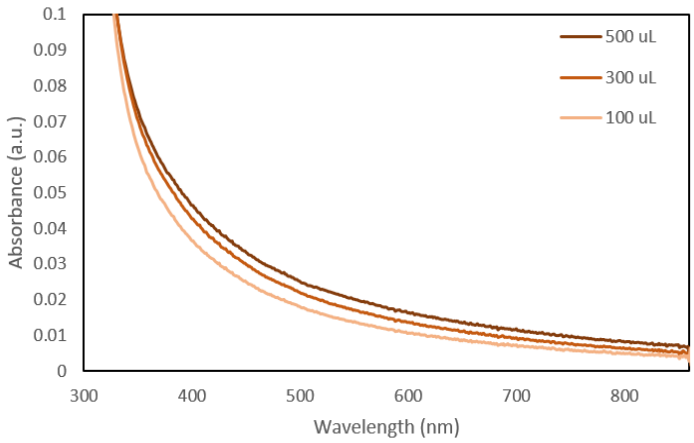

Figure 6-47: UV/Visible spectra of CuSCN films spun from DeS solution at 2500 rpm with a dropwise pattern.

There was little difference in UV/Visible spectral shape when the aliquot volume was changed (Figure 6-47). However, as the volume was decreased the absorbance also decreases, with a larger effect visible at the apex of the curve (370 nm – 500 nm). This indicates that a smaller amount of CuSCN was

present in films formed from smaller aliquots, either due to thinner films or films with more air-bubbles or similar defects present.

6.3.4 Molybdenum Oxide and Copper Thiocyanate AFM and SEM images

As for PEDOT:PSS and PANI, both MoO_x and CuSCN (DeS) films were imaged using AFM to measure film height with reference to the aliquot volume and spin speed used.

6.3.4.1 AFM Height Maps of MoO_x Films.

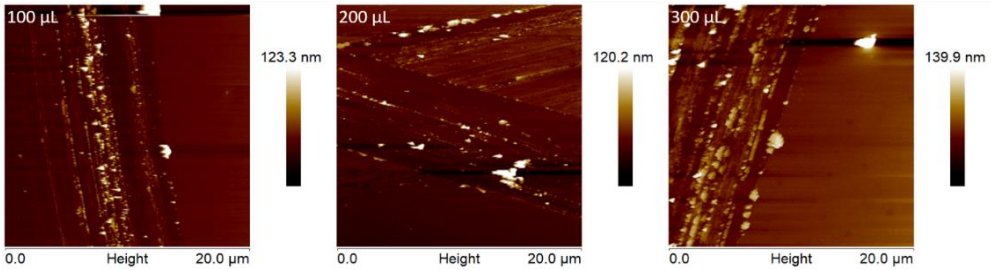

Figure 6-48: AFM height maps of MoO_x films spun from different solution volumes.

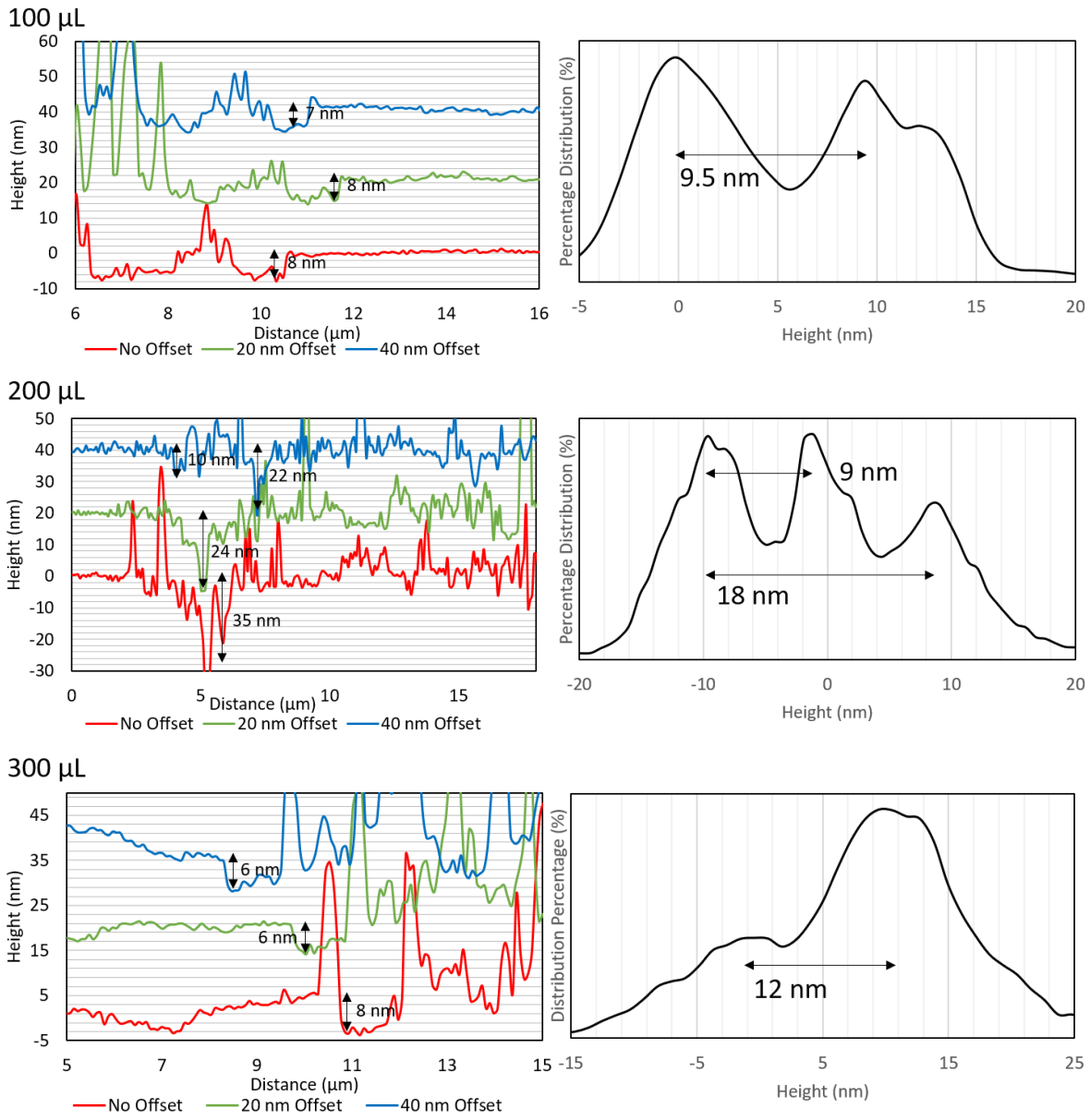

Figure 6-49: Cross-sectional heights for MoO_x films spun from different solution volumes.

The AFM height maps of scratched MoO_x films are shown in Figure 6-48. The scratching did not form large smooth channels that can be observed with some other interlayers (Figure 6-10). This made determining the film thickness more difficult than for other interlayers. Especially with the 200 µL sample. In general, the film thickness appeared to be between 5 nm and 10 nm for each interlayer, although the 200 µL film could be more than 20 nm thick in some places.

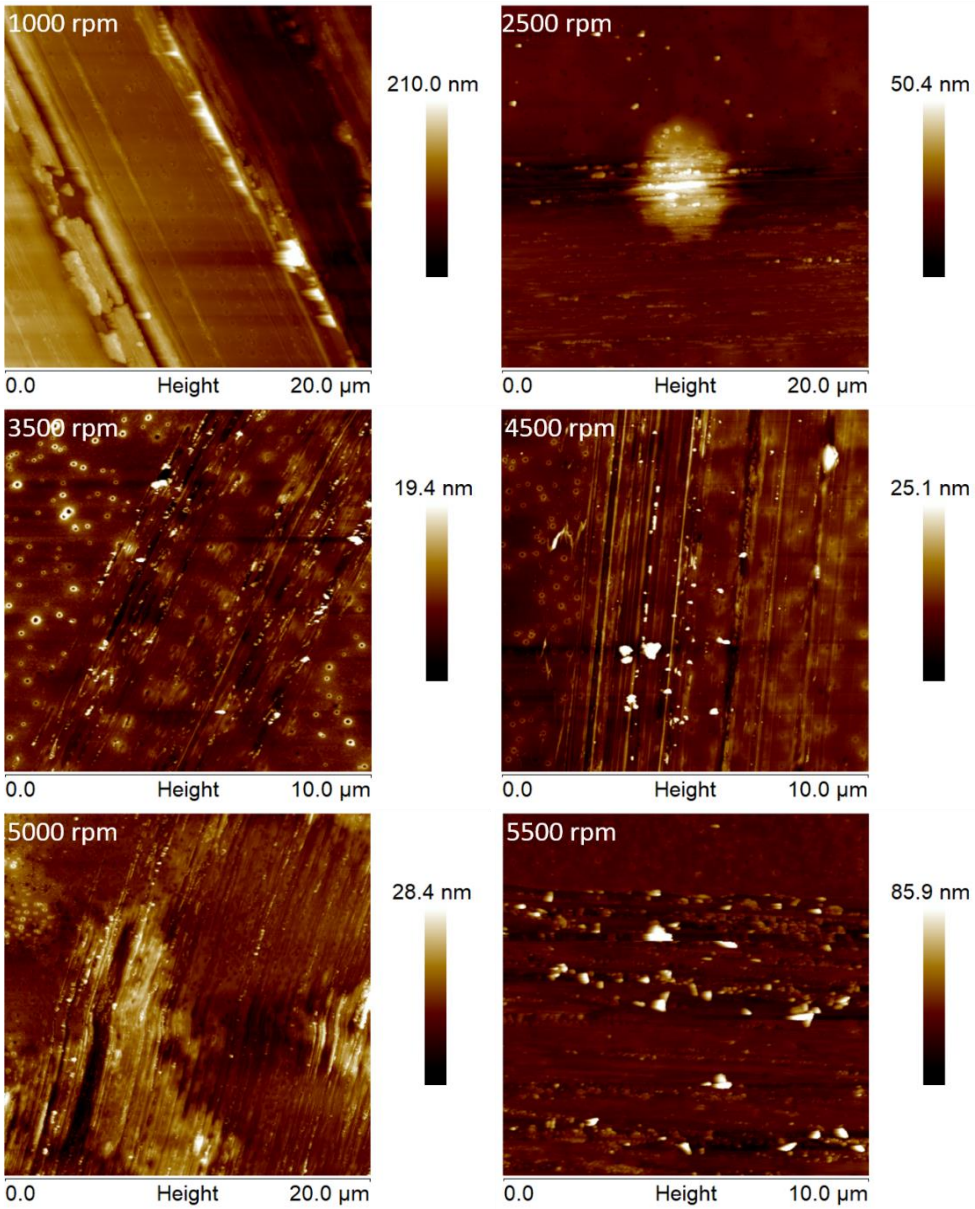

Figure 6-50: AFM height maps of MoO_x films spun at different speeds.

1000 rpm

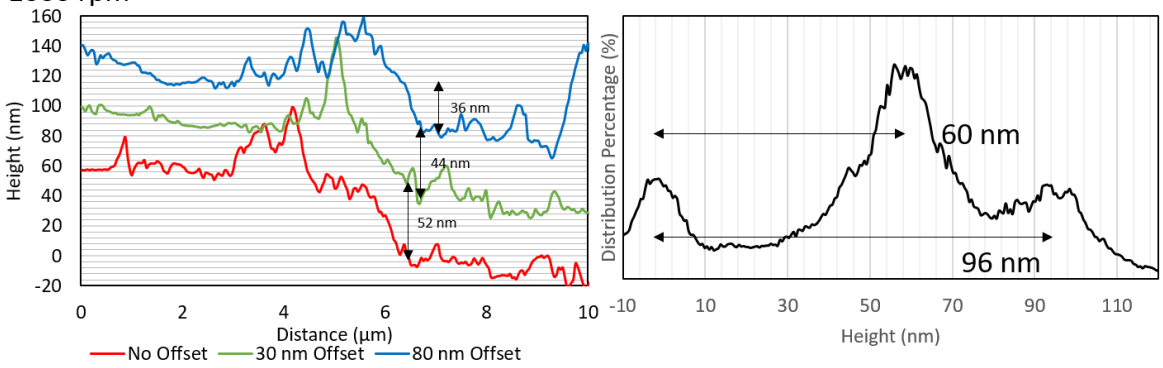

2000 rpm

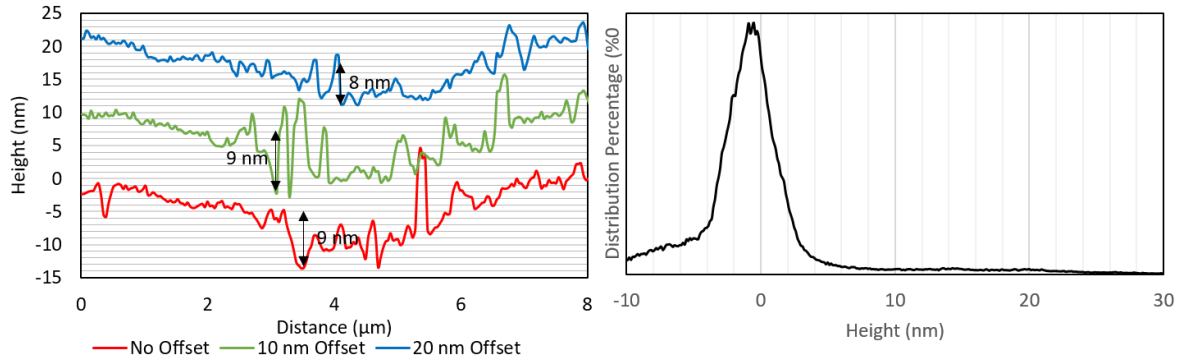

3500 rpm

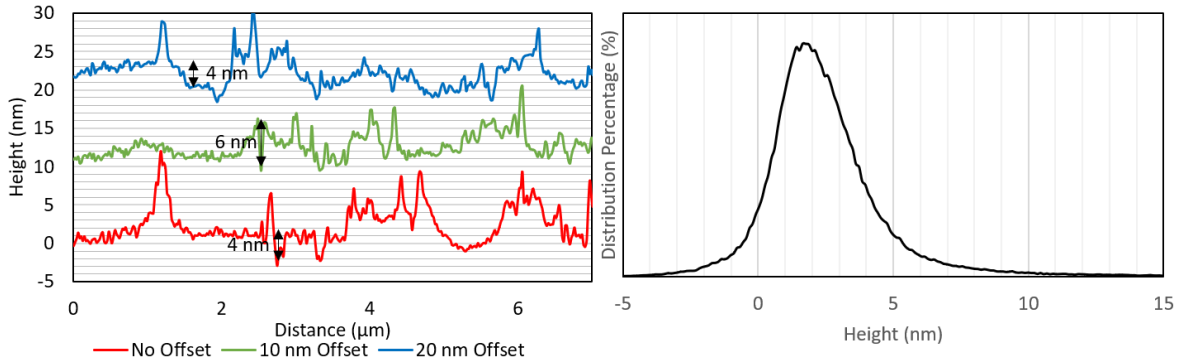

4500 rpm

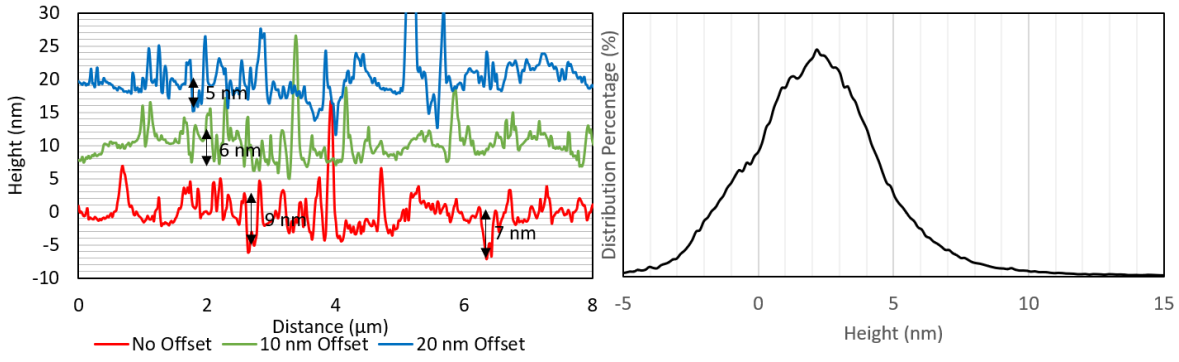

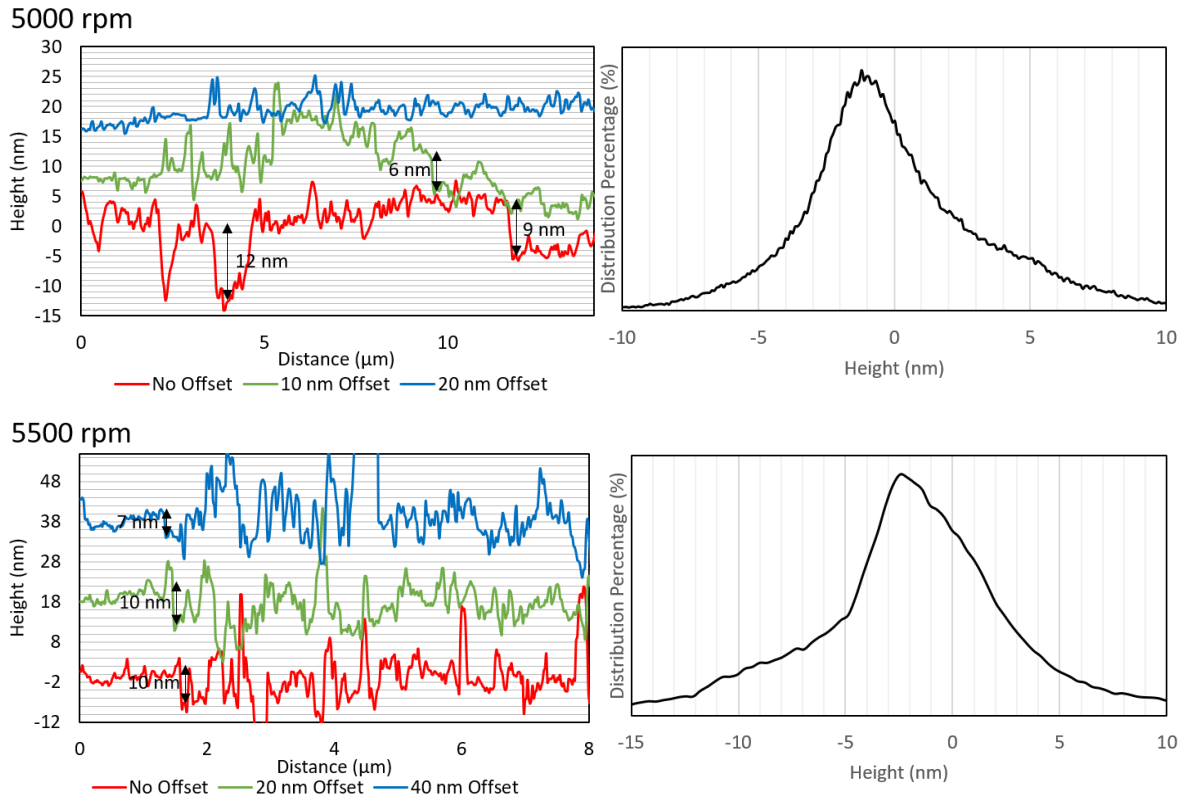

Figure 6-51: Cross sectional maps of MoO_x films spun at different speeds.

Figure 6-50 and Figure 6-51 show AFM height maps, cross-sectional line graphs and height distribution plots of scratch lines made in MoO_x films spun at different speeds. It appears that films spun at 3500 rpm and above are all around 5-7 nm thick and the thin nature of these films makes identification of scratch edges in the films difficult to pin point. An additional problem was the rough nature of the scratched areas. The images were processed by flattening and normalising to the scratch areas for previous AFM cross sectional analysis (as this was assumed to be the lowest area). The rough scratch areas made this more complex as the surfaces were not flat enough to provide a good baseline. This led to malformed background shapes in the cross-sectional line graphs for the 2500 rpm and 5000 rpm samples. An alternate method of measuring film thickness was attempted. The AFM probe was passed over un-scratched sections of the MoO_x film and the depth of the holes formed in the surface during film formation was measured. A clear downside of this method is that it cannot be certain that the holes descend through the entire film or stops part-way down.

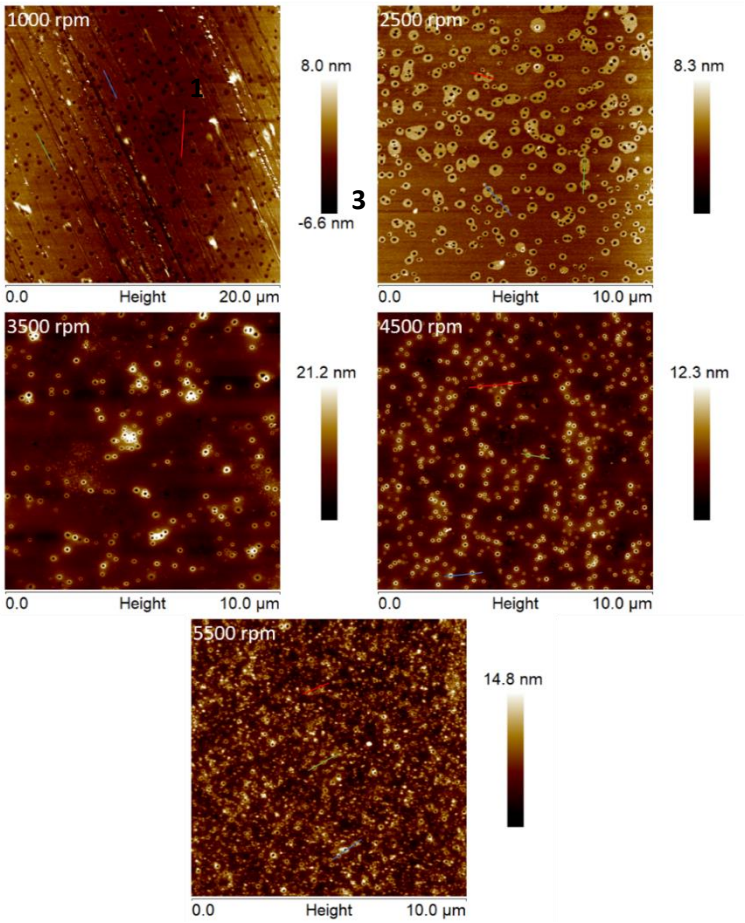

Figure 6-52: AFM image of holes on MoO_x film spun at different spin speeds. Coloured lines show the cross-sectional graph locations.

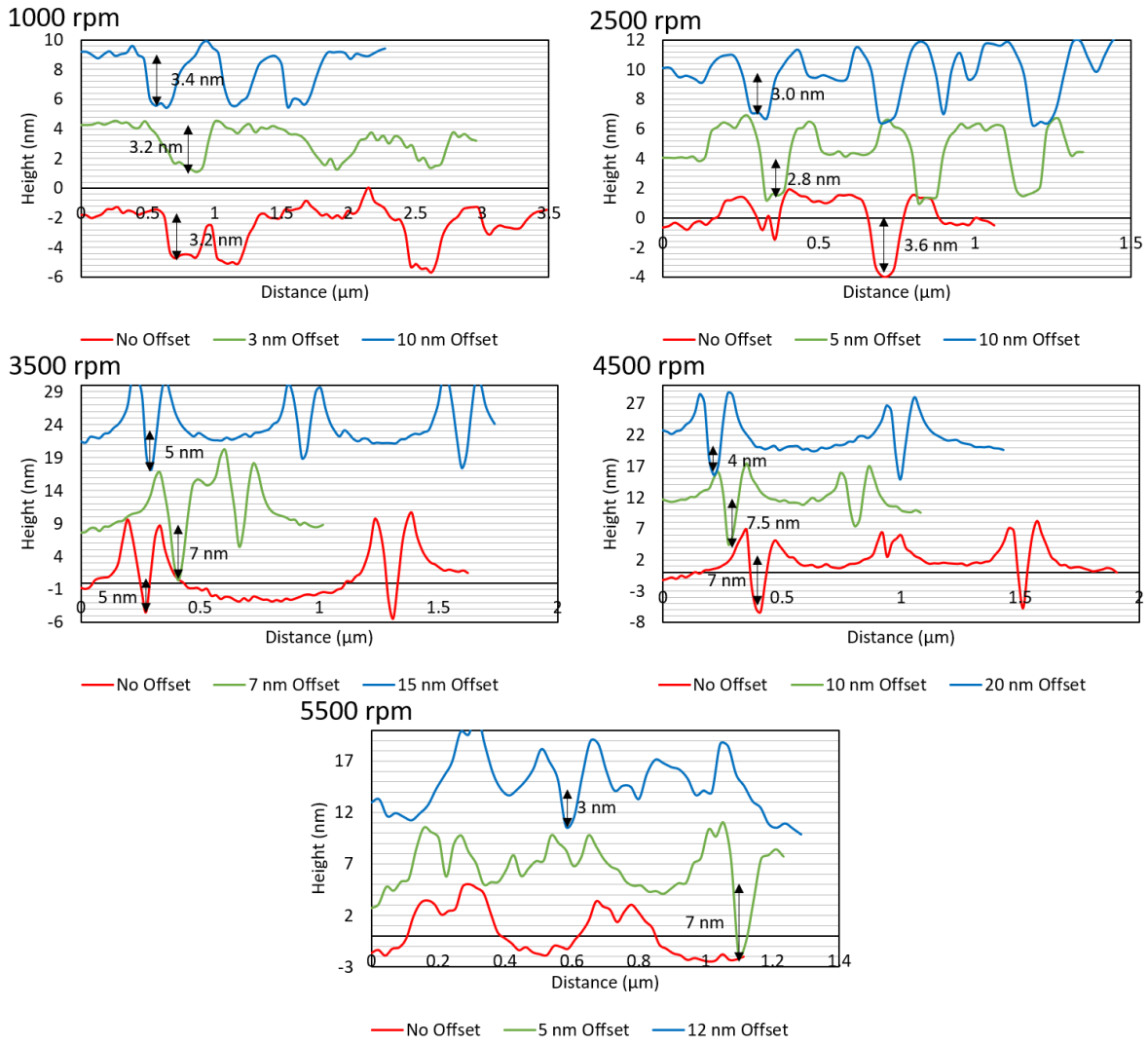

Figure 6-53: Cross sectional height maps of holes in MoO_x film spun at different speeds.

Figure 6-52 and Figure 6-53 show height maps and cross-sectional line graphs of holes in MoO_x films spun at different speeds. There are no height distribution plots presented as the vast majority of points on the height maps were the surface of the film and thus no clear separation between a surface peak and a film peak was visible. The heights measured for the 1000 rpm and 2500 rpm samples are significantly lower than those observed in the scratched images (Figure 6-51). This indicates either that the holes do not pass through the entire film, that the heights determined from the scratched images are incorrect, or that there is a high degree of thickness variance in the MoO_x films. The remainder of the samples show similar heights to those from the scratched images with heights up to 7 nm. It is apparent that there is little change in film height from 3500 rpm to 5500 rpm.

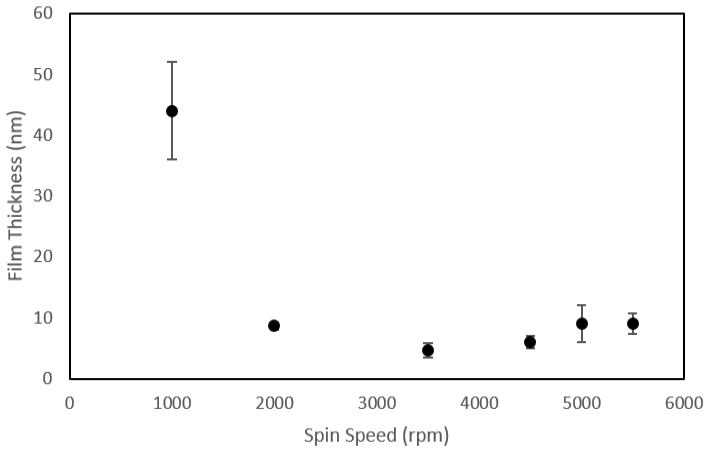

Figure 6-54: Film thickness vs spin speed plot for MoO_x films.

Figure 6-54 shows the relationship between film thickness and spin speed for MoO_x films. A clear plateau is present at 3500 rpm and onwards. This plateau somewhat matched the plateau seen in the UV/Visible spectra of MoO_x films at different spin speeds (Figure 6-34. The AFM height maps (Figure 6-50 and Figure 6-52) show that the MoO_x films have a high concentration of holes across the film. Dark circles are also visible on the films in Figure 6-48 and are likely similar defects. These holes are probably caused by air bubbles formed within the layer during spin coating which burst free from the film during solvent evaporation. It is uncertain what effect these holes will have on device performance. They may damage the integrity of the interlayer. However, they may also allow CNTs to access the silicon layer beneath, thus improving CNT/Si heterojunction formation.

6.3.4.2 SEM images of MoO_x films.

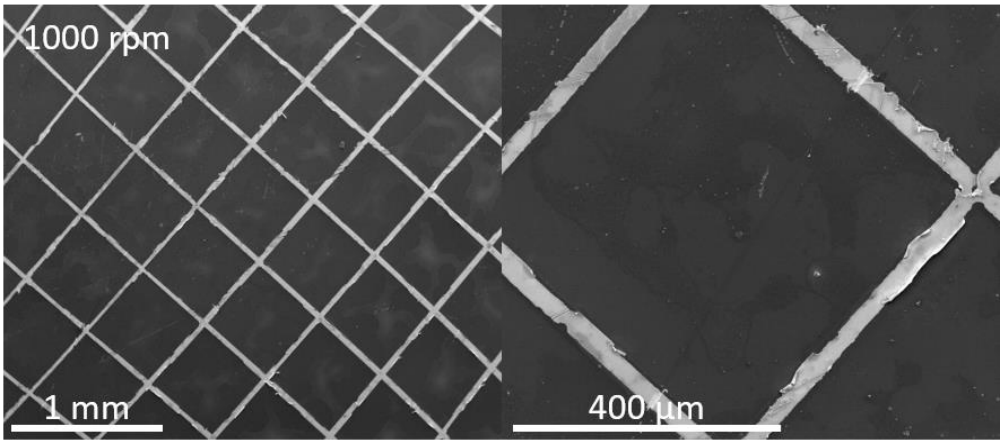

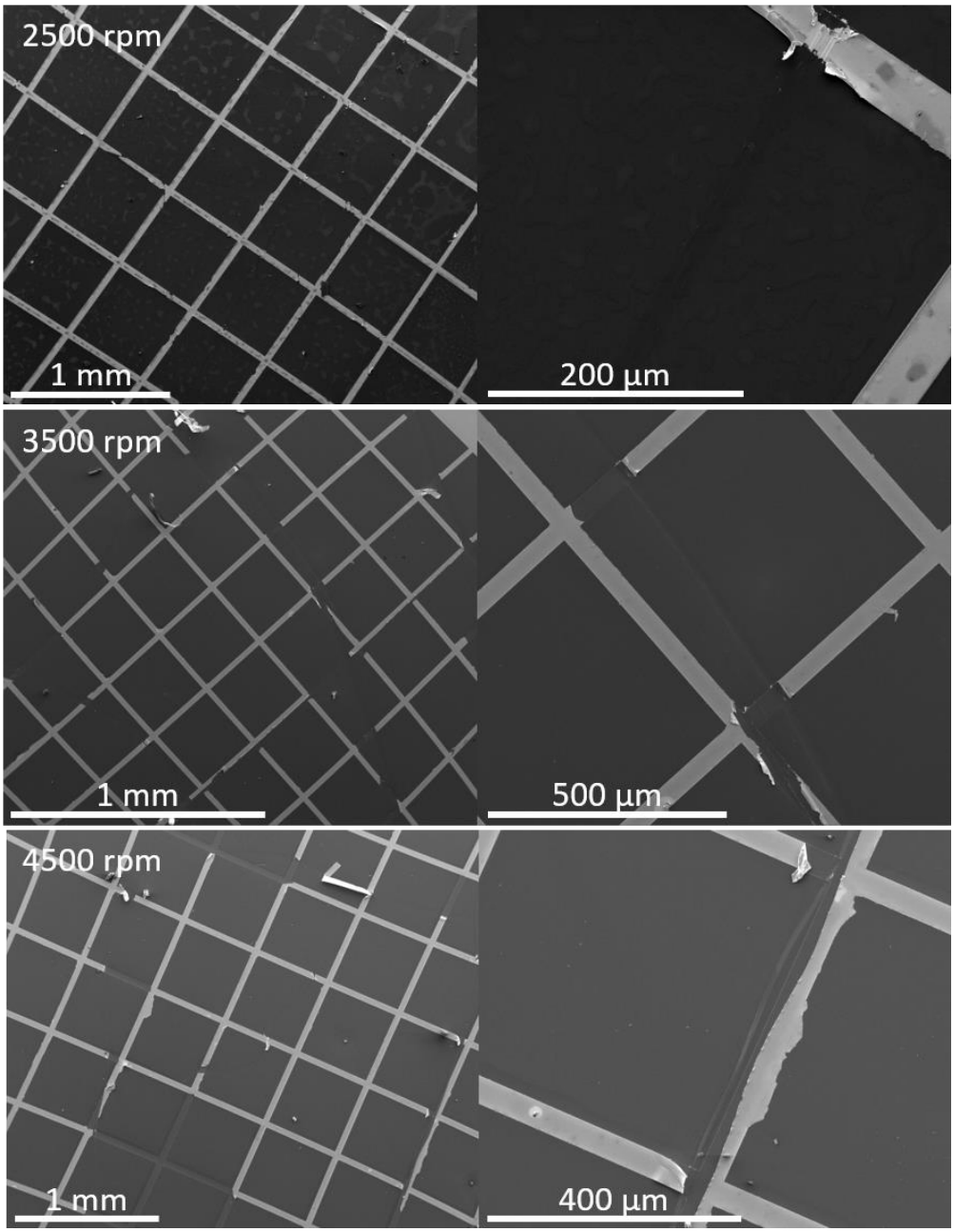
2500 rpm
1 mm
200 µm
3500 rpm
1 mm
500 µm
4500 rpm
1 mm
400 µm

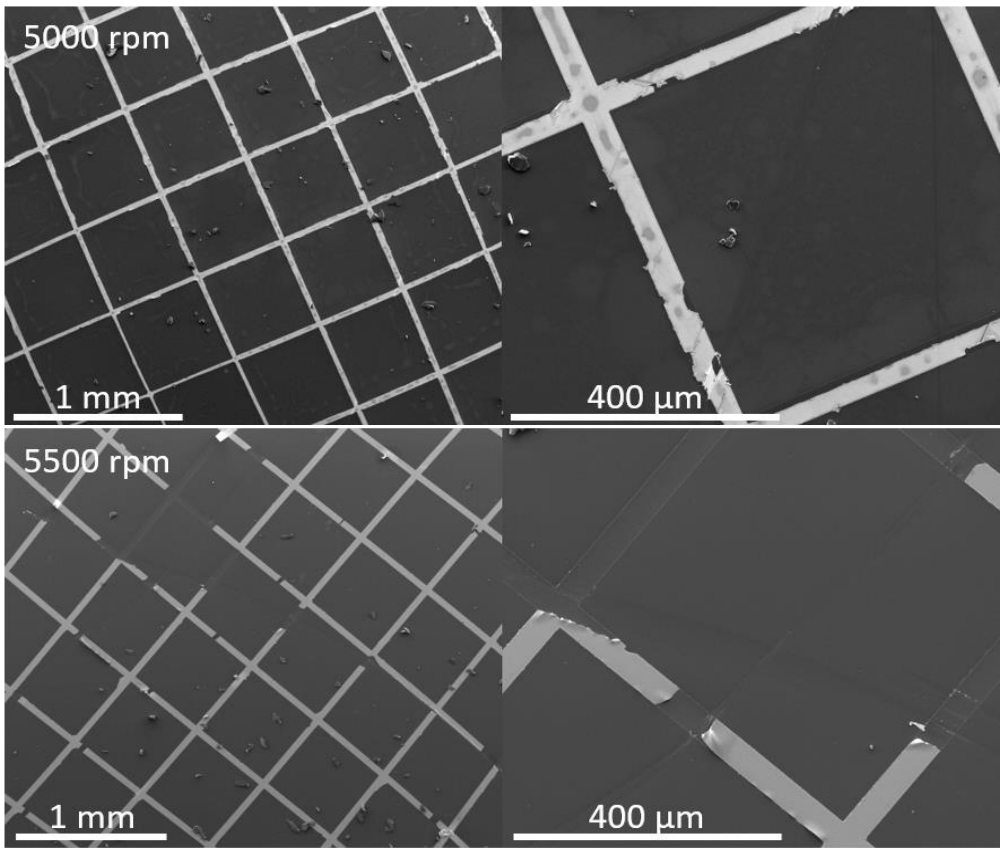

Figure 6-55: SEM images of MoO_x films formed at different spin speeds.

SEM images of MoO_x films (Figure 6-55) show that the slower spin speed films did not form homogeneous layers on the surface of the silicon/gold substrate. The 1000 rpm and 2500 rpm samples produced patchy coverings, although the presence of a scratch line across the whole area in the zoomed 2500 rpm sample indicates that the surface is still covered with MoO_x but with varied thickness. From the 3500 rpm sample and up, the films appeared more homogeneous. The exception is the 5000 rpm sample which appeared similar to the lower spin speed samples. Overall, this indicates that at higher spin speeds more homogeneous films are formed, however they are thin and have a high concentration of holes. This information will be compared with device data in Figure 6-68.

6.3.4.3 AFM Height Maps of CuSCN Films.

CuSCN films spun from DeS were imaged using AFM at three different concentrations and for a variety of spin speeds to determine both effects on film thickness. The reason for varying the concentration was that the thinnest layer produced with the initial concentration of 15 mg mL^{-1} was 16 nm thick. The concentration was reduced to 10 mg mL^{-1} and 5 mg mL^{-1} to produce thinner films to observe the performance effect for films thinner than 16 nm.

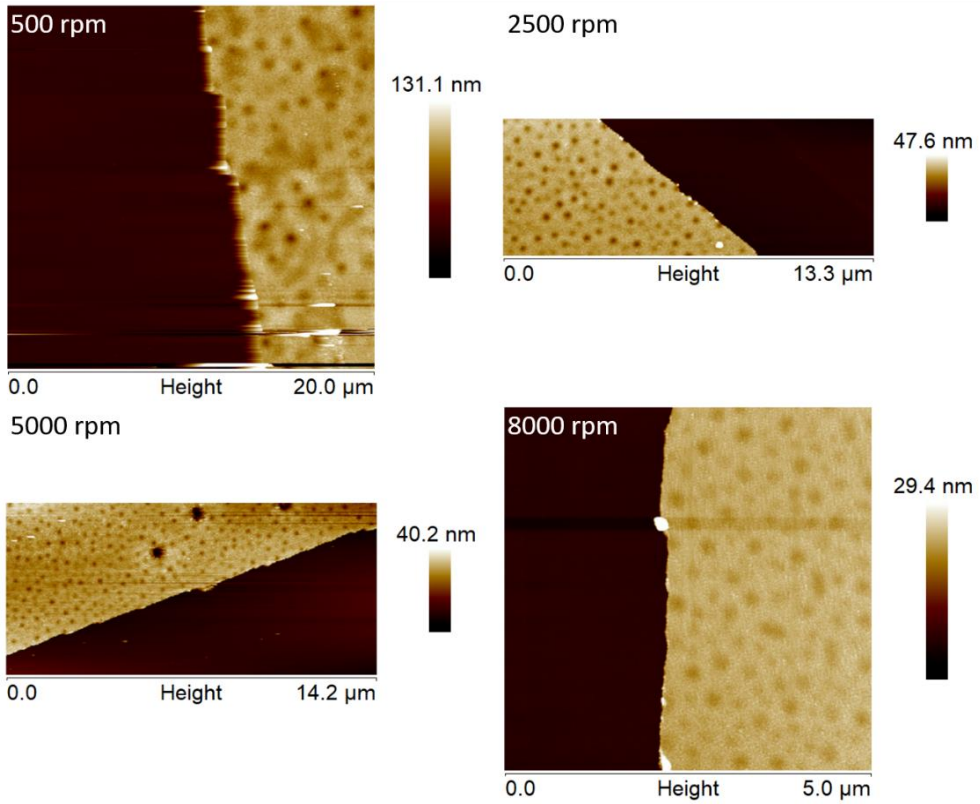

Figure 6-56: AFM height maps of CuSCN films spun from 15 mg mL^{-1} DeS suspension at a range of spin speeds. The 2500 rpm and 5000 rpm images have been cropped to assist in finding a flat base line.

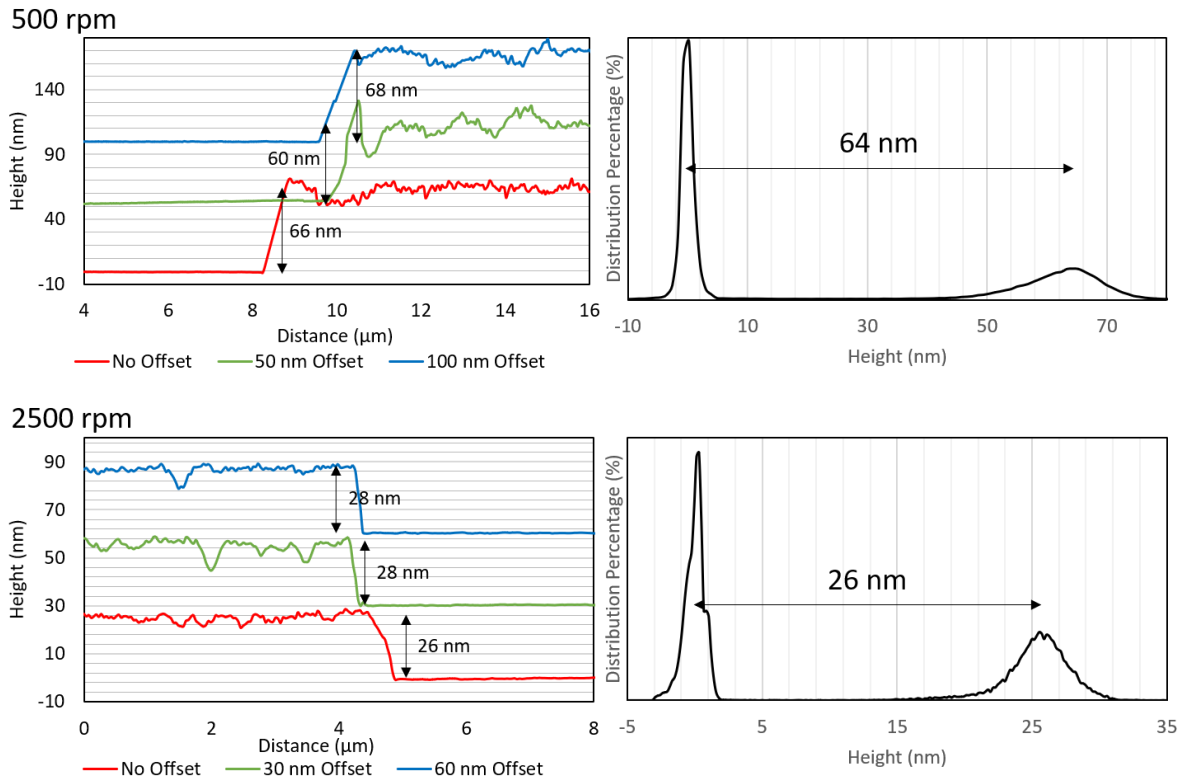

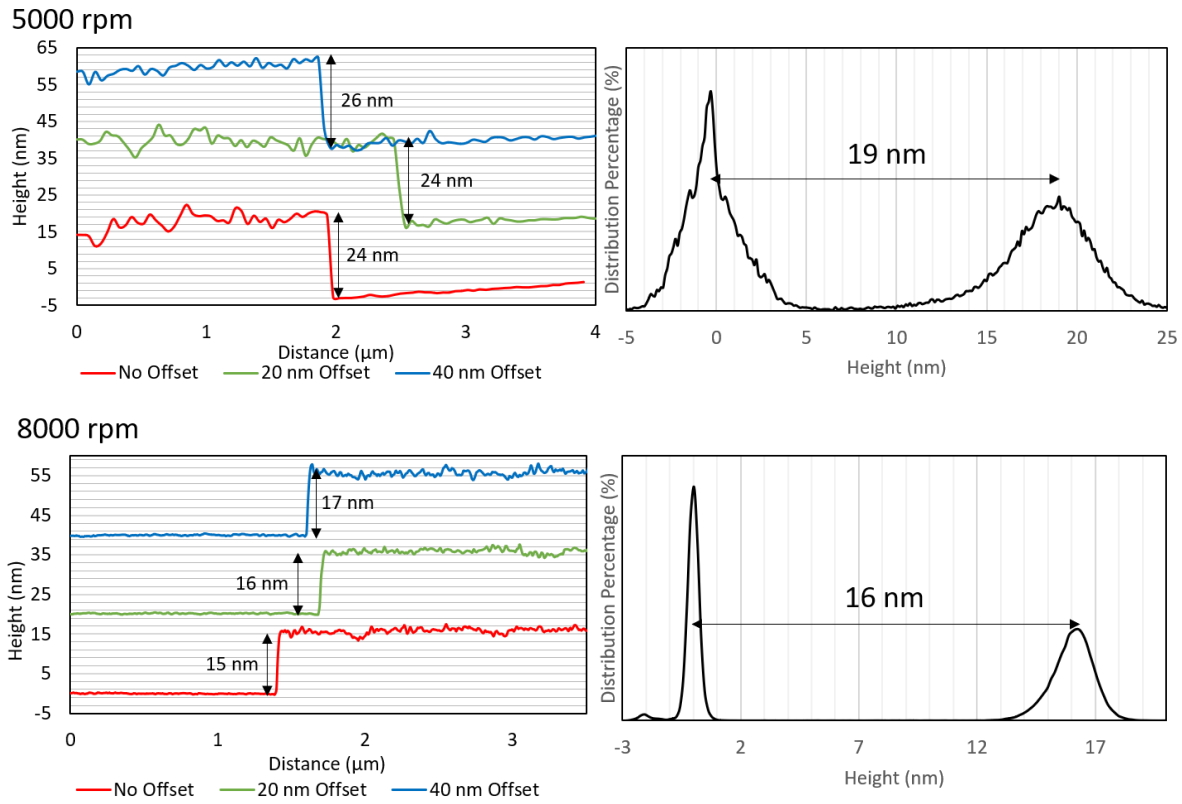

Figure 6-57: AFM cross-sectional line graphs and height distribution plots of CuSCN films spun from 15 mg mL^{-1} DeS suspension at a range of spin speeds.

Figure 6-56 and Figure 6-57 show the effect of spin speed on film thickness. As expected, the film thickness decreases with increasing spin speed. Compared to the MoO_x films, the thickness of the CuSCN films was significantly easier to determine as there is a clear distinction between the film surface and the substrate surface. The percentage distribution plots are well resolved and give good agreement with the cross-sectional line graphs. An exception is the 5000 rpm sample. The height distribution plot gives a film thickness of 19 nm whereas the line graphs show thicknesses of 24 nm - 26 nm. This could be simply due to the areas picked for cross-sectional analysis. In addition, the baseline is not flat for the cross-sectional graphs for this sample, which could be the reason for the difference in height measurements.

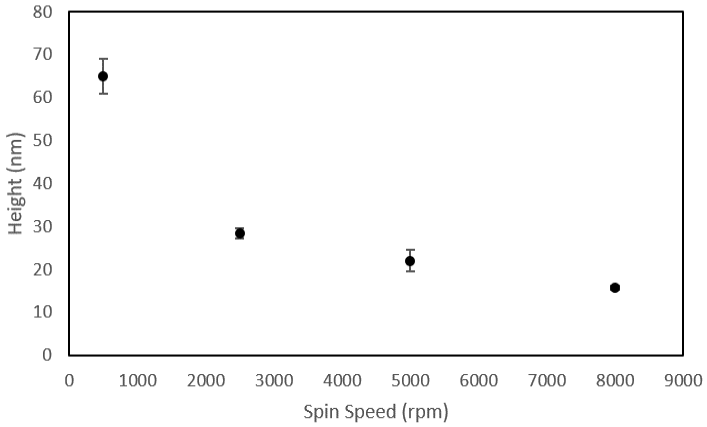

Figure 6-58: Film thickness vs rpm for CuSCN films spun from 15 mg mL^{-1} DeS solutions.

Figure 6-58 shows the trend in film thickness as spin speed is increased for CuSCN films spun from 15 mg mL^{-1} DeS suspension. There is a sharp drop present from 500 rpm to 2500 rpm followed by a shallower linear decrease in thickness with increasing spin speed. The same experiments were performed on CuSCN films spun from 10 mg mL^{-1} and 5 mg mL^{-1} DeS suspensions.

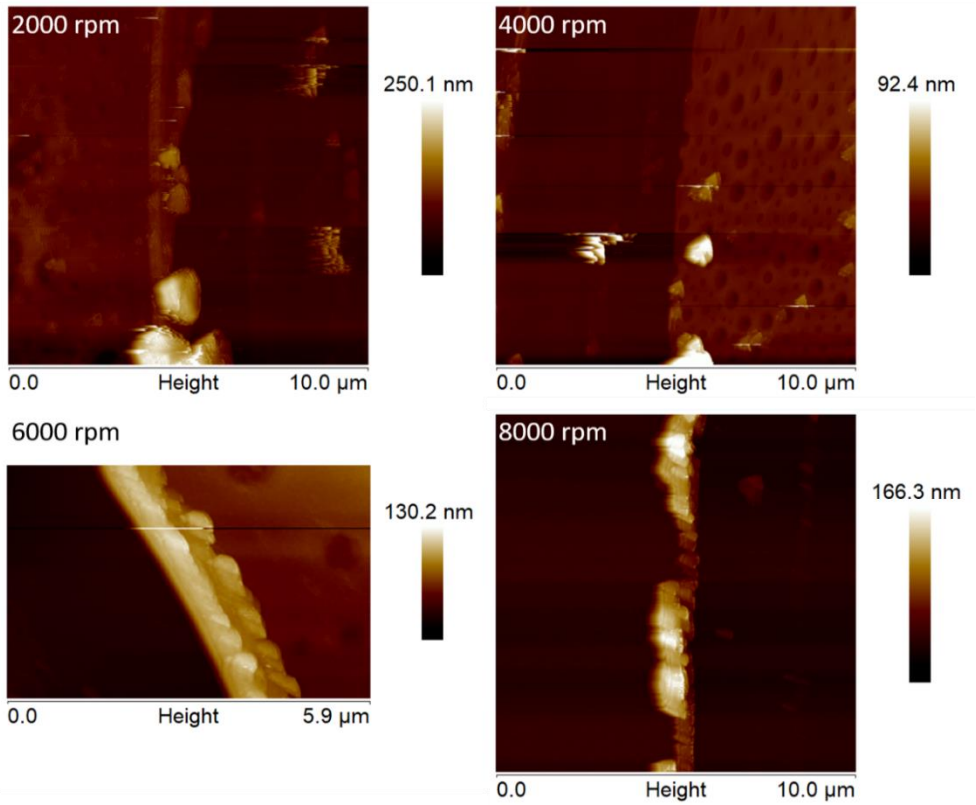

Figure 6-59: AFM height maps of CuSCN films spun from 10 mg mL^{-1} DeS suspension at different spin speeds. The 6000 rpm image have been cropped to assist in finding a flat base line.

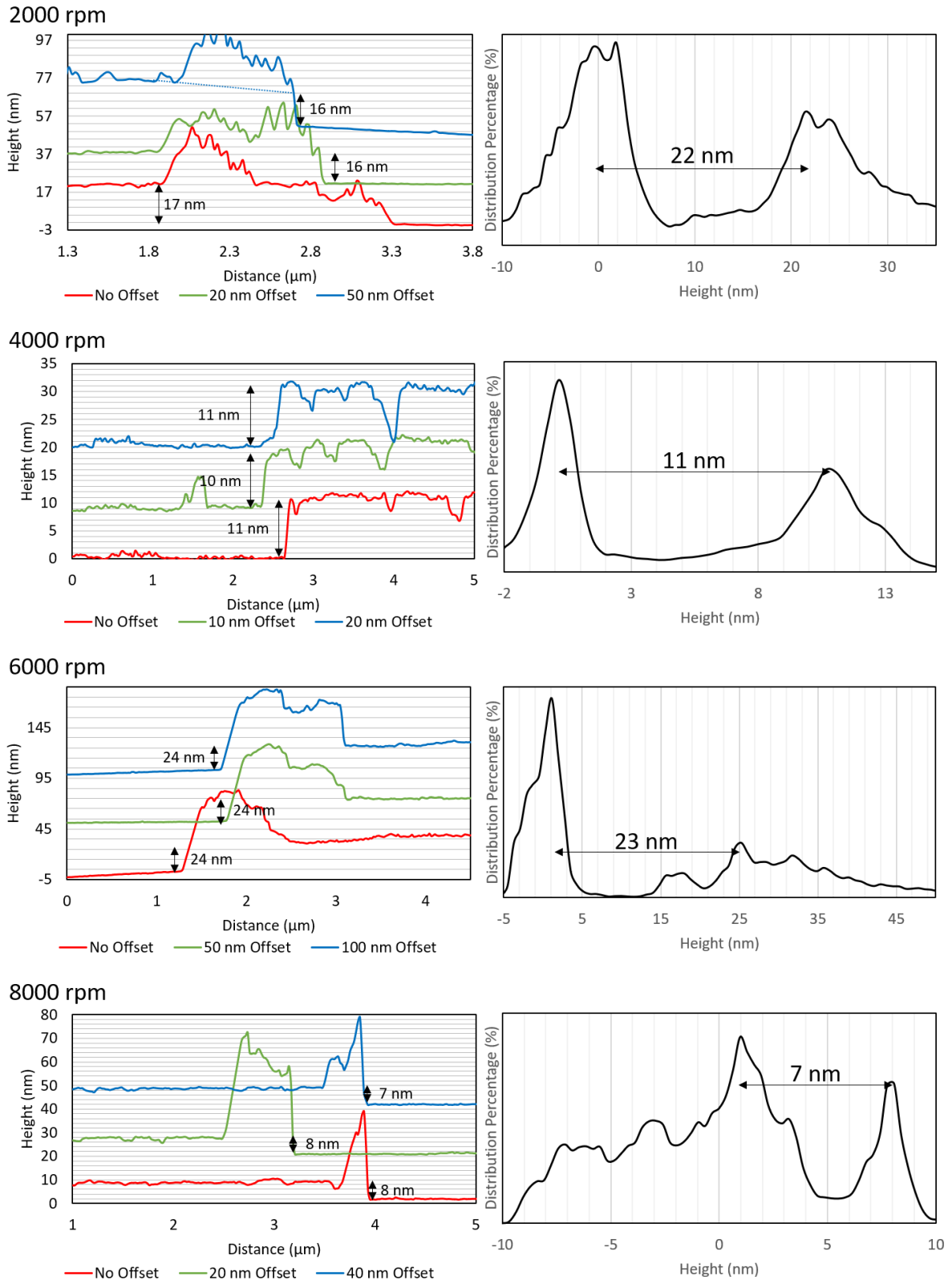

Figure 6-60: Cross sectional plots and percentage distribution plots of CuSCN films spun from 10 mg mL^{-1} DeS solution at different spin speeds.

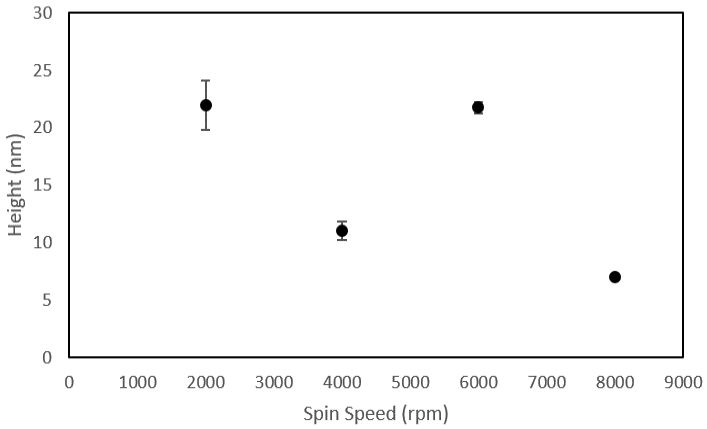

Figure 6-61: Film thickness vs spin speed for CuSCN films spun from 10 mg mL^{-1} DeS solution.

Figure 6-59 and Figure 6-60 show the AFM height maps, cross-sectional line graphs, and percentage distribution plots for CuSCN films spun from 10 mg mL^{-1} suspension. There is good agreement between the cross-sectional graphs and the percentage distribution plots with the exception of the 2000 rpm sample where the percentage distribution plot gave a thicker measurement than the cross-sectional line graphs. This could be due to the large amount of distortion and shadowing visible in the AFM height map for this sample (Figure 6-60). The large lumps on the edge of the film area (100 nm high in some cases) cause shadowing where the film areas next to these are measured as being lower in thickness, due to the feedback mechanism of AFM imaging, compared to the areas that have smaller lumps on the edge of the film area. This causes peak broadening and leads to broad, noisy distribution plots. The trend in thickness vs rpm in Figure 6-61, is similar to that in Figure 6-58 with a sharp drop from 2000 rpm to 4000 rpm and a shallower drop down to 8000 rpm. The film thickness of 22 nm for the 6000 rpm film is likely an outlier. The 6000 rpm sample was observed to also have thinner areas of film that were around 10 nm in thickness although these areas have poor homogeneity and thus the thicker, more homgeneous areas were used in Figure 6-59 and Figure 6-60.

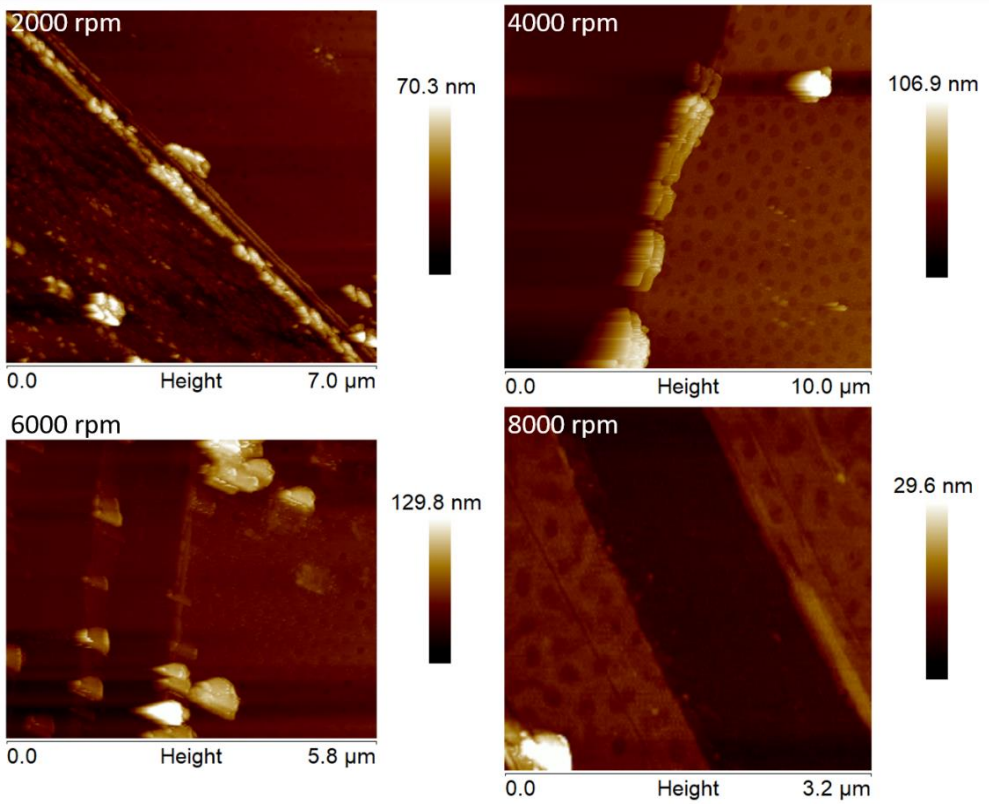

Figure 6-62: AFM height maps of CuSCN films spun from 5 mg mL^{-1} DeS suspension. The 6000 rpm and 8000 rpm images have been cropped to assist in finding a flat base line.

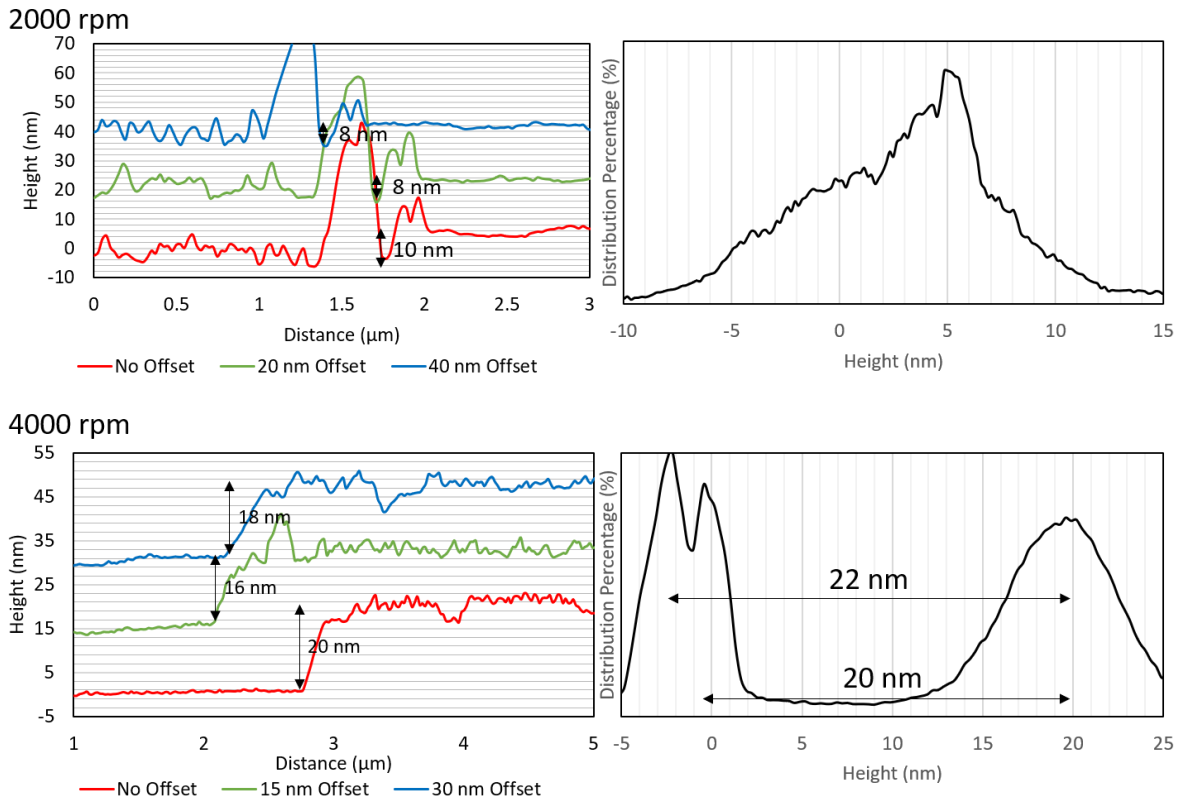

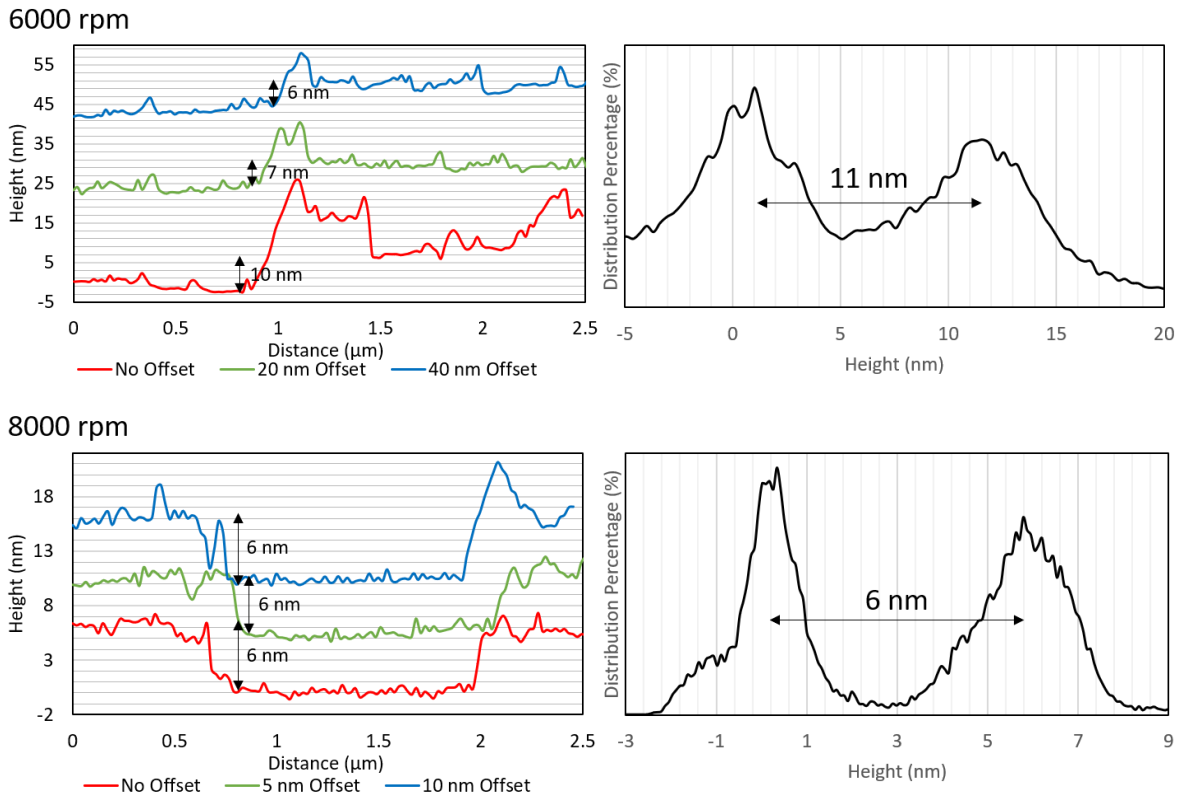

Figure 6-63: Cross-sectional line graphs and height distribution plots of CuSCN films spun from 5 mg mL^{-1} DeS suspension.

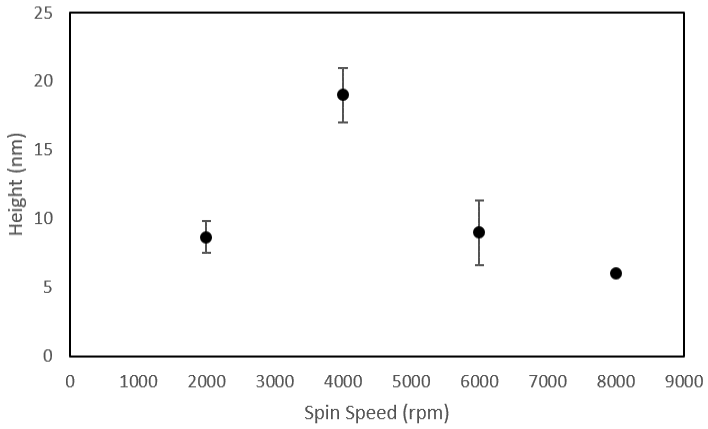

Figure 6-64: Film thickness vs spin speed for CuSCN films spun from 5 mg mL^{-1} DeS suspension.

Figure 6-62 and Figure 6-63 show AFM height maps, cross-sectional line graphs and height distribution plots for CuSCN films spun from 5 mg mL^{-1} DeS suspension. There is decent agreement between the line graphs and the distribution plots, although the 4000 rpm and 6000 rpm samples appear thicker in the distribution plots compared to the line graphs. The 2000 rpm distribution plot does not display two resolved peaks, whilst the cross-sectional line graphs give a film thickness of 8-10 nm. When compared to the other three data points, the 2000 rpm sample appears to be significantly thinner than expected. The AFM height map for this sample shows a large amount of debris in the scratched

channel. This is likely the reason for the poor distribution plot and may be the cause of the thinner than expected film height. Alternatively, the 2000 rpm film may simply have been thinner than the other three. The plot gives a clear decrease in film thickness with spin speed if the 2000 rpm point is ignored, however this would indicate that a 5 mg mL^{-1} solution spun at 4000 rpm is thicker than a 10 mg mL^{-1} solution spun at 4000 rpm which opposes the generally observed trend of a decrease in film thickness with lower concentration. Overall, by lowering the CuSCN concentration, films around 10 nm and 5 nm in thickness were produced.

6.3.4.4 SEM images of CuSCN films.

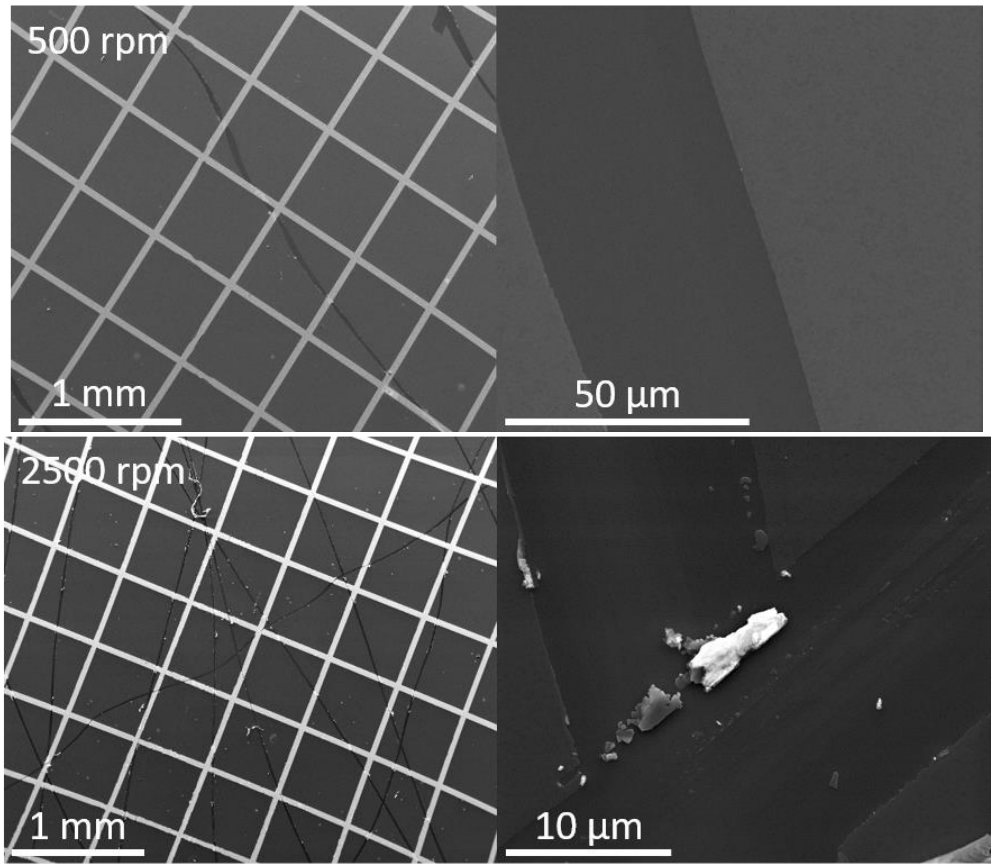

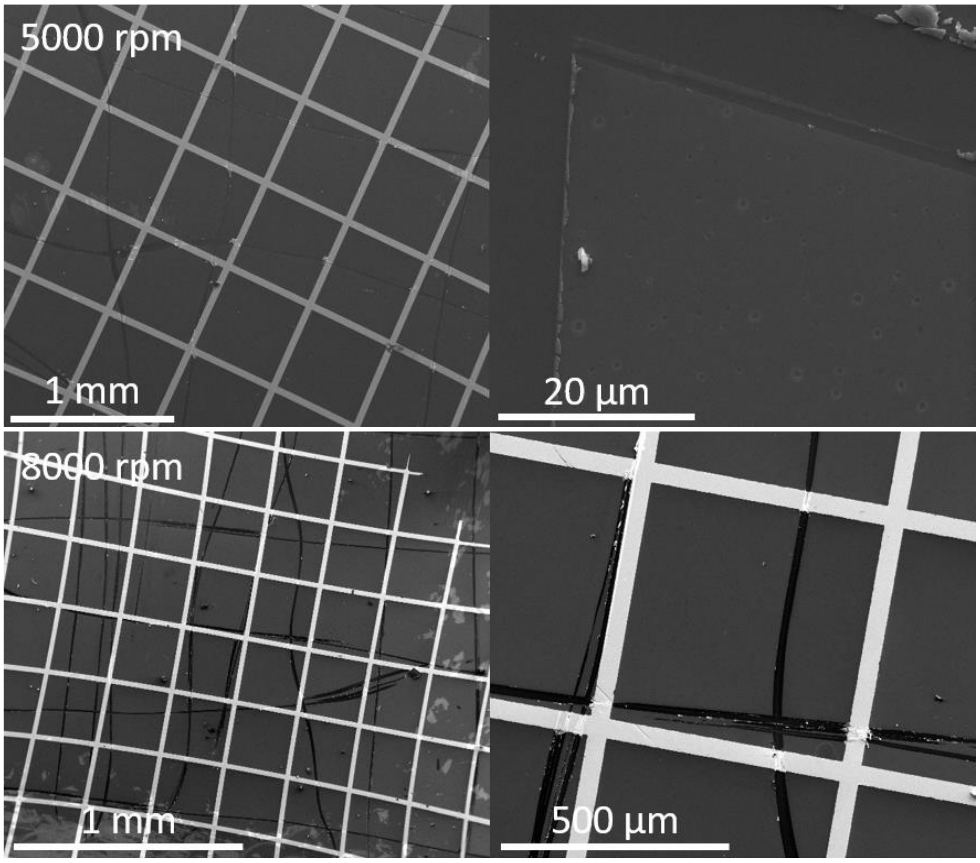

Figure 6-65: SEM images of CuSCN films spun from 15 mg mL^{-1} DeS suspension at different spin speeds.

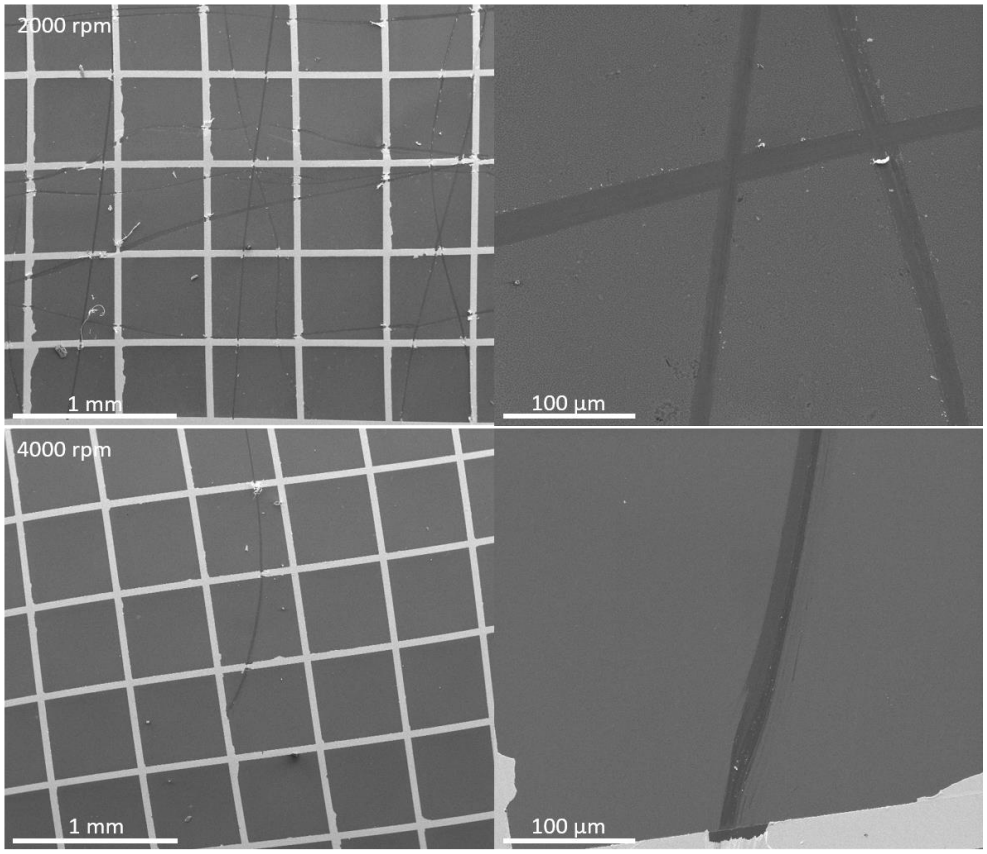

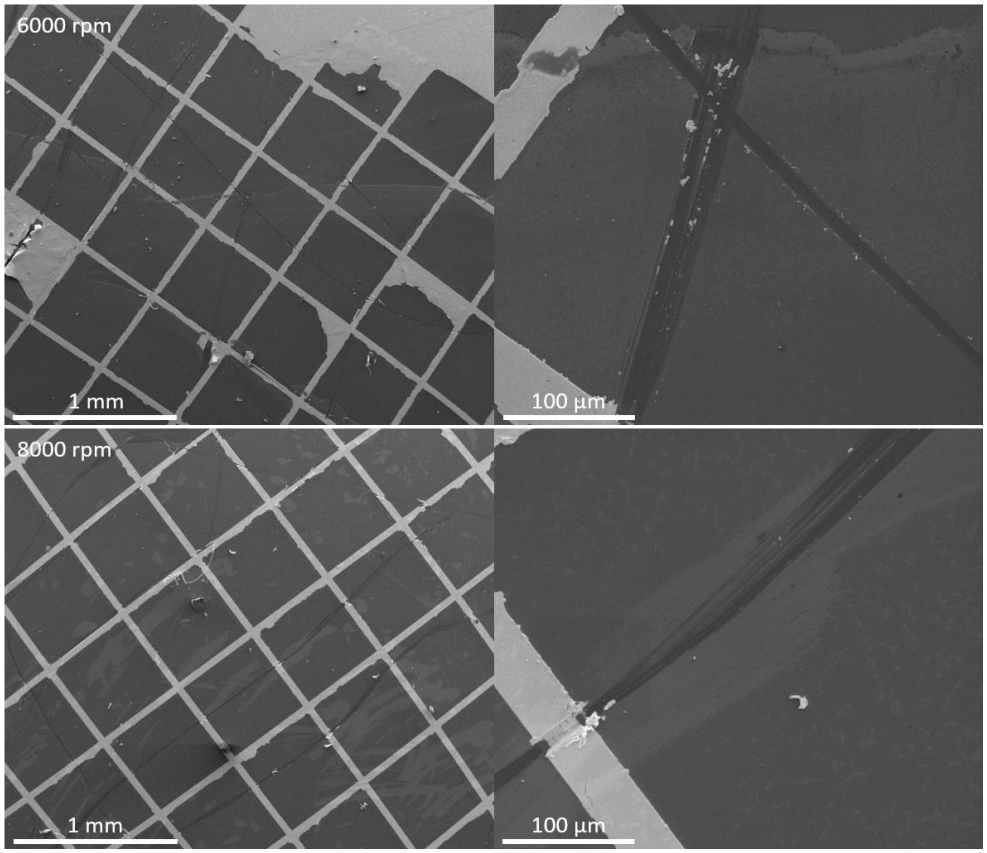

Figure 6-66: SEM images of CuSCN films spun from 10 mg mL^{-1} DeS suspension at different spin speeds.

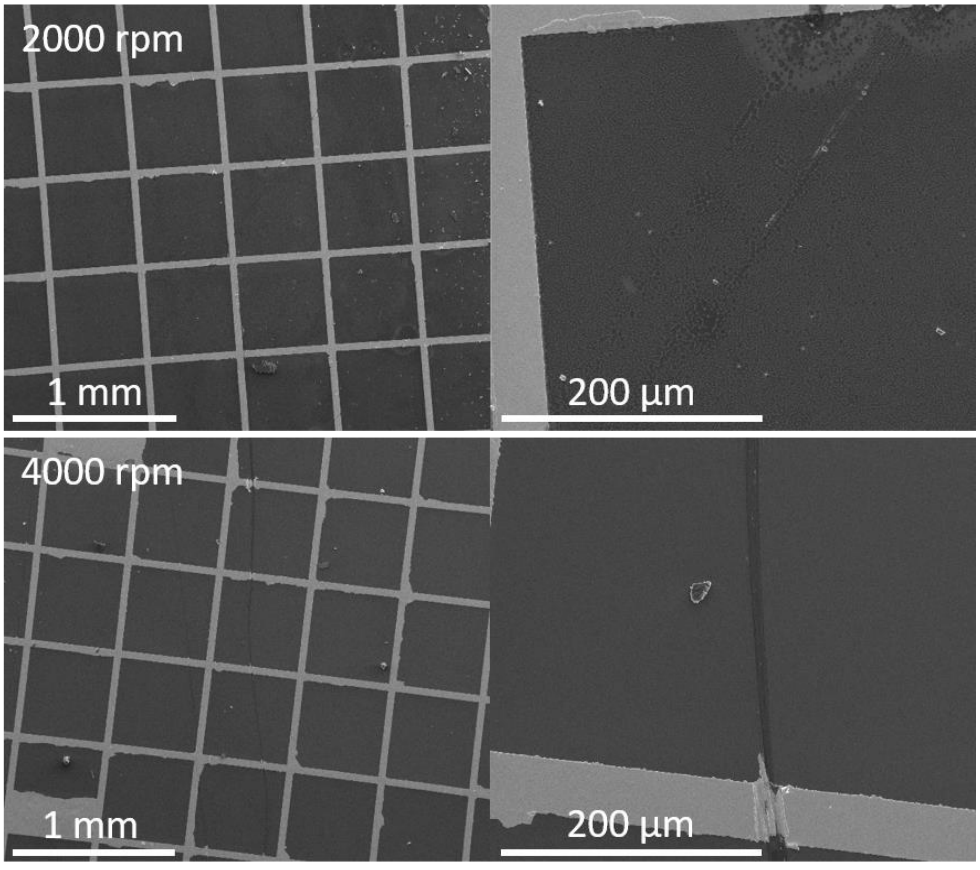

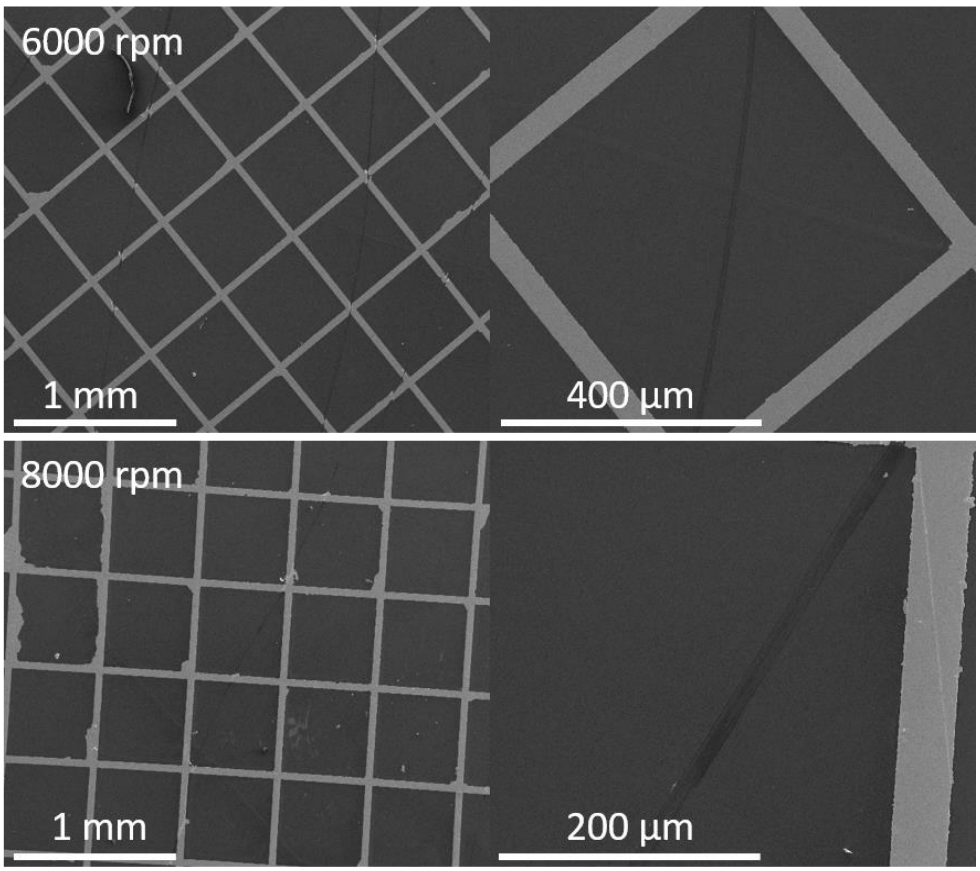

Figure 6-67: SEM images of CuSCN films spun from 5 mg mL^{-1} suspension at different spin speeds.

Figure 6-65, Figure 6-66, and Figure 6-67 show SEM images of CuSCN films spun at different spin speeds and from different solution concentrations. In all 15 mg mL^{-1} films, small holes are present in the film, similar to those seen in the MoO_x films. For the 10 mg mL^{-1} films (Figure 6-66) there is a clear lack of morphological consistency between the films. The 2000 rpm sample is heavily pockmarked, whilst the 4000 rpm sample displays a smooth consistent film. The 6000 rpm sample shows two regions of different morphology, separated by a thicker CuSCN line. This likely corresponded to swirl marks in the direction of spin which were occasionally visible on substrates after spin coating. The 8000 rpm sample shows differing regions across the CuSCN film and wrinkled artefacts on the darker areas. The films spun from 5 mg mL^{-1} DeS suspension (Figure 6-67) exhibit some poor film formation. The 2000 rpm sample exhibits very poor coverage which explains the poor AFM height distribution and cross section plots for this sample (Figure 6-63) indicating that this point was the outlier in the film height vs spin speed plot (Figure 6-64). In addition, the 8000 rpm sample shows small regions of poor coverage. In general, the CuSCN films appear to form reasonably homogeneous surface

coverages. However, it was clear that there were problems with consistently forming good films across substrates, despite identical substrate preparation regimes. This inconsistency was likely the reason for outlier values in the film thickness vs spin speed plots (Figure 6-61 and Figure 6-64).

6.3.5 Solar Device Data

As for the other interlayers examined in this chapter, devices were fabricated with different volumes of interlayer solution to determine an optimal volume.

6.3.5.1 MoO_x Devices with Varied Solution Volume

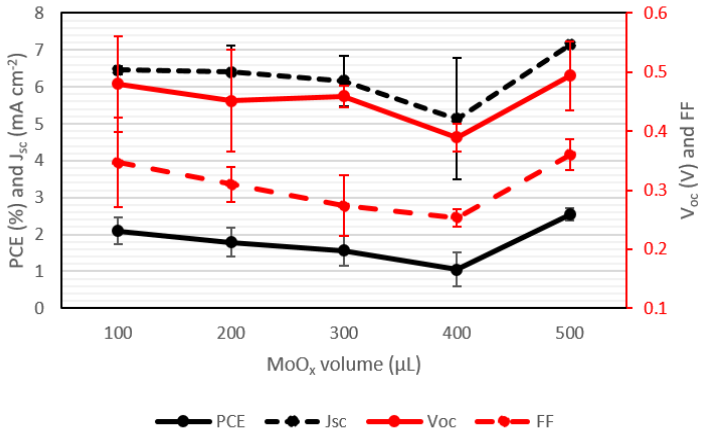

Figure 6-68: J/V properties for devices with MoO_x interlayers formed from different deposition volumes after doping with $AuCl_3$ solution.

Figure 6-68 shows that the performance of the CNT/MoO_x/Si device drops with an increase in volume, before a sharp increase occurs from 400 µL to 500 µL. The best performing devices were those produced with a 500 µL aliquot. Based on this, a volume of 500 µL was used in future CNT/MoO_x/Si device experiments. The J_{sc}, V_{oc}, and FF all displayed the same trend as the PCE, indicating that no particular parameter was the reason for the PCE change with aliquot volume. The best performing set of devices recorded an average PCE of 2.54 % ± 0.17, an average V_{oc} of 0.494 V ± 0.058, an average J_{sc} of 7.13 mA cm^{-2} ± 0.03, and an average FF of 0.36 ± 0.027. A concurrent set of devices with no interlayer was produced which recorded an average PCE of 2.89 % ± 0.40, an average V_{oc} of 0.476 V ± 0.017, an average J_{sc} of 6.65 mA cm^{-2} ± 0.30, and an average FF of 0.45 ± 0.035. The CNT/Si devices outperformed the CNT/MoO_x/Si devices in PCE. This was entirely due to their superior FF values, both the average V_{oc} and J_{sc} values were higher for the devices with a MoO_x interlayer. However, these devices were measured prior to the discovery that water dissolves the MoO_x layer. Thus, the AP data

was measured after CNT/GO film attachment in a water bath and the $AuCl_3$ data was measured after spin coating with an aqueous suspension. Therefore, the comparative data shown in Figure 6-69 may just be comparing two sets of devices with no interlayer, justifying the average PCE values being within error for both sets after $AuCl_3$ treatment. Although this doesn't explain the differences in device performance observed in Figure 6-68. It is possible that the 30 min 80 °C annealing process slightly lowers device performance when no interlayer is present.

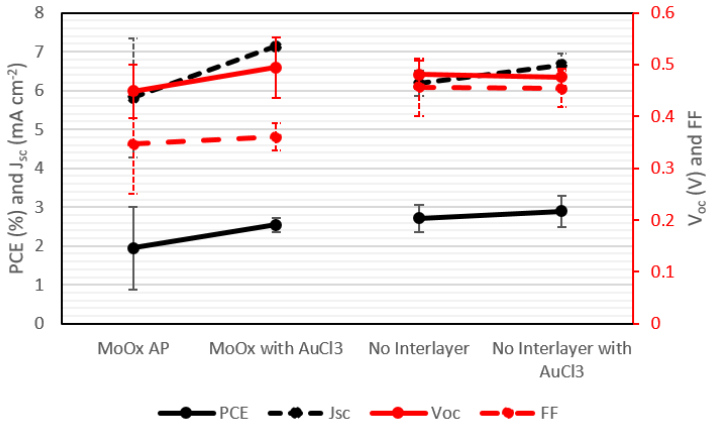

Figure 6-69: J/V properties for best performing MoO_x devices compared with devices with no interlayer.

6.3.5.2 MoO_x Devices with Varied Film Thickness

Devices with a MoO_x interlayer were prepared at 2500 rpm and 3500 rpm and the CNT film was attached directly from the acetone bath to avoid any contact with water. Due to the effect of water on the MoO_x film no 2 % HF etch could be performed prior to doping and thus, a vapour thionyl chloride dope was the only post fabrication treatment performed.

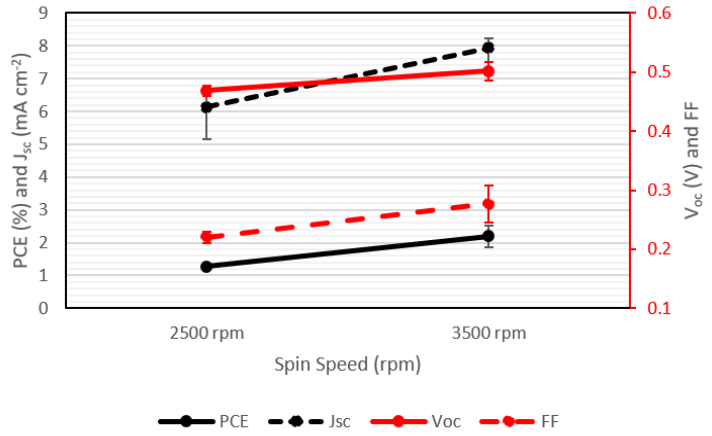

Figure 6-70: J/V properties of devices with a MoO_x interlayer after doping with thionyl chloride vapour.

Figure 6-70 shows that a higher spin speed gives improved performance for CNT/MoO_x/Si devices, indicating that a thin layer of 5-6 nm is optimal for these devices. Although, as the thickness of the MoO_x film did not change much across these spin speeds this is inconclusive. The 3500 rpm sample produced an average PCE of 2.20 % ± 0.32 after doping. This is lower than the average PCE of CNT/Si devices produced concurrently of 4.98 % ± 0.14. Thus, a MoO_x film applied from solution as described in this thesis does not improve the performance of CNT/Si devices. This may be due to the MoO_x inhibiting the CNT/Si junction. It is known that MoO_x improves the ability of the CNT film to transport charge carriers and the Au/CNT top contact junction.[16] Thus, the presence of MoO_x on the CNT/Si junction may be detrimental to device performance. Additionally, the thickness of the MoO_x layer shown to give significant device improvement was 40 nm, which is significantly thicker than the layers applied in this experiment.[16]

Wang *et al*. found that thermally deposited MoO_x layers acted as a light-trapping layer on CNT/Si devices.[16] Thus, CNT/Si devices with no interlayer were spin-coated with solution processed MoO_x to determine if a similar effect could be seen with this method.

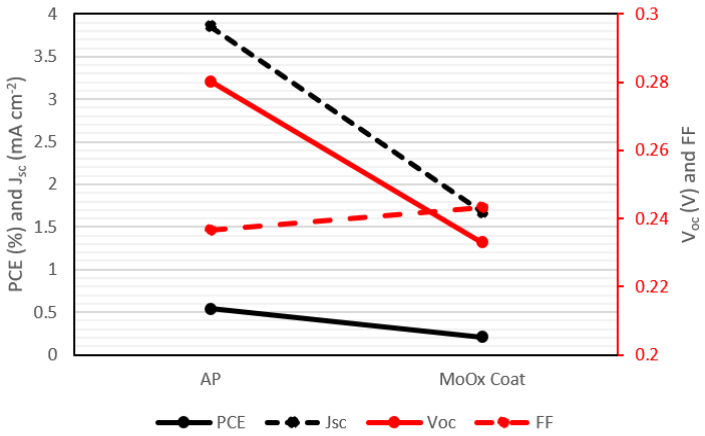

Figure 6-71: J/V properties for CNT/Si before and after coating with MoO_x.

Figure 6-71 shows that performance decreased for a set of devices produced with no interlayer when coated with a MoO_x layer with no doping treatment. The film was coated using a spin speed of 2500 rpm and thus was around 15 nm thick. The MoO_x layer which lead to significant improvement in the

work by Wang *et al.*[16] was shown to be 40 nm thick. This difference in MoO_x film thickness may explain the poor performance of CNT/MoO_x/Si devices in this section.

6.3.5.3 CuSCN Devices with Varied Solution Volume

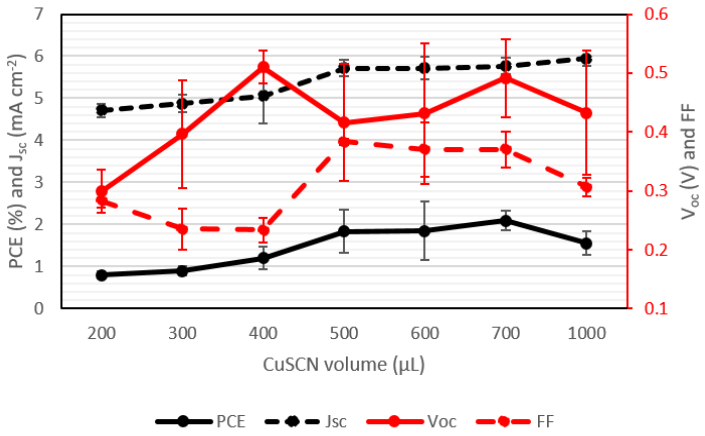

Figure 6-72: J/V properties for devices with CuSCN interlayers spun from different deposition volumes of a 15 mg mL^{-1} DeS suspension at a spin speed of 3500 rpm after doping with $AuCl_3$ solution.

Figure 6-72 shows that PCE of CNT/CuSCN/Si devices increases with an increase in volume up until around the 500 µL – 700 µL mark where all three sets of devices recorded PCE averages within error range. When the volume was increased up to 1 mL the performance decreased. The decrease exhibited by the 1 mL set of devices was due to decreases in V_{oc} and FF, whilst the J_{sc} increased slightly for this set. The reason for the increase in PCE from the 200 µL to 500 µL sets is more difficult to identify. The J_{sc} increased or remained steady throughout the increase in deposition volume. The V_{oc}, meanwhile, peaked at 400 µL and again at 700 µL with a trough in between. The average FF values formed a plateau from 500 µL to 700 µL higher than any other sets of devices. However, the average FF dropped from 200 µL to 400 µL before rising sharply to the 500 µL high. It is apparent that, within the 500 µL, 600 µL, and 700 µL sets the difference in performance is due to an increase in V_{oc} with increasing deposition volume. The best performing set of devices (in terms of PCE) recorded an average PCE of 2.09 % ± 0.23, an average V_{oc} of 0.49 V ± 0.07, an average J_{sc} of 5.77 mA cm^{-2} ± 0.19, and an average FF of 0.37 ± 0.03. A concurrent set of devices were produced with no interlayer which recorded an average PCE of 1.77 % ± 0.69, an average V_{oc} of 0.38 V ± 0.05, an average J_{sc} of 5.77 mA cm^{-2} ± 0.29, and an average FF of 0.39 ± 0.096. The devices with no interlayer shown here performed worse than those shown in other cases (Figure 6-19 and Figure 6-30) this was due to the use of H_2O_2

for SiO_x growth in the devices in Figure 6-72 which was later found to severely diminish device performance (Section 5.5). In this case, the two sets of devices display identical average J_{sc} values and average FF values that fall within error of each other. The difference between the sets was the average V_{oc} values which were higher for the CNT/CuSCN/Si devices which lead to these devices outperforming the CNT/Si devices after $AuCl_3$ doping. The CNT/CuSCN/Si devices improved by roughly 0.5 % PCE with the doping, whilst the CNT/Si devices deteriorated by roughly 0.4 % PCE with doping. Prior to doping, the CNT/Si devices outperformed the CNT/CuSCN/Si devices.

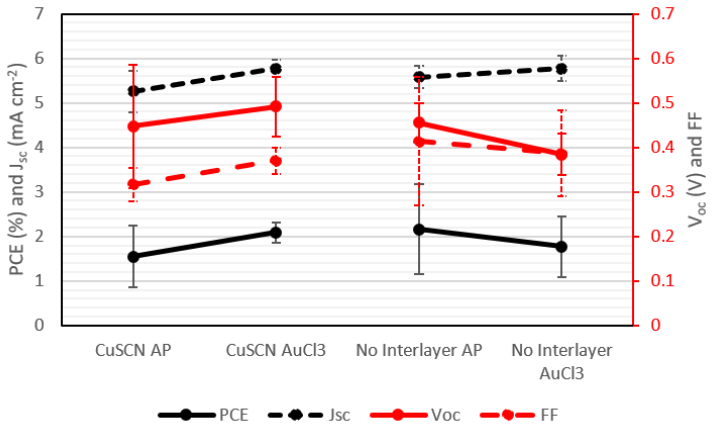

Figure 6-73: J/V properties for best performing CuSCN devices (700 µL) compared with devices with no interlayer both before and after $AuCl_3$ doping.

6.3.5.4 CuSCN Devices with Varied Film Thickness

The spin speed used in CuSCN interlayer formation was varied in order to determine the effect of CuSCN film thickness on device performance. Initially a CuSCN solution of 15 mg mL^{-1} in DeS was used, however this was decreased later to achieve thinner CuSCN layers.

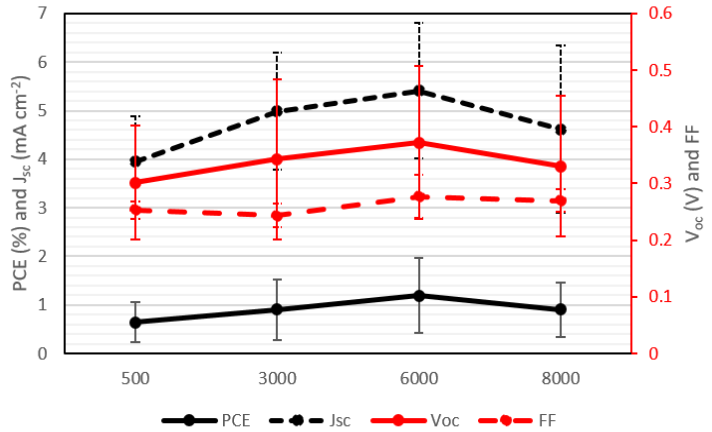

Figure 6-74: J/V properties for devices with CuSCN interlayers spun from 15 mg mL^{-1} DeS solution at different spin speeds after doping with $AuCl_3$

Figure 6-74 shows that there is a local maximum in PCE at a spin speed of 6000 rpm (a film thickness of between 20 nm and 16 nm). The PCE trend is due to a trend of increasing J_{sc}, V_{oc}, and FF from 500 rpm to 6000 rpm and a decrease down to 8000 rpm. However, all the average data points are within error values of one another and the performance is poor with the average PCE for the 6000 rpm set 1.19 % ± 0.77. This is caused by low average J_{sc} (5.41 mA cm^{-2} ± 1.40), V_{oc} (0.37 V ± 0.12), and FF (0.28 ± 0.04) values. A set of devices were fabricated using the same spin speed but with a 5 mg mL^{-1} DeS solution. This set of devices outperformed the best performing set of devices from Figure 6-74 with an average PCE of 1.60 % ± 0.22, an average V_{oc} of 0.40 V ± 0.02, an average J_{sc} of 6.34 mA cm^{-2} ± 0.32, and an average FF of 0.32 ± 0.03. Thus, the devices with the thinner film performed more favourably than the devices in Figure 6-74. In order to further test the effect of much thinner films, three sets of devices were produced with film thicknesses of 16-20 nm (6000 rpm 15 mg mL^{-1}), 10 nm (6000 rpm 10 mg mL^{-1}), and 5 nm (8000 rpm 5 mg mL^{-1}). These devices were fabricated with CNT/GO films of higher transmittance than those used in the previous CuSCN devices (65 % - 68 % vs 50 %).

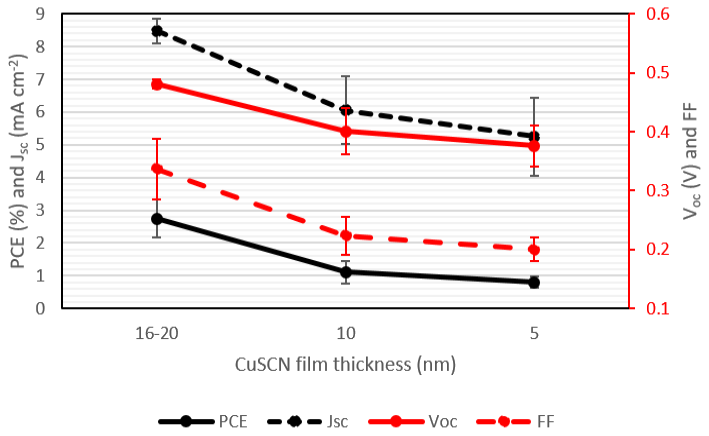

Figure 6-75: J/V properties for devices with CuSCN layers with different thicknesses after doping with $SOCl_2$.

Figure 6-75 shows that the CNT/CuSCN/Si devices decreased in performance across all parameters as the film thickness decreased. This is contrary to what was suggested by the results from the above experiment. The highest PCE data in Figure 6-75 is superior to that seen in Figure 6-72 and Figure 6-73. This is due to the use of CNT/GO films with higher transmittance than used previously. However, this performance is still low compared to concurrent CNT/Si devices, also with high CNT/GO film transmittance, which recorded an average PCE of 4.98 % ± 0.14.

6.3.5.5 Devices without CNTs

As with PEDOT:PSS and PANI, the two interlayers studied in this section were spun onto substrates and tested with no CNT film, with and without a 5 nm gold surface layer.

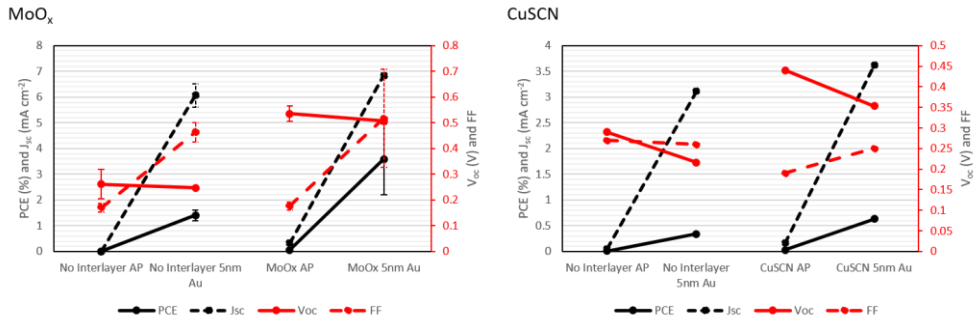

Figure 6-76: J/V properties for devices with no CNT film.

Figure 6-76 shows that devices with a MoO_x layer and a 5 nm gold layer showed significantly better performance than those with a CNT/GO film with an average PCE of 3.59 % ± 1.37 and a best performing PCE of 4.67 %. This was due to a V_{oc} roughly twice as much that of the devices with no interlayer. There was a significant increase in performance once the 5 nm gold layer was added. The V_{oc} was decreased slightly but the J_{sc}, and FF significantly improved, leading to the improvement in PCE. This indicates that the interlayer is insufficiently conductive to provide good extraction of charge carriers and the gold film is required to allow for good extraction. The device with a CuSCN interlayer also displayed a higher V_{oc} than the device with no interlayer however not to the extent of the MoO_x devices. These devices also showed the pattern of increasing J_{sc} with the application of a gold layer. However, there was little FF improvement and the V_{oc} decreased for both devices. The device with a CuSCN interlayer outperformed the device with no interlayer, yet not to the extent seen with the MoO_x devices. This suggests that Au/MoO_x/Si devices may be an interesting future research pathway.

6.3.5.6 Final Devices

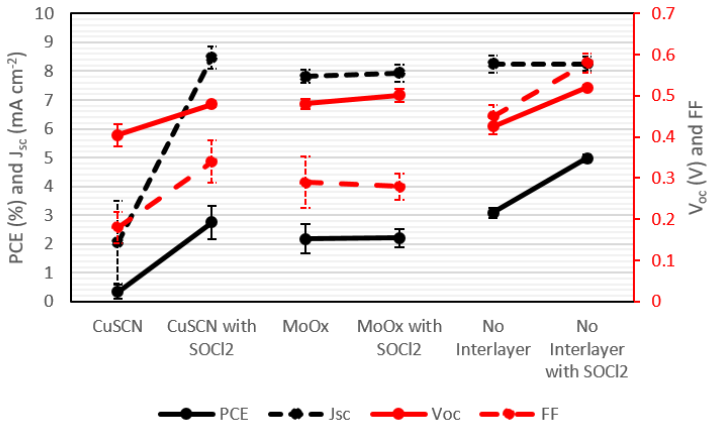

Figure 6-77: J/V properties for devices with optimal CuSCN and MoO_x interlayers or no interlayer both before and after doping with $SOCl_2$. The CNT/GO films used had transmittances from 65 %- 68 %

As with PEDOT:PSS and PANI interlayers (Figure 6-30), once optimal CuSCN and MoO_x film formation parameters were determined devices were produced with CNT/GO films with significantly higher transmittances than in previous experiments. The data from these devices are shown in Figure 6-77. The PCE for the CuSCN and MoO_x devices did not appear to be significantly higher than those seen in Figure 6-69 and Figure 6-75 for MoO_x and CuSCN respectively. The CuSCN devices achieved a PCE high of 3.23 % with an average of 2.75 % ± 0.58, whilst the MoO_x devices achieved a PCE high of 2.43 % with an average of 2.20 % ± 0.32. This was compared with devices with no interlayer, which achieved a PCE high of 5.12 % and an average of 4.98 % ± 0.14. It is clear that the increase in CNT/GO film transmittance has had a much more pronounced effect on the performance of the devices with no interlayer compared with devices with CuSCN or MoO_x interlayers. $SOCl_2$ doping significantly improved the performance of both the CuSCN devices and the devices with no interlayers, whilst having a negligible effect on devices with a MoO_x interlayer. The main reason for the PCE differences between the device sets is the FF. Devices with either CuSCN or MoO_x interlayers displayed FF values from 0.25 to 0.35 on average after doping, compared with 0.45 and 0.58 for the devices with no interlayers before and after doping. This indicates that the devices with interlayers experience a higher degree of surface recombination, possibly due to poor surface passivation. In contrast, the J_{sc} values are roughly equivalent post doping, with the devices with CuSCN interlayers producing the best J_{sc} of 8.77 mA cm^{-2}.

Previously, MoO_x has been shown to give good device performance when incorporated as an interlayer in the CNT/Si heterojunction device.[16] It is obvious that this was not achieved with the MoO_x layers applied in this chapter. This could be due to the poor film morphology exhibited by the MoO_x films, additionally, the optimal thickness of the MoO_x layer in the work by Wang *et al.* was 40 nm[16] which is thicker than the MoO_x films present in the best performing devices in this chapter. Alternatively, the difference in MoO_x layer formation could be a cause. The layers in the work by Wang *et al*. were produced via thermal evaporation[16] whereas the films in this chapter were solution processed. However, solution processed MoO_x layers have been successfully incorporated as hole transporting layers in polymer solar cells[220] and in inverted organic solar cells.[221] Li *et al*. similarly used IPA as the solvent for solution processed MoO_x layer formation with vacuum treatment used to functionalise the material instead of thermal annealing. These MoO_x layers gave high performance inverted organic solar cells.[221] This suggests that the change from thermally evaporated MoO_x to a solution processed method is unlikely to be the reason for poor device performance. An additional reason for the difference in performance is that the devices used by Wang *et al.* had an active area 1 mm in diameter[16] which is considerably smaller than the large area devices used in this thesis. Ideally, the solution processed MoO_x film would be formed so it only affected the Au/CNT junction as this is the junction where it is expected to give improvement.

The CuSCN layers produced consisted of a larger range of thicknesses and exhibited superior film morphology to the MoO_x layers observed from the much clearer height differences visible between the silicon surface and the CuSCN films in AFM height analysis than for the MoO_x films. Research by Wijeyasinghe *et al*. used CuSCN suspended in both NH_3(aq) and DeS.[174] It was found that CuSCN films produced from NH_3(aq) suspensions display improved hole mobilities and vastly superior compositional purity and surface uniformity relative to CuSCN films produced from DeS suspension or PEDOT:PSS.[174] This indicates that the reason why no improvement in device performance was observed with the CuSCN layers examined in this chapter may be that DeS suspension is not the ideal method of forming solution processed CuSCN layers. The FF was the main discrepancy between the

devices with MoO_x and CuSCN layers compared to devices with no interlayer (Figure 6-77). It is possible that the MoO_x or CuSCN present on the silicon surface is increasing the amount of recombination and leading to a lower FF and lower device performance.

6.3.6 CuSCN and MoO_x Interlayer Conclusions

Both CuSCN and MoO_x films were fabricated via spin coating at a range of volumes and spin speeds. An optimal volume and spin speed was determined for CNT/interlayer/Si device performance. However, both interlayers did not produce devices which performed favourably compared to devices with no interlayer for the most part. The early CuSCN devices produced higher PCE values than devices with no interlayer (Figure 6-72), however later CuSCN devices failed to replicate this. The MoO_x films generally were very thin (around 5 nm) with a high concentration of holes present and, in some cases did not produce films that evenly coated the substrate surface. CuSCN in general, formed more homogeneous films than MoO_x. This may be an explanation for why devices with CuSCN interlayers generally outperformed devices with MoO_x interlayers. It was found that devices with a MoO_x interlayer and with a thin gold film in lieu of the CNT/GO film gave significantly higher performance than the other devices investigated in this section.

Overall, it is clear that both MoO_x and CuSCN layers spin coated from solution do not currently present promising hole-transport media for application in future CNT/Si heterojunction solar device designs. Unless changes are made to improve film morphology, film thickness, or to allow CuSCN films spun from NH_3(aq) suspensions to fully wet the substrate surface.

6.4 Novel Organic Interlayer

6.4.1 Introduction

As well as known interlayer materials, a novel organic interlayer was applied to the CNT/Si heterojunction solar device. The material's chemical name is 4,10-bis(bis(4-methoxyphenyl)amino)naptho[7,8,1,2,3-*nopqr*]tetraphene-6,12-dione. It consists of an anthanthrone (ANT) dye with functionalised diphenylamine (DPA) end caps and which is abbreviated to DAD (from

Dpa-Ant-Dpa). It was prepared in a one-step facile synthesis by Pham *et al*.[173] for use as a solution processed thin hole transport medium (HTM) in photovoltaic devices.

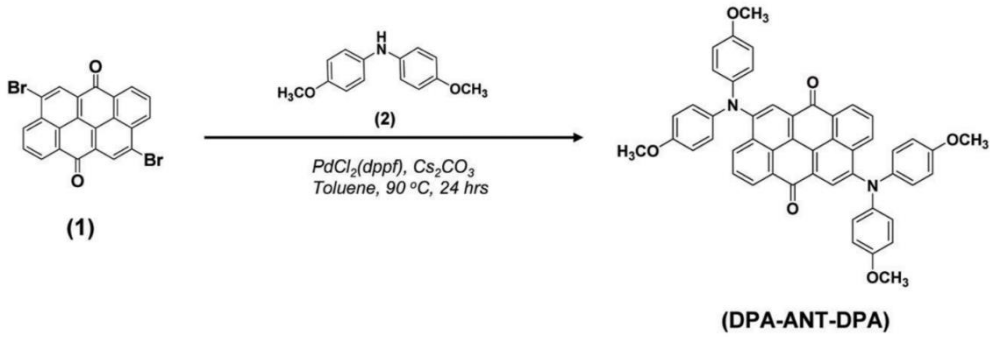

Figure 6-78: Schematic of the facile one-step synthesis of DAD.[173]

This novel interlayer material is of interest as it has been shown to provide similar benefits to device performance as the previously investigated 2,2',7,7' – tetrakis(N,N'-di-*p*-methoxyphenylamine)-9,9'-spirobifluorene, (Spiro-OMeTAD)[100, 173] with the advantage that the material can be prepared for spin coating in ambient conditions and without the need of a dopant chemical.[173] Alternative novel hole transporting materials from the same research group have been applied to small area CNT/Si heterojunction devices.[132] These materials were 4,4'-(naphthalene-2,6-diyl)bis(N,N-bis(4-methoxyphenyl)aniline) (NAP), and (E)-4',4'''-etene-1,2-diyl)bis(N,N-bis(4-methoxyphenyl)-[1'',1'''-biphenyl]-4-amine) (BPV). Both were shown to produce CNT/Interlayer/Si devices with PCEs higher than 10 % thanks to a reduction in recombination at the heterojunction interface.[132] Thus it can be seen that continued research in this area will lead to a suite of solution processed interlayers for improving device performance which can be applied in ambient conditions. Application in ambient conditions is preferred as it reduces cost and processing time.

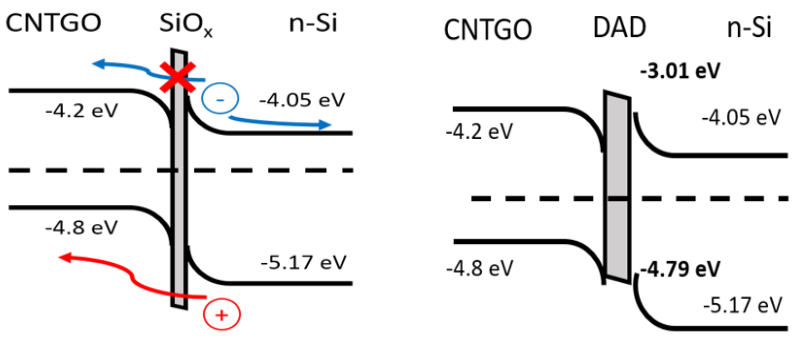

Figure 6-79: Energy diagrams for CNT/Si heterojunction solar devices with and without a DAD interlayer.

6.4.2 DAD Film Characterisation

Films of DAD spun from chlorobenzene were formed on glass slides at different spin speeds and UV/Visible spectra were measured. The films were created solely using a dropwise deposition method as this has been shown with previous films to give the best film formation.

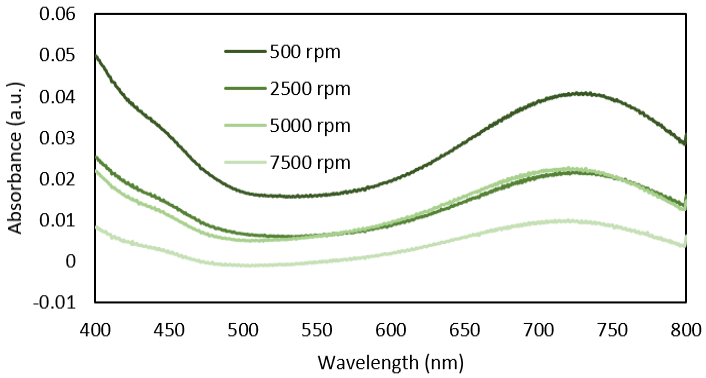

Figure 6-80: UV/Visible spectra of DAD films on glass spun from 200 µL aliquots dropwise for a variety of spin speeds.

Figure 6-80 shows a similar change in spectral shape with a change in spin speed on UV/Visible spectra to the other interlayers examined in this chapter (Figure 6-2, Figure 6-7, Figure 6-34, and Figure 6-46) The characteristic peak at roughly 730 nm decreases as the spin speed is increased, indicating that thinner films were produced at higher spin speeds. It is notable that there is no change in spectral shape between different spin speeds, indicating that the films were of the same structural composition, and just differed in volume of material on the surface. In order to analyse the change in peak height, with reference to the background of each sample, the difference was found between the peak at 730 nm and the baseline at 510 nm to give a relative peak height. The difference in absorbance was plotted against spin speed. Note that the fact that the 7500 rpm sample's spectrum dropped below an absorbance of 0 is due to the extremely low absorbance values recorded which will exacerbate any slight difference between the sample and the baseline glass slide.

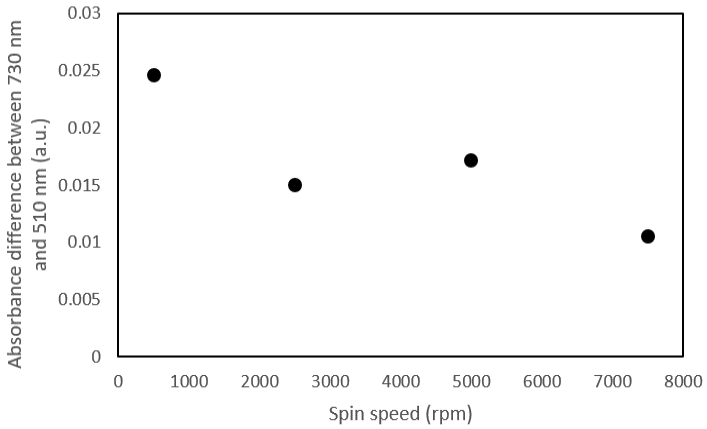

Figure 6-81: A plot of relative peak absorbance vs spin speed of DAD films on glass.

Furthermore, UV/Visible spectra were compared for DAD films on glass both before and after exposure to the doping chemicals $AuCl_3$ (spin coated from aqueous solution) and $SOCl_2$ (vapour exposure for 2 min).

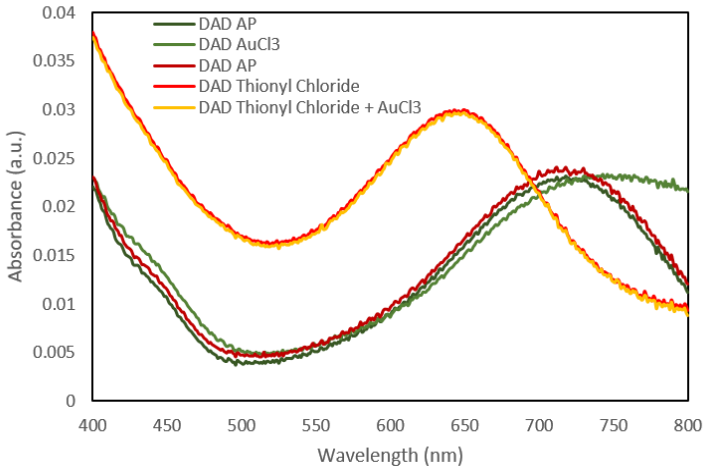

Figure 6-82: UV/Vis spectra of 2500 rpm DAD films on glass before and after exposure to two different doping chemicals.

Figure 6-82 shows the effect of $AuCl_3$ and $SOCl_2$ as doping chemicals on the spectra of DAD films. It is apparent that the $SOCl_2$ vapour exposure has a much greater effect on the DAD film than the aqueous $AuCl_3$ solution. The $SOCl_2$ vapour exposure caused a significant peak shift from around 720 nm to around 650 nm. The $AuCl_3$ exposure, on the other hand, caused a peak broadening effect on the DAD spectrum with a slight shift in peak position to around 750 nm. Interestingly, once the peak shift due to $SOCl_2$ exposure had occurred, subsequent $AuCl_3$ treatment made no difference to the spectrum. In order to further examine the effect of $SOCl_2$ on DAD films the exposure time was varied and spectra obtained at time intervals of 30 s, 90 s, 300 s, and after direct contact with $SOCl_2$ solution.

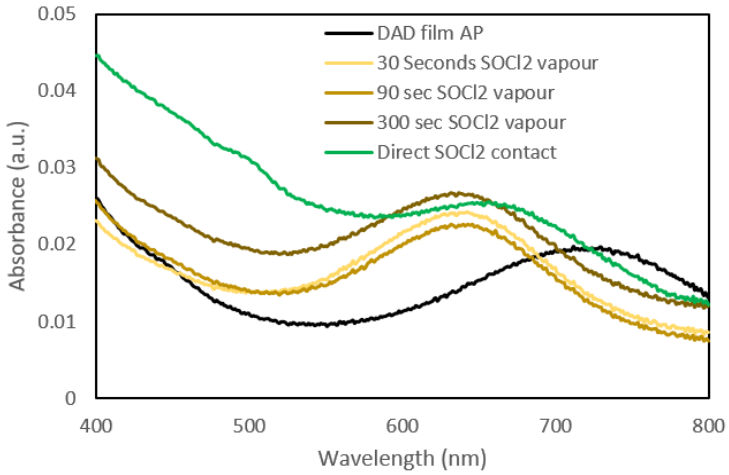

Figure 6-83: UV/Vis spectra of DAD films exposed to $SOCl_2$ for different time intervals and with direct $SoCl_2$ contact.

Figure 6-83 shows that the amount of time the DAD is exposed to $SOCl_2$ plays little part in the peak shift. The peak shifted to around 640 nm and stayed there whether the exposure time was 30 s or 300 s. It is noticeable that there is a rise in absorbance for the 300 s sample compared to the 30 s and 90 s samples. However, as this absorbance rise was present across the entire spectrum, it is expected that this was due to differences in the background spectra. Also, in Figure 6-83 is the spectrum of a DAD film after being placed directly in contact with $SOCl_2$ solution. The peak shifts to a lower wavelength as per the vapour exposed samples, however to a lesser degree as the peak appears to be at around 660 nm. In addition, there is a general increase in absorbance as wavelength decreased.

6.4.3 AFM and SEM Images

6.4.3.1 AFM Images of DAD Films

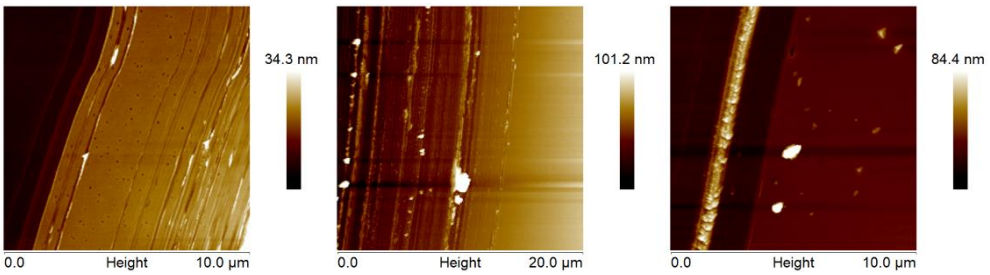

Figure 6-84: AFM height maps of DAD films spun from different solution volumes.

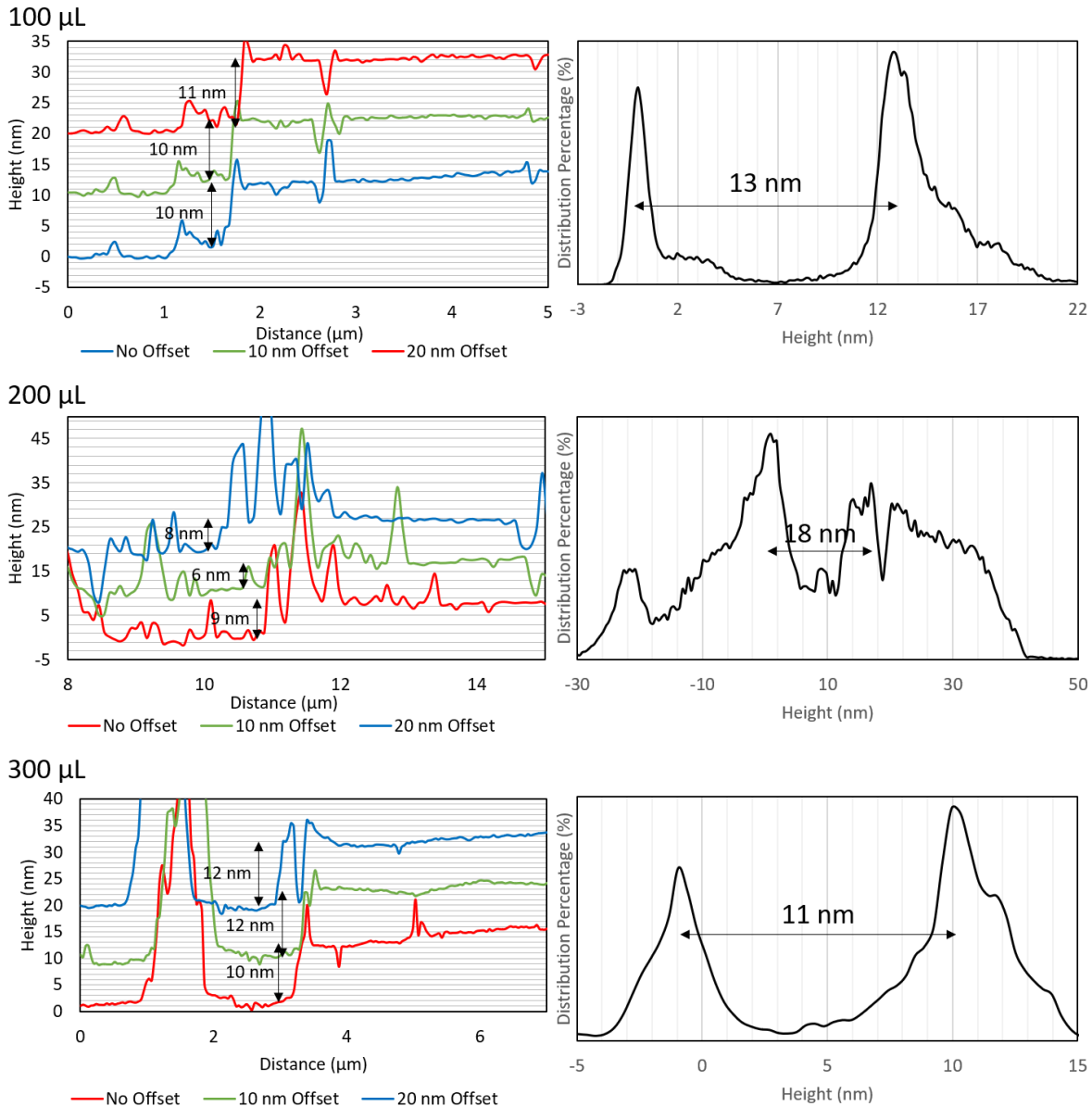

Figure 6-85: AFM cross sectional line graphs and percentage height distribution plots of DAD films spun from different solution volumes.

Figure 6-84 and Figure 6-85 shows height maps, cross-sectional graphs, and percentage distribution plots of scratches made in DAD films spun from different solution volumes. The height distribution

plot for the 200 µL is more difficult to resolve than the other two. This is due to the rougher nature of this film (see Figure 6-84) which leads to broadening of the distribution peaks. The rough height distribution plot for the 200 µL sample also suggests a thicker film than the cross-sectional line graphs, however the clear cliff edge visible in the line graphs indicates that the average height of 7.70 nm is likely correct. Overall, there is little difference in film thickness with changing aliquot volume as expected.

AFM height maps were produced for films spun at 500 rpm, 2500 rpm, 5000 rpm, and 7000 rpm to categorise the change in film thickness expected from a change in spin speed. However, Figure 6-86 shows that the films formed were significantly less homogenous and smooth than the DAD films previously examined (Figure 6-88 to Figure 6-84). This may be because the DAD spun in this experiment was a different batch of material to that imaged initially (Figure 6-89, Figure 6-90, and Figure 6-84). There were large holes present in the films and clear cross-sectional data for film thickness measurements was difficult to obtain. Percentage height distribution graphs were obtained but the peaks were not well resolved. It was apparent that the ability for the DAD in chlorobenzene to wet the substrate surface and thus form a homogenous film had deteriorated. This was supported by visual observation of the devices after spin coating of DAD was performed. The initial devices had an even green tinge, but the more recent devices displayed a less homogenous pattern. It is unclear why the ability for DAD suspension to wet the surface had deteriorated. The same cleaning regime was observed for the substrates in all DAD experiments.

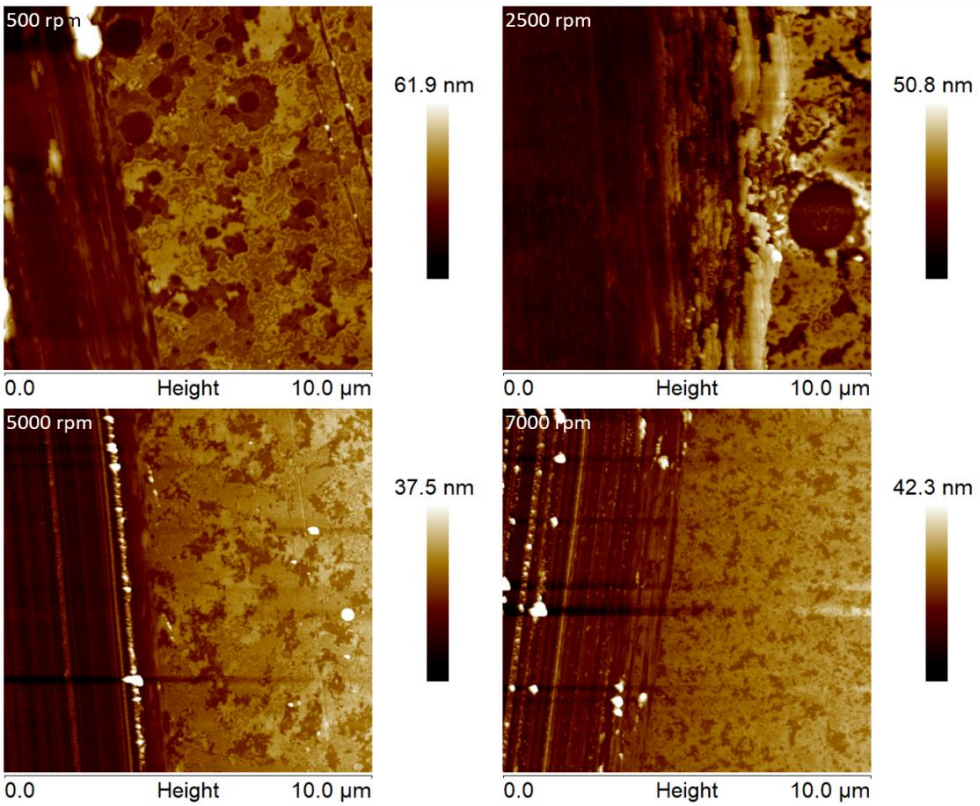

Figure 6-86: AFM height maps of DAD films spun at different speeds.

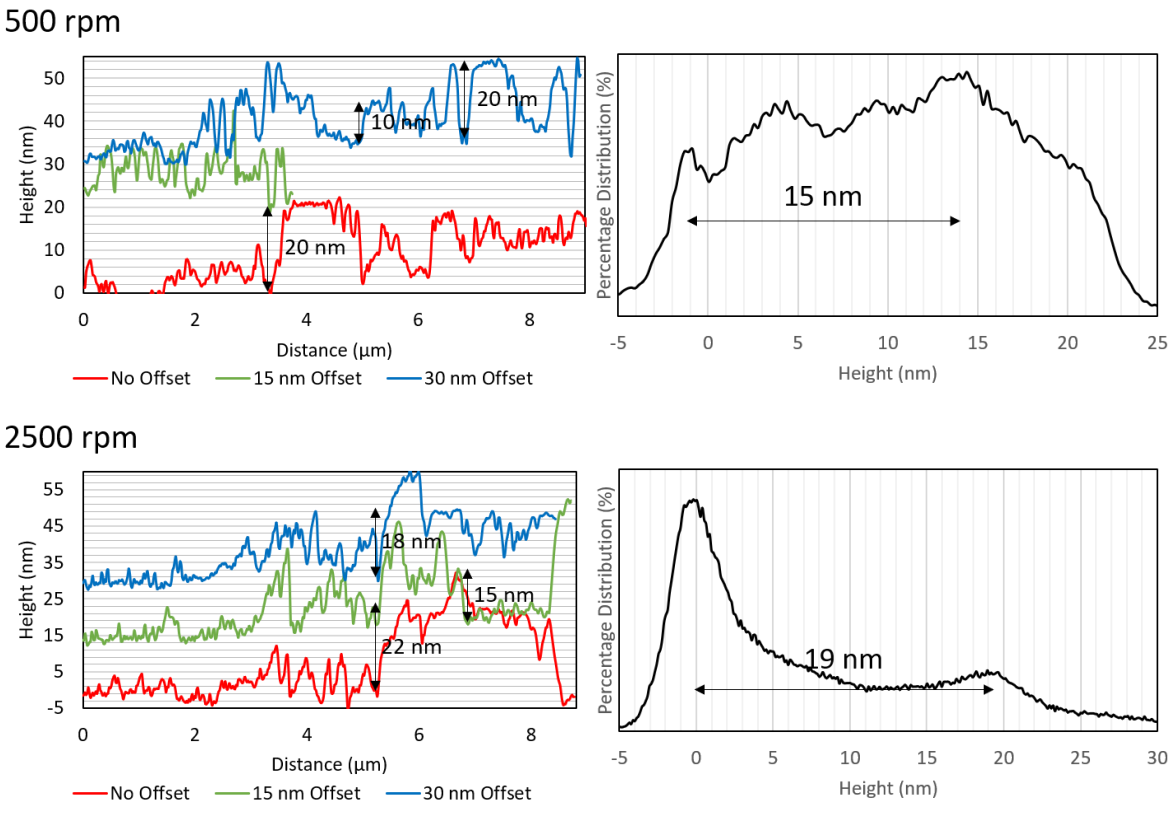

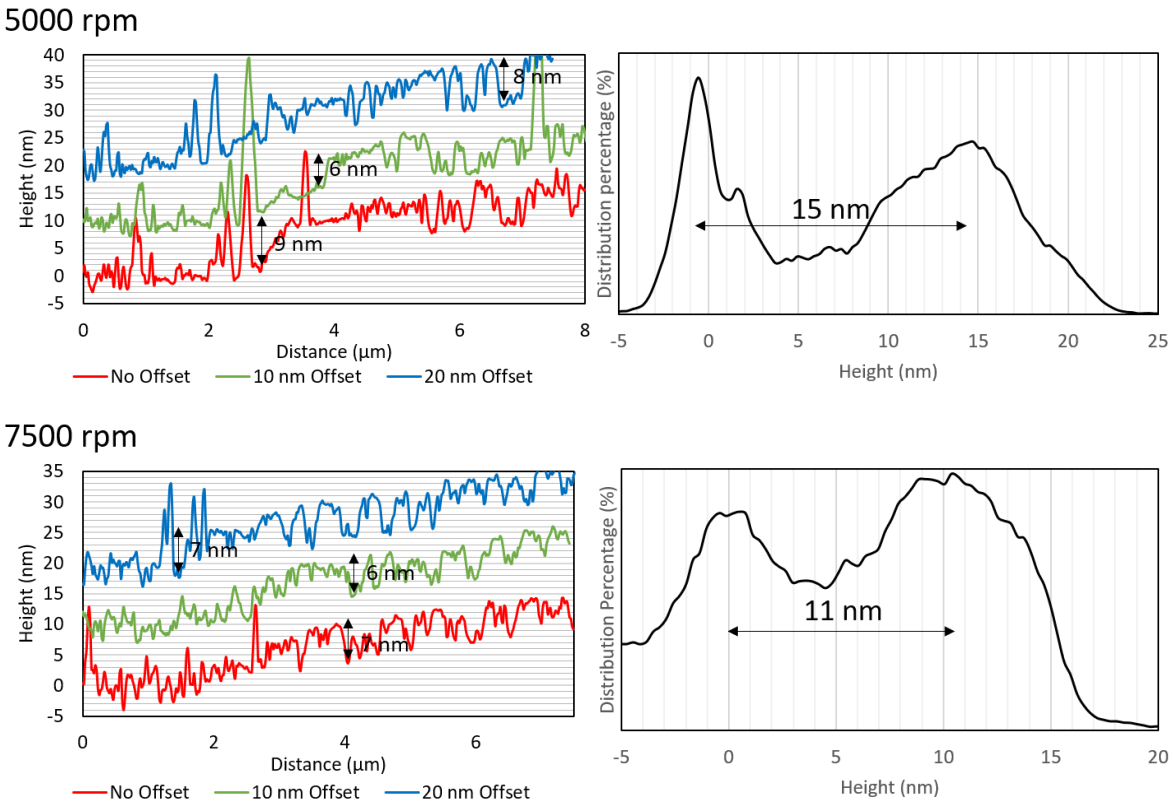

Figure 6-87: Cross-sectional line graphs and height distribution plots for DAD films spun at different spin speeds.

The height distribution plots in Figure 6-87 show a decrease in film thickness as spin speed increases. The exception is the 500 rpm sample where there are no distinct peaks in the distribution plot. In general, the peak corresponding to the film surface (the right peak) is significantly broader than the peak corresponding to the silicon surface. This is due to the large variation in film surface height which is seen in Figure 6-86. The cross-sectional line graphs do not show good agreement with the height distribution plots, particularly for the 5000 rpm and 7500 rpm samples where the cross-sectional graphs indicate a film thickness two thirds that indicated by the distribution plots. This is likely also due to the inhomogeneous nature of the DAD films.

6.4.3.2 SEM Images of DAD Films

SEM images were formed of DAD films on device substrates (Figure 6-89 and Figure 6-90). An alternate method of damaging sections of the film to make it observable in an SEM image was used for this interlayer. A Raman laser beam was focussed on the DAD film producing a spectrum with large silicon peaks accompanied by significant noise interference. Over time, the noise reduced to become negligible. At this point, the laser was stopped as it was interpreted that a clean silicon spectrum

indicated that essentially all the DAD in the laser area was burnt from the surface. The resultant surface had small holes burnt through the film, allowing the difference between silicon substrate and DAD film to be observed. In Figure 6-88 the DAD films both with and without laser holes burnt can be seen. The laser damages the film in small distinct areas that can be observed under SEM.

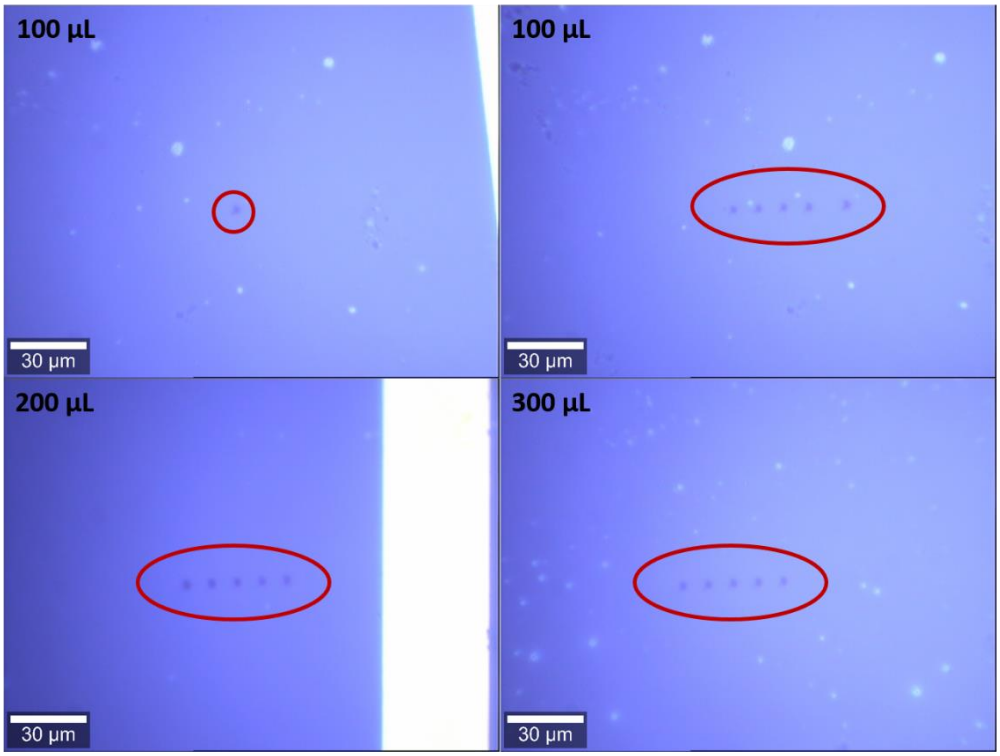

Figure 6-88: Optical microscope images of DAD films spun from different solution volumes. The blue areas are the DAD film, the large white areas are gold grid lines and the small white dots are air bubble holes in the film. The dark dots, highlighted with red circles, are burnt holes.

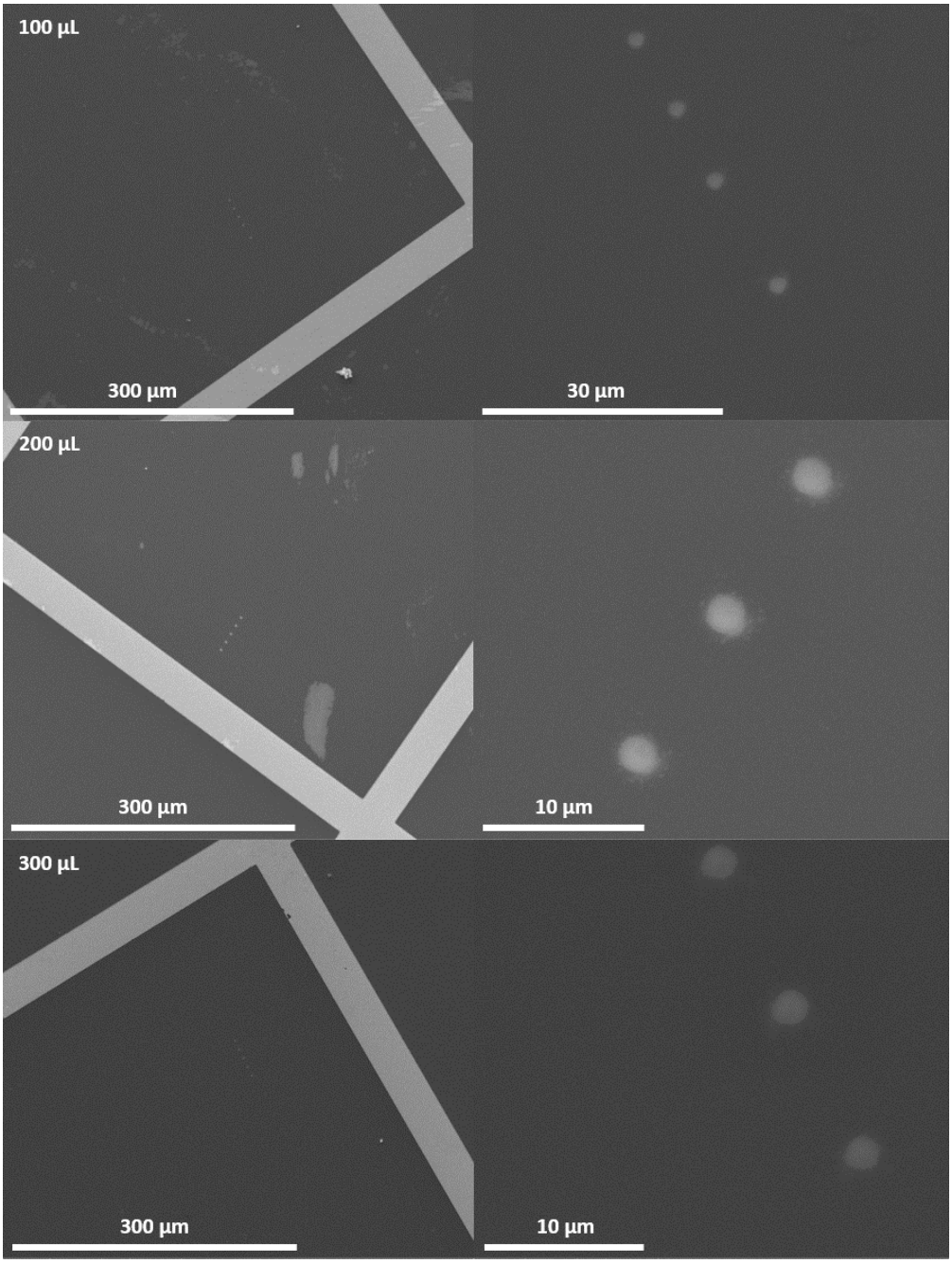

Figure 6-89: SEM images of DAD films spun from different solution volumes.

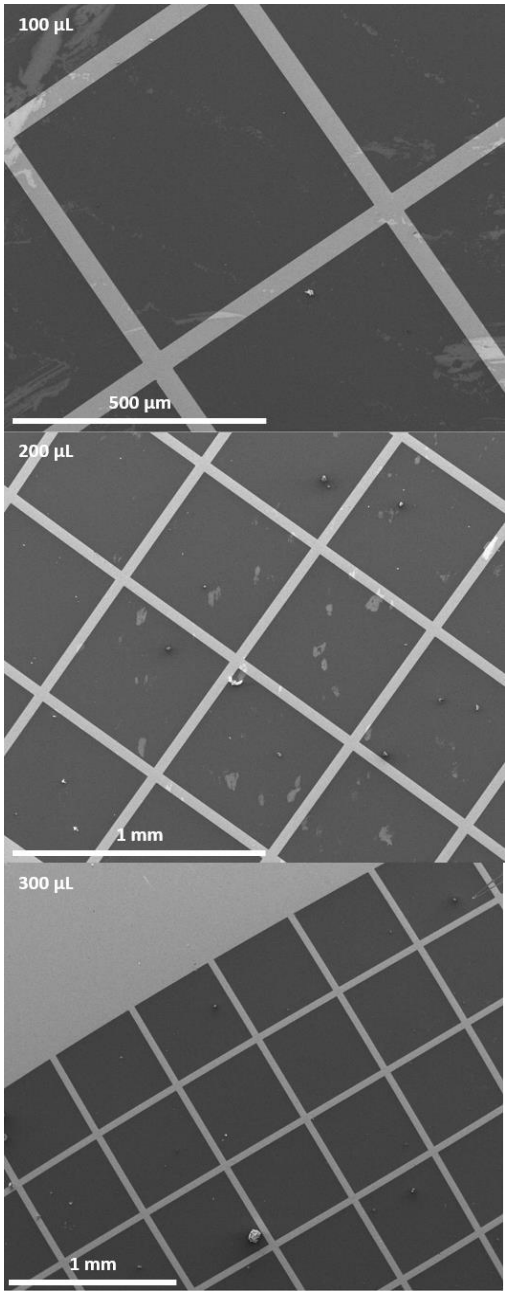

Figure 6-90: Larger area SEM images of DAD films spun from different solution volumes.

When imaging the DAD films under SEM the laser holes burnt through the layer allow the film to be easily observable. From the images in Figure 6-89 and Figure 6-90, it is apparent that the volume of solution spun on the surface has an effect on the film morphology. Lighter coloured regions are visible on the films. They are larger and more frequent in the 100 µL film than in the 200 µL film and there are none visible at all in the 300 µL sample. It is apparent that a volume of at least 300 µL is required to produce a smooth homogenous film. The light-coloured regions are likely thinner areas of film. This film coverage information will be compared with device data results later in this section (Figure 6-91).

6.4.4 Solar Device Data

6.4.5.1 DAD Devices with Varied Solution Volume

Initially, a series of different volumes of DAD solution were spin coated at 5000 rpm on to sets of device substrates at five different volumes ranging from 100 µL to 300 µL.

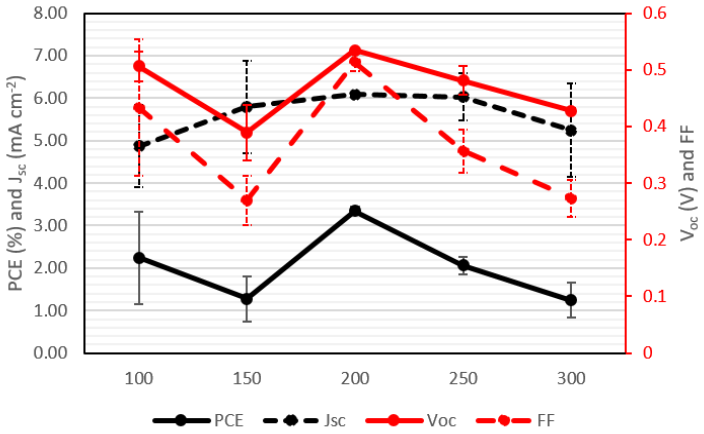

Figure 6-91: J/V properties for devices with DAD interlayers spun from different solution volumes after an aqueous $AuCl_3$ treatment.

The addition of DAD has a significant effect on the performance of the devices when different volumes are added (Figure 6-91). The data shows that a volume of 200 µL is optimal to produce the best performing devices as they outperformed the other sets across all parameters. The 150 µL set was the worst performing. However, when the J_{sc} trend is observed, it is clear that there is still a general trend of improvement with volume up until the 200 µL point. The decrease in performance for the 150 µL devices is due to concurrent drops in V_{oc} and FF. The J_{sc} displays the clearest trend, with a peak at 200 µL. Additionally, the 200 µL samples displayed the highest consistency (demonstrated by smaller error bars). The information in Figure 6-91 is presented in Table 6-3 alongside device data for control devices with no interlayer.

Table 6-3: Device properties of gold chloride doped devices at different DAD volumes vs devices with no interlayer.

	PCE (%)	*V_{oc} (V)*	*J_{sc} (mA cm^{-2})*	*FF*
Control Devices	**2.89 ± 0.40**	**0.48 ± 0.02**	**6.65 ± 0.30**	**0.45 ± 0.04**
100 µL	2.24 ± 1.09	0.51 ± 0.03	4.87 ± 0.97	0.43 ± 0.12
150 µL	1.28 ± 0.53	0.39 ± 0.05	5.80 ± 1.09	0.27 ± 0.04
200 µL	**3.34 ± 0.10**	**0.53 ± 0.00**	**6.09 ± 0.02**	**0.51 ± 0.02**
250 µL	2.06 ± 0.20	0.48 ± 0.03	6.03 ± 0.55	0.36 ± 0.04

300 µL	1.24 ± 0.41	0.43 ± 0.00	5.24 ± 1.09	0.27 ± 0.03

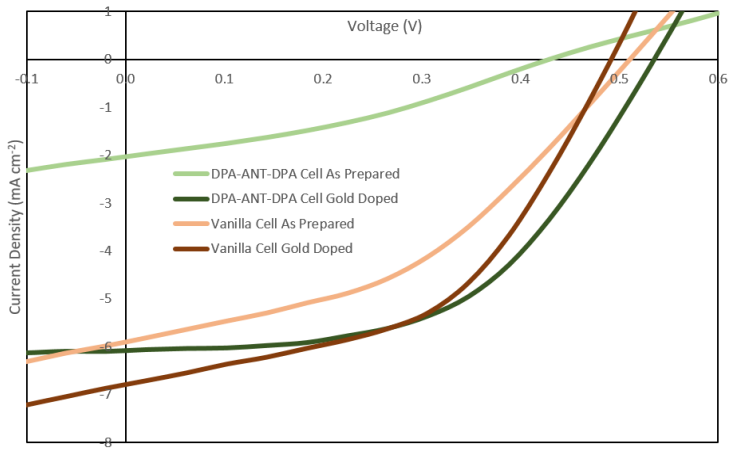

Figure 6-92: J/V Curves for the best performing device with and without a DAD interlayer.

Table 6-3 shows that the optimal volume of 200 µL outperforms devices with no interlayer by almost 1 %. This is due to an improved V_{oc} from 0.47 ± 0.02 V to 0.53 ± 0 V and a significantly improved FF from 0.38 ± 0.10 to 0.51 ± 0.02. It is interesting to note that the J_{sc} is actually lower in the devices with a DAD interlayer than in the devices with no interlayer. However, the difference is less than 1 mA cm^{-2} in values greater than 6 mA cm^{-2} and thus it can be seen that the enhancements in V_{oc} and FF outweigh the decrease in J_{sc}. The increase in FF indicates that the DAD film has improved the passivation of the silicon surface and thus, reduced recombination. The J/V curves for the best performing device with DAD and without are shown in Figure 6-92. These curves show the difference in effect of the $AuCl_3$ dopant on devices with and without the DAD interlayer. For the device with no interlayer, the $AuCl_3$ improved the J_{sc} from 5.90 mA cm^{-2} to 6.79 mA cm^{-2} (a 15.1% improvement), improved the FF from 0.42 to 0.49 and lowered the V_{oc} from 0.51 V to 0.49 V. Overall this produced a PCE gain from 2.52 % to 3.24% (a 28.6% improvement). The changes exhibited in the device with a DAD interlayer were far more pronounced. The J_{sc} improved from 2.03 mA cm^{-2} to 6.08 mA cm^{-2} (a 200 % improvement), the FF increased from 0.34 to 0.53 and the V_{oc} increased from 0.43 V to 0.53 V. Giving an overall PCE improvement from 0.59 % to 3.44 % (a 483 % improvement). After $AuCl_3$ doping, the parameters for the device with the DAD interlayer are superior to the device with no interlayer, with the exception of the J_{sc}. This matches the comparison seen between the average values (Table 6-3). Additionally, the

deviation in PCE values was much smaller for the devices with the DAD interlayer than in those without, ± 0.10 % vs ± 0.66 %. This clearly indicates that the addition of a DAD HTM improves the performance of the large area CNT/Si heterojunction device.

The most smooth and homogenous film is not the one that gives the best device performance (Figure 6-89 and Figure 6-90). The existence of the lighter coloured regions appears to be required to improve device performance as the homogeneous films formed with a 300 µL did not produce the best performing devices. The reason for this could be that the thinner regions allow a better CNT/Si junction to be formed. Thus, the peak in PCE for different DAD volumes is a trade-off between having enough thin areas in the DAD film to allow CNT/Si junction formation whilst the film being homogeneous enough to improve charge carrier extraction.

6.4.5.2 DAD Devices with Varied Spin Speed

As with the other interlayers investigated in this thesis the spin speed was varied to examine any change in performance due to DAD film thickness. Devices were fabricated with DAD spun from solution at 5000 rpm based on research from Pham *et al.*[173] and at 2500 rpm. The performance of these devices was compared with devices fabricated with no DAD interlayer and treated following the same method. The dopant scheme used was $SOCl_2$ Vapour – $AuCl_3$ – 2 % HF. The data is shown in Figure 6-93. The devices with no interlayer started with high PCE values and dropped with each successive treatment step. This was unexpected as the $SOCl_2$, in particular, is expected to give an improvement in device performance. The drop may be due to the absence of a 2% HF etch prior to doping, but it is unclear why this would be the case. The devices with a DAD interlayer were found to initially perform poorly and improve with the first two dopant steps, similar to the trend seen with initial device performance (Figure 6-91). However, they were found to either plateau or decrease with the final 2% HF treatment.

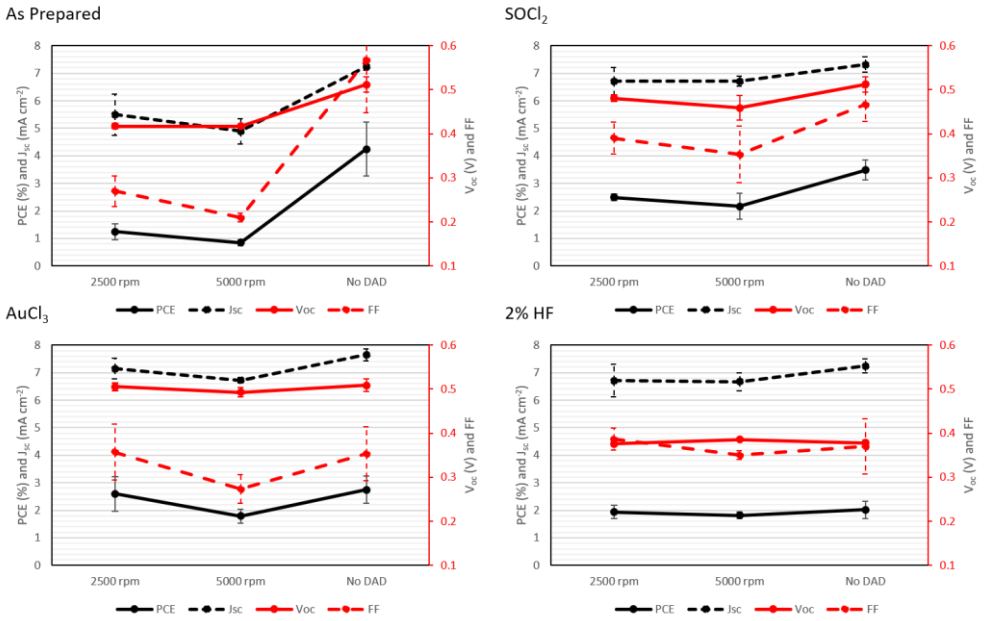

Figure 6-93: J/V properties for devices with DAD layers spun at different speeds and devices with no interlayer.

After two stages of chemical treatment the DAD devices had almost reached parity with the control devices. The average PCEs were 2.60 % ± 0.62 and 1.79 % ± 0.25 for the two sets of devices with a DAD interlayer and 2.75 % ± 0.50 for the devices with no interlayer. The devices with a DAD interlayer are out performed overall by the devices with no interlayer present, which is the opposite trend to that observed when the DAD interlayer was first implemented (Figure 6-91 and Table 6-3). The DAD material used for this experiment was a different batch than that used in the initial experiments (Figure 6-91). It is possible that the newer material did not form a hole transportation layer as well as the original material. As was observed in Figure 6-86, the newer DAD batch did not form the smooth homogenous films that were observed with the initial batch (Figure 6-84, Figure 6-89, and Figure 6-90).

6.4.5.3 Small Area Devices with DAD Films

In order to compare the improvements found using DAD on large area devices to the comparatively larger field of research done on small area devices, small area devices (0.09 cm^2) were fabricated with the same aluminium back contact. The front gold grid design was the optimal design discovered by Yu *et al*.[136] and the top layer was 5 nm of chromium with 145 nm of gold. Devices with and without a DAD interlayer were tested with different treatment regimes. The data is shown in Figure 6-94.

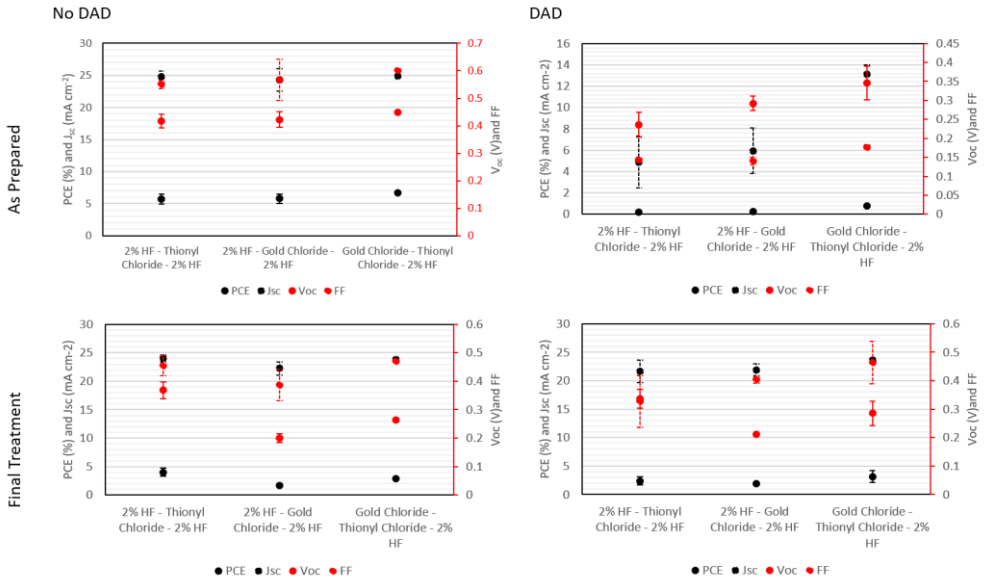

Figure 6-94: J/V properties for small area devices with and without a DAD interlayer following different treatment types at both as prepared and after final treatment.

Whilst initially the devices with no DAD interlayer vastly outperformed devices with an interlayer, this changed with chemical treatment. Initially poor PCE values, increasing significantly with chemical treatment is a pattern that has been seen for all the previous devices with a DAD interlayer. In particular, the trend for both devices with and without a DAD interlayer is similar to that seen in the experiments with varying RPM (Figure 6-93). When the treatment pattern has been completed, the devices with a DAD interlayer have roughly obtained parity, in terms of PCE, with the devices with no DAD layer. The exception being the devices treated with the 2% HF – $SOCl_2$ – 2% HF pattern where devices with no interlayer did not experience the same degree of performance degradation with treatment as the other samples. This parity, whilst due in part to the rise in PCE seen in the devices with a DAD interlayer, is also due to a drop in PCE seen in the devices with no interlayer. This indicates that devices with no interlayer are outperforming devices with a DAD interlayer in general. This is the opposite trend to that seen when large area devices were initially tested with and without a DAD interlayer (Figure 6-91). The reason for the low performance of the DAD devices may be due to the use of a different batch of DAD than that used in the initial devices which outperformed devices with no interlayer (Figure 6-92).

6.4.5.4 Devices without CNT/GO Films

As with other interlayers investigated in this chapter, an experiment was performed where the interlayer was spun on device substrates and the J/V curve measured with a thin gold layer instead of the CNT/GO film. This was compared with substrates with no interlayer and a thin gold layer with similar transmittance to the CNT/GO film. Prior to this, device substrates with a DAD interlayer were tested with neither a gold layer or a CNT/GO film on the top contact. The DAD film is not conductive enough in its own right to give any meaningful photovoltaic data.

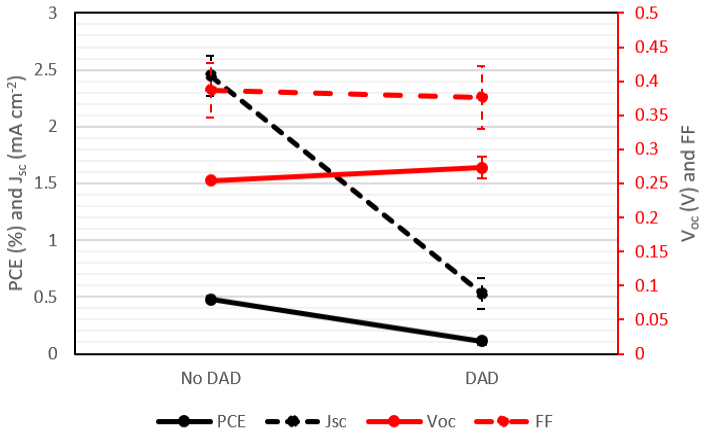

Figure 6-95: J/V properties for devices with a 10 nm gold top contact instead of a CNT/GO film with a DAD interlayer and without.

Figure 6-95 shows that, even with a conductive gold top layer the device substrates produce PCE values significantly lower than that of devices with a CNT/GO film. Importantly, the presence of a DAD interlayer significantly reduces the J_{sc} of the device and thus also the PCE. The V_{oc} and FF experience small changes, but not to the extent of the J_{sc}. This indicates that the improvement in device performance when a DAD interlayer is added to a CNT/Si heterojunction device are not due to a simple increase in current carrying capacity, as the DAD itself does not perform well in this role. It is important to note that devices with a DAD interlayer and a CNT/GO film did not perform well until the devices were doped. A 10 nm thick gold coating was used in this experiment, which is thicker than that used in the previous experiments with no CNT/GO film (Figure 6-28 and Figure 6-76). Thus, the UV/visible transmittance spectra are shown here in Figure 6-96. Whilst the transmittance is lower for the 10 nm film, it is still analogous to the CNT/GO film.

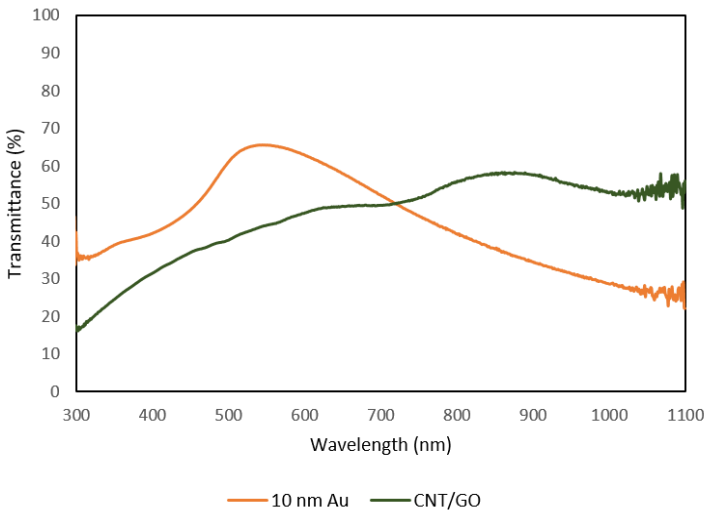

Figure 6-96: UV/Visible spectra of a CNT/GO film with a transmittance of 45 % and a 10 nm gold film.

6.4.5.5 Final Devices with Low Transmittance Films

A final set of large area devices was produced and compared with a set of devices with no interlayer. Both sets were produced with thinner CNT/GO films. However, poor film attachment again affected this set of devices, with a maximum performance of 1.31 % achieved for devices with DAD interlayers after a thionyl chloride vapour dope. The main issue appeared to be the fill factor of these devices, with the best performing device recording a V_{oc} of 0.467 V and a J_{sc} of 6.77 mA cm^{-2} and a FF of 0.21. The best performing device with no interlayer which recorded a PCE of 5.12 %, a V_{oc} of 0.515 V, a J_{sc} of 8.38 mA cm^{-2} and a FF of 0.59. Thus, it can be seen that the 74 % difference in PCE was most caused by the 64 % difference in FF, accompanied by a 9% difference in V_{oc} and a 19% difference in J_{sc}. In Table 6-3 the average FF of the best performing DAD devices was higher than the average FF in devices with no interlayer. Thus, it appears that the poor DAD film formation is causing significant problems in device performance, with an emphasis on FF.

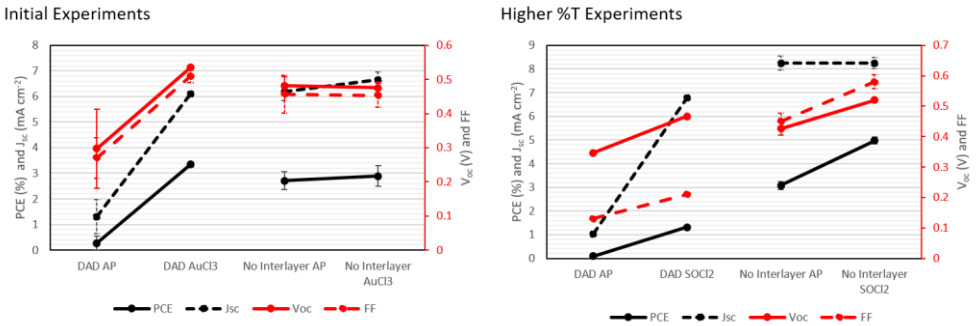

Figure 6-97: J/V properties for DAD devices vs no interlayer devices for both initial experiments (Table 6-3) and final experiments with CNT/GO films with higher transmittance.

6.4.6 DAD Interlayer Conclusions

Overall, it is clear that a well formed, homogenous DAD interlayer serves to improve device performance by providing gains in FF and in V_{oc}. However, further testing of the DAD interlayer was inconclusive due to the effect of poor film formation on device performance. It was also determined that dopant chemicals used to improve the performance of the CNT/GO film in the device have a significantly stronger effect on devices with a DAD interlayer. As prepared DAD containing devices vastly underperformed compared to devices with no interlayer but the devices approached parity and beyond with the application of a dopant chemical. It was apparent that the morphology of the DAD film was of high importance when considering device performance. Initially, it was found that a DAD film with some morphological inconsistencies was optimal over a DAD film with no blemishes. In future experiments, the morphology of the DAD film was found to be vastly inconsistent and considerably rougher than initial films. This caused performance issues in devices fabricated with DAD films. It is likely that these morphological and performance problems were due to differences between the first and second batch of DAD material used in the experiments.

6.5 Final Device Comparison and Conclusion

An issue was occasionally encountered when spin coating interlayer films onto large area substrates. The coating would form a visible, smooth, thin film on the surface for the most part, but swirl patterns of varying thickness could be visible on some substrates. In batches produced with substrates prepared and cleaned in the same manner and coated with the same solution volume at the same spin speed differences could be seen in macro-scale morphology (see Figure 6-98). These swirl patterns suggest that the majority of the substrate was coated with a thin and even film, but some areas had a thicker or a thinner coating. This may have led to consistency issues in performance between devices in the same batch. A possible cause for this could be the dropwise deposition method. The solution droplets were deposited manually. Thus, the angle of deposition and the rate would have variations between substrates. To avoid this in future, an automated solution deposition system could be implemented.

Figure 6-98: CuSCN thin coatings on device substrates demonstrating the macro-scale morphology differences.

Table 6-4: Full device data for final devices for each interlayer and variation part 1.

		No Interlayer	PEDOT:PSS	DAD	DAD	PANI	CuSCN	MoO_x
Film Transmittance (%)		65	68	67	~50%	68	68	64
Interlayer Thickness (nm)		N/A	17 - 18	10 - 15	10 - 15	2 - 3	15 - 20	> 5
Dopant		$SOCl_2$	$SOCl_2$	$SOCl_2$	$AuCl_3$	$SOCl_2$	$SOCl_2$	$SOCl_2$
CNT Film Sheet Resistance	As Prepared	2670 ± 833	2070 ± 457	2380 ± 340	~ 600	~ 2000	1920 ± 715	~ 1900
	Doped	1210 ± 321	953 ± 66.6	868 ± 119	~ 200	~ 1000	1000 ± 460	911 ± 417
PCE (%)	As Prepared	**3.08** ± 0.17	**4.06** ± 0.18	**0.09**	**0.27** ± 0.28	**1.76** ± 0.60	**0.33** ± 0.25	**2.17** ± 0.51
	After 2 % HF	**2.88** ± 0.52	**2.23** ± 0.56	**0.17**		**1.82** ± 0.80	**0.08** ± 0.03	
	After Dopant	**4.98** ± 0.14	**2.29** ± 0.26	**1.31**	**3.34** ± 0.10	**2.15** ± 0.68	**2.75** ± 0.58	**2.20** ± 0.32
	After 2 % HF	**2.29** ± 0.29		**1.32**		**1.75** ± 0.35	**1.32** ± 0.23	
	4 Month Wait	**1.10** ± 0.41	**0.79** ± 0.12	**0.18**		**0.48** ± 0.21	**0.18** ± 0.12	**0.46** ± 0.14
J_{SC} (mA cm^{-2})	As Prepared	**8.24** ± 0.29	**8.82** ± 0.18	**1.028**	**1.31** ± 0.66	**7.18** ± 1.69	**2.05** ± 1.44	**7.82** ± 0.22
	After 2 % HF	**8.26** ± 0.29	**8.16** ± 0.67	**1.656**		**6.67** ± 1.67	**0.84** ± 0.26	
	After Dopant	**8.25** ± 0.25	**8.57** ± 0.11	**6.765**	**6.09** ± 0.025	**7.25** ± 1.79	**8.48** ± 0.38	**7.94** ± 0.30
	After 2 % HF	**8.24** ± 0.22		**7.455**		**7.08** ± 1.70	**5.69** ± 0.57	
	4 Month Wait	**5.24** ± 1.75	**4.88** ± 0.54	**1.692**		**3.04** ± 1.42	**0.998** ± 0.52	**2.66** ± 1.17
V_{OC} (V)	As Prepared	**0.426** ± 0.020	**0.542** ± 0.007	**0.347**	**0.297** ± 0.115	**0.501** ± 0.018	**0.405** ± 0.027	**0.481** ± 0.012
	After 2 % HF	**0.404** ± 0.025	**0.461** ± 0.014	**0.375**		**0.418** ± 0.013	**0.268** ± 0.021	
	After Dopant	**0.520** ± 0.006	**0.473** ± 0.008	**0.467**	**0.535** ± 0.004	**0.461** ± 0.006	**0.480** ± 0.008	**0.502** ± 0.016
	After 2 % HF	**0.368** ± 0.016		**0.352**		**0.399** ± 0.016	**0.438** ± 0.017	
	4 Month Wait	**0.436** ± 0.010	**0.391** ± 0.002	**0.329**		**0.416** ± 0.017	**0.420** ± 0.025	**0.487** ± 0.022
FF	As Prepared	**0.45** ± 0.027	**0.43** ± 0.025	**0.13**	**0.27** ± 0.06	**0.24** ± 0.027	**0.18** ± 0.038	**0.29** ± 0.062
	After 2 % HF	**0.43** ± 0.066	**0.29** ± 0.051	**0.14**		**0.32** ± 0.071	**0.19** ± 0.035	
	After Dopant	**0.58** ± 0.023	**0.28** ± 0.025	**0.21**	**0.51** ± 0.02	**0.32** ± 0.050	**0.34** ± 0.051	**0.28** ± 0.032
	After 2 % HF	**0.38** ± 0.036		**0.25**		**0.32** ± 0.032	**0.26** ± 0.015	
	4 Month Wait	**0.24** ± 0.015	**0.21** ± 0.012	**0.16**		**0.19** ± 0.012	**0.19** ± 0.047	**0.19** ± 0.015

J_{Sat} (mA cm^{-2})	As Prepared	**8.7 x 10^{-5}**	**6.2 x 10^{-6}**	**2.4 x 10^{-4}**	**9.9 x 10^{-2}**	**1.08 x 10^{-4}**	**6.21 x 10^{-6}**	**9.9 x 10^{-4}**
	After 2 % HF	**1.1 x 10^{-4}**	**3.9 x 10^{-4}**	**5.7 x 10^{-4}**		**4.34 x 10^{-4}**	**5.99 x 10^{-5}**	
	After Dopant	**4.8 x 10^{-6}**	**4.3 x 10^{-4}**	**2.3 x 10^{-4}**	**2.4 x 10^{-2}**	**1.53 x 10^{-4}**	**1.36 x 10^{-3}**	**5.7 x 10^{-5}**
	After 2 % HF	**1.9 x 10^{-4}**		**6.1 x 10^{-4}**		**1.53 x 10^{-4}**	**3.45 x 10^{-4}**	
	4 Month Wait	**2.5 x 10^{-5}**	**1.8 x 10^{-4}**	**1.1 x 10^{-2}**		**7.42 x 10^{-5}**	**1.21 x 10^{-4}**	**2.78 x 10^{-5}**
Ideality	As Prepared	**1.46** ± 0.387	**1.66** ± 0.208	**2.132**	**4.26** ± 0.129	**1.88** ± 0.605	**1.31** ± 0.136	**2.54** ± 0.986
	After 2 % HF	**1.42** ± 0.137	**2.00** ± 0.542	**3.439**		**1.81** ± 0.320	**2.44** ± 0.615	
	After Dopant	**1.53** ± 0.169	**2.33** ± 0.465	**2.421**	**3.73** ± 0.391	**2.02** ± 0.233	**3.17** ± 0.492	**2.22** ± 0.151
	After 2 % HF	**1.40** ± 0.240		**1.731**		**1.58** ± 0.036	**1.87** ± 0.308	
	4 Month Wait	**1.45** ± 0.052	**2.15** ± 0.175	**2.992**		**1.89** ± 0.059	**3.02** ± 1.689	**2.04** ± 0.192
R_{Shunt} (Ω)	As Prepared	**648** ± 273	**1032** ± 492	**64.1**	**112.7** ± 36.5	**134** ± 113	**103** ± 87.9	**215** ± 99
	After 2 % HF	**743** ± 648	**143** ± 163	**55.9**		**150** ± 108	**97.7** ± 25.2	
	After Dopant	**630** ± 219	**201** ± 195	**26.9**	**368.3** ± 111.5	**2514** ± 3841	**288** ± 287	**737** ± 877
	After 2 % HF	**1607** ± 2117		**26.1**		**159** ± 107	**39** ± 3	
	4 Month Wait	**58** ± 12.9	**44.2** ± 12.4	**52.3**		**50.8** ± 19.3	**149** ± 42.5	**65.5** ± 29.7
R_{Series} (Ω)	As Prepared	**11.5** ± 1	**15** ± 0.9	**826**	**104.5** ± 37.8	**77.6** ± 36.9	**756** ± 1103	**67.5** ± 41.4
	After 2 % HF	**12.7** ± 2.2	**29** ± 7.2	**579**		**25.1** ± 7.83	**348** ± 281	
	After Dopant	**9.1** ± 0.6	**34** ± 6.3	**75.1**	**14.2** ± 1.3	**26.5** ± 7.21	**19.1** ± 4.43	**47.8** ± 21.1
	After 2 % HF	**12.5** ± 0.8		**22.1**		**20.9** ± 4.71	**31.6** ± 4.52	
	4 Month Wait	**48** ± 14.4	**193** ± 70	**463**		**195** ± 27	**854** ± 1123	**263** ± 24

Table 6-5: Full device data for final devices for each interlayer and variation part 2.

		No Interlayer	PANI (DMF)	CuSCN (Pre BOE)	No Interlayer (Small Area)	DAD (Small Area)	PANI
Film Transmittance (%)		66	65	66	66	66	50-60
Interlayer Thickness (nm)		N/A	9 - 16	16-19	N/A	Unknown	2 - 3
Dopant		$AuCl_3$	$SOCl_2$	$SOCl_2$	$AuCl_3$ + $SOCl_2$	$AuCl_3$ + $SOCl_2$	$AuCl_3$
CNT Film Sheet Reistance	As Prepared	2180 ± 841	798 ± 94	1220 ± 223	~ 1200	~ 1200	~ 600
	Doped	624 ± 125	568 ± 70.7	813 ± 407	~ 800	~ 800	~ 200
PCE (%)	As Prepared	**3.32** ± 0.61	**0.23** ± 0.07	**0.51** ± 0.23	**6.73**	**0.37** ± 0.24	**1.52** ± 0.81
	After 2 % HF	**2.50** ± 0.72	**0.24** ± 0.07	**0.26** ± 0.03	**2.71**	**1.06** ± 0.79	
	After Dopant	**0.88** ± 0.04	**2.02** ± 0.24	**1.19** ± 0.11	**3.25**	**1.35** ± 1.11	**2.03** ± 0.89
	After 2 % HF	**1.75** ± 0.21	**0.51** ± 0.20	**0.47** ± 0.03	**2.93**	**3.15** ± 1.41	
	4 Month Wait	**0.24** ± 0.10					
J_{SC} (mA cm^{-2})	As Prepared	**7.96** ± 0.69	**1.68** ± 0.36	**2.14** ± 0.26	**24.9**	**7.9** ± 3.85	**6.36** ± 0.68
	After 2 % HF	**7.70** ± 0.58	**1.69** ± 0.65	**1.73** ± 0.23	**24.2**	**15.5** ± 4.95	
	After Dopant	**5.18** ± 0.67	**7.35** ± 0.21	**5.29** ± 0.91	**24.6**	**17.0** ± 3.93	**7.27** ± 0.28
	After 2 % HF	**7.43** ± 0.89	**3.03** ± 0.97	**2.42** ± 0.19	**23.9**	**22.7** ± 1.49	
	4 Month Wait	**2.06** ± 0.88					
V_{OC} (V)	As Prepared	**0.471** ± 0.012	**0.407** ± 0.041	**0.432** ± 0.017	**0.450**	**0.318** ± 0.096	**0.43** ± 0.069
	After 2 % HF	**0.453** ± 0.018	**0.315** ± 0.018	**0.302** ± 0.020	**0.391**	**0.327** ± 0.091	
	After Dopant	**0.402** ± 0.026	**0.480** ± 0.001	**0.473** ± 0.027	**0.416**	**0.329** ± 0.087	**0.41** ± 0.076
	After 2 % HF	**0.325** ± 0.003	**0.336** ± 0.031	**0.393** ± 0.027	**0.264**	**0.283** ± 0.070	
	4 Month Wait	**0.299** ± 0.009					
FF	As Prepared	**0.44** ± 0.07	**0.16** ± 0.01	**0.27** ± 0.09	**0.60**	**0.14** ± 0.01	**0.26** ± 0.07
	After 2 % HF	**0.35** ± 0.07	**0.23** ± 0.01	**0.26** ± 0.03	**0.29**	**0.19** ± 0.03	
	After Dopant	**0.21** ± 0.01	**0.29** ± 0.02	**0.24** ± 0.01	**0.32**	**0.21** ± 0.07	**0.33** ± 0.07
	After 2 % HF	**0.36** ± 0.04	**0.25** ± 0.01	**0.25** ± 0.01	**0.47**	**0.48** ± 0.13	
	4 Month Wait	**0.20** ± 0.01					

J_{Sat} (mA cm^{-2})	**As Prepared**	**4.6×10^{-5}**	**3.02×10^{-6}**	**1.5×10^{-4}**	**6.16×10^{-6}**	**2.0×10^{-3}**	**2.15×10^{-5}**
	After 2 % HF	**2.4×10^{-4}**	**2.94×10^{-3}**	**1.9×10^{-3}**	**3.31×10^{-6}**	**6.0×10^{-4}**	
	After Dopant	**1.0×10^{-4}**	**8.12×10^{-5}**	**2.2×10^{-4}**	**2.51×10^{-6}**	**1.2×10^{-3}**	**4.16×10^{-5}**
	After 2 % HF	**1.3×10^{-4}**	**1.45×10^{-3}**	**1.5×10^{-3}**	**1.17×10^{-4}**	**2.0×10^{-4}**	
	4 Month Wait	**2.8×10^{-4}**					
Ideality	As Prepared	**1.44** ± 0.348	**1.14** ± 0.095	**1.73** ± 0.45	**1.41**	**2.67** ± 0.11	**1.67** ± 0.546
	After 2 % HF	**1.84** ± 0.252	**2.48** ± 0.242	**2.28** ± 0.48	**1.34**	**1.80** ± 0.74	
	After Dopant	**1.73** ± 0.213	**2.15** ± 0.397	**2.58** ± 0.18	**1.34**	**1.81** ± 0.70	**1.98** ± 0.383
	After 2 % HF	**1.26** ± 0.048	**1.95** ± 0.372	**2.35** ± 0.28	**1.11**	**1.21** ± 0.16	
	4 Month Wait	**1.54** ± 0.033					
R_{Shunt} (Ω)	As Prepared	**2357** ± 3128	**64.4** ± 13.4	**84.6** ± 25.6	**20700**	**246.7** ± 52.8	**239** ± 291
	After 2 % HF	**373** ± 291	**80.4** ± 32.1	**90.8** ± 26.1	**2030**	**348** ± 334	
	After Dopant	**31.7** ± 7.0	**96.8** ± 54.1	**38.5** ± 7.30	**2520**	**4594** ± 7713	**228** ± 186
	After 2 % HF	**262** ± 148	**52.1** ± 13.1	**73.1** ± 9.92	**5830000**	**6567** ± 3840	
	4 Month Wait	**56.9** ± 30.9					
R_{Series} (Ω)	As Prepared	**13.3** ± 2.65	**433** ± 141	**98.6** ± 64.8	**61.1**	**4200** ± 3202	**57.4** ± 18.6
	After 2 % HF	**18.7** ± 4.72	**104** ± 31.3	**77.4** ± 10.3	**232**	**700** ± 162	
	After Dopant	**62.5** ± 3.52	**25.4** ± 3.04	**43.8** ± 6.95	**164**	**700** ± 37.9	**20.7** ± 1.59
	After 2 % HF	**12.6** ± 1.59	**53.6** ± 16.5	**74.4** ± 10.2	**57.3**	**59.4** ± 10.9	
	4 Month Wait	**163** ± 50.3					

Table 6-4 and Table 6-5 display the complete device data for the final devices with thinner CNT/GO films and with optimal interlayer thicknesses. The data in the table is presented in this chapter in Figure 6-30, Figure 6-21, Figure 6-77, Figure 6-97, and Figure 6-94. The best performing devices pre-treatment were devices with a 17 nm – 18 nm PEDOT:PSS interlayer with an average PCE of 4.06 % ± 0.18. The best performing devices after doping were devices with no interlayer and $SOCl_2$ vapour doping with an average PCE of 4.98 % ± 0.14. These devices are also the best performing overall. The fact that devices with no interlayer out performed all other devices is an issue. PEDOT:PSS, PANI and DAD devices were all shown to outperform devices with no interlayers in some experiments (Figure 6-19 and Table 6-3). PEDOT:PSS devices outperform devices with no interlayer prior to doping, which matches the commonly observed decrease in performance with doping for devices with PEDOT:PSS interlayers. The degradation in performance exhibited by devices with PANI or DAD interlayers is likely due to film morphology. AFM images of PANI films showed them to be very rough and thin (Figure 6-14 and Figure 6-15). DAD films were initially observed to be smooth and homogeneous (Figure 6-84, Figure 6-85, and Figure 6-89) and gave improved device properties at this stage. However, experiments conducted with a second batch of DAD showed rough and disordered films (Figure 6-86 and Figure 6-87), and devices with this batch of DAD displayed inferior performance compared to the initial devices.

The final devices with the optimal interlayer thicknesses and high transmittance CNT/GO films were retested four months after the final doping. In each case the device performance decreased significantly, with only the devices with no interlayer and a $SOCl_2$ doping recording an average PCE higher than 1 %. The significant PCE degradation was due to a decrease in J_{sc} and FF. Additionally, after 4 months the shunt resistance was lower than the series resistance except for the devices with no interlayer and a $SOCl_2$ doping. As the shunt resistance is the resistance against unwanted circuit paths and the series resistance is the resistance against the desired circuit path it can be seen why a higher shunt resistance is problematic. The difference was an order of magnitude for the other devices except for the optimal CuSCN devices where the average shunt resistance was 149 Ω and the average series

resistance was 854 Ω. The degradation in performance was due to the lessened doping effect with time and an increase in the interfacial oxide layer between the silicon and the CNT/GO film. It is worth noting that the final 2% HF performed on most devices invariably lowered performance. Thus, the 4 month data point was after the devices were already producing a lower PCE than optimal.

Overall, it is clear that interlayer materials can serve to improve the performance of the large area CNT/Si device. This was expected as these interlayers give improvement in small area devices. The major issue that is encountered is that forming smooth, homogeneous films from spin coating becomes less reproducible as the area of the substrate is increased. This led to visual differences being observed on substrates coated under the same conditions and with the same parameters, and to thin, disordered films being formed. Thus, it is apparent that tailoring the surface of the substrates to provide optimal attachment to the interlayer precursor material is vital for producing high performing large area CNT/Si devices.

Table 6-6: Best performing device average J_{sc} and PCE values for each device design both as recorded and adjusted for lamp spot inhomogeneity (x 1.11). Asterix-marked interlayers indicate the data came from devices not included in Table 6-4 or Table 6-5.

	Initial J_{sc} ($mA\ cm^{-2}$)	*Scaled J_{sc} ($mA\ cm^{-2}$)*	*Initial PCE (%)*	*Scaled PCE (%)*
No Interlayer	8.25	**9.16**	4.98	**5.53**
PEDOT:PSS	8.82	**9.79**	4.06	**4.51**
*PANI**	7.01	**7.78**	2.62	**2.91**
MoO_x	7.94	**8.81**	2.20	**2.44**
CuSCN	8.48	**9.41**	2.75	**3.05**
*DAD**	6.09	**6.76**	3.34	**3.70**

In Section 2.2.2.1 a multiplicative scaling factor for adjusting J_{sc} (and thus PCE as they are proportional) to correct for the intensity gradient in the lamp spot was determined as 1.11. Table 6-6 shows the J_{sc} and PCE data for the best performing device sets for each interlayer both before and after adjustment by the scaling factor. Whilst this does not change the comparison between device sets (as all sets were scaled by the same factor) it is interesting to note that, when scaled, large area CNT/Si devices with no interlayer produced an average PCE above 5 %.

CHAPTER 7 CONCLUSIONS

7.1 Conclusions

Overall, the effect of changes in CNT type and to CNT film morphology in the CNT/Si heterojunction solar device were investigated. The work done has clearly shown that the ideal CNT type is SWCNTs with a large diameter. Film morphology improvement with decreased filtration rate was investigated and it was demonstrated that this produced flatter films which acted as improved thin film conductors. The work in this thesis did demonstrate the scalability of the design with the active area increased 25-fold with a moderate decrease in device performance. The highest PCE of the large area devices observed was 5 %. In depth conclusions from each section of this thesis will be summarised here section by section, in order of appearance.

When varying the type of CNT used (in terms of wall number and diameter) in the CNT/Si heterojunction device, the largest effect was found to be the ability of the CNTs to form stable and concentrated suspensions and thus, homogeneous films. In general, it was found that SWCNT species form better suspensions and more homogeneous films when filtered from suspension. It was found that, in some cases, DWCNTs formed suspensions so poor that homogeneous films could not be produced. It was confirmed that Raman spectroscopy is a useful technique for determining the structure of CNT in a given sample, with clear distinctions visible between spectra obtained from SWCNTs, DWCNTs, and MWCNTs. Specifically, a high D/G ratio (>1) is seen from MWCNT samples, and mixed semiconducting and metallic SWCNT samples display a BWF peak (seen as a shoulder on the G band peak), which is not visible in DWCNT or MWCNT samples. Additionally, the wavenumber of RBM peaks in a Raman spectrum allowed the diameter of SWCNT samples to be accurately determined, although determining the diameter of DWCNTs using this method is more convoluted as the peaks appear to be due to the inner tubes only. UV/Visible spectroscopy was also shown to be important for characterising CNT species. Clear S_{xx} and M_{xx} transitions were visible for SWCNT species, but no such peaks were visible on DWCNT and MWCNT species, as these species do not possess the VHS DOS structure to produce these optical transitions.

In terms of small active area device performance, it was found that SWCNTs with large diameters produced the best performing devices with a PCE average of 4.21 ± 18.74%. It was found that MWCNT films produced devices that performed comparatively well initially, but chemical doping gave greater performance increases in the devices with SWCNT and DWCNT films. From sheet resistance measurements it was determined that the series of chemical doping used (2% HF - $SOCl_2$ – 2% HF) had a significantly reduced effect on MWCNT films. The sheet resistance was reduced by only 13% for the MWCNT films, compared to 52% and 41% for the two SWCNT samples used. This was a reason for the superiority of SWCNT films in devices over MWCNT films. Overall, devices with SWCNT films produced superior short circuit current densities, whilst devices with DWCNT or MWCNT films produced superior open circuit voltages.

It was determined that allowing suspensions of SWCNTs to filter under gravity, instead of under vacuum, lead to significant decreases in film roughness on the microscale. However, the films were not homogeneous on the macroscale. The films produced consisted of small, dark areas of high SWCNT density surrounded by larger, pale areas of low SWCNT density. This meant that a consistent transmittance value across the film for slow-filtered films could not easily be achieved. It was found that slow-filtered SWCNT films used in CNT/Si devices gave equivalent performances to CNT/Si devices containing fast-filtered SWCNT films that were much thicker. The slow-filtered films had lower sheet resistances compared to fast-filtered films with equivalent transmittance. They were also found to produce higher σ_{dc}: σ_{OP} ratios of approximately 0.065 compared to fast-filtered films, which produced ratios of approximately 0.044. This indicated that, at high transmittance (85 % - 95 %) a slow-filtered SWCNT film is a superior thin conductive film to a fast-filtered SWCNT film.

The active area of the CNT/Si device was scaled up from 0.09 cm^2 to 2.25 cm^2. It was discovered that the application of a conductive grid over the front of the device to assist the CNT film to transport charge carriers was essential for optimal device performance. A thermally evaporated aluminium back contact was applied and optimised for use in the CNT/Si device. As expected, the performance of the

large active area device was found to be poor compared to small active area devices, due to significantly lower current density production. One major reason for this was due to diminishing light intensity towards the edges of the light source used for solar testing. A 2D map of the light spot used was produced and used to determine a multiplicative scaling factor of 1.11 to adjust the current density for this phenomenon. The remaining difference in current density between the large and small active area devices was attributed to the lessened ability of the thin gold top contact to transport charge carriers effectively as the transport distance required increased from the small area devices to the large area devices. The thickness of the top gold contact was investigated for the large active devices and a total thickness of 450 nm (5 nm Cr + 445 nm Au) was found to be optimal, with local current density and fill factor maxima located at this thickness. Additionally, it was determined that the presence of a thin chromium cap on the top contact did not provide improved device performance.

Manipulation of the silicon oxide layer that grows between the silicon substrate and CNT film was investigated. The application of H_2O_2 to force the growth of a thin oxide layer prior to CNT film attachment was found to severely diminish device performance. Alternatively, it was determined that allowing substrates to sit in air for 120 min prior to CNT film attachment was found to lead to a silicon oxide layer thickness that gave optimal device performance.

The use of alumina filtration membranes for CNT film formation in order to improve film morphology was investigated. However, it was determined that the use of cellulose ester filtration membranes was preferable for the devices used in this thesis. The reasons for this were, firstly, devices with alumina filtered CNT films were found to have a decreased current production and voltage compared to devices with cellulose ester filtered CNT films, although an improvement in diode properties was observed. In addition to this, the alumina filter papers are more expensive than the cellulose ester filter papers and significantly more brittle. This brittleness lead to increased processing time and processing difficulty compared to using cellulose ester filter papers.

Five interlayer materials were studied in order to improve the performance of the large area CNT/Si heterojunction device. These were PEDOT:PSS, PANI, CuSCN, MoO_x, and DAD. Substrates were coated with thin films of each interlayer via spin coating. UV/Visible spectroscopy, SEM, and AFM were used to investigate film morphology and thickness when parameters such as deposition volume and spin speed were varied. For most interlayer materials, a trend of decreasing film thickness versus increased spin coating speed was determined. The interlayers were all applied in large area CNT/Si devices and optimal film thicknesses for ideal performance were established. PEDOT:PSS was found to give improved performance over devices with no interlayer directly after preparation. However, the situation reversed after chemical doping of the CNT film as the performance of devices with no interlayer increased and devices with PEDOT:PSS decreased. PANI and DAD were found to increase the performance of CNT/Si devices in some experiments but poor film formation appeared to lead to difficulty in replicating these results. CuSCN and MoO_x were not found to give improvement in CNT/Si device performance. This may have been due to interlayer interference in the CNT/Si heterojunction formation as a MoO_x interlayer is expected to improve the Au/CNT junction and the overall charge carrying ability of the CNT film. Additionally, the MoO_x layers produced in this thesis were thinner than those previously found to give improved device performance. Overall, it was apparent that PEDOT:PSS, PANI, and DAD showed promise for use in the large active area CNT/Si heterojunction solar device with device improvement documented when homogeneous thin films of each were applied. However, it was also apparent that the formation of these interlayers via spin coating was not consistent, even when identical substrate treatment regimens were observed. The best performing CNT/Si device had no interlayer and recorded a PCE of 5 %. Additionally, the performance of devices with each interlayer present and with no CNT film was studied both with and without a thin gold layer over the top contact. It was found that Au/MoO_x/Si devices were superior to CNT/MoO_x/Si devices with a maximum PCE of 4.7 % produced.

7.2 Future Work

The research presented in this thesis has probed and answered many questions about the CNT/Si heterojunction device. However, as with all research, it has led to more questions and paths for future research and investigation. Presented here are some clear future research pathways that could be taken.

The research performed in Chapter 3 on the effect of nanotube wall number and diameter on CNT/Si device performance showed that these properties did have an effect on device performance. However, the length of the CNTs was not investigated, yet this will also have an effect on performance. Longer CNTs will reduce the number of CNT-CNT junctions within the film and thus should produce films with superior conductivity.[14] An issue is that CNTs are generally processed into solution for filtration or spray coating onto the device substrates. This processing is likely to shorten the tubes and thus increase film resistance. Some proposed methods for applying long CNTs into CNT/Si devices are by taking films of CNTs formed on the inside of the CNT fabrication chamber and applying them directly to the device or, by placing device substrates in front of a CNT fabrication source during CNT fabrication to catch a, as-grown, network of CNTs.[14] However, these techniques do not allow any CNT sorting or purification to take place. Thus, an important area of future research would be to investigate methods of fabricating long CNTs, and applying them to CNT/Si devices without reducing their average length whilst also allowing sorting and purification to take place.

It was apparent that filtering SWCNT suspensions under gravity produced CNT films with improved σ_{DC}:σ_{OP} ratios but with poor macroscale homogeneity. Thus, it is important to further research the formation of these films in order to produce homogeneous films on the macroscale with improved σ_{DC}:σ_{OP} ratios for use, not only in the CNT/Si device, but also as highly transparent conductors in other applications. Firstly, topographical inconsistencies in the filtration membranes used may have led to localised regions of high CNT concentration. Thus, ensuring a highly flattened filter surface may improve the macroscale formation of the CNT films. Alternatively, other filter materials may provide an improved deposition surface. For example, alumina membranes were used in Chapter 5.7 of this

thesis, these membranes produced flatter films when vacuum filtration was performed. Thus, these membranes (or similar, flatter membranes) may improve the slow filtration process. Additionally, as filtration under vacuum produced rougher cells than filter by gravity, there likely exists a spectrum of film roughness with increasing CNT deposition bias (whether solely gravity or gravity plus vacuum). Research to determine the trend in roughness with applied bias would be useful to find an optimal vacuum to produce thinner CNT films with high σ_{DC}:σ_{OP} ratios, whilst also retaining macroscale homogeneity.

Control of the SiO_x layer between the silicon substrate and the CNT film also requires more research. It is clear from past studies that a thin oxide layer is ideal for optimising photovoltaic performance in CNT/Si devices,[24] likely due to passivation of the silicon surface.[14] However, in this thesis, oxide growth is controlled by different preparation techniques followed by wet etching with HF and the total thickness of the oxide layer is unknown. It was found in this work that H_2O_2 treatment of the substrate to grow a SiO_x layer was inappropriate and an optimal waiting time in between BOE etch and film attachment was determined. However, this was hardly a robust study and the optimal time is likely dependent on ambient temperature and humidity. There likely exists an optimal preparation technique to fabricate devices with the perfect oxide thickness and retain it at this thickness. Such a preparation technique would have to be performed in climate controlled conditions, as oxide growth is affected by ambient temperature and humidity.

An important area of future research in the large area CNT/Si device is in optimization of the top contact grid design. The design used in this thesis was taken from an optimized design for the small area (0.09 cm^2) device,[136] but this is likely not an optimal design for the large area device. It is possible that a design involving fingers, rather than a grid network, may be more suitable as the current grid design covers a large proportion of the area of the device. The exposed silicon area of the large area devices was only 1.95 cm^2 compared to the overall area inside the gold edge of 2.25 cm^2. This is an area loss of over 10 %. Thus, a top contact finger design, which uses an overall smaller area

of metal, would serve to improve the device by allowing more silicon to be accessible to incident photons.

Other previous research done to scale up the active area of the CNT/Si device used strips of high density CNTs to assist the CNT film in charge carrier transport instead of a metallic top contact grid network.[135] The CNT strips were fabricated by manually twisting free floating films into thin, high density strips. An alternate method could be to use dip-pen lithography to draw high-density CNT lines on the surface of the film. An advantage of using CNT lines over gold lines (as used in this research) is that the CNT lines could theoretically have higher transmittance values than the gold lines while still exhibiting low resistance if the CNTs were long and well aligned. Additionally, CNT lines would be cheaper and more flexible than gold grid lines. Dip-pen drawn thin SWCNT lines have been successfully drawn at lengths over 1 mm and applied in CNT/Si devices, giving a significant improvement in device performance.[168] Thus, incorporation of dip-pen drawn CNT lines into the large area devices would be an important field of future research.

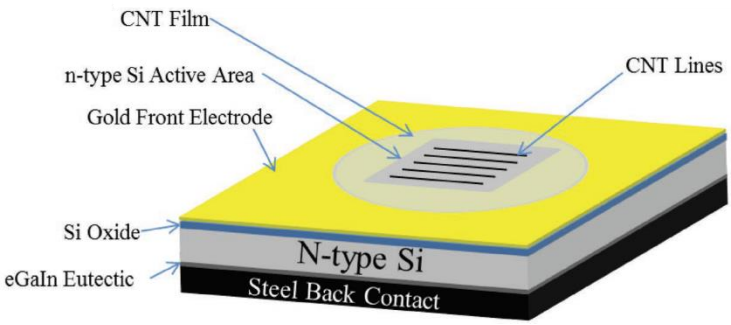

Figure 7-1: Schematic of CNT/Si device with dip-pen lithography drawn CNT lines from Corletto *et al.*[168]

It became apparent during the testing of large area devices with various spin coated interlayers that the homogeneous formation of the interlayer material on the silicon/gold substrate was of vital importance for ensuring good device performance. It was observed that a drop in homogeneity of the DAD and the PANI interlayers corresponded with a significant decrease in device performance, relative to concurrent devices with no interlayer material. Spin coating the materials on small areas seems to be a good technique however it was clear that, on the large area devices, changes in surface wettability could drastically affect the interlayer film formation. Thus, alternative film formation

processes with an emphasis on good large area formation could be investigated in the future. One novel technique for thin interlayer film deposition is the use of plasma deposition. Plasma deposition is substrate independent and is controllable via precursor and plasma condition choices. Additionally this technique allows coating of complex substrate geometries.[222] Plasma deposition has been used to produce pyrrole films,[222] fluorocarbons,[223] electrolyte membranes for fuel cells,[224] hydroxide exchange membranes,[225] and silane polymers such as APTES.[226] Thus, discovering polymers with appropriate HOMO LUMO gaps to match the needs of the CNT/Si device which can be deposited using plasma could be a significant boon. Recently, electrodeposition of PEDOT:PSS and PEDOT:PSS/GO composites on gold electrodes has been achieved by Lee *et al*.[227] Thus, electrodeposition could also be a viable attachment method for interlayer materials. Alternatively, a consistent treatment regime to prepare the substrates prior to thin film deposition, taking into account SiO_x growth, could be determined which will allow spin coating to be a more consistent deposition than observed in this thesis.

A further area of study with the large area CNT/Si heterojunction solar device is continue to implement techniques that have shown promise in small area CNT/Si solar device research. Light trapping strategies that could be implemented included polymeric coatings such as polystyrene as researched by Yu *et al.*[80], etching of the silicon substrate to produce light trapping structures in the silicon surface[124], and thermally evaporated metal oxide films such as MoO_x and ZnO as researched by Wang *et al.*[16]. Research by Yu *et al.*[228] has shown that $Ti_3C_2T_x$ (MXene) compounds give good photovoltaic performance when used to replace the CNT film in the CNT/Si device structure to give a MXene/Si heterojunction. This research was done on small area silicon substrates, thus it would be of great interest to manufacture MXene/Si heterojunction devices using the large active area substrates used in this thesis.

An alternative device design could also be implemented, where the top gold electrode is attached after interlayer/CNT film deposition. This would enable the effect of interlayers on the Au/CNT and

CNT/Si junctions to be probed individually, unlike in this thesis where any applied interlayer will be between the CNT film and both the gold and the silicon. In addition to this, applying the interlayer/CNT film prior to the metal top contact will lead to improved film formation and contact with silicon as the film will not be required to bend over the gold grid lines**.** A major hurdle to clear in this design would be attaching the top electrode to the soft and highly porous interlayer/CNT, CNT/interlayer, interlayer/CNT/interlayer or pure CNT film. In the current fabrication regime, any interlayer material would be exposed to UV light, various organic solvents, and high voltage and high vacuum environments whilst the sample is patterned and the chromium/gold layer sputter coated.

One possible solution could be that employed by the original researches behind the CNT/Si device. Wei *et al.*[25] used a silver paint to connect their CNT films with a top contact. Alternatively, to avoid creating new Au/Ag and Ag/CNT junctions, thick strips of long CNTs could be used to connect the CNT film to the top contact, although in this case Au/interlayer/CNT effects would be more difficult to observe. The recent call for wearable electronic devices had sparked investigations into alternate electrode fabrication methods to thermal deposition and sputtering. These new methods involve solution-based wet chemical techniques which avoid the high temperature and vacuum environments required for conventional electrode fabrication. The metal is coated on flexible polymer or elastomers to produce flexible thin electrodes that can then be applied to devices.[229] Metal electrodes can also be printed or written on to a substrate, however these techniques produce metal layers over 1 µm in thickness.[229] Low temperature electrode deposition could be used to form thin metal electrodes on solar devices after CNT/interlayer film deposition. However, these techniques will still require patterning with photolithography or similar and thus, the use of organic solvents.[229] Another novel electrode material is a combination of hydrogels and liquid metals (such as eGaIn) to form soft, flexible electrodes that can also be prepared separate from the devices and applied after CNT/interlayer attachment[230]. A simpler option, which avoids the need to pattern the surface, is to coat the entire substrate with a thin layer of gold (5-10 nm). It has been shown in the work in this thesis, where a thin gold layer was used instead of a CNT film, that a 5 nm layer of gold is sufficient to give reasonable

current flow. A downside with this idea is that the gold will inhibit photons passing through to the silicon surface. Additionally, it would need to be ensured that there was no direct contact between the gold top coating and the silicon surface as this would lead to a short circuit.

A design can be envisaged where a thick metal contact is formed prior to CNT/interlayer attachment but far enough from the active area such that the CNT/interlayer film does not connect to the contact. The gap between the active area of the device and the pre-formed thick metal contact could then be bridged using silver paint, thick CNT strips, flexible soft metal electrodes[229] or a surface covering thin gold layer. This design would give the benefits of separating the top electrode/CNT and CNT/Si junctions with regards to interlayer effect and improved CNT/Si contact formation whilst reducing the distance required by the thin electrodes to transport charge carriers.

CHAPTER 8 REFERENCES

1. Arnold, M.S., et al., *Recent developments in the photophysics of single-walled carbon nanotubes for their use as active and passive material elements in thin film photovoltaics.* Physical Chemistry Chemical Physics, 2013. **15**(36): p. 14896-14918.
2. REN21 Steering Committee, *Renewables 2014 Global Status Report*. 2014. p. 16.
3. Pintossi, C., et al., *Steering the Efficiency of Carbon Nanotube-Silicon Photovoltaic Cells by Acid Vapor Exposure: a Real-Time Spectroscopic Tracking.* ACS applied materials & interfaces, 2015.
4. Tune, D.D. and J.G. Shapter, *Effect of Nanotube Film Thickness on the Performance of Nanotube-Silicon Hybrid Solar Cells.* Nanomaterials, 2013. **3**(4): p. 655-673.
5. Tune, D.D., *Single Walled Carbon Nanotube Photovoltaics*, in *School of Chemical and Physical Sciences*. 2013, Flinders University. p. 221.
6. Colinge, J.-P. and C.A. Colinge, *Physics of Semiconductor Devices*. 2002, United States of America: Kluwer Academic Publishers. 436.
7. Shi, E., et al., *TiO2-Coated Carbon Nanotube-Silicon Solar Cells with Efficiency of 15%.* Scientific Reports, 2012. **2**.
8. Batmunkh, M., M.J. Biggs, and J.G. Shapter, *Carbon Nanotubes for Dye-Sensitized Solar Cells.* Small, 2015. **11**(25): p. 2963-2989.
9. Rowell, M.W., et al., *Organic solar cells with carbon nanotube network electrodes.* Applied Physics Letters, 2006. **88**(23): p. 233506.
10. Pasquier, A.D., et al., *Conducting and transparent single-wall carbon nanotube electrodes for polymer-fullerene solar cells.* Applied physics letters, 2005. **87**(20): p. 203511.
11. Van De Lagemaat, J., et al., *Organic solar cells with carbon nanotubes replacing In 2 O 3: Sn as the transparent electrode.* Applied Physics Letters, 2006. **88**(23): p. 233503.
12. Batmunkh, M., et al., *Carbon Nanotubes in TiO2 Nanofiber Photoelectrodes for High-Performance Perovskite Solar Cells.* Advanced Science, 2017. **4**(4): p. 1600504.
13. Habisreutinger, S.N., et al., *Carbon nanotube/polymer composites as a highly stable hole collection layer in perovskite solar cells.* Nano letters, 2014. **14**(10): p. 5561-5568.
14. Tune, D.D. and B.S. Flavel, *Advances in Carbon Nanotube–Silicon Heterojunction Solar Cells.* Advanced Energy Materials, 2018.
15. Dai, H., *Carbon nanotubes: synthesis, integration, and properties.* Accounts of chemical research, 2002. **35**(12): p. 1035-1044.
16. Wang, F., et al., *Considerably improved photovoltaic performance of carbon nanotube-based solar cells using metal oxide layers.* Nature communications, 2015. **6**.
17. Tzolov, M.B., et al., *Carbon nanotube-silicon heterojunction arrays and infrared photocurrent responses.* The Journal of Physical Chemistry C, 2007. **111**(15): p. 5800-5804.
18. Javey, A.G., J. Farmer, D.B. Wang, Q. Yenilmez, E. Gordon, R.G. Lundstrom, M. Dai, H., *Self-Aligned Ballistic Molecular Transistors and Electrically Parallel Nanotube Arrays.* Nano Letters, 2004. **4**(7): p. 1319-1322.
19. Kongkanand, A., R. Martínez Domínguez, and P.V. Kamat, *Single wall carbon nanotube scaffolds for photoelectrochemical solar cells. Capture and transport of photogenerated electrons.* Nano letters, 2007. **7**(3): p. 676-680.
20. Baughman, R.H.Z., A.A. de Heer, W.A., *Carbon Nanotubes - the Route Toward Applications.* Science, 2002. **297**(5582): p. 787-792.
21. Durkop, T.G., S.A. Cobas, Fuhrer, M.S., *Extraordinary Mobility in Semiconducting Carbon Nanotubes.* Nano Letters, 2004. **4**(1): p. 35-39.
22. Barnes, T.M.B., J.L. van de Lagemaat, J. Coutts, T.J. Heben, M.J., *Reversibility, Dopand Desorption, and Tunneling in the Temperature-Dependent Conductivity of*

Type-Separated, Conductive Carbon Nanotube Networks. ACS Nano, 2008. **2**(9): p. 1968–1976.
23. Arena, A., et al., *Photovoltaic properties of multi-walled carbon nanotubes deposited on n-doped silicon.* Microelectronics Journal, 2008. **39**(12): p. 1659-1662.
24. Tune, D.D.F., B S. Krupke, R. Shapter, J G. , *Carbon Nanotube-Silicon Solar Cells.* Advanced Energy Materials, 2012. **2**(9): p. 1043-1055.
25. Wei, J.J., Y. Shu, Q. Gu, Z. Wang, K. Zhuang, D. Zhang, G. Wang, Z. Luo, J. Cao, A. Wu, D, *Double-Walled Carbon Nanotube Solar Cells.* Nano Letters, 2007. **7**(8): p. 2317-2321.
26. Iijima, S., *Helical microtubules of graphitic carbon.* Nature, 1991. **354**(6348): p. 56.
27. Calvert, P., *Nanotube composites: a recipe for strength.* Nature, 1999. **399**(6733): p. 210.
28. Ebbesen, T., et al., *Electrical conductivity of individual carbon nanotubes.* Nature, 1996. **382**(6586): p. 54.
29. Lau, A.K.-T. and D. Hui, *The revolutionary creation of new advanced materials—carbon nanotube composites.* Composites Part B: Engineering, 2002. **33**(4): p. 263-277.
30. Yu, M.-F., et al., *Strength and breaking mechanism of multiwalled carbon nanotubes under tensile load.* Science, 2000. **287**(5453): p. 637-640.
31. Grace, T., et al., *Investigating the Effect of Carbon Nanotube Diameter and Wall Number in Carbon Nanotube/Silicon Heterojunction Solar Cells.* Nanomaterials, 2016. **6**(3): p. 52.
32. Baughman, R.H., A.A. Zakhidov, and W.A. de Heer, *Carbon Nanotubes - the Route Toward Applications.* Science, 2002. **297**(5582): p. 787-792.
33. Liu, B., et al., *Chirality-controlled synthesis and applications of single-wall carbon nanotubes.* ACS Nano, 2017. **11**(1): p. 31-53.
34. Biercuk, M., et al., *Carbon nanotube composites for thermal management.* Applied Physics Letters, 2002. **80**(15): p. 2767-2769.
35. MacDonald, R.A., et al., *Collagen–carbon nanotube composite materials as scaffolds in tissue engineering.* Journal of Biomedical Materials Research Part A: An Official Journal of The Society for Biomaterials, The Japanese Society for Biomaterials, The Australian Society for Biomaterials, The Korean Society for Biomaterials, 2005. **74**(3): p. 489-496.
36. Mirri, F., et al., *Lightweight, flexible, high-performance carbon nanotube cables made by scalable flow coating.* ACS applied materials interfaces, 2016. **8**(7): p. 4903-4910.
37. Peng, H.L., Qingwen; Chen, Tao, *Industrial Applications of Carbon Nanotubes*. 1st Edition ed. 2017: Elsevier.
38. Hirsch, A., *Functionalization of single-walled carbon nanotubes.* Angewandte Chemie International Edition, 2002. **41**(11): p. 1853-1859.
39. Yao, Z., et al., *Polymerization from the surface of single-walled carbon nanotubes− preparation and characterization of nanocomposites.* Journal of the American Chemical Society, 2003. **125**(51): p. 16015-16024.
40. Sun, Y.-P., et al., *Functionalized carbon nanotubes: properties and applications.* Accounts of Chemical Research, 2002. **35**(12): p. 1096-1104.
41. Chen, R.J., et al., *Noncovalent sidewall functionalization of single-walled carbon nanotubes for protein immobilization.* Journal of the American Chemical Society, 2001. **123**(16): p. 3838-3839.
42. H. Qiu, J.Y., *Structure and Properties of Carbon Nanotubes*, in *Industrial Applications of Carbon Nanotubes*, Q.L. H. Peng, T. Chen, Editor. 2017, Elsevier. p. 47-66.
43. Das, S., *A review on Carbon nano-tubes-A new era of nanotechnology.* Int J Emer Tech Adv Eng, 2013. **3**(3): p. 774-783.
44. Hirschmann, T.C., et al., *Characterization of bundled and individual triple-walled carbon nanotubes by resonant Raman spectroscopy.* ACS nano, 2013. **7**(3): p. 2381-2387.

45. Crochet, J.J., et al., *Free-carrier generation in aggregates of single-wall carbon nanotubes by photoexcitation in the ultraviolet regime.* Physical review letters, 2011. **107**(25): p. 257402.
46. J. An, Z.Z., L. Zheng, *Controllable Synthesis of Carbon Nanotubes*, in *Industrial Applications of Carbon Nanotubes*, Q.L. H. Peng, T. Chen, Editor. 2017, Elsevier. p. 2-36.
47. Belin, T. and F. Epron, *Characterization methods of carbon nanotubes: a review.* Materials Science and Engineering: B, 2005. **119**(2): p. 105-118.
48. Ugawa, A., et al., *Far-infrared to visible optical conductivity of single-wall carbon nanotubes.* Current applied physics, 2001. **1**(1): p. 45-49.
49. Vijayaraghavan, A., et al., *Toward single-chirality carbon nanotube device arrays.* ACS nano, 2010. **4**(5): p. 2748-2754.
50. Blanch, A.J., *Aqueous Dispersion of Carbon Nanotubes for Electronic Type-Selective Reactions with Aryl Diazonium Salts*, in *School of Chemical and Physical Sciences*. 2011, Flinders University. p. 262.
51. Dresselhaus, M.S.D., G. Jorio, A., *Unusual Properties and Structure of Carbon Nanotubes.* Annu. Rev. Mater. Res., 2004. **34**: p. 247-278.
52. O'Connell, M.J., E.E. Eibergen, and S.K. Doorn, *Chiral selectivity in the charge-transfer bleaching of single-walled carbon-nanotube spectra.* Nature Materials, 2005. **4**(5): p. 412.
53. Dresselhaus, M.S., et al., *Raman spectroscopy of carbon nanotubes.* Physics reports, 2005. **409**(2): p. 47-99.
54. Ávila, A.F. and G.S.R. Lacerda, *Molecular mechanics applied to single-walled carbon nanotubes.* Materials Research, 2008. **11**(3): p. 325-333.
55. Iijima, S. and T. Ichihashi, *Single-shell carbon nanotubes of 1-nm diameter.* Nature, 1993. **363**(6430): p. 603.
56. Journet, C., et al., *Large-scale production of single-walled carbon nanotubes by the electric-arc technique.* Nature, 1997. **388**(6644): p. 756.
57. Bethune, D., et al., *Cobalt-catalysed growth of carbon nanotubes with single-atomic-layer walls.* Nature, 1993. **363**(6430): p. 605-607.
58. Bronikowski, M.J., et al., *Gas-phase production of carbon single-walled nanotubes from carbon monoxide via the HiPco process: A parametric study.* Journal of Vacuum ScienceTechnology A: Vacuum, Surfaces Films, 2001. **19**(4): p. 1800-1805.
59. Thess, A., et al., *Crystalline ropes of metallic carbon nanotubes.* Science, 1996. **273**(5274): p. 483-487.
60. Cassell, A.M., et al., *Large scale CVD synthesis of single-walled carbon nanotubes.* The Journal of Physical Chemistry B, 1999. **103**(31): p. 6484-6492.
61. Hafner, J.H., et al., *Catalytic growth of single-wall carbon nanotubes from metal particles.* Chemical Physics Letters, 1998. **296**(1-2): p. 195-202.
62. Bachilo, S.M., et al., *Narrow (n, m)-distribution of single-walled carbon nanotubes grown using a solid supported catalyst.* Journal of the American Chemical Society, 2003. **125**(37): p. 11186-11187.
63. Wang, Y., et al., *The large-scale production of carbon nanotubes in a nano-agglomerate fluidized-bed reactor.* Chemical Physics Letters, 2002. **364**(5-6): p. 568-572.
64. Yao, Y., et al., *"Cloning" of single-walled carbon nanotubes via open-end growth mechanism.* Nano Letters, 2009. **9**(4): p. 1673-1677.
65. Sanchez-Valencia, J.R., et al., *Controlled synthesis of single-chirality carbon nanotubes.* Nature, 2014. **512**(7512): p. 61.
66. Yang, F., et al., *Chirality-specific growth of single-walled carbon nanotubes on solid alloy catalysts.* Nature, 2014. **510**(7506): p. 522.
67. An, J.Z., Z. Zheng, L., *Controllable Synthesis of Carbon Nanotubes*, in *Industrial Applications of Carbon Nanotubes*, H.L. Peng, Q. Chen, T., Editor. 2017, Elsevier. p. 1-36.

68. Blanch, A.J.Q., S.J. Shapter, J.G., *The role of sodium dodecyl sulfate concentration in the separation of carbon nanotubes using gel chromatography.* Carbon, 2013. **60**: p. 471-480.
69. Hersam, M.C., *Progress towards monodisperse single-walled carbon nanotubes.* Nature Nanotechnology, 2008. **3**(7): p. 387.
70. Fong, D. and A. Adronov, *Recent developments in the selective dispersion of single-walled carbon nanotubes using conjugated polymers.* Chemical science, 2017. **8**(11): p. 7292-7305.
71. Maultzsch, J., et al., *Exciton binding energies in carbon nanotubes from two-photon photoluminescence.* Physical Review B, 2005. **72**(24): p. 241402.
72. Maultzsch, J., et al., *Excitons in carbon nanotubes.* Physica Status Solidi, 2006. **243**(13): p. 3204-3208.
73. Wang, F., et al., *The Optical Resonances in Carbon Nanotubes Arise from Excitons.* Science, 2005. **308**: p. 838.
74. Li, Z.K., V P. Saini, V. Xu, Y. Dervishi, E. Salamo, G J. Biris, A R. Biris, A S., *SOCl2 Enhanced Photovoltaic Conversion of Single Wall Carbon Nanotube/ n-Silicon Heterojunctions.* Applied Physics Letters, 2008. **93**(24): p. 243117-243117.
75. Jia, Y.W., J. Wang, K. Cao, A. Shi, Q. Gui, X. Zhu, Y. Zhuang, G. Ma, B. Wang, L. Liu, W. Wang, Z. Luo, J. Wu, D., *Nanotube-Silicon Heterojunction Solar Cells.* Advanced Materials, 2008. **20**(23): p. 4594-4598.
76. Pintossi, C., et al., *Direct Evidence of Chemically Inhomogeneous, Nanostructured, Si–O Buried Interfaces and Their Effect on the Efficiency of Carbon Nanotube/Si Photovoltaic Heterojunctions.* The Journal of Physical Chemistry C, 2013. **117**(36): p. 18688-18696.
77. Jia, Y., et al., *Nanotube-silicon heterojunction solar cells.* Adv. Mater, 2008. **20**: p. 4594-4598.
78. Wei, J., et al., *Double-walled carbon nanotube solar cells.* Nano letters, 2007. **7**(8): p. 2317-2321.
79. Wadhwa, P., et al., *Electrolyte-induced inversion layer Schottky junction solar cells.* Nano letters, 2011. **11**(6): p. 2419-2423.
80. Yu, L., et al., *Implementation of antireflection layers for improved efficiency of carbon nanotube–silicon heterojunction solar cells.* Solar Energy, 2015. **118**: p. 592-599.
81. Castrucci, P., et al., *Light harvesting with multiwall carbon nanotube/silicon heterojunctions.* Nanotechnology, 2011. **22**(11): p. 115701.
82. Jia, Y., et al., *Encapsulated carbon nanotube-oxide-silicon solar cells with stable 10% efficiency.* Applied Physics Letters, 2011. **98**(13): p. 133115.
83. Jia, Y., et al., *Carbon nanotube films by filtration for nanotube-silicon heterojunction solar cells.* Materials Research Bulletin, 2010. **45**(10): p. 1401-1405.
84. Wadhwa, P., et al., *Electronic junction control in a nanotube-semiconductor Schottky junction solar cell.* Nano letters, 2010. **10**(12): p. 5001-5005.
85. Freitag, M., *Carbon nanotubes: Doped defects tracked down.* J Nature materials, 2008. **7**(11): p. 840.
86. Maciel, I.O., et al., *Electron and phonon renormalization near charged defects in carbon nanotubes.* J Nature materials, 2008. **7**(11): p. 878.
87. Ayala, P., et al., *The doping of carbon nanotubes with nitrogen and their potential applications.* Carbon, 2010. **48**(3): p. 575-586.
88. Li, Z., et al., *Light-harvesting using high density p-type single wall carbon nanotube/n-type silicon heterojunctions.* Acs Nano, 2009. **3**(6): p. 1407-1414.
89. Tune, D.D., et al., *Nanotube film metallicity and its effect on the performance of carbon nanotube–silicon solar cells.* physica status solidi (a), 2014. **211**(7): p. 1479-1487.
90. Jia, Y., et al., *Achieving high efficiency silicon-carbon nanotube heterojunction solar cells by acid doping.* Nano letters, 2011. **11**(5): p. 1901-1905.

91. Geng, H.-Z., et al., *Effect of acid treatment on carbon nanotube-based flexible transparent conducting films.* Journal of the American Chemical Society, 2007. **129**(25): p. 7758-7759.
92. Tantang, H., et al., *Using oxidation to increase the electrical conductivity of carbon nanotube electrodes.* Carbon, 2009. **47**(7): p. 1867-1870.
93. Blackburn, J.L., et al., *Transparent conductive single-walled carbon nanotube networks with precisely tunable ratios of semiconducting and metallic nanotubes.* Acs Nano, 2008. **2**(6): p. 1266-1274.
94. Sun, H., et al., *Flexible carbon nanotube/mono-crystalline Si thin-film solar cells.* Nanoscale Research Letters, 2014. **9**(1): p. 514.
95. Jung, Y., et al., *Record high efficiency single-walled carbon nanotube/silicon p–n junction solar cells.* Nano letters, 2012. **13**(1): p. 95-99.
96. Li, X., et al., *Improved efficiency of smooth and aligned single walled carbon nanotube/silicon hybrid solar cells.* Energy & Environmental Science, 2013. **6**: p. 879-887.
97. Kim, S.M., et al., *Role of anions in the AuCl3-doping of carbon nanotubes.* Acs Nano, 2011. **5**(2): p. 1236-1242.
98. Harris, J.M., et al., *The Nature of Record Efficiency Fluid-Processed Nanotube-Silicon Heterojunctions.* The Journal of Physical Chemistry C, 2015.
99. Li, X., et al., *Device Area Scale-Up and Improvement of SWNT/Si Solar Cells Using Silver Nanowires.* Advanced Energy Materials, 2014. **4**(12).
100. Yu, L., et al., *Application of a hole transporting organic interlayer in graphene oxide/single walled carbon nanotube–silicon heterojunction solar cells.* Journal of Materials Chemistry A, 2017. **5**(18): p. 8624-8634.
101. Li, X., et al., *Controlled doping of carbon nanotubes with metallocenes for application in hybrid carbon nanotube/Si solar cells.* Nano letters, 2014. **14**(6): p. 3388-3394.
102. Cui, K., et al., *Scalable and Solid-State Redox Functionalization of Transparent Single-Walled Carbon Nanotube Films for Highly Efficient and Stable Solar Cells.* Advanced Energy Materials, 2017. **7**(18): p. 1700449.
103. Del Gobbo, S., et al., *Silicon spectral response extension through single wall carbon nanotubes in hybrid solar cells.* Journal of Materials Chemistry C, 2013. **1**(41): p. 6752-6758.
104. Tune, D.D., et al., *The role of nanotubes in carbon nanotube–silicon solar cells.* Advanced Energy Materials, 2013. **3**(8): p. 1091-1097.
105. Tune, D.D.B., A J. Krupke, R. Flave, B S. Shapter, J G., *Nanotube Film Metallicity and its Effects on the Performance of Carbon Nanotube-Silicon Solar Cells.* Physica status solidi (a), 2014. **211**(7): p. 1479-1487.
106. Cui, K., et al., *Air-stable high-efficiency solar cells with dry-transferred single-walled carbon nanotube films.* Journal of Materials Chemistry A, 2014. **2**(29): p. 11311-11318.
107. T. Grace, C.S., D. Tune, L. Yu, M. Batmunkh, MJ. Biggs, Z.A. ALOthman, J.G. Shapter, *Use of Carbon Nanotubes in Third-Generation Solar Cells*, in *Industrial Applications of Carbon Nanotubes*, Q.L. H. Peng, T. Chen, Editor. 2017, Elsevier. p. 201-233.
108. Jia, Y., et al., *Strong and reversible modulation of carbon nanotube–silicon heterojunction solar cells by an interfacial oxide layer.* Physical Chemistry Chemical Physics, 2012. **14**(23): p. 8391-8396.
109. Imran, H. and N.Z. Butt, *Computational study of hybrid nanomaterial/insulator/silicon solar cells.* IEEE Transactions on Electron Devices, 2015. **62**(10): p. 3111-3116.
110. Ong, P.-L., W.B. Euler, and I.A. Levitsky, *Hybrid solar cells based on single-walled carbon nanotubes/Si heterojunctions.* Nanotechnology, 2010. **21**(10): p. 105203.
111. Schroder, D.K., N.R. Thomas, and J.C. Swartz, *Free carrier absorption in silicon.* Solid-State Circuits, IEEE Journal of, 1978. **13**(1): p. 180-187.
112. Spitzer, W. and H. Fan, *Determination of optical constants and carrier effective mass of semiconductors.* Physical Review, 1957. **106**(5): p. 882.

113. Li, X., et al., *Charge Transfer from Carbon Nanotubes to Silicon in Flexible Carbon Nanotube/Silicon Solar Cells.* Small, 2017. **13**(48): p. 1702387.
114. Bindl, D.J., et al., *Free carrier generation and recombination in polymer-wrapped semiconducting carbon nanotube films and heterojunctions.* The Journal of Physical Chemistry Letters, 2013. **4**(21): p. 3550-3559.
115. Sinha, D. and J.U. Lee, *Ideal graphene/silicon Schottky junction diodes.* Nano letters, 2014. **14**(8): p. 4660-4664.
116. Li, R., et al., *Polymethylmethacrylate coating on aligned carbon nanotube–silicon solar cells for performance improvement.* Journal of Materials Chemistry A, 2014. **2**(12): p. 4140-4143.
117. Chattopadhyay, S., et al., *Anti-reflecting and photonic nanostructures.* Materials Science and Engineering: R: Reports, 2010. **69**(1): p. 1-35.
118. Li, X., X. Yu, and Y. Han, *Polymer thin films for antireflection coatings.* Journal of Materials Chemistry C, 2013. **1**(12): p. 2266-2285.
119. Zhong, S., et al., *Influence of the texturing structure on the properties of black silicon solar cell.* Solar Energy Materials and Solar Cells, 2013. **108**: p. 200-204.
120. Xia, Y., et al., *A novel method to produce black silicon for solar cells.* Solar Energy, 2011. **85**(7): p. 1574-1578.
121. Liu, Y., et al., *Hierarchical robust textured structures for large scale self-cleaning black silicon solar cells.* Nano Energy, 2014. **3**: p. 127-133.
122. Petterson, M.K., et al., *On Field-Effect Photovoltaics: Gate Enhancement of the Power Conversion Efficiency in a Nanotube/Silicon-Nanowire Solar Cell.* ACS Applied Materials Interfaces, 2015. **7**(38): p. 21182-21187.
123. Hsu, C.-H., et al., *Fabrication and characteristics of black silicon for solar cell applications: An overview.* Materials Science in Semiconductor Processing, 2014. **25**: p. 2-17.
124. Yu, L., et al., *Pyramid-Textured Antireflective Silicon Surface In Graphene Oxide/Single-Wall Carbon Nanotube–Silicon Heterojunction Solar Cells.* Energy Environmental Materials, 2018.
125. Pettit, R., C. Brinker, and C. Ashley, *Sol-gel double-layer antireflection coatings for silicon solar cells.* Solar Cells, 1985. **15**(3): p. 267-278.
126. Dimitrov, V. and S. Sakka, *Electronic oxide polarizability and optical basicity of simple oxides. I.* Journal of Applied Physics, 1996. **79**(3): p. 1736-1740.
127. Honsberg, C.B., S. *PV CDROM*. [Online reference book] 2014 [cited 2014 September 2014]; Available from: http://www.pveducation.org/pvcdrom.
128. Tune, D.D., et al., *Single-Walled Carbon Nanotube/Polyaniline/n-Silicon Solar Cells: Fabrication, Characterization, and Performance Measurements.* ChemSusChem, 2013. **6**(2): p. 320-327.
129. Wang, W. and E.A. Schiff, *Polyaniline on crystalline silicon heterojunction solar cells.* Applied Physics Letters, 2007.
130. Cardenas, J., et al., *A conducting polymer–silicon heterojunction as a new ultraviolet photodetector.* Applied Surface Science, 2008. **255**(3): p. 688-690.
131. Yu, L., et al., *Application of polymer interlayers in silicon–carbon nanotube heterojunction solar cells.* ChemNanoMat, 2015. **1**(2): p. 115-121.
132. Yu, L., et al., *Application of Hole-Transporting Materials as the Interlayer in Graphene Oxide/Single-Wall Carbon Nanotube Silicon Heterojunction Solar Cells.* Australian Journal of Chemistry, 2017. **70**(11): p. 1202-1211.
133. Pham, H.D., et al., *Thienylvinylenethienyl and Naphthalene Core Substituted with Triphenylamines—Highly Efficient Hole Transporting Materials and Their Comparative Study for Inverted Perovskite Solar Cells.* Solar RRL, 2017. **1**(8): p. 1700105.
134. Kwon, Y.S., et al., *Chemical compatibility between a hole conductor and organic dye enhances the photovoltaic performance of solid-state dye-sensitized solar cells.* Journal of Materials Chemistry A, 2012. **22**(17): p. 8641-8648.

135. Xu, W., et al., *High-Efficiency Large-Area Carbon Nanotube-Silicon Solar Cells.* Advanced Energy Materials, 2016. **6**(12): p. 1600095.
136. Yu, L., et al., *Optimization of the Metal Front Contact Design for Single-Walled Carbon Nanotube-Silicon Heterojunction Solar Cells.* Solar RRL, 2017. **1**(2).
137. Shi, J., et al., *Interfaces in perovskite solar cells.* Small, 2015. **11**(21): p. 2472-2486.
138. Maennig, B., et al., *Organic p-i-n solar cells.* Applied Physics A, 2004. **79**(1): p. 1-14.
139. Tune, D.D.S., J G., *Effect of Nanotube Film Thickness on the Performance of Nanotube-Silicon Hybrid Solar Cells.* Nanomaterials 2013. **3**(4): p. 655-673.
140. Deb, S. and B. Ghosh, *Series resistance and optimum grid design for a thin film solar cell of rectangular shape.* Solar Cells, 1984. **13**(2): p. 145-162.
141. Ong, P.-L.E., W B. Levitsky, I A., *Hybrid Solar Cells Based on Single-Walled Carbon Nanotubes/Si Heterojunctions.* Nanotechnology, 2010. **21**(10): p. 105203.
142. Gruner, G., *Carbon nanotube films for transparent and plastic electronics.* J. Mater. Chem., 2006. **16**(35): p. 3533-3539.
143. Wu, Z., et al., *Transparent, conductive carbon nanotube films.* Science, 2004. **305**(5688): p. 1273-1276.
144. Hu, H., et al., *Nitric acid purification of single-walled carbon nanotubes.* The Journal of Physical Chemistry B, 2003. **107**(50): p. 13838-13842.
145. Behnam, A., et al., *Experimental characterization of single-walled carbon nanotube film-Si Schottky contacts using metal-semiconductor-metal structures.* Applied Physics Letters, 2008. **92**(24): p. 243116.
146. Hu, L., D. Hecht, and G. Grüner, *Percolation in transparent and conducting carbon nanotube networks.* Nano Letters, 2004. **4**(12): p. 2513-2517.
147. Zhang, X., et al., *Photoactuators and motors based on carbon nanotubes with selective chirality distributions.* Nature communications, 2014. **5**.
148. Park, S., et al., *Large-Area Assembly of Densely Aligned Single-Walled Carbon Nanotubes Using Solution Shearing and Their Application to Field-Effect Transistors.* Advanced Materials, 2015. **27**(16): p. 2656-2662.
149. Tune, D.D., et al., *Aligned carbon nanotube thin films from liquid crystal polyelectrolyte inks.* ACS applied materials & interfaces, 2015. **7**(46): p. 25857-25864.
150. Bradford, P.D., et al., *A novel approach to fabricate high volume fraction nanocomposites with long aligned carbon nanotubes.* Composites Science and Technology, 2010. **70**(13): p. 1980-1985.
151. Wang, D., et al., *Highly oriented carbon nanotube papers made of aligned carbon nanotubes.* Nanotechnology, 2008. **19**(7): p. 075609.
152. Bacsa, W., et al., *Aligned carbon nanotube films: production and optical and electronic properties.* Science, 1995. **268**(5212): p. 845-847.
153. Ren, L., et al., *Carbon nanotube terahertz polarizer.* Nano letters, 2009. **9**(7): p. 2610-2613.
154. Wang, K., et al., *Super-Aligned Carbon Nanotube Films as Current Collectors for Lightweight and Flexible Lithium Ion Batteries.* Advanced Functional Materials, 2013. **23**(7): p. 846-853.
155. Shimoda, H., et al., *Self-assembly of carbon nanotubes.* Advanced Materials, 2002. **14**(12): p. 899.
156. Ko, H. and V.V. Tsukruk, *Liquid-crystalline processing of highly oriented carbon nanotube arrays for thin-film transistors.* Nano letters, 2006. **6**(7): p. 1443-1448.
157. Engel, M., et al., *Thin film nanotube transistors based on self-assembled, aligned, semiconducting carbon nanotube arrays.* Acs Nano, 2008. **2**(12): p. 2445-2452.
158. Joo, Y., et al., *Dose-Controlled, Floating Evaporative Self-assembly and Alignment of Semiconducting Carbon Nanotubes from Organic Solvents.* Langmuir, 2014. **30**(12): p. 3460-3466.
159. Olivier, J.H., et al., *Ionic Self-Assembly Provides Dense Arrays of Individualized, Aligned Single-Walled Carbon Nanotubes.* Angewandte Chemie, 2013. **125**(49): p. 13318-13323.

160. Tune, D.D.F., B.S., *A simple, versatile and universal method of aligning carbon nanotubes in ultra-smooth thin films.* Submitted, 2015.
161. Paredes, J. and M. Burghard, *Dispersions of individual single-walled carbon nanotubes of high length.* Langmuir, 2004. **20**(12): p. 5149-5152.
162. Collins, P.G., et al., *Extreme oxygen sensitivity of electronic properties of carbon nanotubes.* science, 2000. **287**(5459): p. 1801-1804.
163. Li, X.H., J-S. Nejeti, S. McMillon, L. Huang, S. Osuji, C.O. Hazari, N. Taylor, A.D., *The Role of HF in Oxygen Removal from Carbon Nanotubes: Implications for High Performance Carbon Electronics.* Nano Letters, 2014. **Accepted**.
164. Li, Z.K., V P. Saini, V. Xu, Y. Dervishi, E. Salamo, G J. Biris, A R. Biris, A S. , *Light-Harvesting Using High Density p-type Single Wall Carbon Nanotube/n-type Silicon Heterojunctions.* ACS Nano, 2009. **3**(6): p. 1407-1414.
165. Jia, Y.C., A. Bai, X. Li, Z. Zhang, L. Guo, N. Wei, J. Wang, K. Zhu, H. Wu, D. Ajayan, P M. , *Achieving High Efficiency Silicon-Carbon Nanotube Heterojunction Solar Cells by Acid Doping.* Nano Letters, 2011. **11**(5): p. 1901-1905.
166. Jia, Y.L., P. Gui, X. Wei, J. Wang, K. Zhu, H. Wu, D. Zhang, L. Cao, A. Xu, Y., *Encapsulated Carbon Nanotube-Oxide-Silicon Solar Cells with Stable 10% Efficiency.* Applied Physics Letters, 2011. **98**(13): p. 133115.
167. De Nicola, F., et al., *100% internal quantum efficiency in polychiral single-walled carbon nanotube bulk heterojunction/silicon solar cells.* Carbon, 2017. **114**: p. 402-410.
168. Corletto, A., et al., *Direct-Patterning SWCNTs Using Dip Pen Nanolithography for SWCNT/Silicon Solar Cells.* Small, 2018. **14**(16): p. 1800247.
169. Jia, Y.C., A. Kang, F. Li, P. Gui, X. Zhang, L. Shi, E. Wei, J. Wang, K. Zhu, H. Wu, D., *Strong and Reversible Modulation of Carbon Nanotube-Silicon Heterojunction Solar Cells by an Interfacial Oxide Layer.* Phys. Chem. Chem. Phys., 2012. **14**: p. 8391-8396.
170. De Nicola, F., et al., *Record efficiency of air-stable multi-walled carbon nanotube/silicon solar cells.* Carbon, 2016. **101**: p. 226-234.
171. Yu, L., et al., *Heterojunction solar cells based on silicon and composite films of graphene oxide and carbon nanotubes.* J ChemSusChem, 2015. **8**(17): p. 2940-2947.
172. Marcano, D.C., et al., *Improved synthesis of graphene oxide.* ACS nano, 2010. **4**(8): p. 4806-4814.
173. Pham, H.D., et al., *One step facile synthesis of a novel anthanthrone dye-based, dopant-free hole transporting material for efficient and stable perovskite solar cells.* Journal of Materials Chemistry C, 2018.
174. Wijeyasinghe, N., et al., *Copper (I) Thiocyanate (CuSCN) Hole-Transport Layers Processed from Aqueous Precursor Solutions and Their Application in Thin-Film Transistors and Highly Efficient Organic and Organometal Halide Perovskite Solar Cells.* Advanced Functional Materials, 2017. **27**(35): p. 1701818.
175. Liu, L., et al., *Microwave dielectric properties of carbon nanotube composites*, in *Carbon nanotubes*. 2010, IntechOpen.
176. Arvanitidis, J., et al., *Pressure screening in the interior of primary shells in double-wall carbon nanotubes.* Physical Review B, 2005. **71**(12): p. 125404.
177. Pfeiffer, R., et al., *Unusual high degree of unperturbed environment in the interior of single-wall carbon nanotubes.* Physical review letters, 2003. **90**(22): p. 225501.
178. Dresselhaus, M., G. Dresselhaus, and R. Saito, *Physics of carbon nanotubes.* Carbon, 1995. **33**(7): p. 883-891.
179. Ren, W., et al., *Morphology, diameter distribution and Raman scattering measurements of double-walled carbon nanotubes synthesized by catalytic decomposition of methane.* Chemical Physics Letters, 2002. **359**(3): p. 196-202.
180. Chen, C.-y., et al., *Preparation and Properties of Double-Sided AgNWs/PVC/AgNWs Flexible Transparent Conductive Film by Dip-Coating Process.* Nanoscale Research Letters, 2015. **10**(1): p. 315.

181. Hecht, D.S., et al., *High conductivity transparent carbon nanotube films deposited from superacid.* Nanotechnology, 2011. **22**(7): p. 075201.
182. Moore, K.E., et al., *Comparison of double-walled with single-walled carbon nanotube electrodes by electrochemistry.* Carbon, 2011. **49**(8): p. 2639-2647.
183. Stolz, B.W., D.D. Tune, and B.S. Flavel, *The effect of dry shear aligning of nanotube thin films on the photovoltaic performance of carbon nanotube–silicon solar cells.* Beilstein Journal of Nanotechnology, 2016. **7**(1): p. 1486-1491.
184. Tune, D., et al., *Dry shear aligning: a simple and versatile method to smooth and align the surfaces of carbon nanotube thin films.* Nanoscale, 2016. **8**(6): p. 3232-3236.
185. DeHeer, W.A., et al., *Aligned carbon nanotube films: production and optical and electronic properties.* Science, 1995. **268**(5212): p. 845-847.
186. Giancane, G., et al., *Aligning Single‐Walled Carbon Nanotubes By Means Of Langmuir–Blodgett Film Deposition: Optical, Morphological, and Photo‐electrochemical Studies.* Advanced Functional Materials, 2010. **20**(15): p. 2481-2488.
187. Cao, Q., et al., *Arrays of single-walled carbon nanotubes with full surface coverage for high-performance electronics.* Nature Nanotechnology, 2013. **8**(3): p. 180.
188. He, X., et al., *Wafer-scale monodomain films of spontaneously aligned single-walled carbon nanotubes.* Nature Nanotechnology, 2016. **11**(7): p. 633.
189. Onsager, L., *The effects of shape on the interaction of colloidal particles.* Annals of the New York Academy of Sciences, 1949. **51**(4): p. 627-659.
190. Song, W., I.A. Kinloch, and A.H. Windle, *Nematic liquid crystallinity of multiwall carbon nanotubes.* Science, 2003. **302**(5649): p. 1363-1363.
191. Moroi, Y., K. Motomura, and R. Matuura, *The critical micelle concentration of sodium dodecyl sulfate-bivalent metal dodecyl sulfate mixtures in aqueous solutions.* Journal of Colloid Interface Science, 1974. **46**(1): p. 111-117.
192. Yu, L., C. Shearer, and J. Shapter, *Recent development of carbon nanotube transparent conductive films.* Chemical Reviews, 2016. **116**(22): p. 13413-13453.
193. Ferrari, A.C., et al., *Raman spectrum of graphene and graphene layers.* Physical review letters, 2006. **97**(18): p. 187401.
194. Feng, J.-M. and Y.-J. Dai, *Water-assisted growth of graphene on carbon nanotubes by the chemical vapor deposition method.* Nanoscale, 2013. **5**(10): p. 4422-4426.
195. Tuschel, D., *Selecting an excitation wavelength for Raman spectroscopy.* Spectroscopy, 2016.
196. Rigoni, F., et al., *A cross-functional nanostructured platform based on carbon nanotube-Si hybrid junctions: where photon harvesting meets gas sensing.* Scientific reports, 2017. **7**: p. 44413.
197. Le Borgne, V., L. Gautier, and M. El Khakani, *Figure of merit based maximization of the quantum efficiency of (single-wall-carbon-nanotubes/n-type silicon) hybrid photovoltaic devices.* Applied Physics Letters, 2013. **103**(7): p. 073103.
198. Schmidt, J., et al., *Surface passivation of high‐efficiency silicon solar cells by atomic‐layer‐deposited Al2O3.* Progress in Photovoltaics: Research Applications, 2008. **16**(6): p. 461-466.
199. Harris, J.M., et al., *Impact of SWCNT processing on nanotube-silicon heterojunctions.* Nanoscale, 2016. **8**(15): p. 7969-7977.
200. Chiechi, R.C., et al., *Eutectic Gallium–Indium (EGaIn): A Moldable Liquid Metal for Electrical Characterization of Self‐Assembled Monolayers.* Angewandte Chemie, 2008. **120**(1): p. 148-150.
201. Eastment, R. and C. Mee, *Work function measurements on (100),(110) and (111) surfaces of aluminium.* Journal of Physics F: Metal Physics, 1973. **3**(9): p. 1738.
202. Kumm, J., et al., *Adhesion quality of evaporated aluminum layers on passivation layers for rear metallization of silicon solar cells.* Thin Solid Films, 2016. **612**: p. 393-399.
203. Dirnstorfer, I. and T. Mikolajick, *Dielectric Nanomaterials for Silicon Solar Cells*, in *Nanomaterials for Sustainable Energy*, Q. Li, Editor. 2016. p. 41-94.

204. Blankenship, R.E., et al., *Comparing photosynthetic and photovoltaic efficiencies and recognizing the potential for improvement.* Science, 2011. **332**(6031): p. 805-809.
205. Morita, M., et al., *Growth of native oxide on a silicon surface.* Journal of Applied Physics, 1990. **68**(3): p. 1272-1281.
206. Belser, R.B., *Alloying behavior of thin bimetal films, simultaneously or successively deposited.* Journal of Applied Physics, 1960. **31**(3): p. 562-570.
207. Weaver, C. and L. Brown, *Diffusion in evaporated films of gold-aluminium.* The Philosophical Magazine: A Journal of Theoretical Experimental and Applied Physics, 1962. **7**(73): p. 1-16.
208. Bishop, C.A. *Oxidation of Aluminium*. Available from: http://www.cabuk1.co.uk/FAQ%207%20Oxidation%20of%20aluminium.pdf.
209. Semaltianos, N., *Thermally evaporated aluminium thin films.* Applied surface science, 2001. **183**(3-4): p. 223-229.
210. Li, X., Z. Lv, and H. Zhu, *Carbon/Silicon Heterojunction Solar Cells: State of the Art and Prospects.* Advanced Materials, 2015. **27**(42): p. 6549-6574.
211. Williams, E.L., et al., *Conducting polymer and hydrogenated amorphous silicon hybrid solar cells.* Applied Physics Letters, 2005. **87**(22): p. 223504.
212. Shiu, S.-C., et al., *Morphology dependence of silicon nanowire/poly (3, 4-ethylenedioxythiophene): poly (styrenesulfonate) heterojunction solar cells.* Chemistry of Materials, 2010. **22**(10): p. 3108-3113.
213. Ozdemir, B., et al., *Silicon nanowire-poly (3, 4-ethylenedioxythiophene)-poly (styrenesulfonate) heterojunction solar cells.* Applied Physics Letters, 2011. **99**(11): p. 113510.
214. Monkman, A., et al., *Electronic energy levels of polyaniline.* Journal of Physics D: Applied Physics, 1987. **20**(11): p. 1337.
215. Pattanasattayavong, P., et al., *Study of the hole transport processes in solution-processed layers of the wide bandgap semiconductor copper (I) thiocyanate (CuSCN).* Advanced Functional Materials, 2015. **25**(43): p. 6802-6813.
216. Pattanasattayavong, P., et al., *Hole-transporting transistors and circuits based on the transparent inorganic semiconductor copper (I) thiocyanate (CuSCN) processed from solution at room temperature.* Advanced Materials, 2013. **25**(10): p. 1504-1509.
217. Petti, L., et al., *Solution-processed p-type copper (I) thiocyanate (CuSCN) for low-voltage flexible thin-film transistors and integrated inverter circuits.* Applied Physics Letters, 2017. **110**(11): p. 113504.
218. Wijeyasinghe, N. and T.D. Anthopoulos, *Copper (I) thiocyanate (CuSCN) as a hole-transport material for large-area opto/electronics.* Semiconductor Science Technology, 2015. **30**(10): p. 104002.
219. Cotton, F.A. and G. Wilkinson, *Advanced Inorganic Chemistry*. 1980: John Wiley & Sons.
220. Tan, Z.a., et al., *Efficient and stable polymer solar cells with solution-processed molybdenum oxide interfacial layer.* Journal of Materials Chemistry A, 2013. **1**(3): p. 657-664.
221. Li, X., et al., *Room-temperature solution-processed molybdenum oxide as a hole transport layer with Ag nanoparticles for highly efficient inverted organic solar cells.* Journal of Materials Chemistry A, 2013. **1**(22): p. 6614-6621.
222. Michelmore, A., et al., *Where physics meets chemistry: Thin film deposition from reactive plasmas.* Frontiers of Chemical Science Engineering, 2016. **10**(4): p. 441-458.
223. Wang, L., et al., *Long-range surface plasmon resonance sensors fabricated with plasma polymerized fluorocarbon thin films.* Sensors Actuators B: Chemical, 2015. **215**: p. 368-372.
224. Jiang, Z. and Z.-J. Jiang, *Plasma techniques for the fabrication of polymer electrolyte membranes for fuel cells.* Journal of Membrane Science, 2014. **456**: p. 85-106.
225. Hu, J., et al., *Plasma graft-polymerization for synthesis of highly stable hydroxide exchange membrane.* Journal of Power Sources, 2014. **248**: p. 831-838.

226. Lecoq, E., et al., *Plasma polymerization of APTES to elaborate nitrogen containing organosilicon thin films: influence of process parameters and discussion about the growing mechanisms.* Plasma Processes Polymers, 2013. **10**(3): p. 250-261.
227. Lee, S., et al., *Durable soft neural micro-electrode coating by an electrochemical synthesis of PEDOT: PSS/graphene oxide composites.* Electrochimica Acta, 2019. **313**: p. 79-90.
228. Yu, L., et al., *Ti3C2Tx (MXene)-Silicon Heterojunction for Efficient Photovoltaic Cells.* Advanced Energy Materials, 2019: p. 1901063.
229. Wang, D., et al., *Chemical formation of soft metal electrodes for flexible and wearable electronics.* Chemical Society Reviews, 2018. **47**(12): p. 4611-4641.
230. Shay, T., O.D. Velev, and M.D. Dickey, *Soft electrodes combining hydrogel and liquid metal.* Soft matter, 2018. **14**(17): p. 3296-3303.